(1)

Bulletin 45
(Part 5 of 5 Parts)

THE SHOCK AND VIBRATION BULLETIN

Part 5
Isolation, Damping, Dynamic Analysis

JUNE 1975

A Publication of
THE SHOCK AND VIBRATION
INFORMATION CENTER
Naval Research Laboratory, Washington, D.C.

Office of
The Director of Defense
Research and Engineering

DISCLAIMER NOTICE

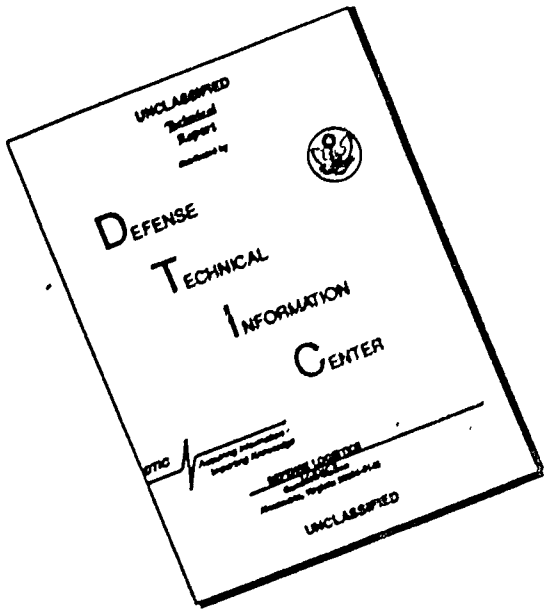

THIS DOCUMENT IS BEST QUALITY AVAILABLE. THE COPY FURNISHED TO DTIC CONTAINED A SIGNIFICANT NUMBER OF PAGES WHICH DO NOT REPRODUCE LEGIBLY.

SYMPOSIUM MANAGEMENT

THE SHOCK AND VIBRATION INFORMATION CENTER

Henry C. Pusey, Director
Edward H. Schell
Rudolph H. Volin
J. Gordan Showalter

Bulletin Production

Graphic Arts Branch, Technical Information Division,
Naval Research Laboratory

Bulletin 45
(Part 5 of 5 Parts)

THE SHOCK AND VIBRATION BULLETIN

JUNE 1975

A Publication of
THE SHOCK AND VIBRATION
INFORMATION CENTER
Naval Research Laboratory, Washington, D.C.

The 45th Symposium on Shock and Vibration was held at the Dayton Convention Center, Dayton, Ohio on October 22-25, 1974. The Air Force Flight Dynamics Laboratory, Air Force Materials Laboratory and Aeronautical Systems Division Air Force Systems Command, Wright-Patterson AFB, Ohio, were hosts.

Office of
The Director of Defense
Research and Engineering

CONTENTS

PAPERS APPEARING IN PART 5

Isolation and Damping

Dynamic Analysis

Continued

PAPERS APPEARING IN PART 2

Invited Papers

Panel Sessions

Seismic

PAPERS APPEARING IN PART 4

Impact

Packaging and Shipping

Blast and Impulsive Loading

ISOLATION AND DAMPING

IMPACT ON COMPLEX MECHANICAL STRUCTURES

S. F. Jan
Bechtel Power Corporation
Houston, Texas

and

E. A. Ripperger
The University of Texas at Austin
Austin, Texas

The principal purpose of this study has been to develop a procedure for analyzing the response of complex structures to impact and to provide a computer code for making the necessary computations. Attention has been focused specifically on the displacements, velocities and accelerations produced at various points in military vehicles subjected to ground impact in airdrop operations.

The vehicle is modeled by a lumped parameter (spring-mass) system. Using the finite element method, a set of equations of motion is formulated for this model. Then these equations are solved numerically by the Runge-Kutta method. A model for representing a specific vehicle, namely the M-37 military truck cushioned for an airdrop is used to illustrate the procedure. Some of the physical constants for the model are modified as required to bring the computed displacements and accelerations at various points in the model into agreement with measured values. It is found that the response of a structure properly cushioned and subjected to impact loading is not sensitive to the elastic properties of the interconnecting members. Thus, the development of a suitable lumped parameter model of a given vehicle is simplified. However, special attention should be given to the more massive and rigid components of the vehicle such as, for example, the engine.

Experimental results show that more than one fourth of the system energy is dissipated through the structural damping. Hence, damping must be included in the equations of motion.

The most essential factor affecting the dynamic response of the system has been found to be the force applied as a result of the impact. In the example used, this force is applied by the cushioning system.

INTRODUCTION

The finite element method appears to be ideally suited to the problem under consideration, namely, the computation of the displacements, velocities and accelerations at selected points in a structure subjected to an impulsive loading. To apply this method of analysis one must first devise a conceptual representation of the continuous structure as an assemblage of structural elements interconnected at nodal points. The idealized structure is assumed to be acted on by external equivalent forces and to possess equivalent inertia properties only at the nodal points. Thus the continuous structure is replaced, for analytical purposes, by a lumped parameter system. The accuracy of the predicted dynamic response of a structure will depend on how well the structure is represented

by the selected lumped-parameter model. It has been reported [1] that even for a very simple beam or uniform plate with boundary conditions which can be exactly expressed mathematically, errors in the predicted responses can easily be as much as 35 percent. Although no investigation of the validity of lumped parameter models for complex structures, such as vehicles, has been reported in the literature, it may be assumed that discrepancies of even more than 35% can be expected for poorly represented structures. The general details of the finite element method have been discussed in the literature[2]. However, the nature of the model which will best represent a structure such as a vehicle, with its varied elements, irregular geometry and discrete masses, is not at all clear. The primary objective in this study will be to select a model and then determine by computation and by experiment how valid the model is. It is expected that some suitable rules can be formulated regarding the representation of vehicles by lumped parameter models. A model for representing a specific vehicle, namely the M-37 military truck, cushioned for an airdrop is used to illustrate the procedure. This particular vehicle was selected because it has been dropped 20 times and a great deal of information regarding its response to impact has been collected. The cushioning system used for the drops that were instrumented particularly for this study evolved and was perfected during those 20 drops. Consequently it was not expected that the results of this study would lead to any changes in the design of that cushioning system. The objective, as indicated above, was not to find out how to model this specific vehicle but rather to formulate rules that would apply to the modeling of any vehicle.

In the procedure followed for this study, the lumped parameter model for the M-37 is first developed. Then the equations of motion of the model are formulated following standard finite element methods. These equations, with appropriate initial conditions are then solved using the Runge-Kutta method.* Some important factors such as structural elastic properties, damping, and impulse loading which affect the dynamic response are investigated. Finally, an experimental program of actual truck drop tests is carried out, and the results are compared with computed results. In the analysis of the mathematical model, the concept of linear transformation is extensively used. Linear transformation techniques streamline and simplify considerably the procedures involved in the analysis. It should be mentioned here that the computer program developed for the vehicle is also applicable to other complex structures.

MATHEMATICAL MODEL

A vehicle such as the M-37 truck may be represented as a first approximation by the model shown in Fig. 1. In this model the engine, transmission, transfer case, differentials and wheels are treated as discrete masses. The mass of the winch is assumed to be distributed uniformly along the front transverse frame member, and the mass of the remaining parts of the structure, and the load on the truckbed are assumed to be distributed uniformly along the two main longitudinal and the remaining transverse members of the truck frame. The adoption of this model is, however, quite arbitrary. Many other arrangements of masses would, no doubt, be equally acceptable.

When a structure such as this vehicle is to be intentionally subjected to an impact, as in an airdrop, cushioning is provided to reduce the severity of the shock produced by the impact. Usually all of the discrete masses shown in Fig. 1 would be cushioned independently, if possible. For the M-37 truck the engine is not cushioned independently, partly because it is shock mounted on the frame, and partly because of geometrical and structural problems. The engine is supported on rubber cushions, or shock mounts at three points, one in front and two in the rear. The action of these mounts can be represented by the spring-damper system shown in Fig. 2. The stiffness and the damping capacity of a mount depends on many factors such as the hardness of the rubber, the shape, and the age [3]. Rather than try to determine a precise set of values for the M-37 mounts, values of 20,000 lb/in. for k and 60% of critical for the damping were arbitrarily assumed. Later these values were varied to improve the "fit" between experimental observations and computed results.

The transmission is actually attached to the engine but since it can be cushioned independently, it has been assumed to be a mass which is attached to the engine by a very stiff element.

*Algorithms for this method are available in most computational facilities.

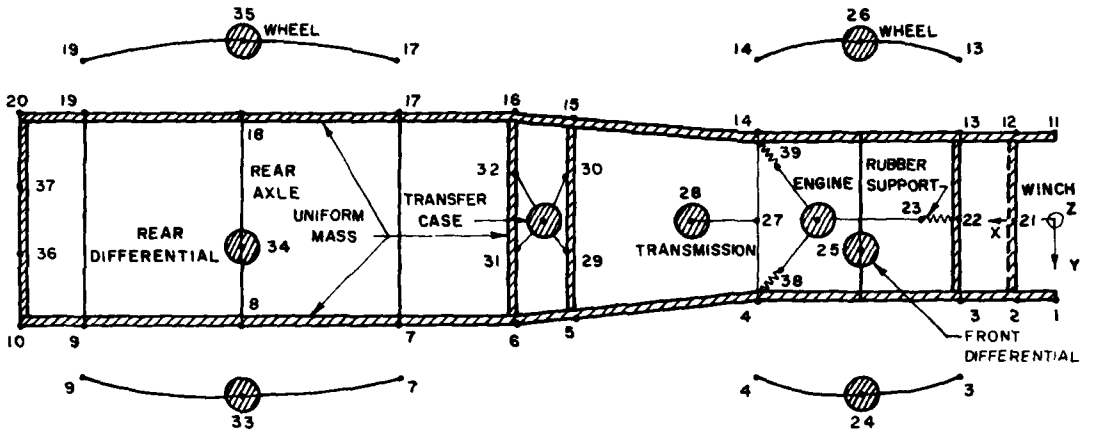

Figure 1 Lumped-Parameter Model - M-37 Truck

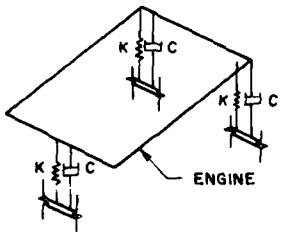

Figure 2 Engine Supports

The transfer case is supported at four points on two central cross frame members which act as spring supports for it.

Wheels and differentials are connected by the axles which in this analysis are assumed to be rigid, massless rods attached to leaf springs. Tires absorb considerable energy and this energy is given back in rebound. Also measured relative displacements between the rear axle and truck frame indicate that little energy can be dissipated through the four shock absorbers associated with the wheels during the impact. Consequently the shock absorbers are neglected and the vehicle is supported by the leaf springs in Fig. 3.

The spring constants K and damping factor C for the tire in Fig. 3 must be determined experimentally, or they must be estimated using whatever guidance is available. These quantities are initially assumed to be 7,000 lb/in. and 20% respectively.

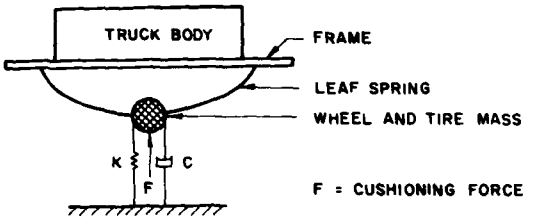

Figure 3 Suspension System of Vehicle

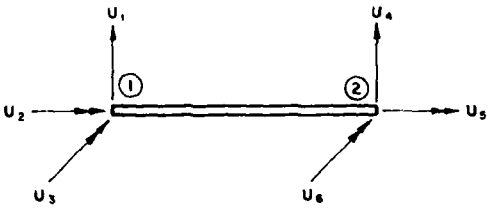

Figure 4 Element Displacements

The winch and the other distributed masses of the truck are cushioned with the two main longitudinal frame members. In the model shown in Fig. 1, all individual components are interconnected at the nodes numbered from 1 to 39. In the present study only a vertical, planar impact is considered. Consequently, each nodal point in the model is allowed to have only 3 degrees of freedom, consisting of one vertical translation and two planar rotations. Three degrees of freedom are associated with each end of all members as shown by the vectors, U_i, in Fig. 4.

ANALYSIS OF THE MODEL

For the model shown in Fig. 1 with assumed damping and subject to impact loading, the equation of motion can be written as:

$$\underline{\underline{M}}\,\ddot{\underline{q}} + \underline{\underline{C}}\,\dot{\underline{q}} + \underline{\underline{K}}\,\underline{q} = \underline{F}(t) \qquad (1)$$

where $\underline{\underline{M}}$, $\underline{\underline{C}}$ and $\underline{\underline{K}}$ are square matrices of inertia, damping and stiffness respectively and $\underline{F}(t)$ is the column matrix of cushion forces. The generalized displacement matrix $\underline{q}$ is numbered in sequence according to the joint numbers. For example, coordinates q_{3i-2}, q_{3i-1}, and q_{3i} are associated with the translatory and two rotattional motions about common datum axes, at the i^{th} nodal joint of the model. For example at joint 5, the coordinates are q_{15-2}, q_{15-1}, q_{15-0} or q_{13}, q_{14} and q_{15}.

The stiffness matrix $\underline{\underline{K}}$ of the complete element assembly is obtained by the direct stiffness method [4]. This method consists of first deriving the individual element stiffnesses in element coordinates, followed by a coordinate transformation and the subsequent superposition of each element stiffness so that the translational and rotational degrees of freedom of all elements which share a common nodal point are expressed in the same coordinates. The superposition of each transformed stiffness is accomplished by adding its individual terms into the complete stiffness matrix according to the element nodal point numbers. The same method can be employed to obtain the mass matrix $\underline{\underline{M}}$ and the force vector $\underline{F}$. Since the derivations of mass matrix $\underline{\underline{M}}$, stiffness matrix $\underline{\underline{K}}$, force vector $\underline{F}$ and damping matrix $\underline{\underline{C}}$ are quite lengthy and tedious only the end results are presented here. Readers interested in the details should consult reference 6.

The element coordinate scheme is shown in Fig. 5.

1. Element Displacement Functions

Consider a uniform structural element in the horizontal plane as shown in Fig. 5. The common datum (X, Y, Z) is established for all structural elements so that all displacements and corresponding forces will be referred to this common coordinate system. The origin of element coordinates (x, y, z) is located at node 1 with the o-x axis taken along the length of element and with the o-y and o-z axes as the principal axes of the element cross section.

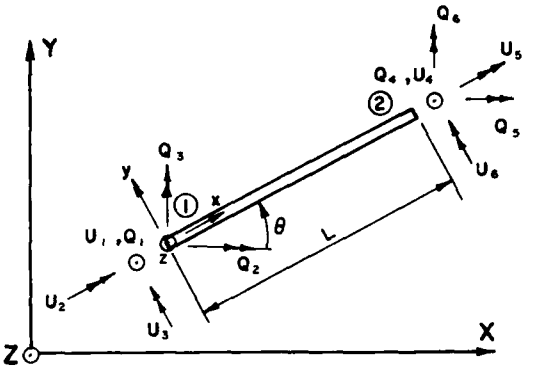

Figure 5 Element Coordinates

The column matrix $\underline{U}$ for this element, as mentioned before, consists of six displacements, two vertical (Z direction) deflections U_1 and U_4 and four rotations, U_2, U_3, U_5, and U_6. The displacement functions in element coordinates are w_x, w_y, and w_z. These are assumed to be functions of the coordinates x and y. They can be expressed in terms of the discrete displacements U by the relationship

$$\underline{W} = \underline{\underline{a}}\,\underline{U} \qquad (2)$$

where $\underline{\underline{a}}$ is a 3 x 6 matrix in terms of the non-dimensional element coordinates

$$r = \frac{x}{L} \qquad s = \frac{y}{L} \qquad t = \frac{z}{L} \qquad (3)$$

3. Element Mass Matrix

The element mass matrix is derived from the work done by the inertia force of the element during a virtual displacement. Thus

$$\delta W = \delta \underline{U}^T \left(\int_V \rho\, \underline{\underline{a}}\, \underline{\underline{a}}^T\, dV \right) \ddot{\underline{U}} \qquad (4)$$

where ρ is a density parameter. By analogy with the basic work expression

$$\underline{\underline{m}} = \int_V \rho\, \underline{\underline{a}}\, \underline{\underline{a}}^T\, dV \qquad (5)$$

where the integration would be performed over the whole volume of the element. Results of computations show that the effects of rotary and torsional inertia of the element during impact are negligible so these terms are eventually neglected.

3. Element Stiffness Matrix

The stress-strain relationship in matrix form is

$$\underline{S} = \underline{A}\ \underline{e} \tag{6}$$

where

$$\underline{S} = \begin{bmatrix} S_b \\ S_t \end{bmatrix} \quad \text{and} \quad \underline{A} = \begin{bmatrix} EI_y & o \\ o & GJ \end{bmatrix} \tag{7}$$

S_b and S_t are bending moment and twisting moment respectively, and $\underline{e}$ is total strain. By writing the expression for virtual strain energy and again using the analogy with the well known strain energy expression the element stiffness expression

$$\underline{k} = \int_0^L \underline{b}^T\ \underline{A}\ \underline{b}\ dx \tag{8}$$

is obtained.

4. Element End Forces

The force matrix is obtained by considering the virtual work done by the external forces when a virtual displacement δw occurs. Thus the equivalent concentrated force $\underline{f}$ at the element ends due to a distributed loading $\underline{p}$ over the element surface is

$$\underline{f} = \int_S \underline{a}^T\ \underline{p}\ ds \tag{9}$$

5. Linear Transformation

If the set of coordinates $\underline{q}$ with n degrees of freedom in the equation of motion Eq. (2) is a linear combination of a different set of coordinates $\underline{u}$ with m degrees of freedom,

$$\underline{q} = \underline{B}\ \underline{u} \tag{10}$$

then the mass, damping, stiffness and force matrices in u coordinates can be expressed in terms of q coordinates as follows:

$$\begin{aligned} \underline{M} &= \underline{B}^T\ \underline{M}\ \underline{B} \\ \underline{k} &= \underline{B}^T\ \underline{K}\ \underline{B} \\ \underline{f} &= \underline{B}^T\ \underline{F} \end{aligned} \tag{11}$$

The upper case matrices are in terms of the q coordinates.

A viscous damping force D can be expressed as

$$\underline{D} = -\underline{C}\ \dot{\underline{q}} \tag{12}$$

where $\underline{C}$ is the damping matrix in q coordinates. By means of the virtual work consideration again it may be shown that

$$\underline{c} = \underline{B}^T\ \underline{C}\ \underline{B} \tag{13}$$

where $\underline{c}$ is the damping matrix in u coordinates.

6. Transformation of Element Coordinates to Datum Coordinates

Since the element mass matrix $\underline{m}$, stiffness matrix $\underline{k}$, and end force vector $\underline{f}$ are initially calculated in local element coordinates, suitably oriented to minimize the computing effort, it is necessary to introduce transformation matrices changing the frame of reference from a local to a datum coordinate system. Consider again the element shown in Fig. 5. U_1 to U_6 are displacements in the direction of local coordinates x, y, z and Q_1 to Q_6 are displacements in the directions of datum coordinates XYZ. θ is the angle between the x and X axes. The relationship between the displacements $\underline{U}$ and displacements $\underline{Q}$ is

$$\underline{U} = \underline{B}\ \underline{Q} \tag{14}$$

where

$$\underline{B} = \begin{bmatrix} 1 & 0 & 0 & & & \\ 0 & \cos\theta & \sin\theta & & & \\ 0 & -\sin\theta & \cos\theta & & & \\ & & & 1 & 0 & 0 \\ & & & 0 & \cos\theta & \sin\theta \\ & & & & -\sin\theta & \cos\theta \end{bmatrix} \tag{15}$$

The element mass matrix $\underline{m}$,* stiffness matrix $\underline{k}$,* and the force vector $\underline{f}$* in q- displacements can be obtained by using the transformations of Eqs. (11) and (12) as:

$$\begin{aligned} \underline{m}^* &= \underline{B}^T\ \underline{m}\ \underline{B} \\ \underline{k}^* &= \underline{B}^T\ \underline{k}\ \underline{B} \\ \underline{f}^* &= \underline{B}^T\ \underline{f} \end{aligned} \tag{16}$$

7. System of Assembled Structure

Since all element stiffness matrices, mass matrices and force vectors are now referred to the common datum, the stiffness matrix, mass matrix and force vector of the complete element assemblage can be obtained by the direct stiffness method as mentioned previously. The concentrated masses at nodal joints such as transmission, differentials and wheels are simply

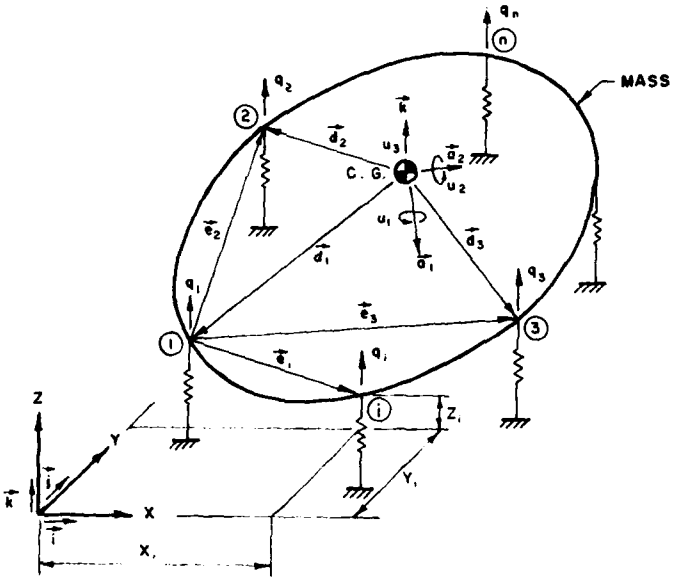

Figure 6 Mass Supported at Several Points

added to the corresponding diagonal terms in the assembled mass matrix. The concentrated cushion forces applied at nodal points are also simply added to the corresponding terms in the system force vector. However, the discrete masses such as the engine and transfer case which connect several nodal points cannot be superimposed on the system directly. A special study of these masses is necessary.

8. Engine and Transfer Case

Since the engine, transfer case and similar masses are all supported at several nodal points, special consideration of these parts is required. Consider now a discrete mass supported by n-springs with coordinates $q_1 \ldots q_2$.

Since three points define a plane, q_1, q_2, and q_3, as generalized coordinates, sufficiently define the motions of mass. Let u_1, u_2, and u_3 be the rotations about the principal axes of mass and the vertical translation respectively. The relationships between coordinates q's and u's can be found in the following way:

Fig. 6 shows the system under consideration:

- $\vec{a}_1$, $\vec{a}_2$ = The unit vectors along two principal directions of the mass.
- $\vec{i}$, $\vec{j}$, $\vec{k}$ = unit vectors along datum coordinates X, Y, Z.
- X_i, Y_i, Z_i = coordinates of supports.
- $\vec{d}_1, \vec{d}_2, \vec{d}_3$ = position vectors of points where the springs attach to the mass, referred to the center of mass.
- $\vec{e}_i$ = vectors from support point q_i to q_2.

for small rotations,

$$\begin{bmatrix} q_1 \\ q_2 \\ q_3 \end{bmatrix} = \begin{bmatrix} \vec{a}_1 \times \vec{d}_1 \cdot \vec{k} & \vec{a}_2 \times \vec{d}_1 \cdot \vec{k} & 1 \\ \vec{a}_1 \times \vec{d}_2 \cdot \vec{k} & \vec{a}_2 \times \vec{d}_2 \cdot \vec{k} & 1 \\ \vec{a}_1 \times \vec{d}_3 \cdot \vec{k} & \vec{a}_2 \times \vec{d}_3 \cdot \vec{k} & 1 \end{bmatrix} \begin{bmatrix} u_1 \\ u_2 \\ u_3 \end{bmatrix} \qquad (17)$$

or $\underline{q} = \underline{\underline{A}}\ \underline{u}$

Thus

$$\underline{u} = \underline{\underline{A}}^{-1}\underline{q} = \underline{\underline{B}}\ \underline{q} \tag{18}$$

Where $\underline{\underline{B}} = \underline{\underline{A}}^{-1}$ (19)

If m_1, m_2, and m_3 are the mass moments of inertia and the mass, then the matrix of the discrete masses in the u coordinate system can be represented as:

$$\underline{\underline{m}} = \begin{bmatrix} m_1 & & 0 \\ & m_2 & \\ 0 & & m_3 \end{bmatrix}$$

According to the linear transformation (18), the mass matrix corresponding to the q coordinate system is:

$$\underline{\underline{m}}^* = \underline{\underline{B}}^T \underline{\underline{m}} \underline{\underline{B}} \tag{20}$$

If there are cushioning forces f_1, f_2, and f_3 directly applied in u_1, u_2, and u_3 directions, then the forces in the q_1, q_2, and q_3 directions are:

$$\underline{f}^* = \underline{\underline{B}}^T \underline{f} \tag{21}$$

Now the mass matrix $\underline{\underline{m}}^*$ can be added to the mass matrix of the complete element assemblage and the forces f* can be added to the system forces. It must be noted that before taking this step, the constraint coordinates q_4 through q_n should be eliminated from the system. To do this, first find a transformation matrix $\underline{\underline{B}}$ such that:

$$\begin{bmatrix} q_4 \\ \cdot \\ \cdot \\ \cdot \\ \cdot \\ \cdot \\ q_n \end{bmatrix} = \underline{\underline{B}} \begin{bmatrix} q_1 \\ \\ q_2 \\ \\ q_3 \end{bmatrix} \tag{22}$$

and then by linear transformation get the modified mass, stiffness and force matrix of the whole system.

The transformation matrix $\underline{\underline{B}}$ in Eq. (22) is formulated by finding all the expressions of q_4 through q_n in terms of q_1, q_2, and q_3. Consider now the displacement q_i as indicated in Fig. 6. The vectors from support 1 to 2, 3 and i can be expressed in the form

$$\vec{e}_i = (x_i - x_1)\vec{I} + (y_i - y_1)\vec{J} + (q_i - q_1)\vec{k}$$

Since supports 1, 2, 3 and i are in a plane,

$$\vec{e}_2 \times \vec{e}_3 \cdot \vec{e}_i = 0$$

or

$$\begin{vmatrix} x_2 - x_1 & y_2 - y_1 & q_2 - q_1 \\ x_3 - x_1 & y_3 - y_1 & q_3 - q_1 \\ x_i - x_1 & y_i - y_1 & q_i - q_1 \end{vmatrix} = 0 \tag{23}$$

Solving this equation for q_i results in

$$q_i = \frac{E_1 - E_2 + E_3}{E_3}\ q_1 - E_1 q_2 + E_2 q_3 \tag{24}$$

where

$$E_1 = \begin{vmatrix} x_3 - x_1 & y_3 - y_1 \\ x_i - x_1 & y_i - y_1 \end{vmatrix} \tag{25}$$

$$E_2 = \begin{vmatrix} x_2 - x_1 & y_2 - y_1 \\ x_i - x_1 & y_i - y_1 \end{vmatrix} \tag{26}$$

$$E_3 = \begin{vmatrix} x_2 - x_1 & y_2 - y_1 \\ x_3 - x_1 & y_3 - y_1 \end{vmatrix} \tag{27}$$

Thus all displacements q_4 through q_n can be expressed in terms of q_1, q_2, and q_3 simply by replacing the index i in the determinants E_1 and E_2 by the numbers 4 to n.

9. Static Condensation

If an element is not rigidly connected to another element, for example, a hinged connection, the element stiffness matrix, mass matrix and fixed end force vector must be modified. If some coordinates included in the static analysis are excluded from the dynamic analysis, or some coordinates with zero or very small mass must be removed from the equations of motion to avoid unreasonable numerical results (infinite values in computed accelerations), then the system mass matrix, stiffness matrix and system force vector must all be modified. All the modifications can be achieved by a static condensation technique[2]. By using this technique a transformation matrix similar to the matrix $\underline{\underline{B}}$ in Eq. (10) can be formulated. Then the modified matrices can be written in the format of Eq. (11).

The first step is to partition the mass matrix $\underline{\underline{M}}$, stiffness matrix $\underline{\underline{K}}$, force matrix $\underline{F}$ and displacement matrix $\underline{U}$ into:

$$\underline{\underline{M}} = \begin{bmatrix} \underline{\underline{M}}_{11} & \underline{\underline{M}}_{12} \\ \underline{\underline{M}}_{21} & \underline{\underline{M}}_{22} \end{bmatrix} \tag{28}$$

$$\underline{\underline{K}} = \begin{bmatrix} \underline{\underline{K}}_{11} & \underline{\underline{K}}_{12} \\ \underline{\underline{K}}_{21} & \underline{\underline{K}}_{22} \end{bmatrix} \tag{29}$$

$$\underline{F} = \begin{bmatrix} \underline{F}_1 \\ \underline{F}_2 \end{bmatrix} \tag{30}$$

$$\underline{U} = \begin{bmatrix} \underline{U}_1 \\ \underline{U}_2 \end{bmatrix} \tag{31}$$

The column matrix $\underline{U}_1$ refers to all the displacements that are to be retained, while $\underline{U}_2$ denotes all the remaining displacements which will not be employed in formulating the new equivalent matrices. The displacements $\underline{U}_2$ may be determined from the static equilibrium equation $\underline{F} = \underline{\underline{K}}\,\underline{U}$ by assuming that the forces $\underline{F}_2$ corresponding to the displacements $\underline{U}_2$ are all equal to zero. Hence:

$$\underline{U}_2 = -\underline{\underline{K}}_{22}^{-1}\,\underline{\underline{k}}_{21}\,\underline{U}_1 \tag{32}$$

Thus:

$$\underline{U} = \begin{bmatrix} \underline{\underline{I}} \\ \underline{\underline{K}}_{22}^{-1}\,\underline{\underline{K}}_{21} \end{bmatrix} \underline{U}_1 = \underline{\underline{B}}^*\,\underline{U}_1 \tag{33}$$

where $\underline{\underline{I}}$ is a unit matrix and

$$\underline{\underline{B}}^* = \begin{bmatrix} \underline{\underline{I}} \\ -\underline{\underline{K}}_{22}^{-1}\,\underline{\underline{K}}_{21} \end{bmatrix} \tag{34}$$

Thus the modified mass matrix M*, stiffness matrix K*, and force matrix F* for displacements $\underline{U}_1$ are obtained from Eq. (11) as:

$$\begin{aligned} M^* &= \underline{\underline{B}}^{*T}\underline{\underline{M}}\,\underline{\underline{B}}^*, \\ K^* &= \underline{\underline{B}}^{T}\underline{\underline{K}}\,\underline{\underline{B}}^*, \\ F^* &= \underline{\underline{B}}^{*T}\underline{F} \end{aligned} \tag{35}$$

10. Structural Damping

Until now the discussion of the damping matrix in the equations of motion Eq. (1) has been intentionally avoided. However, earlier experimental studies of the M-37 truck indicate that an appreciable amount of energy may be dissipated through internal friction within the truck body or at joints between frame elements. This damping matrix may be assumed to be proportional to the mass and stiffness matrices as:

$$\underline{\underline{C}} = a\,\underline{\underline{M}} + b\,\underline{\underline{K}} \tag{36}$$

where a and b are constants and can be determined so as to give reasonable damping in the system. If Eq. (36) is substituted into Eq.(1), the modified differential equation is obtained

$$\underline{\underline{M}}\,\ddot{\underline{q}} + (a\,\underline{\underline{M}} + b\,\underline{\underline{K}})\,\dot{\underline{q}} + \underline{\underline{K}}\,\underline{q} = \underline{F}(t). \tag{37}$$

NUMERICAL SOLUTION

1. Runge-Kutta Method

The equations of motion Eq.(37) can be solved numerically by using the Runge-Kutta method. However, the equation must first be decomposed into first order differential equations.

Premultiply all terms in the equations of motion Eq. (37) by $\underline{\underline{M}}^{-1}$ and eliminate the coefficient of $\ddot{\underline{q}}$. Thus

$$\ddot{\underline{q}} + (a\underline{\underline{I}} + b\underline{\underline{M}}^{-1}\underline{\underline{K}})\dot{\underline{q}} + \underline{\underline{M}}^{-1}\underline{\underline{K}}\,\underline{q} = \underline{\underline{M}}^{-1}\underline{F}(t) \tag{38}$$

where $\underline{\underline{I}}$ is a unit matrix, and all matrices are modified as discussed in the section on static condensation. By letting

$$\underline{u} = \dot{\underline{q}} \tag{39}$$

the set of equations (38) is then decomposed into 2 sets of first order ordinary differential equations:*

$$\begin{aligned} \dot{\underline{q}} &= \underline{u} \\ \dot{\underline{u}} &= \underline{\underline{M}}^{-1}\underline{F} - \underline{\underline{M}}^{-1}\underline{\underline{K}}\,\underline{q} - (a\underline{\underline{I}} + b\underline{\underline{M}}^{-1}\underline{\underline{K}})\underline{u} \end{aligned} \tag{40}$$

with initial conditions:

$$\underline{q} = \underline{q}_o \text{ and } \underline{u} = \dot{\underline{q}}_o \tag{41}$$

Equation (40) with initial conditions as expressed by Eq. (41) can be solved numerically by the Runge-Kutta [5] method.

2. Digital Computer Program

The required input data are nodal point coordinates, mass distribution, cushioning forces, initial displacements and velocities, damping coefficients,

*u should not be confused with a displacement. It is introduced here purely for convenience and is as defined by Eq. (39).

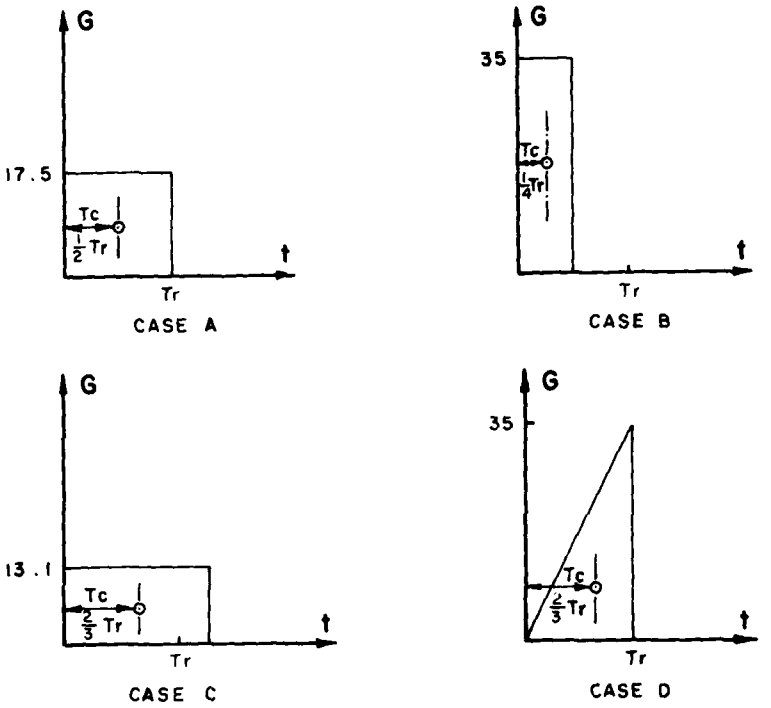

Figure 7 Impulse Shapes

and member properties such as cross sectional area, flexural rigidity EI, torsional rigidity GJ, and torsional inertia I_x. The computer program automatically generates the structural mass matrix, stiffness matrix and force matrix and then solves the equations of motion by the Runge-Kutta method. The displacements, velocity and acceleration at any coordinate at any time may be printed out. The printed out displacement is relative to the position where impact begins. From these displacements the relative displacement of any two points can be computed.

FACTORS AFFECTING THE RESPONSE TO IMPACT

The previous analysis shows that the dynamic response of a structure is dependent upon the nature of the applied forcing function, the elastic and inertia properties of the structure, and the damping characteristics of the system. By study of these factors, information on design of cushioning systems and the design of the structure itself may be obtained. Insight into the appropriateness of the lumped-parameter model should also be provided. In following sections, these factors are discussed in detail. The effects of the tires on the structural response to the impact, and the dynamic behavior of the engine on the rubber supports will also be considered.

1. Time Variation of the Applied Force

For the airdrop application toward which this study is oriented the applied force is essentially rectangular in time. Therefore a limited study has been made of the effects on response of the structure of variations in the amplitude and duration of the applied force. Three rectangular pulses and one triangular pulse, shown in Fig. 7, were selected for study. For simplicity, the area of each pulse was kept the same. Thus the momentum imparted to the structure is the same for each pulse. In order to simplify the analysis, the centroid position of the pulse has been chosen as a characteristic parameter.

Neglecting the damping, the maximum displacements and peak accelerations at all nodal points in Fig. 1 for all four force inputs have been calculated. The maximum displacements at

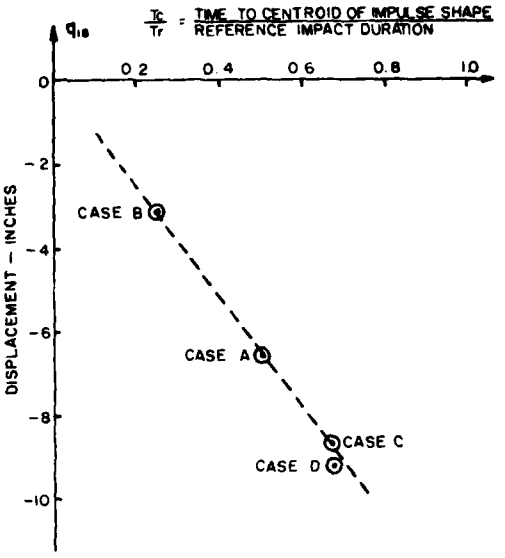

Figure 8 Impulse Shape Effect on Maximum Displacement

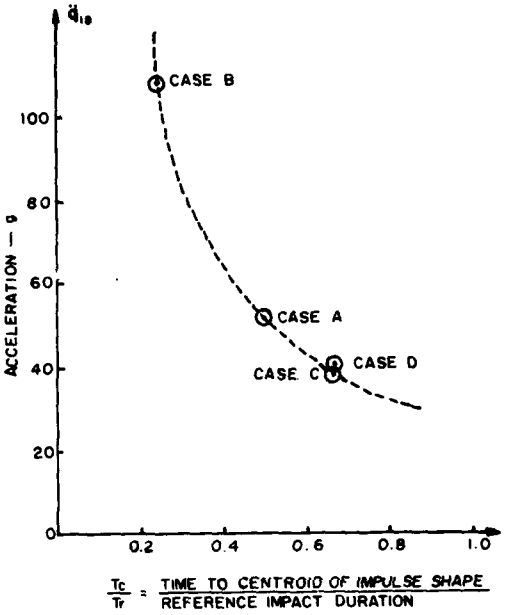

Figure 9 Impuse Shape Effects on Peak Acceleration

node 18 are shown in Fig. 8. This node is on the frame over the left rear wheel of the truck. There is no force applied directly at this point. Fig. 8 shows that the maximum vertical displacement of this point as a result of the application of the four different pulse shapes to the truck is almost linearly proportional to the time to the centroid of the pulse shape.

The peak accelerations at node 18, produced by each of the different impulses, are shown in Fig. 9. These results suggest that both the displacement and acceleration produced by a given impulse depend essentially on the time to the centroid of the area under the force-time (impulse) curve.

2. Structural Properties

The structure of an M-37 truck or any other vehicle is so complicated that simplifications must be made for analytical studies. If the truck is to be represented by a simplified model, the question of how to estimate the stiffness of the structure must be answered. As a part of the attack on this problem the significance of changes in the impact response with variation in the structural properties has been investigated. Consider now the mathematical model of the M-37 truck shown in Fig. 1. Three different sets of values of stiffness are assumed:

Case 1: All member stiffnesses are estimated based on the truck frame only.

Case 2: All member stiffnesses of case 1 are multiplied by five.

Case 3: All member stiffnesses of case 1 are multiplied by ten.

Computed total displacements and peak accelerations along the main frame joint No. 1 through No. 10 for the above three cases are shown in Figs. 10 and 11. All calculations were made for a vertical impact velocity of 25 fps and a force level equivalent to 17.5g acceleration. The resultant force is applied a little forward of the center of gravity. This force is supplied by a crushable cushioning material which crushes more toward the rear (because there is a disproportionate amount of the material at the front) and produces the tilt in the displacement curves shown in Fig. 10. The peak accelerations at each nodal point are shown in Fig. 11. In both Fig. 10 and Fig. 11, the three curves representing the 3 different stiffnesses are relatively close together. Thus it appears that rough approximations to structural stiffness will be satisfactory for computational purposes.

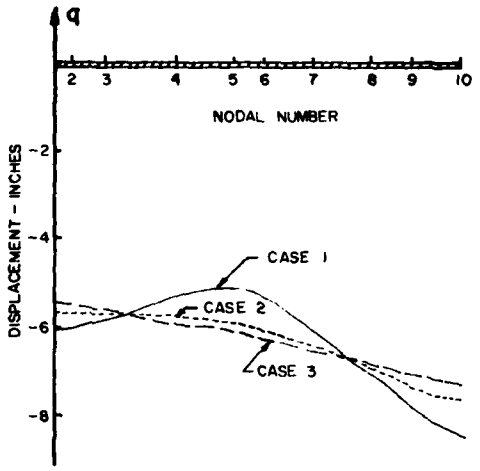

Figure 10 Structural Stiffness Effect on Maximum Displacements

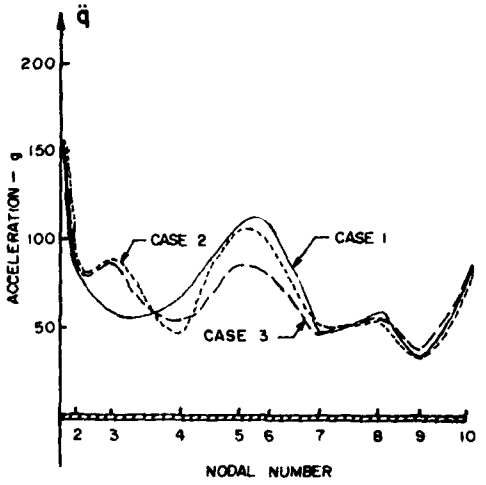

Figure 11 Structural Stiffness Effect on Peak Accelerations

3. Damping

The amount of structural damping in the vehicle must be determined by experimentation. If experimental data or reliable information is not available, no damping should be assumed in the analysis since the omission of damping results in conservative estimates of deflections. Numerical computations for the M-37 model show that at all points of the truck frame the absolute magnitudes of displacements are increasing as damping decreases but the peak accelerations are affected very little. Fig. 12 shows the maximum displacements for a damping ratio range from zero up to 0.015. There is no change in the configuration of the truck for all three cases. The crushing displacement curve with 0.009 as the damping ratio is the one which approximates most closely the experimental M-37 measurements.

4. The Effect of Tires on the Response of Vehicle Body

Since the vehicle body is connected to the wheels through a leaf spring arrangement, the magnitude and shape of forces transmitted to the vehicle body as the result of an impact would be significantly affected by the material properties of the tires. These forces must be considered in computations of the overall response of the vehicle body.

For the purpose of analysis, the wheel and tire are replaced by a mass, a spring K, and dashpot C arrangement as depicted in Fig. 3. Using different sets of values of K and C for the tire, the maximum displacements and maximum acceleration at point No. 3 (q_3) of the vehicle body, and the wheel at point No. 24 (q_{24}) have been calculated and plotted in Fig. 13.

In general, the larger the spring constants and the damping ratio, the smaller the displacement of the vehicle. Also the peak acceleration of the vehicle body does not show any significant variation as the spring constant and damping ratio of the tire is varied.

5. The Effect of Engine Supports on the Behavior of Engine

The idealized engine supporting arrangement is shown in Fig. 2. Computational results indicate that the values of the spring constant K and damping ratio C have no significant effect on either the peak accelerations or the maximum displacements at any point in the vehicle except the engine itself during the period of impact.

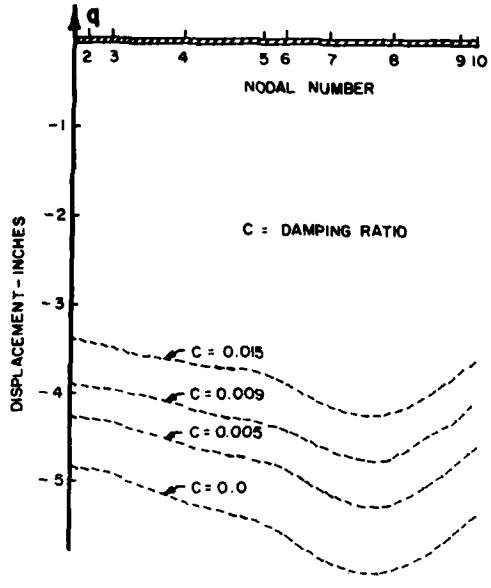

Figure 12 Structural Damping Effect on Maximum Displacements

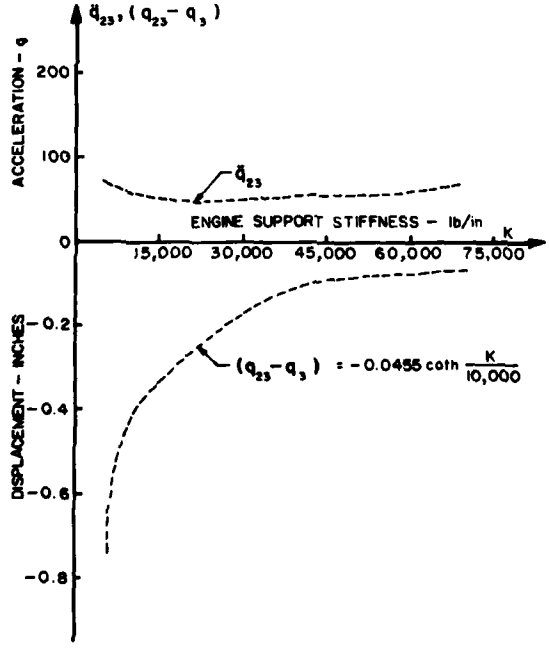

Figure 14 Engine Support Stiffness Effect on Maximum Displacement and Acceleration of Engine

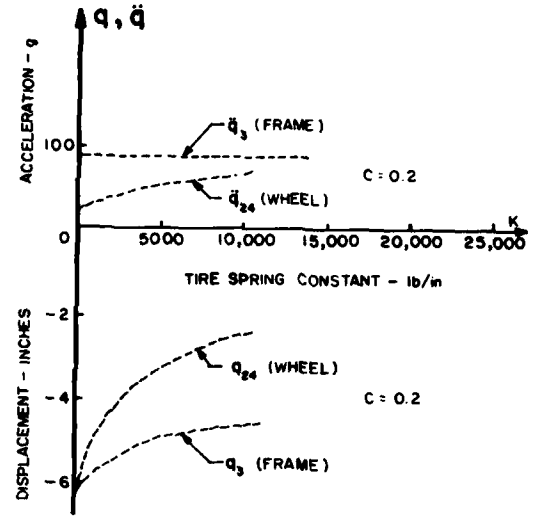

Figure 13 Spring Constant Effect of Tire on Maximum Displacements and Accelerations

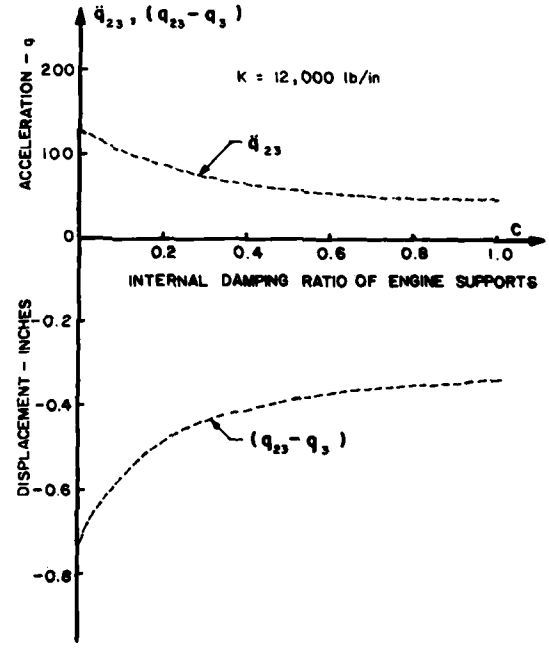

Figure 15 Internal Damping Effect of Engine Support on Maximum Displacement and Acceleration of Engine

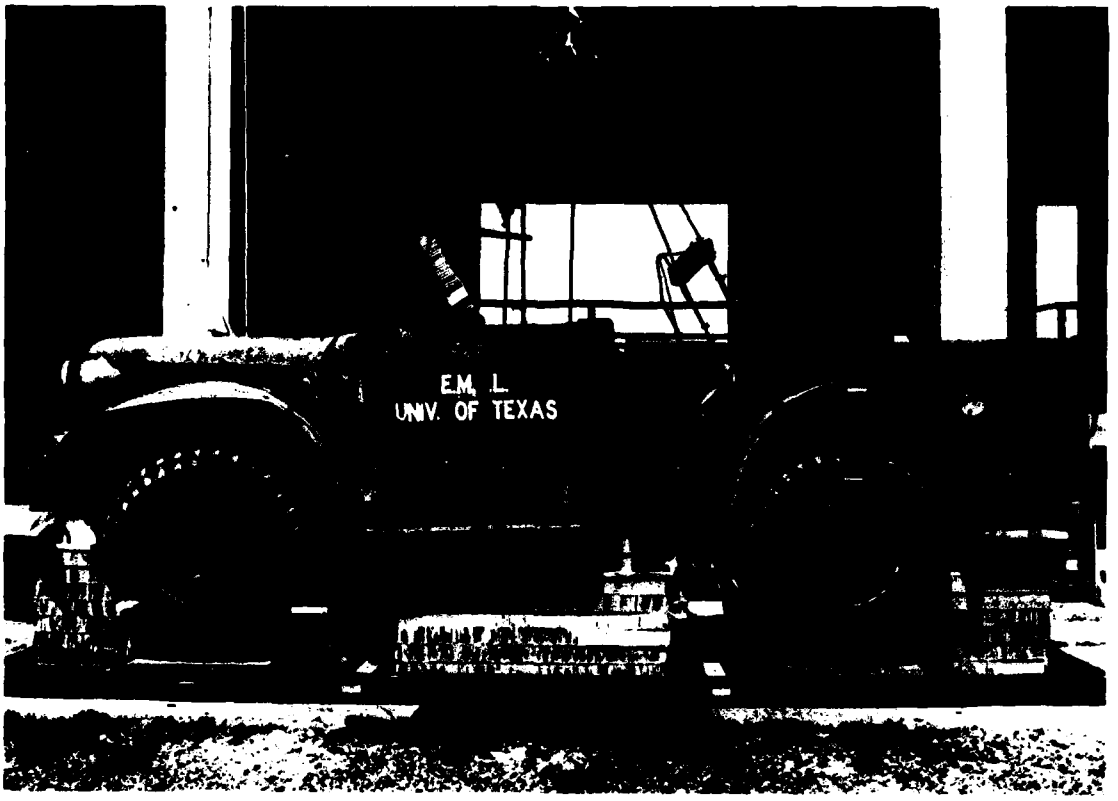

Figure 16 Rigging for Lifting the Vehicle

Figs. 14 and 15 show the effects of the elastic stiffness and internal damping of engine supports on the dynamic responses of the engine. As in the case of the tire, in general, the larger the spring constant and internal damping of the supports, the smaller the engine relative displacement to the truck frame.

The peak acceleration of the engine is not influenced much by the spring constant of the supports but it decreases with an increase in internal damping of the support.

EXPERIMENTAL INVESTIGATION - M-37 TRUCK DROP TEST

To obtain some experimental data for comparison with the computed results as described in the previous chapters, three drops of the M-37, 3/4 ton truck with a 1500 lb. simulated load of sandbags have been made from a drop height of 10 ft., and at a design acceleration of 17.5 g. The truck was cushioned with paper honeycomb and rigged for dropping as shown in Fig. 16.

Accelerations were measured at selected points using fluid-damped accelerometers to minimize overshoot and ringing. Engine displacement relative to the frame and various other displacements were measured and recorded during the impact.

Numerical values for the weights of various parts of the vehicle were taken from the technical manual or were estimated. Member properties were calculated using truck frame cross sectional dimensions. Tire spring constants were assumed to be 7000 lb/in and the damping ratio 0.2. Spring constants for the engine support are 12000 lb/in at the front and 40000 lb/in at the rear, and the damping ratio 0.6. Structural damping ratio was assumed to be 0.09.

Some measured and calculated results are shown in Figs. 17, 18, 19,

20 and 21. Further results and a more detailed account of both the calculations and the experiments are available in Ref. 6.

DISCUSSION

1. Mathematical Model

(a) It is impractical to try to include all the components of a complex structure in a model. Include only those components whose motions are considered to be most important. For example, in an airdrop of a vehicle, the motion of the engine block, transmission, differentials, and wheels may be the important parameters for the proper design of a cushioning system to protect the vehicle. Consequently the model should be so designed as to represent the motions of these components as realistically as possible. On the other hand, if the task is to design a cushioning system for the protection of a car radio, a completely different model will be needed. There is no unique model. The model shown in Fig. 1 is a particular model. Many other model configurations could have served quite as well for this study.

(b) Information on the environment that the structure is likely to be subjected to is also very important. In airdrop of a vehicle, the whole structure is expected to land with an impact velocity of approximately 30 fps, and the rise time of the impulse imparted to the vehicle is of the order of milliseconds. These are important data. A continuous elastic structure, such as a vehicle, has, in principle, an infinite number of modes of vibration that can be excited. A lumped parameter system can be excited in only as many modes as it has degrees of freedom. Therefore a lumped parameter system will not accurately represent a continuous structure under conditions in which the higher modes of the structure might be excited. The long rise time of the impulse applied to the vehicle means that the higher modes will most likely not be excited. The lumped parameter model can therefore provide a suitable approximation to the motion of the prototype system. On the other hand, an input force with a very short rise time would tend to excite higher modes of vibration. As a consequence a lumped parameter model would most likely not adequately represent the motion of the prototype structure.

In the present work, the whole truck body is modeled by a lumped parameter system with 39 nodal points. Since there are six degrees of freedom at each nodal point, the total number of degrees of freedom of the system is 234. Only a normal impact (in the vertical direction) is considered here, hence the vertical displacements of the nodal points are of the main concern. The six displacements possible at each nodal point consist of three translational motions and three rotational motions. Two of the translational displacements and one of the rotational displacements can be disregarded. Thus the total number of degrees of freedom is reduced to 117. This number can be further reduced to 39 by eliminating the remaining two rotational components at the nodal points by the static condensation process [4].

The amount of computer storage required by the program for this analysis is 30,000 words. For the CDC 6600 computer, the formulation of the equations of motion requires three minutes of central processing time. The numerical integrations by the Runge-Kutta method require 1.5 minutes for an impact duration of 45 milliseconds, using an integration step size of 0.1 milliseconds.

2. Comparison of Measured and Computed Results

From Figs. 17 through 21, it may be seen that agreement between measured and computed results is, in general, not very good, so far as the shapes of the curves are concerned. It is especially poor so far as accelerations are concerned. This is undoubtedly due to the contributions to the acceleration by the higher modes of vibration which are not provided for in the model. Displacements are not affected very much by these higher modes. Hence the agreement, particularly in amplitudes, between measured and computed results is much better. It probably is naive to expect that accelerations at arbitrarily selected points in a complex structure such as this truck can ever be computed with any degree of accuracy. However, it is not too much to expect that displacements might be computed with acceptable accuracy, and as indicated previously displacements are probably much better indicators of possible damage, than are accelerations. Agreement between measured and computed results may be improved in several ways, all of which would involve making the computer input parameters match closely the corresponding quantities in the model, and of course, the model can also be improved.

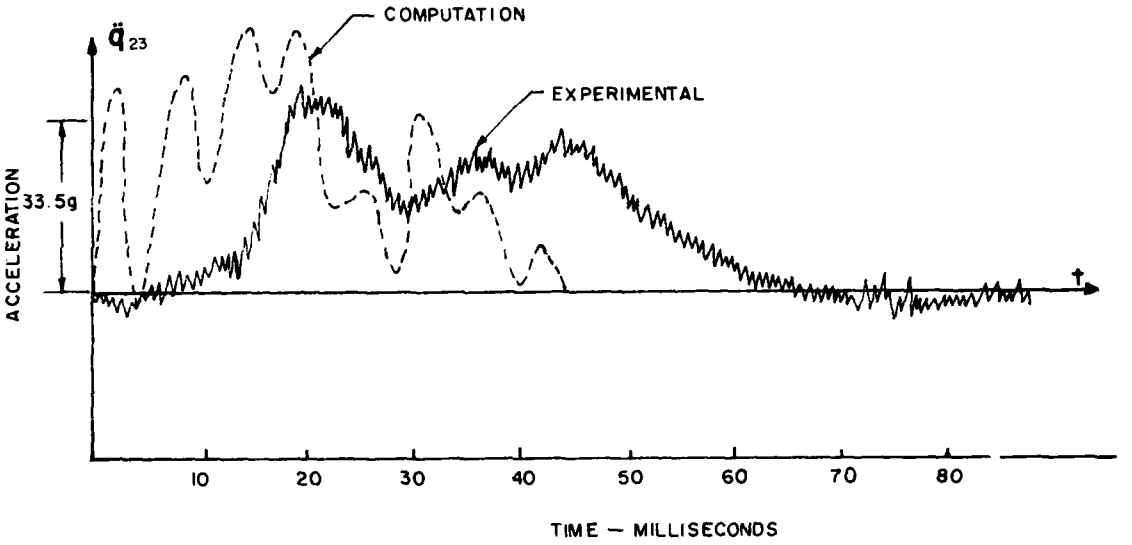

Figure 17 Measured and Computed Acceleration of q_{23} - Engine

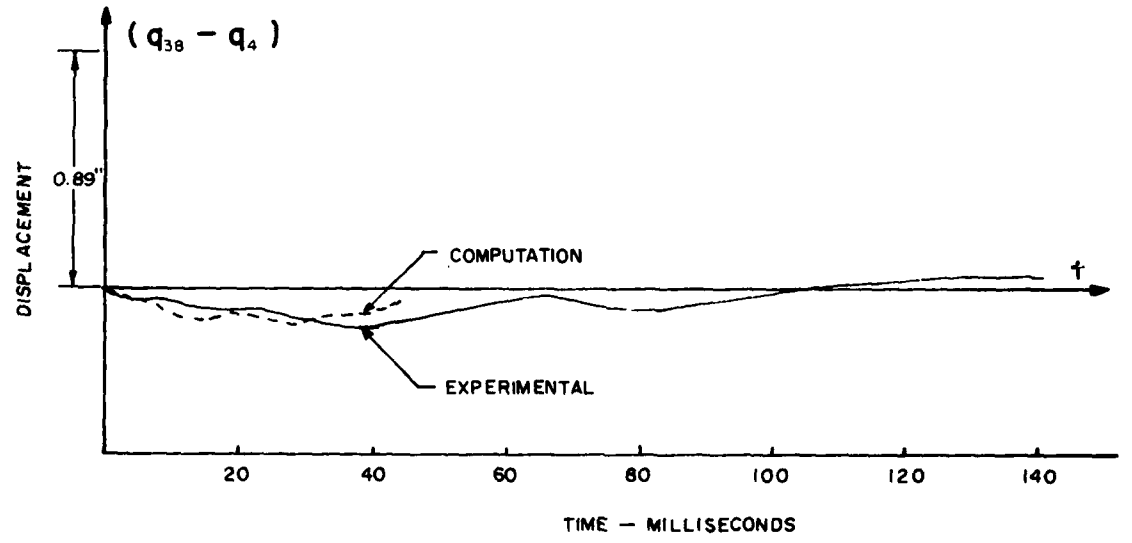

Figure 18 Measured and Computed Relative Displacement of $(q_{38} - q_4)$ - *Engine* Relative to the Frame

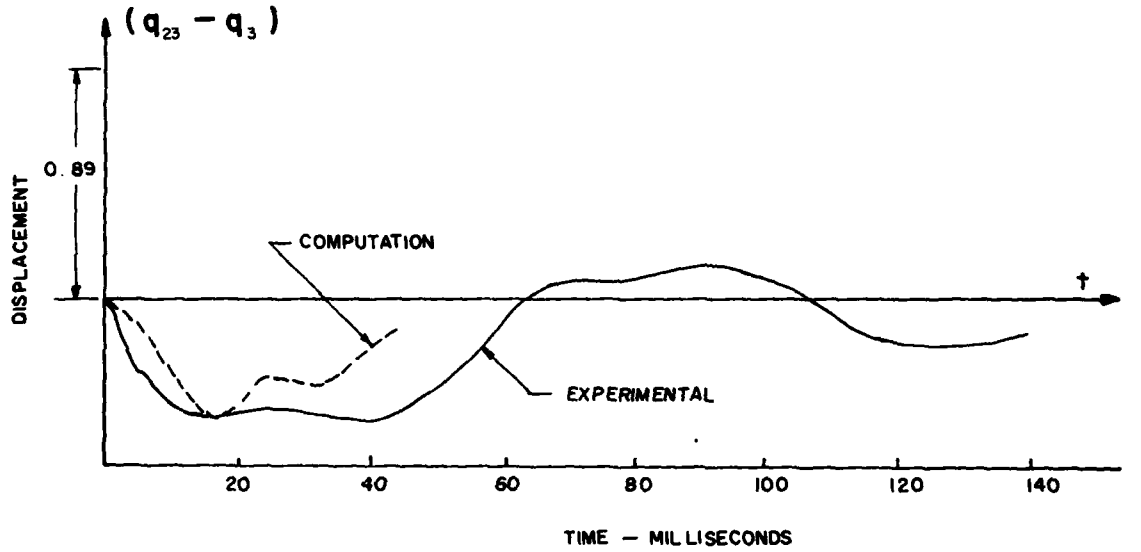

Figure 19 Measured and Computed Relative Displacement of $(q_{23} - q_3)$ - Engine Relative to the Frame

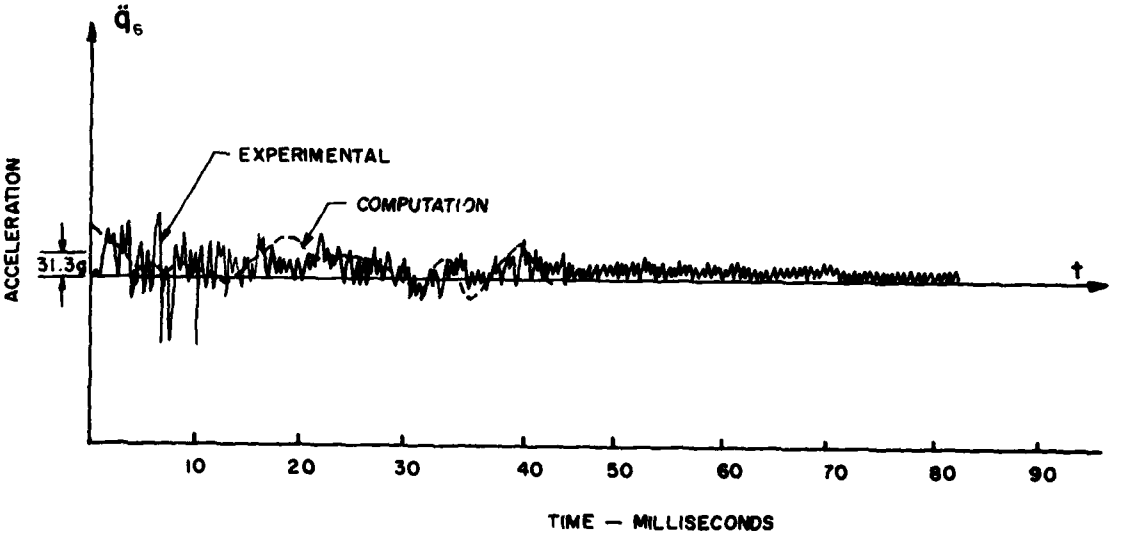

Figure 20 Measured and Computed Acceleration of q_6 - Middle Frame

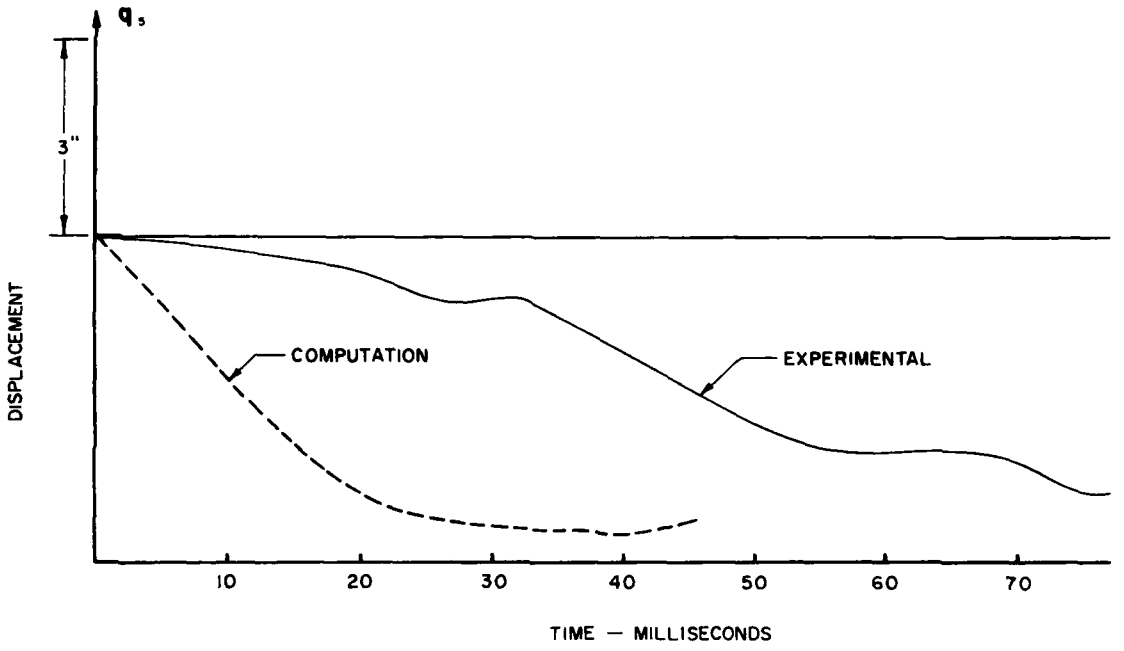

Figure 21 Measured and Computed Displacement of q_5 - Middle Frame

CONCLUSIONS

1. Displacements at various points of a complex mechanical structure can be satisfactorily predicted using a lumped parameter mathematical model and a numerical computation procedure.

2. The dynamic response of a complex structure when properly cushioned and subjected to an impact loading is not sensitive to the elastic properties of the structure. Thus the elastic coupling between masses in the lumped parameter model need not be known to any great degree of precision.

3. Structural damping dissipates a considerable amount of energy, and as a consequence decreases the displacements. However, the peak accelerations at various points in the structure are affected very little by the structural damping.

4. The forcing function is the major factor which affects the dynamic response of the system. It must be represented as exactly as possible.

5. The procedure for handling the engine and transfer case in the analysis can be applied to any rigid discrete mass which cannot be included in the elastic properties of the structure.

6. The developed computer program can be employed to predict the dynamic displacements of any complex mechanical structure if the structure can be represented by a grid type model.

7. Although the analysis requires the assumption of linear elastic behavior and therefore cannot predict permanent deformations it can indicate where permanent deformations are likely to occur.

Acknowledgements

This work was supported by the U. S. Army Natick Laboratories.

REFERENCES

1. Wilfred E. Baker, Validity of Mathematical Models of Dynamic Response of Structures to Transient Loads, The Shock and Vibration Bulletin, No. 4, Part 7, pp 19-28, 1970.

2. J. S. Przemieniecki, Theory of Matrix Structural Analysis, New York, McGraw-Hill, 1968.

3. C. M. Harris and C. E. Crede, Shock and Vibration Handbook, Chapter 35, New York, McGraw-Hill, 1961.

4. John Robinson, Structural Matrix Analysis for the Engineer, New York, John Wiley & Sons, 1966.

5. R. L. Ketter and S. P. Prawal, Modern Methods of Engineering Computation, New York, McGraw-Hill, 1969.

6. S. F. Jan, Impact on Complex Mechanical Structures, PhD dissertation, The University of Texas at Austin, 1971.

ENERGY ABSORPTION AND PHASE EFFECTS

IN SHOCK EXCITED COUPLED SYSTEMS

Charles T. Morrow
Advanced Technology Center, Inc.
Dallas, Texas

This analysis of energy absorption and phase-related uncertainties is based on an idealized model consisting of two simple damped resonators, the second resonator being attached to the mass of the first. If the first resonance frequency is allowed to increase beyond limit, the model becomes a single simple resonator, as a special case. The focus of the analysis is on the peak acceleration of the second mass and the energy absorbed in the second damper. To simplify the mathematics and make the model correspond to a critical case for reliability, it is assumed that the second resonator does not load the first, but the conclusions are not limited to this assumption. The analysis is limited to shock pulses (such as the terminal peak sawtooth) whose dominant feature is a terminal step function, so that we can assume for the two-resonator model a residual response consisting of two transients at the natural frequencies of the two resonators, and these transients become the primary cause of energy dissipation and peak response.

The introduction of energy dissipated as an additional factor in the severity of a shock makes the residual spectrum a more general criterion, less dependent on the assumption of failure modes resembling brittle fracture. If energy increases with peak response, a ductile material that could otherwise survive one extreme strain becomes more likely to fail. Malfunctions that might be insensitive to one peak response become more likely to occur.

It is shown that variability of response energy and peak response can be held within reasonable limits by tolerances placed on a nominal phase versus frequency characteristic as well as a nominal magnitude versus frequency characteristic. The best way to establish the nominal phase characteristic for the simulation of particular shocks would require further analysis.

INTRODUCTION

The purposes of this study are two-fold--to explore any correlation between the residual shock spectrum (preferably undamped, for simplicity) and the energy absorbed at a failure point or malfunction point, and to explore any uncertainty of peak response or energy absorption because of variability of phasing or timing of response transients.

The shock spectrum originated as a spectrum of possible responses of hardware. It has been considered indicative of damage potential primarily on the assumption of something like a brittle fracture type of failure such that the largest value of response acceleration is the primary concern. Such an assumption is obviously restrictive. We cannot readily prescribe alternate criteria for all specific types of failure or malfunction, but if the energy absorbed in the test item could also be shown to correlate in a simple way with the shock spectrum, we would have a more general foundation for spectral descriptions of shock severity. Because of the simple relationship, already known, between the undamped residual shock spectrum and the Fourier transform, the

former has a more fundamental nature than was originally expected. On this basis, a relationship to energy absorbed will be derived.

The use of the shock spectrum does not necessarily require an assumption that all resonators in a test item be simple. For example, in an earlier study[1], the author treated a special case of a two degree of freedom system. One situation leading to failure or malfunction is a light flexible resonator, such as a potentiometer wiper, mounted on something more massive that happens to be tuned to approximately the same frequency. The final mass becomes subject to a "whipping" action because of the double amplification by resonance. Accordingly, the author assumed two resonators in tandem as in Figure 1, with no loading of the first by the second, and focused on the response of the final mass. The residual response turned out to be the sum of two transients, each proportional to the Laplace transform (or, in the absence of damping, the Fourier transform) of the excitation. It followed that if one shock had a higher undamped residual spectrum than another at every frequency, or a higher Fourier transform magnitude, it would always produce the higher peak residual acceleration of the final mass, except for uncertainty due to relative phasing and possibly starting time of the response transients. This type of conclusion probably holds true for a wider variety of multiple degree of freedom systems than those covered by the particular idealized model. For example, if the second resonator is allowed to load the first, the characteristic frequencies of the transients become system frequencies differing somewhat from the frequencies of resonance of the individual resonators. But there are still two transients of the same character as for negligible loading.

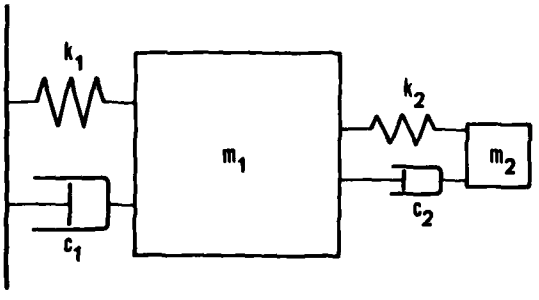

Figure 1. Two Coupled Resonators

In the present study, we will assume two response transients and explore the effect of phasing and starting time on both peak response and energy absorbed. Generally, the transients will be interpreted as residual two degree of freedom responses, but they could represent the response of a single degree of freedom system excited by an exponentially decaying transient. This excitation would be transmitted with some change of magnitude and a response at the natural frequency of the resonator would be superposed.

Uncertainty of Peak Response

Let the response of a resonant mechanical system be the sum of two exponentially decaying transients, which at first are assumed to start at the same instant, but which may differ in phase as well as frequency and damping.

$$a = A_1 e^{-\alpha_1 t} \sin(\omega_1 t - \phi_1) + A_2 e^{-\alpha_2 t} \sin(\omega_2 t - \phi_2), \quad (1)$$

$$\text{with} \qquad \alpha_1 = \omega_1/2Q_1 \quad (2)$$

$$\text{and} \qquad \alpha_2 = \omega_2/2Q_2 \quad (3)$$

According to Appendix I, this can be expressed as

$$a = (A_1 e^{-\alpha_1 t} - A_2 e^{-\alpha_2 t}) \times \sin \tfrac{1}{2}(\omega_1 t - \omega_2 t - \phi_1 + \phi_2) \cos \tfrac{1}{2}(\omega_1 t + \omega_2 t - \phi_1 - \phi_2) + (A_1 e^{-\alpha_1 t} + A_2 e^{-\alpha_2 t}) \times \sin \tfrac{1}{2}(\omega_1 t + \omega_2 t - \phi_1 - \phi_2) \cos \tfrac{1}{2}(\omega_1 t - \omega_2 t - \phi_1 + \phi_2), \quad (4)$$

which may be interpreted as a "carrier" signal at half the sum of the two original frequencies modulated in accordance with an exponentially decaying signal at half the difference of the two frequencies. In short, the half-sum frequency signal has an envelope given by

$$A_e = [(A_1 e^{-\alpha_1 t} - A_2 e^{-\alpha_2 t})^2 \times \sin^2 \tfrac{1}{2}(\omega_1 t - \omega_2 t - \phi_1 + \phi_2) + (A_1 e^{-\alpha_1 t} + A_2 e^{-\alpha_2 t})^2 \times \cos^2 \tfrac{1}{2}(\omega_1 t - \omega_2 t - \phi_1 + \phi_2)]^{1/2}, \quad (5)$$

which reduces to

$$A_e = 2A_1 e^{-\alpha_1 t} \cos \tfrac{1}{2}(\omega_1 t - \omega_2 t - \phi_1 + \phi_2)$$

$$= 2A_2 e^{-\alpha_2 t} \cos \tfrac{1}{2}(\omega_1 t - \omega_2 t - \phi_1 + \phi_2) \quad (6)$$

If $A_1 = A_2$ and $\alpha_1 = \alpha_2$.

As dominance by one transient or the other tends to decrease any uncertainty dependent on their relative phasing, Equation (6) is based on a worst case, or conditions close to it.

If in addition, $\omega_1 = \omega_2$, Equation (6) reduces to

$$A_e = 2A_1 e^{-\alpha_1 t} \cos \tfrac{1}{2}(\phi_2 - \phi_1), \quad (7)$$

which has its largest value at the beginning, corresponding to a simple exponential decay with relative phase influencing the magnitude but not the shape. The first peak of the half-sum frequency response is the largest.

However, if ω_1 and ω_2 differ, there is cosine as well as exponential modulation with time. Depending on the relative phase, the peak response is delayed in time and is decreased in magnitude because of the exponential decay of both transients in the meantime. It is reasonable to assume that the time of the peak response is approximately equal to the time of the first maximum of the envelope, obtained by differentiating Equation (6) with respect to time and equating the result to zero.

$$t_p = \frac{\phi_1 - \phi_2 - 2\tan^{-1}\frac{2\alpha_1}{\omega_1 - \omega_2}}{\omega_1 - \omega_2}$$

$$= \frac{\phi_1 - \phi_2 - 2\tan^{-1}\frac{2\alpha_2}{\omega_1 - \omega_2}}{\omega_1 - \omega_2}$$

$$= \frac{\phi_1 - \phi_2 - 2\tan^{-1}\frac{\omega_1}{Q_1(\omega_1 - \omega_2)}}{\omega_1 - \omega_2}$$

$$= \frac{\phi_1 - \phi_2 - 2\tan^{-1}\frac{\omega_2}{Q_2(\omega_1 - \omega_2)}}{\omega_1 - \omega_2}, \quad (8)$$

with aid from Equations (2) and (3). For frequency differences of the order of a bandwidth, we can take $Q_1 = Q_2$ to be constant with frequency when $\alpha_1 = \alpha_2$ is constant, or to be equally representative of a worst case.

But we are interested, in this study, not so much in the absolute response as in any uncertainty due to small increments in $\phi_1 - \phi_2$ from a nominal value. In other words, we will study tolerances in relation to reproducibility of shock response. By differentiation of Equation 8,

$$dt_p = d(\phi_1 - \phi_2)/(\omega_1 - \omega_2), \quad (9)$$

or, for small nonzero increments,

$$\Delta t_p = \Delta(\phi_1 - \phi_2)/(\omega_1 - \omega_2) . \quad (10)$$

In this time increment, the decay of the exponential factor, in terms of α_1 is

$$e^{-\alpha_1 \Delta t_p} = e^{-\omega_1 \Delta(\phi_1 - \phi_2)/2Q_1(\omega_1 - \omega_2)}$$

$$= e^{-f_1 (\phi_1 - \phi_2)/2Q_1(f_1 - f_2)} \quad (11)$$

If we limit this to a 10 percent decrease as a point of departure,

$$\Delta(\phi_1 - \phi_2) \leq \frac{2Q(f_1 - f_2)}{f_1} \log_e (.9)$$

$$= .21 \; Q(f_1 - f_2)/f_1 \quad (12)$$

Note that the permissible phase shift is directly proportional to $(f_1 - f_2)/f_1$. If we set this equal to .1, corresponding to a 10 percent change in frequency separation and assume $Q \geq 10$ except in the case of an intentionally installed isolator, we obtain

$$\Delta(\phi_1 - \phi_2) = .21 \text{ rad/10\% change in separation}$$

$$= 12 \text{ degrees/10\% change in separation} \quad (13)$$

for a 10 percent peak response uncertainty.

In deriving this result, we tacitly assumed $\Delta(\phi_1 - \phi_2)$ has the same sign as $(f_1 - f_2)$. We could have readily obtained a similar tolerance for the opposite sign by permitting the exponential to increase (for negative Δt_p) rather than decrease.

At another extreme let us consider two widely different response frequencies and try to set up something like a worst case even if it is rather unlikely. Figure 2 shows two such transients with approximately the same initial magnitude. Only the first half cycle of the lower frequency transient is shown. The phase angle

is chosen so the time dependence will be a slowly decaying sine function. By the time it reaches its first maximum, the higher frequency transient has become negligible. The peak of the total response is insensitive to the phase of the higher frequency transient, but altering the low frequency transient from a sine to a cosine would double the response peak. The greatest variability comes when it is phased approximately as a sine wave. Let us require that

$$\sin \phi \simeq \phi \leq .2 \text{ rad}$$

$$\simeq 12 \text{ degrees} \qquad (14)$$

for the lower frequency transient, for a 10 percent variation in peak total response.

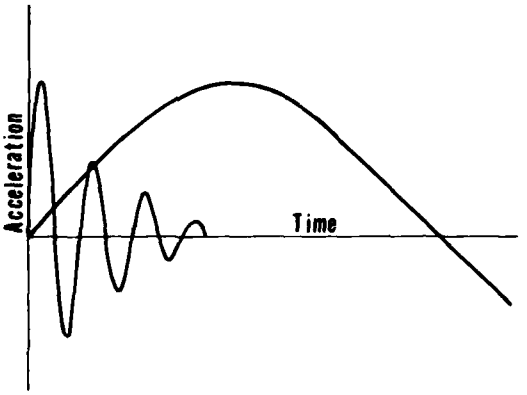

Figure 2. Two Response Transients

Finally, suppose that either transient is initiated a time interval t_o before the other but we desire, as a point of departure, to control t_o so that this transient will not be diminished by more than ten percent before the other is initiated.

$$e^{-\alpha t_o} = e^{-\omega t_o/2Q} \geq .9$$

or

$$\omega t_o/2Q \leq .1$$

or

$$t_o \leq .2Q/\omega \qquad (15)$$

If we take the lowest Q to be Q = 10

$$t_o \leq 2/\omega \text{ rad}/(\text{rad/sec})$$

$$= 110 \text{ deg}/(\text{rad/sec}). \qquad (16)$$

Energy Absorbed

An additional measure of the severity of the effect of shock on the second resonator is the energy absorbed in the damper c_2. As before, let the response of a resonant mechanical system be the sum of two exponentially decaying transients as in Equation (1), which are at first assumed to start at the same instant, but which may differ in phase as well as frequency and damping. If c_2 is viscous, linear and independent of frequency, the energy absorbed in it during the residual response is

$$E = c_2 \int_o^\infty v^2 \, dt \qquad (17)$$

where the instantaneous velocity

$$v = \int_o^t a \, dt$$

$$\simeq \frac{A_1}{\omega_1} e^{-\alpha_1 t} \cos(\omega_1 t - \phi_1) + \frac{A_2}{\omega_2} e^{-\alpha_2 t} \cos(\omega_2 t - \phi_2)$$

$$= V_1 e^{-\alpha_1 t} \cos(\omega_1 t - \phi_1) + V_2 e^{-\alpha_2 t} \cos(\omega_2 t - \phi_2), \qquad (18)$$

unless the transients decay very rapidly. In any event, the velocity can be reduced to the final form except for minor changes in the proportionality constant relating V_1 to A_1 or V_2 to A_2, and in the relationships of velocity phase to acceleration phase. It follows that

$$E = c_2 \int_o^\infty [V_1 e^{-\alpha_1 t} \cos(\omega_1 t - \phi_1)$$

$$+ V_2 \cos(\omega_2 t - \phi_2)]^2 \, dt$$

$$= c_2 V_1^2 \int_o^\infty e^{-2\alpha_1 t} \cos^2(\omega_1 t - \phi_1) \, dt$$

$$+ c_2 V_2^2 \int_o^\infty e^{-2\alpha_2 t} \cos^2(\omega_2 t - \phi_2) \, dt$$

$$+ 2 c_2 V_1 V_2 \int_o^\infty e^{-(\alpha_1 + \alpha_2) t} \cos(\omega_1 t - \phi_1) \cos(\omega_2 t - \phi_2) \, dt$$

$$\simeq \frac{c_2 V_1^2}{4\alpha_1} + \frac{c_2 V_2^2}{4\alpha_2} + c_2 V_1 V_2$$

$$\times \frac{(\alpha_1 + \alpha_2) \cos(\phi_1 - \phi_2) + (\omega_1 - \omega_2) \sin(\phi_1 - \phi_2)}{(\alpha_1 + \alpha_2)^2 + (\omega_1 - \omega_2)^2} \qquad (19)$$

unless $|\omega_1-\omega_2|$ is extremely large. The third term is a phase dependent uncertainty.

Note that, apart from the uncertainty, the energy absorbed increases as either V_1 or V_2 is increased and consequently as either A_1 or A_2 is increased. If the two transients are those of the double resonator of Figure 1, A_1 and A_2 are proportional to the Laplace transforms of the shock excitation obtained by inserting the complex frequencies of the two resonators in the Fourier transform of the shock time history. This was shown in the previous study[1]. Consequently, apart from the phase dependent uncertainty, whichever of two shocks has the greater Fourier transform (or undamped residual shock spectrum) is the shock that imparts the larger total energy to the second resonator during the residual time interval.

As in the case of peak response, the energy absorbed is particularly sensitive to phase difference when the two transients are otherwise closely similar. For reference purposes, if $V_1 = V_2$, $\alpha_1 = \alpha_2$ and $\omega_1 = \omega_2$, the energy absorbed is given by

$$E = \frac{c_2 V_1^2}{2\alpha_1} [1 + \cos(\phi_1-\phi_2)] \qquad (20)$$

which is capable of 100 percent variation with relative phase angle.

But as $(\omega_1-\omega_2)$ increases with $V_1 = V_2$ and $\alpha_1 = \alpha_2$, the variability of response with $(\phi_1-\phi_2)$ decreases, for Equation (19) reduces more generally to

$$\frac{2\alpha_1 E}{c_2 V_1^2}$$

$$= 1 + \frac{4\alpha_1^2 \cos(\phi_1-\phi_2) + 2\alpha_1(\omega_1-\omega_2)\sin(\phi_1-\phi_2)}{4\alpha_1^2 + (\omega_1-\omega_2)^2}$$

$$= 1 + \frac{\cos(\phi_1-\phi_2) + [(f_1-f_2)/B_1]\sin(\phi_1-\phi_2)}{1 + (f_1-f_2)^2/B_1^2}$$

$$= 1 + N/D, \qquad (21)$$

where N/D is the variation,

$$N = \cos(\phi_1-\phi_2) + [(f_1-f_2)/B_1]\sin(\phi_1-\phi_2), \qquad (22)$$

and

$$D = 1 + (f_1-f_2)^2/B_1^2. \qquad (23)$$

To obtain the maximum value of N/D, we set $\partial N/\partial(\phi_1-\phi_2) = 0$ to get

$$(\phi_1-\phi_2) = \tan^{-1}[(f_1-f_2)/B_1] \qquad (24)$$

and combine this with Equation (22) and (23), or with Equation (21) with the unity term omitted. $(N/D)_{max}$ is plotted versus $(f_1-f_2)/B$ in Figure 3. It decreases monotonically as $(f_1-f_2)/B$ increases.

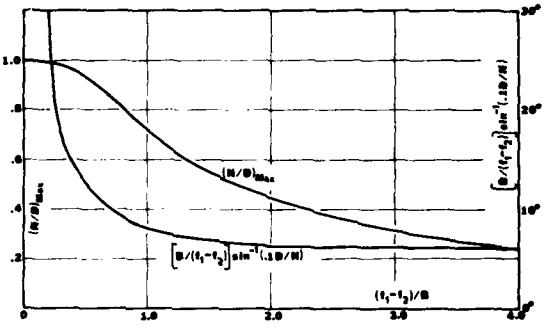

Figure 3. Phase Sensitivity When $\alpha_1 = \alpha_2$ and $V_1 = V_2$

Now, N/D could be expressed as a sinusoidal function of $\Delta\phi$, of amplitude $(N/D)_{max}$, where $\Delta\phi$ is measured from the value of $(\phi_1-\phi_2)$ for which N = 0. We can ensure, as a point of departure, that the variation be limited to 10 percent by requiring

$$\sin \Delta\phi \leq .1/(N/D)_{max} \qquad (25)$$

or

$$\Delta\phi \leq \sin^{-1}[.1/(N/D)_{max}] \qquad (26)$$

or

$$[B/(f_1-f_2)]\,\Delta\phi \leq [B/(f_1-f_2)\sin^{-1}[.1/(N/D)_{max}] \qquad (27)$$

in degrees per fractional bandwidth. Equation (27) is also plotted in Figure (3). It descends rapidly at first but settles down to about 6 degrees as $(f_1-f_2) = 2B$. But

$$[B/(f_1-f_2)]\,\Delta\phi = [f_1/(f_1-f_2)Q_1]\Delta\phi. \qquad (28)$$

As in the analysis of uncertainty of peak response, we set $(f_1-f_2)/f_1 = .1$ and assume a minimum Q = 10. Then, Equation (26), as plotted

in Figure (3) becomes also the permissible phase increment per 10 percent change in frequency separation for at most a 10 percent uncertainty of response. Consequently an upper limit of 6 degrees per ten percent change should be sufficient--about half the number yielded by Equation (13).

Time Delay Versus Phase Shift

In connection with the uncertainty of peak response of a double resonator, we touched briefly on the effect on initiating one response transient before the other. However, tolerances on relative initiation time are not independent of tolerances on relative phase shift.

We can start our investigation of this by asking what sort of phase shift versus frequency may be equivalent to a constant time delay t_o so that

$$\sin \omega(t-t_o) = \sin (\omega t-\phi). \qquad (29)$$

It follows that

$$\omega(t-t_o) = \omega t-\phi$$

and, therefore,

$$\phi = \omega t_o \qquad (30)$$

is simply a phase angle proportional to frequency.

More generally, the delay in any narrow frequency band, according to Appendix 2, is given by

$$t_o = d\phi/d\omega \qquad (31)$$

Equation (16) gave the maximum time delay of one transient such that the other would not decay more than 10 percent in the meantime. Substitution in Equation (31) yields

$$\frac{\omega d\phi}{d\omega} = \frac{fd\phi}{df} = \frac{f\Delta\phi}{\Delta f}$$

$$\leq 110 \text{ degrees per fractional bandwidth.} \qquad (32)$$

If we set $\Delta f/f = .1$, we obtain

$\Delta\phi \leq 11$ degrees per 10 percent change in frequency separation. (33)

For simplicity, this was computed as if only one transient could be subject to a time delay because of phase versus frequency characteristic, but, more generally, it applies on a relative basis. The phase angle must not change by more than 11 degrees from a nominal curve with a 10 percent change in frequency separation. This is almost the same as the results obtained previously on the assumption that the transients started at the same time, or that we will look at peak response or energy absorption only after initiation of the second transient.

If two transients have approximately the same amplitude and decay rate, but one decays 10 percent before the other is initiated, the peak response subsequently is possibly decreased by 10 percent. Total power dissipation is less sensitive to starting time. From Equation (19), if one transient decays 10 percent before the other is initiated, the energy dissipated thereafter may decrease about 10 percent of the total energy has been dissipated already, so the net change is much smaller. However, it follows from Equations (19) and (21) that the power dissipated after the initiation of the second transient remains sensitive to relative phase at that instant.

A computer study of peak response and energy dissipation in a double resonator would provide more insight into the permissible phase versus frequency variations in the Fourier transform or residual undamped shock spectrum of a shock excitation. In the meantime, it is reasonable to use our worst case estimates as points of departure for shocks whose dominant feature resembles a terminal step function. We should keep in mind that the direct effect of phase angle on peak response, and the indirect effect, by way of transient initiation time, can be cumulative; that we have not examined any effect there may be from overlap of the pulse with initiation of transients and, finally, that there could occasionally be three resonators coupled together.

We have three estimates of phase rate tolerances with frequency, from a nominal curve, based on 10 percent variations in an aspect of response of a double resonator. Equation (13) permitted 12 degrees per 10 percent change in frequency. From Equations (27) and (28), we obtained 6 degrees per 10 percent change in frequency. Equation (33) permitted 11 degrees per 10 percent change in frequency. Equation (33) permitted 11 degrees per 10 percent change, with some additive effects on the other uncertainties. To be conservative, we might suggest a tolerance of ± 2 degrees per 10 percent change in frequency, if it is not too difficult to achieve. This should keep worst case combined effects on response within about ± 5 percent.

In addition, for a rather unlikely worst case, Equation (14) permitted a tolerance of about 12 degrees for a 10 percent response peak variation--a tolerance on deviaiton of phase angle rather than phase rate from a nominal

curve. We suggest, as a practical tolerance, ± 6 degrees for a ± 5 percent variation, if it is not too difficult to achieve.

Conclusion

We have extended the utility of the shock spectrum concept by showing that the peak residual response and residual energy absorption in both simple and coupled resonators are related to undamped residual shock spectrum.

Actually, these results for residual response should not be surprising. Such response consists of one or more transients at frequencies and decay rates determined by resonances of the hardware. Transients with higher initial peaks will tend to dissipate more energy. For shock excitations that do not have a definite ending or tend to overlap the residual response or to contribute significantly, by their own transmission into a test item, to peak response and energy absorption, analysis would be more complicated.

Consideration of energy dissipated reinforce the theme of the previous study[1] that the residual shock spectrum is more important than the initial in a test specification. The dissipation of energy tends to be more by induced transients than by transmitted pulses. For example, a step function was shown in the previous study[1] to be transmitted through a linear resonant system without modification. Consequently, this by itself involves no relative motion and no energy dissipation.

We showed also that, for one special type of shock time history, responses can be made reproducible by placing tolerances on maximum deviation of phase angle from a nominal curve and on phase rate with frequency, as well as on the magnitude of the Fourier transform or shock spectrum. This would indirectly limit any variation in shock excitation time history. If such a practice were widely followed in specifying shock tests, it would undoubtedly answer the misgivings many engineers have about current use of the shock spectrum. It is too early, however, to make a firm recommendation of such practice, as other types of time history need to be studied, either by mathematical analysis or by computer.

The simplest way to specify a nominal curve is to make it relative to some standard frequency more or less in the middle of the range of interest. Phase can be defined as an additional feature of the undamped residual shock spectrum by measuring the phase of each residual transient relative to the transient at the standard frequency.

One question left unanswered is what is the best way to select a nominal spectral phase characteristic so as to ensure with minimum excess margin that the response of coupled resonators will be at least as great as for a shock to be simulated. A terminal step function tends to initiate all response transients simultaneously so they can start interacting before any decay occurs. However, examination of the previous study shows that the relative phase for two response transients close together in frequency is such that the peak response may not occur for several cycles; this latter consideration tends to make a shock test less conservative. If the terminal step were modified by a fractional octave filter, the response transients would not be initiated simultaneously, but the total response peak or energy absorption might in some cases be greater.

Appendix I

Sum of Two Transients

$$a = A_1 e^{-\alpha_1 t} \sin(\omega_1 t - \phi_1) + A_2 e^{-\alpha_2 t} \sin(\omega_2 t - \phi_2)$$

$$= A_1 e^{-\alpha_1 t} \sin(\omega_1 t - \phi_1) - A_2 e^{-\alpha_2 t} \sin(\omega_1 t - \phi_1)$$

$$+ A_2 e^{-\alpha_2 t} [\sin(\omega_1 t - \phi_1) + \sin(\omega_2 t - \phi_2)]$$

$$= (A_1 e^{-\alpha_1 t} - A_2 e^{-\alpha_2 t}) \sin(\omega_2 t - \phi_2)$$

$$+ A_2 e^{-\alpha_2 t} [\sin(\omega_1 t - \phi_1) + \sin(\omega_2 t - \phi_2)] \qquad (34)$$

Similarly,

$$a = (A_2 e^{-\alpha_2 t} - A_1 e^{-\alpha_1 t}) \sin(\omega_1 t - \phi_1)$$

$$+ A_1 e^{-\alpha_1 t} [\sin(\omega_1 t - \phi_1) + \sin(\omega_2 t - \phi_2)] \qquad (35)$$

Now, we take the arithmetic average

$$a = \frac{1}{2} (A_1 e^{-\alpha_1 t} - A_2 e^{-\alpha_2 t}) [\sin(\omega_1 t - \phi_1)$$

$$- \sin(\omega_2 t - \phi_2)]$$

$$+ \frac{1}{2} (A_1 e^{-\alpha_1 t} + A_2 e^{-\alpha_2 t}) [\sin(\omega_1 t - \phi_1)$$

$$+ \sin(\omega_2 t - \phi_2)], \qquad (36)$$

which leads directly to Equation (4) because

$$\sin x+\sin y = 2 \sin \frac{1}{2} (x+y) \cos \frac{1}{2} (x-y). \quad (37)$$

Appendix 2

Relation Between Envelope Time Delay and Phase Versus Frequency Characteristic

It follows from Equation (37) that

$$\sin \omega_1(t-t_o) + \sin \omega_2(t-t_o)$$

$$= 2 \sin \left[\frac{1}{2} (\omega_1+\omega_2) (t-t_o)\right]$$

$$\times \cos\left[\frac{1}{2} (\omega_1-\omega_2) (t-t_o)\right]$$

and

$$\sin(\omega_1 t-\phi_1) + \sin(\omega_2 t-\phi_2)$$

$$= 2 \sin \frac{1}{2} [(\omega_1+\omega_2) t-(\phi_1+\phi_2)]$$

$$\times \cos \frac{1}{2} [(\omega_1-\omega_2) t-(\phi_1-\phi_2)] \quad (38)$$

If the envelopes are to be identical functions of time,

$$(\omega_1-\omega_2) t_o = (\phi_1-\phi_2)$$

or

$$t_o = \frac{\phi_1-\phi_2}{\omega_1-\omega_2} = \frac{\Delta\phi}{\Delta\omega}$$

$$\rightarrow \frac{d\phi}{d\omega} \quad (39)$$

as $\omega_2 \rightarrow \omega_1$,

REFERENCE

1. C. T. Morrow, "Shock Spectra, Residual, Initial and Maximax as Criteria of Shock Severity," Shock and Vibration Bulletin 45, part 5.

HIGH PERFORMANCE VIBRATION ISOLATION SYSTEM FOR THE DD963 GEARS

P.C. Warner
Westinghouse Electric Corporation
Marine Division
Sunnyvale, California 94088

D.V. Wright
Westinghouse Electric Corporation
Research and Development Center
Pittsburgh, Pennsylvania 15235

A system that effectively vibration-isolates a large high horsepower marine gear of conventional design from its foundation has been developed. Although it has not yet been tested at sea, its performance has been verified by extensive shop tests on fully loaded gears. The system is unconventional in that loads are carried through damped metallic members, thus avoiding problems associated with creep effects in elastomeric isolators. Further, isolator system stiffness is approximately ten times that of conventional isolation systems employing Navy rubber mounts, thereby alleviating problems due to large excursions during shock or other extreme operating conditions. Design considerations and restrictions are discussed. The isolator system is described and information on its vibration transmission characteristics is presented.

INTRODUCTION

Specification for gears, Figure 1, for the DD963 Class destroyers called for structureborne vibration levels markedly lower than vibration levels measured on the similar, though smaller gears supplied for the DE 1052 Class destroyer escorts. It was judged that such a large incremental improvement in structureborne noise levels could not be obtained with assurance by any conventional gear design and manufacturing technique, particularly in view of weight and cost limitations. Thus, a gear isolation system was proposed. This system has to provide 20 to 25 dB insertion loss in certain critical frequency ranges, not require a flexible coupling in the line shaft for stress reasons, and be designed around essentially committed gearcase and engine room designs. It will be appreciated that the latter restrictions in effect precluded a 'center of gravity' mounting, and thus led to an undesirable amount of spread of the rigid body natural frequencies of the gearcase on the isolation system.

To achieve the full benefits of such a 'hard' isolation system, it is essential for the ship designer to provide a foundation with a number of high impedance points at which to connect the isolators. Clearly, such an isolation system cannot be expected to carry shock loads and other extreme operating loads, hence a separate, though carefully integrated snubber system was designed.

While an isolation system using elastomeric materials can be designed to meet these requirements, there are distinct advantages to the use of a damped, metallic system. One of the important advantages is that in a metallic system, the system stiffness is approximately

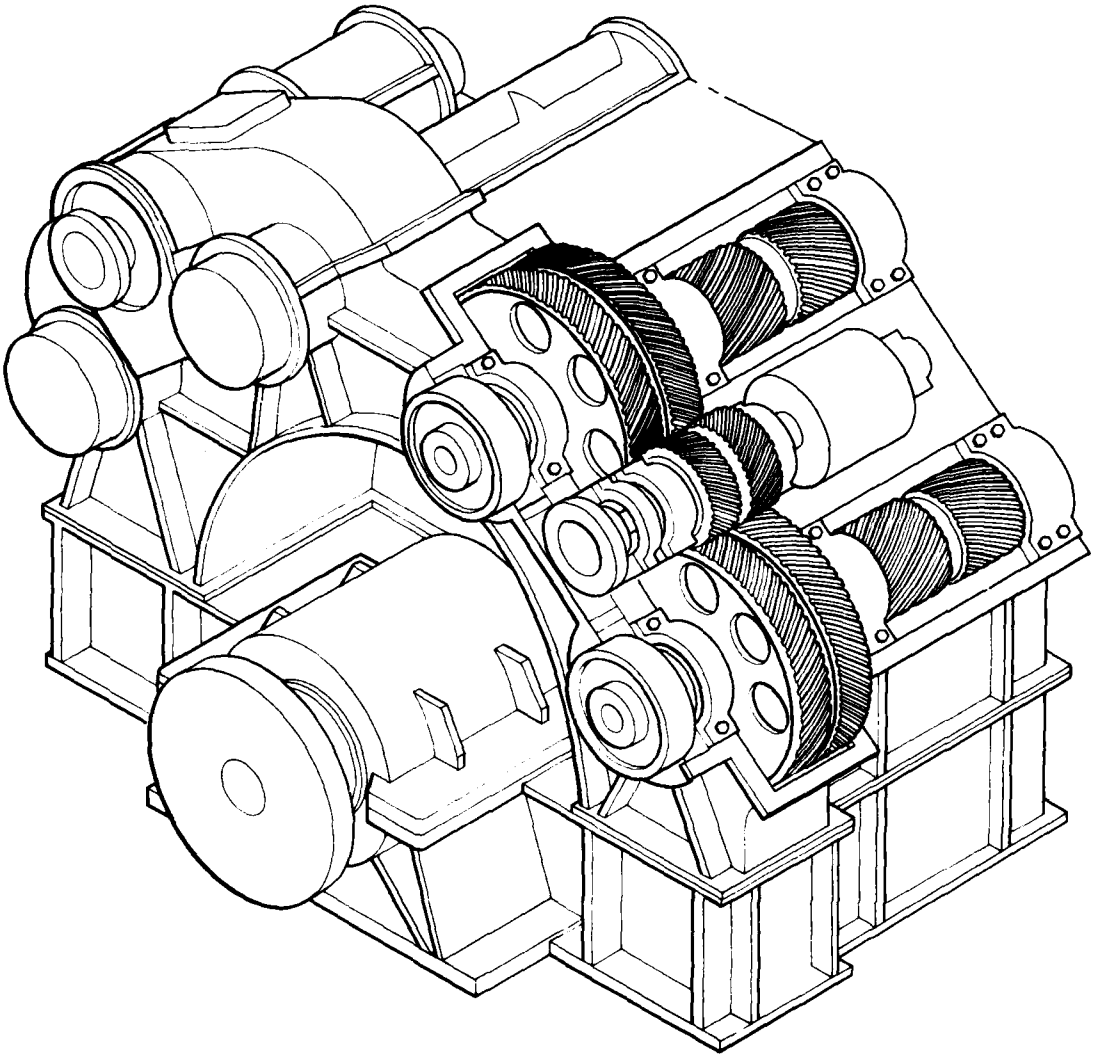

Figure 1. Main Reduction Gear 40,000 HP, 3600 RPM/168 PRPM

the same statically as dynamically, and does not change appreciably with frequency. Thus, minimum stiffness values set by design considerations of stress or deflection, gear tooth misalignment stresses in the present case, do not result in dynamic stiffnesses which cause excessive vibration transmission over that to be expected from static stiffness values. (Typically this metallic isolator system has a dynamic to static stiffness ratio of approximately 1.1 as compared to a ratio of about 1.5 for typical rubber mounts, and approximately 3 for a design using Fabreeka, a fabric stiffened elastomer). A further advantage of the use of such metals as aluminum, titanium, or steel for the load carrying members is the absence of creep effects such as commonly occur in mounts of elastomeric materials. Thus, no portion of allowable deformations need be reserved for such effects. Additionally, the metallic isolator system is compact. A vertical isolator which carries static loads up to about 45,000 pounds occupies a space of only about 8 inches in diameter and 20 inches long. The 8 inch diameter, in the plan view, compares

with an equivalent required load carrying area for Navy 10,000 pound mounts of two square feet in the plan view. In addition to the geometrical advantage, the metallic isolator has, by virtue of its small cross sectional area, approximately the same high frequency characteristic impedance in the load carrying direction as the static load equivalent in Navy 10,000 pound mounts, and a large advantage in the other five degrees of freedom, which also can transmit appreciable vibration.

DESIGN OBJECTIVES

Our experience shows that there are many sources of vibration excitation in a marine reduction gear, and that the energy source for any particular observed frequency of vibration may be difficult or even impossible to identify even though the vibration itself may be quite large at times. Despite this, for a modern gear, it can usually be assumed that the chief source of either airborne or structureborne noise will be transmission error at second reduction (low speed) mesh frequency. On occasion, however, transmission error at the first reduction mesh frequency will be a contender for 'most troublesome' honors. Thus, an isolation system which is to produce acceptably low levels of vibration at the top of a DD963 foundation must provide large insertion loss over the frequency range occupied by these two sources of energy for the range of propeller speed to be tested; in this case, from roughly ⅓ to ¾ full speed. See Figure 2.

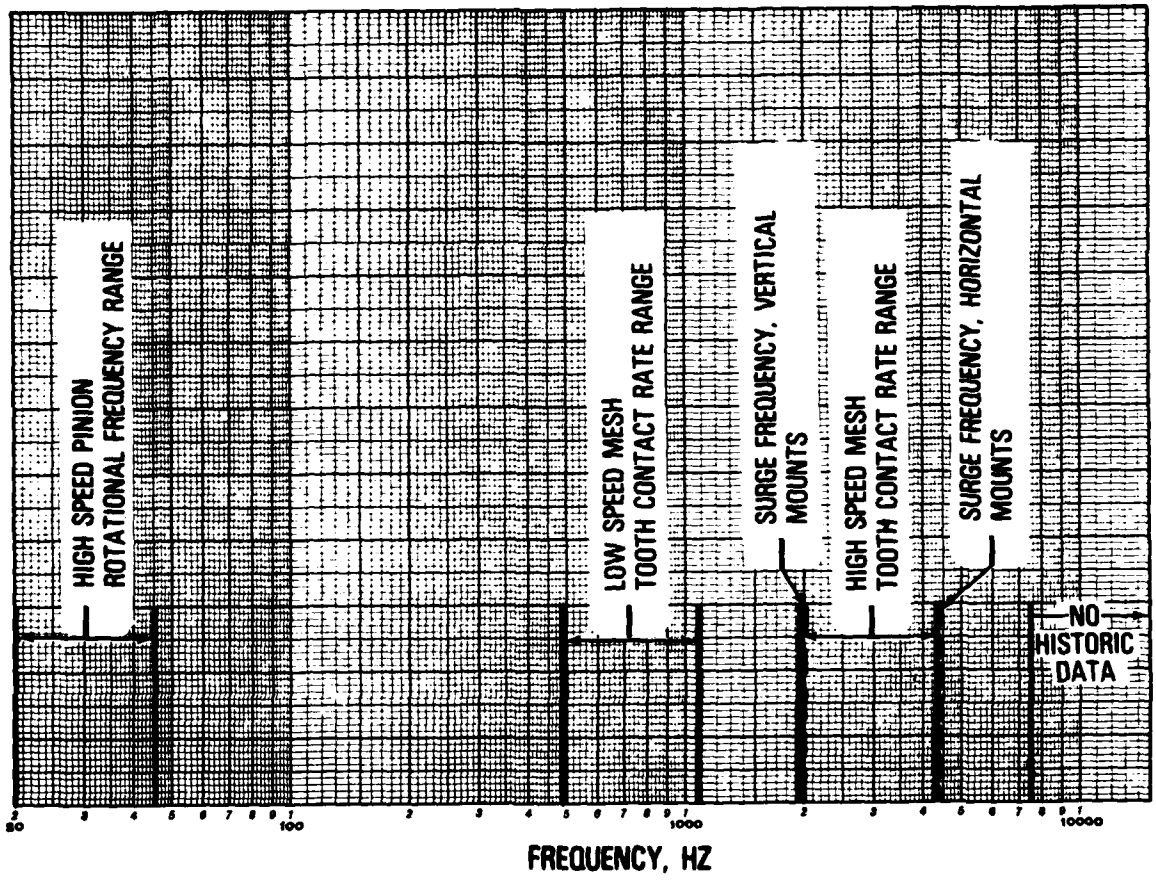

Figure 2. Main Excitation Frequencies (33 to 74% RPM Range)

Another known energy source which at times can dominate noise considerations is the vibration due to unbalance in the various shafts in the gear, but particularly the high speed pinion shafts. These sources lie in the low end of the frequency range of interest, and should preferably not coincide with any rigid body mode of the gearcase at any test speed. While these energy sources may not require isolation, they probably can't in general stand a large amplification. Thus, it is necessary to damp the isolators to control the Q of the rigid body modes, particularly those modes in the fore and aft direction where no appreciable oil film damping between rotating and stationary parts exists. In addition, propeller excited motions and motions due to various sea states and the possibility of impacting hard snubbers also dictate that the rigid body modes be well damped, say Q ($\frac{1}{2\delta}$) less than 25.

At the high end of the frequency range of interest, insertion loss is limited in part by the Q of the isolators at the surge frequencies. Thus, there is good reason to obtain reasonable damping at high frequencies, and to place the first surge frequency well away from any of the known chief sources of excitation in the speed range of primary interest. Furthermore, the frequency range of interest for the DD963 contains at least an octave in frequency above 10 KHZ in which there did not appear to be any valid data on structureborne vibration levels. Hence, it appeared highly desirable not only to have appriciable high frequency damping in the isolators, but also to minimize their high frequency characteristic impedance (ρCA).

In addition to the frequency considerations outlined previously, it is also necessary to determine the foundation impedance into which the isolators will work in order to permit final isolator design for a given estimated required transmission loss. Evidently the higher the foundation impedance, the easier the isolation design and vice versa. After much investigation and negotiation it was finally agreed to use as the nominal foundation impedance, an idealization of the impedance measured on a DE 1052 Class gear foundation. The curve used in design, and to which the measured structureborne vibration results are corrected is given in Figure 3.

The desirable life of an isolator system in terms of elapsed time may well be readily evident. The attainable, or even necessary life in more fundamental terms such as number of excursions of an isolator through the full snubber clearance due to ship motion and operating loads may be difficult to assess. Indeed, it will usually depend strongly on the speed-load-sea state operating profile and dynamic characteristics of the ship itself. Clearly, required snubber clearances themselves depend on such factors, while the stress levels induced in an isolator during excursions will be proportional to the clearance. In the present case, the process of estimating the necessary cyclic life, hence the design life, was both long and tortuous. It culminated essentially in an agreement on a design objective life of 10^7 cycles and an accelerated fatigue test demonstration of 10^6 cycles minimum. This agreement resulted in a modest, though very effective, redesign of the vertical isolators, and a minor redesign of the athwartship isolators.

The essentials of the isolation system are probably seen most clearly in Figure 4. Vertical forces including torque reactions are carried by the eight vertical isolators. Fore and aft forces are carried by four fore and aft isolators and athwartship forces are carried by eight athwartship isolators. All isolators, Figures 5 and 6, transmit forces principally along one axis and each obtains its flexibility along this axis by virtue of tension-compression strains rather than bending strains. This tends to maximize the value of the first surge frequency and to minimize the high frequency characteristic impedance, since isolator area is small. For the same Q, it does require a greater ratio of damping material area to isolator material area since the strains in both materials are the same.

The steel snubber system, which is also shown in Figure 4, carries all shock loads and the higher range of 'normal' loads due to ship motions, etc. The system is designed to be clear of the snubbers (that is, isolating) up through sea state four, though not quite to full power.

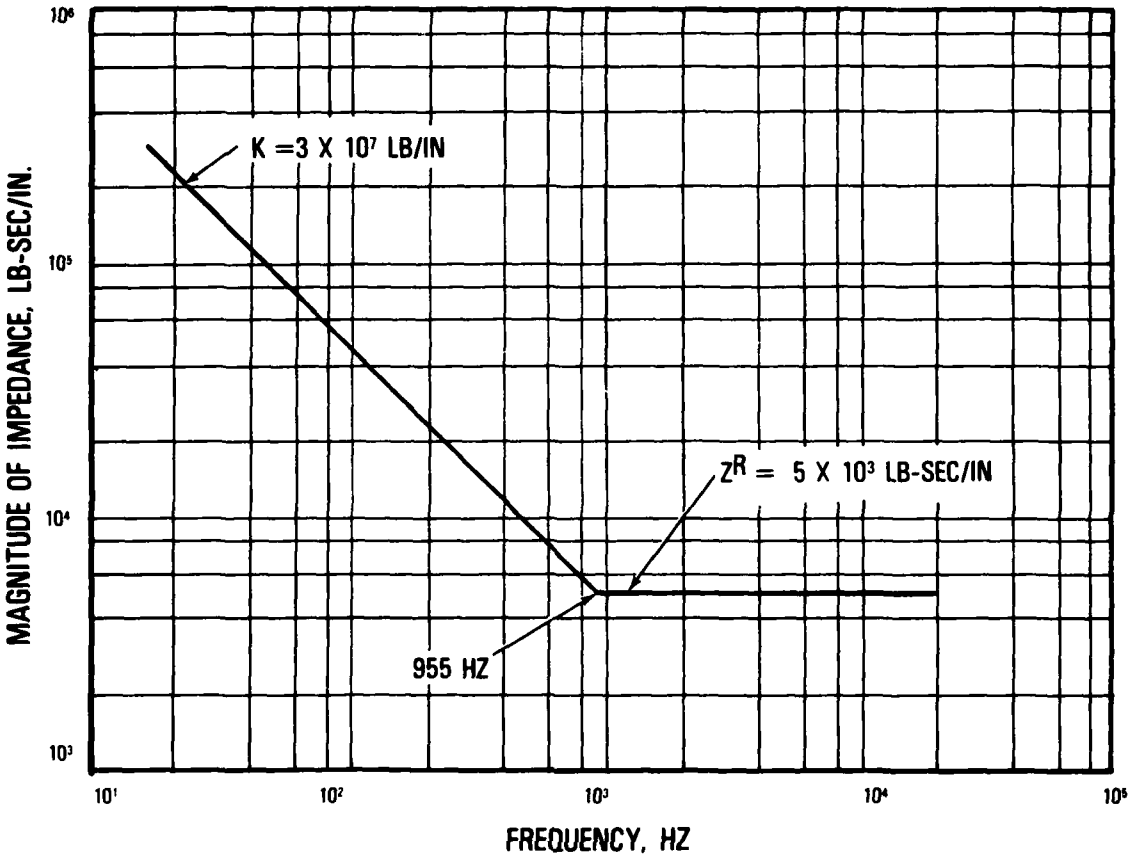

Figure 3. Design Foundation Impedance

VERTICAL ISOLATORS

The vertical isolators, Figure 5, have a stiffness in the load carrying direction of .71 x 10^6 lb/in. and they are damped by Lord LD 502 damping material to a Q of 28 at low frequencies and 125°F. The first surge frequency occurs at 2,000 Hz.

The isolator is made from an extruded bar of 7075 aluminum in the T73 condition by trepanning the annular area between the inner and outer tubes. The need for welding or an intermediate bolted flange design is thus eliminated. The T73 condition was chosen for stress corrosion reasons and the isolator has, as additional protection, a proven urethane paint system applied. Since required cyclic life is high, and peak stresses are of necessity also reasonably high (up to 30,000 psi tension for maximum excursion), the isolator is shotpeened all over to Almen intensity of .010-.014. Further, the contours at both flanges and at the top "fold over" section are carefully designed to minimize stress concentrations. Additionally, the stainless steel tapered collar and stainless steel tapered adapter piece not only minimize stresses, but also impart a favorable setup stress in the critical flange area. These measures resulted from finite element stress calculations, strain gage tests, and full scale fatigue tests. Fatigue tests to date indicate an acceptable margin in cyclic life.

The LD 502 damping tile has favorable properties, Figure 7, for the required temperature range. The properties are relatively insensitive to frequency. We did find it difficult to apply in that it was difficult to get

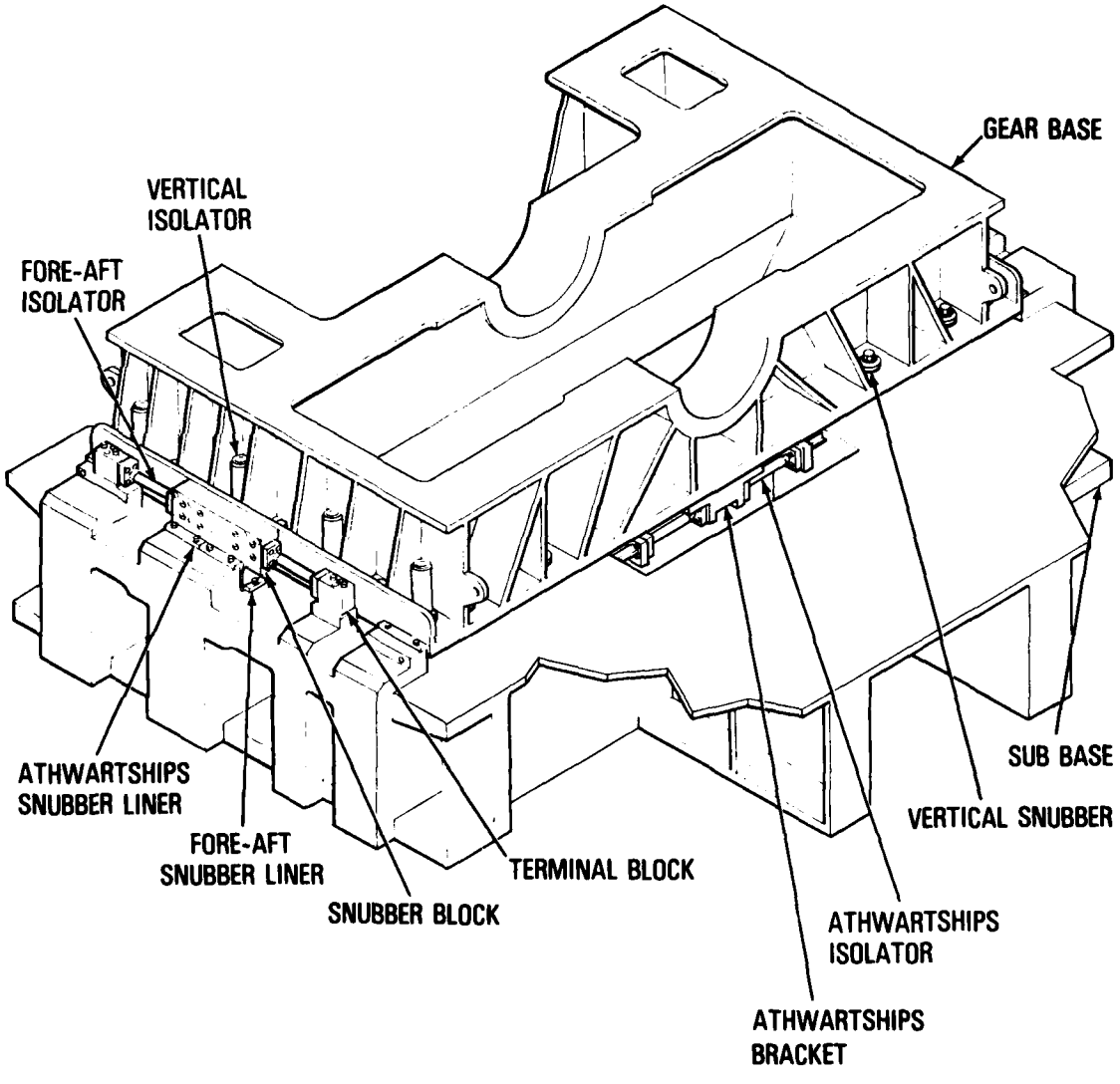

Figure 4. DD963 Gear Support System

good bonding of tile to isolator, particularly to the inner tube. More disconcerting, in fatigue at high tensile strain levels, say .003 inch/inch, the tile itself tended to fatigue and break away adjacent to the adhesive joint if operated below the glass transition temperature (about 90°F). This problem was overcome by starting the damping tile in the low stress region of the isolator, contouring the end of the tile to reduce the strain concentration, and testing in a temperature range closer to the actual use range of 110°F to 140°F. It should be noted also that, for economy reasons, our test strain rates were at least an order of magnitude greater than those which might be expected in service. Thus, the test tends to exaggerate the strain in the tile over maximum operating strain. Latest tests, when conducted at the proper temperature, show that the damping tile survives 1.5×10^6 cycles at full strain of .003 in/in without noticeable degradation.

HORIZONTAL ISOLATORS

The horizontal isolators, Figure 6, have a sitffness in the load carrying direction of .9 x 10^6 lb/in., and they are damped by LD 502 damping tile to a Q of about 10 at 125°F. The first surge frequency occurs at 4400 Hz.

These isolators are made of 6 A1 4V titanium by electron beam welding a rod into two flange pieces. The circumferential weld is outside of the highest stress zone. The isolators are shotpeened to Almen .010 - .014 all over the central section, and the junction between the rod and flange is an approximate 'waterfall' (variable radius) fillet design to minimize stress concentration. Peak stresses for excursion through the complete snubber clearance fall considerably below the estimated fatigue limit of the material, so that the design will have essentially unlimited life.

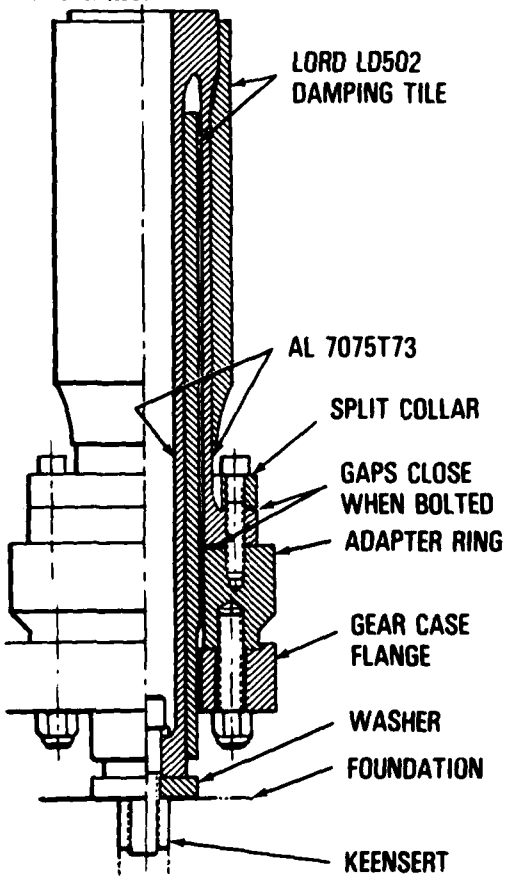

Figure 5. Vertical Isolator

The horizontal isolators are damped by LD 502 material also. As with the vertical isolators, both contouring of the tile ends and avoidance of excessively low temperature testing were necessary to avoid failures of the damping material.

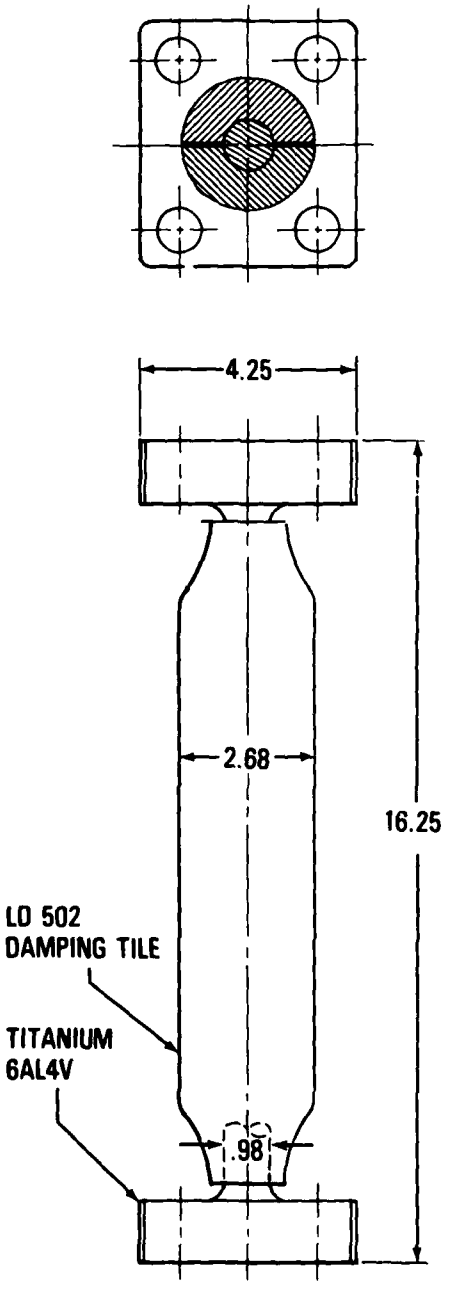

Figure 6. Horizontal Isolator

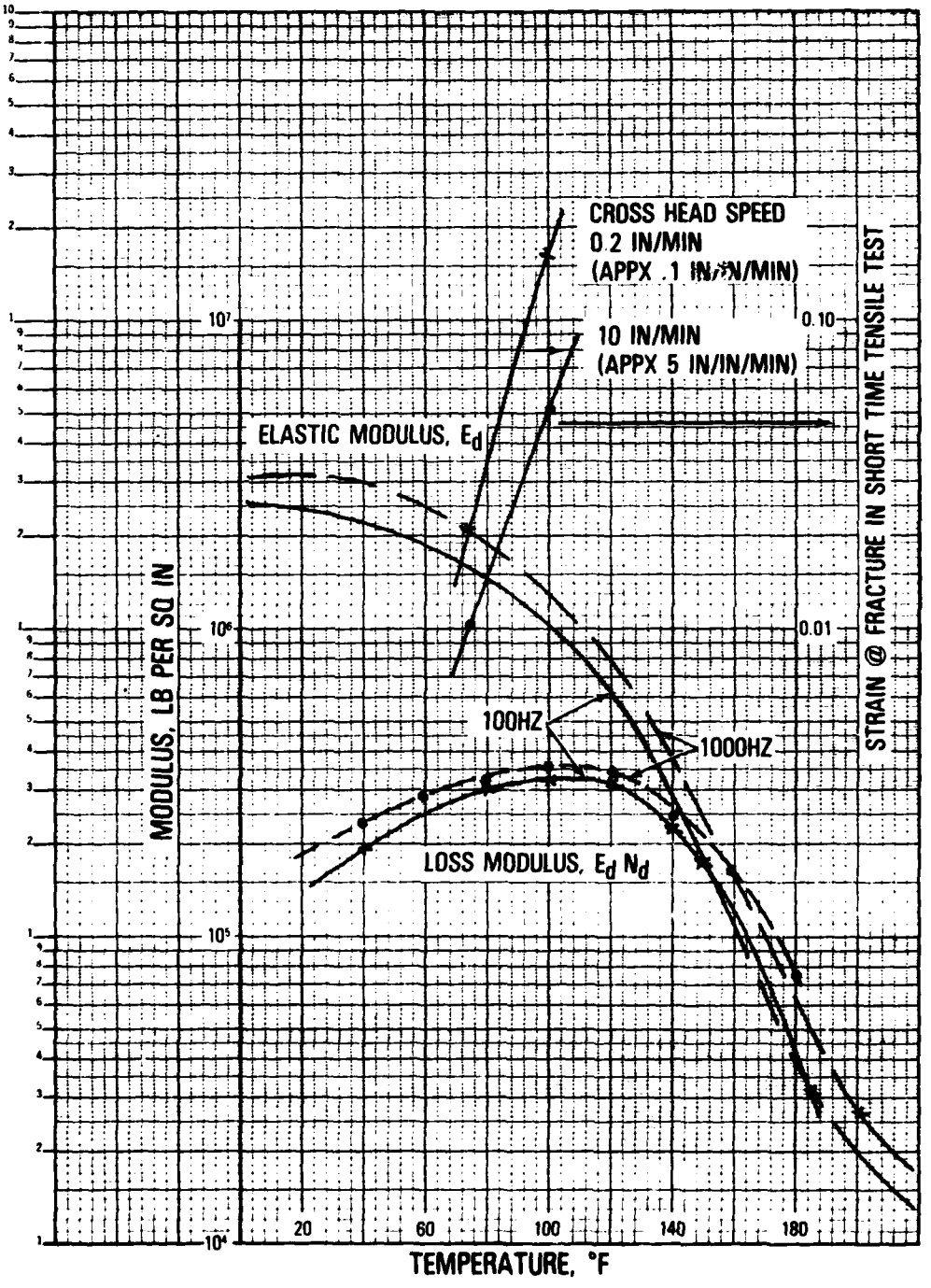

Figure 7. LD 502 Damping Mtl, Sp. Gr. = 1.6 (E_d, N_d From Lord Corp)

ISOLATOR TESTS

During the design process certain key spot checks were made on material properties and isolator design. In particular, experimental evaluations of the dynamical properties of LD 502 gave damping and stiffness values slightly more favorable than Lord's curves. Figure 8 gives results of tests on a fore and aft isolator terminated by a mass. Agreement with calculation is good, particularly relative to Q estimates. Other data, with greatly expanded vertical scale, and accurate frequency determination at the 3 dB down points also give results which agree well with computation. Figure 9 gives results of the horizontal isolator mounted on a fore and aft terminator. The solid line, measured acceleration ratio, curve is corrected for variance of foundation impedance from the design values of Figure 3, giving the dashed curve. The accuracy limitations inherent in such a large correction factor are evident. Neverthless, the low frequency transmission loss, first surge frequency, and transmission loss at the surge frequency all match calculations to a reasonable degree although there is evidently more flexibility in the connections than has been accounted for. Only the crudest estimate of average acceleration transmissibility, about 40 dB, is available at higher frequencies. This compares to an estimated 32 dB at the broad minimums of the calculated transmission curve. Figure 10 gives similar results on the current design of vertical isolators. (It has been fatigue tested for 3×10^6 full deflection cycles, the last 1.5×10^6 cycles with the damping tile on). Again, transmission calculations and experimental results are in reasonable agreement. Figure

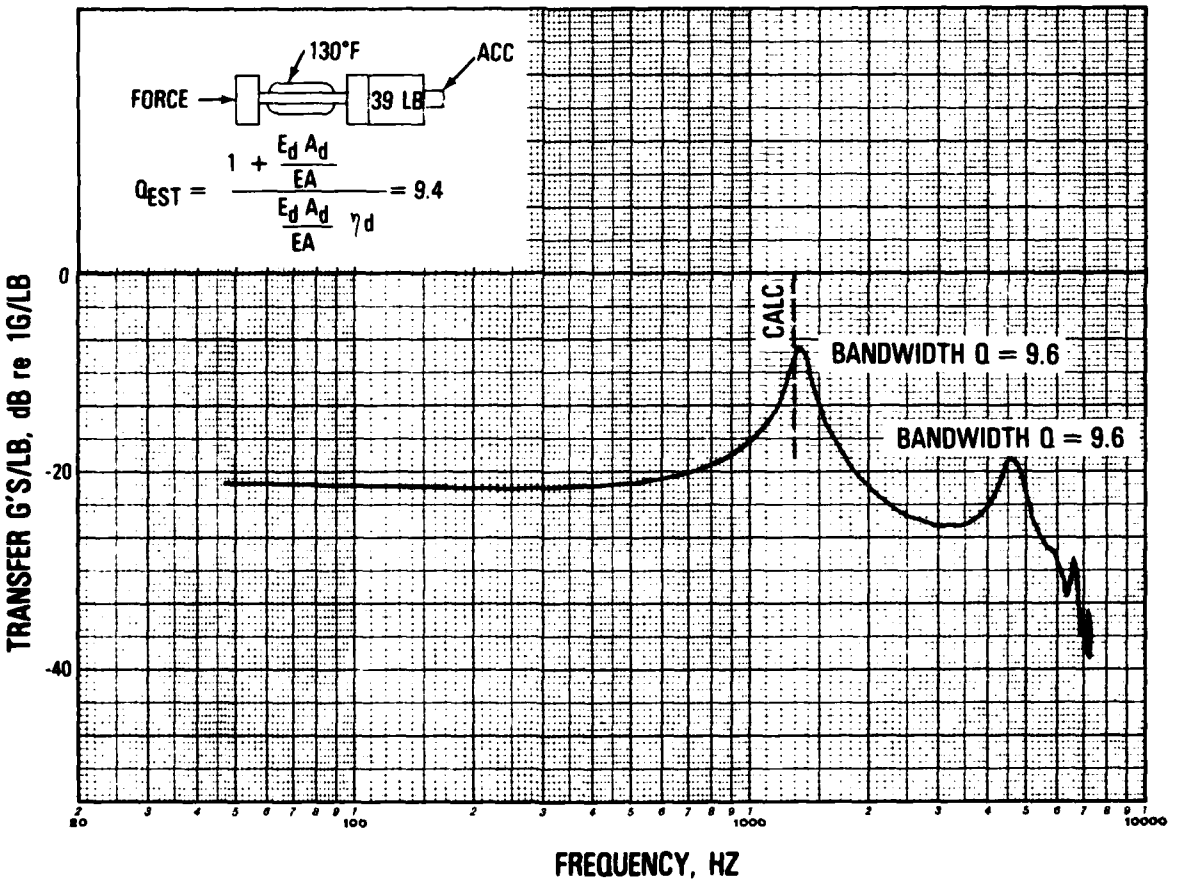

Figure 8. Mass Terminated Fore and Aft Isolator

11 gives the results of testing the vertical isolator on its terminator for transmission loss. Results have been corrected on a point by point basis for the difference between terminator impedance and the design objective impedance of Figure 3. Since this correction can be as large as 20 dB, and since both the correction curve and the basic response curve show many peaks and valleys above 1500 Hz, it is difficult to obtain an accurate, corrected curve. Thus, Figure 11 must be used with caution. It does, however, bear out both the design calculations and other test results both as to basic levels of transmission loss and as to location and severity of surge frequency transmission peaks.

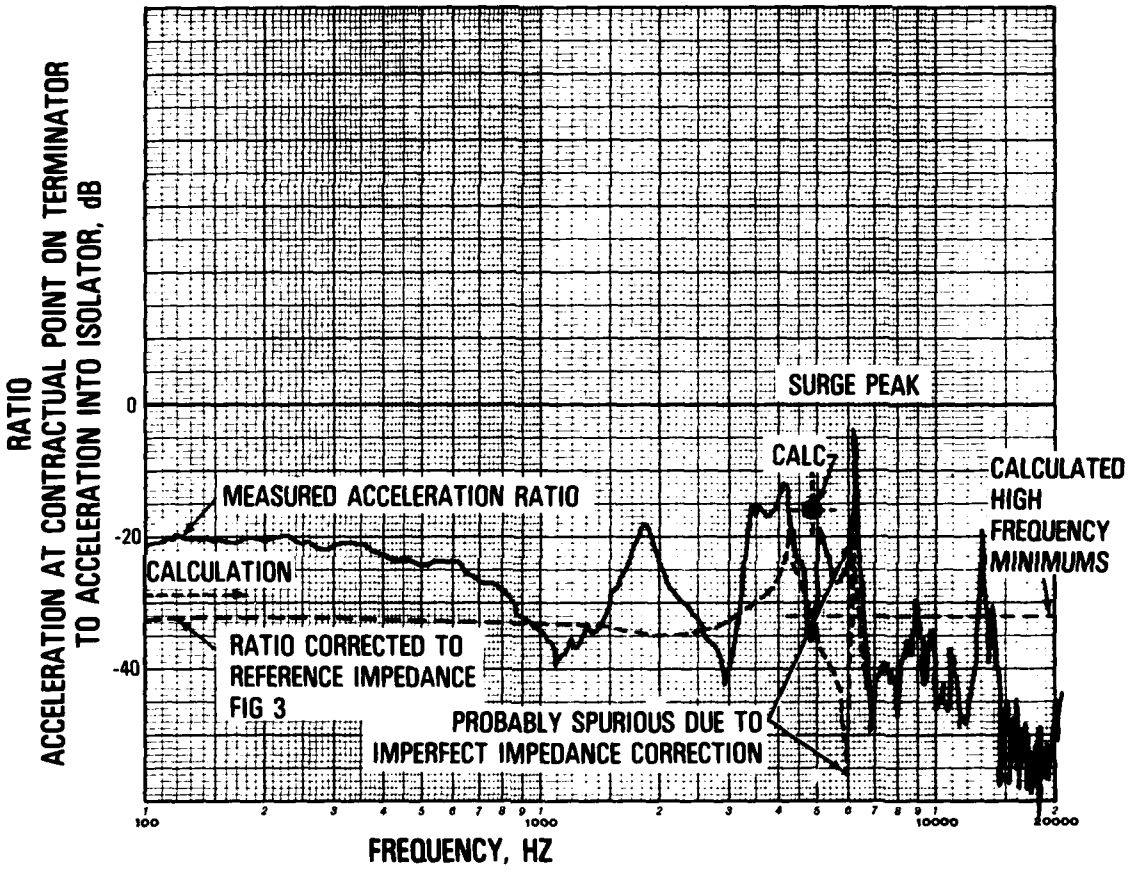

Figure 9. Fore and Aft Isolator on Terminator (Isolator @ 127°F, F-1 Terminator @ 105°F)

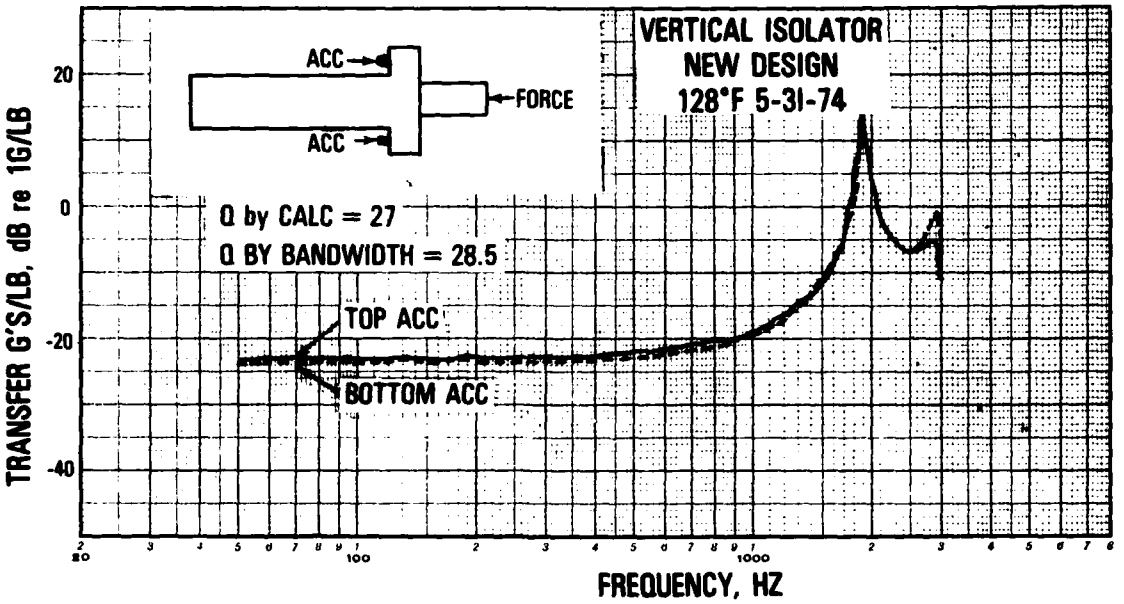

Figure 10. Free-Free Test of Vertical Isolator

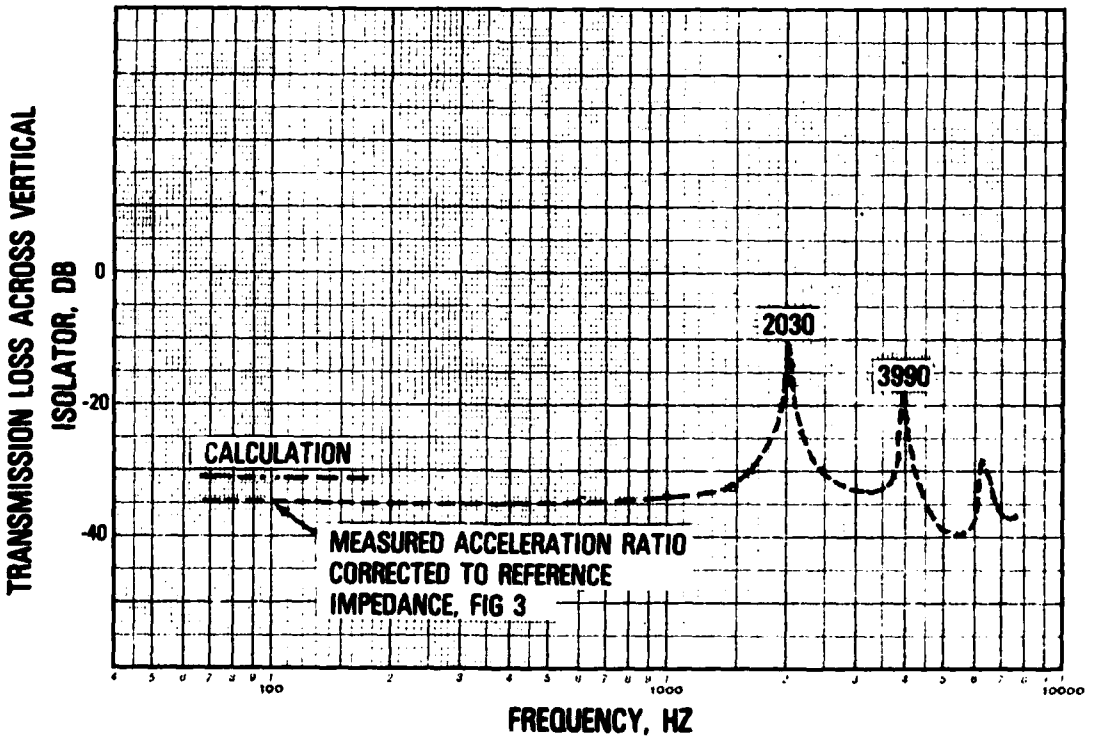

Figure 11. Vertical Isolator @123° On V5 Terminator @105 °F

STRUCTUREBORNE VIBRATION TESTS

One of the key acceptance tests performed on the DD963 gears is the structureborne vibration test. In this test, two gears are driven 'back-to-back' by a steam turbine as shown in Figure 12. Proper torques are obtained by means of torque appliers in the high speed connecting shafting. (These torque appliers permit one gear to be torqued against the other). Thus, any torque and speed conditions can be obtained on the test gear. To minimize the uncertainties of correcting gear vibration output for test foundation and gear impedances, and to determine the true performance of the gear and isolation system, a special 1 x 10^6 lb concrete, steel, and epoxy foundation was built to approximate the reference impedance curve shown in Figure 3. The design and testing of this foundation is treated in detail elsewhere (*). It is sufficient for present purposes to observe that measured structureborne vibration data are corrected for differences between

(*) J. R. Hupton - "The Design and Measurement of a High Impedance Foundation to 20 KHZ and the Use of the Data in Correcting Noise Measurements." 45th Shock and Vibration Symposium

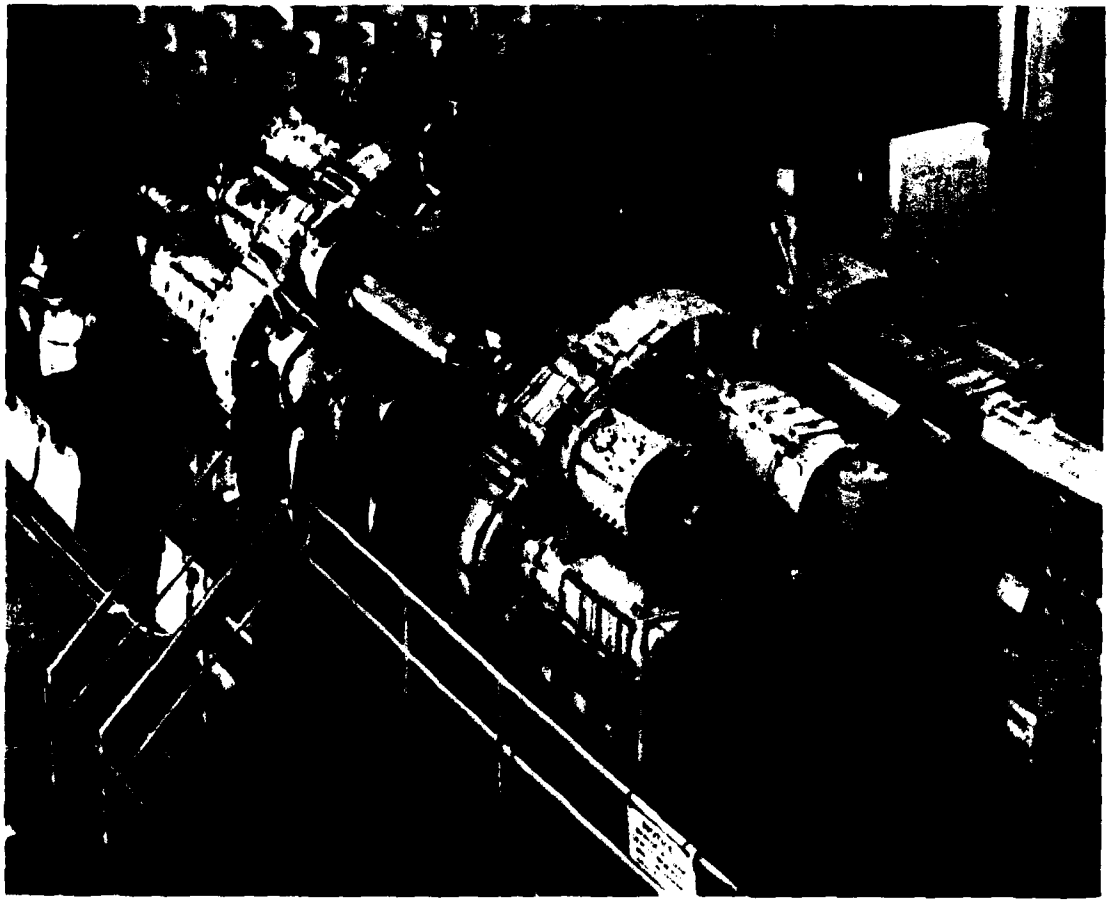

Figure 12. Back-to-Back Gear Test Driven By Steam Turbine

measured termination impedance and target values of Figure 3 based on the assumptions that the isolators are flexible compared to gear and terminator, and on complete decoupling from terminator to terminator. Corrected structureborne vibration values are power summed over 1/3 octave bands and power averaged over all isolators for a given direction. These values are then compared to specification values.

Each gear is vibration tested at a number of speed and load points. Initially, at each test speed, the test values were taken as the worst values over a speed range of ±3% of the test speed. Subsequently, certain of the ±3% test points were eliminated. All gears have passed these tests with minimum margin ranging from 4 dB to about 12 dB. The point of closest approach in all vertical cases has been at the first surge frequency of the isolator despite there not being a major noise source coincident at this frequency except at the lowest test speed. However, as specification limits have not been threatened, no effort has been made to operate the isolators at proper (more favorable) temperatures. Figure 13 shows a typical composite test result for the test speed 2680 RPM and the ±3% points.

Since it is not possible to ascertain from curves such as Figure 13 whether the isolation system is performing approximately as designed, some testing was done with the vertical isolators replaced by stiff steel connectors. (Low frequency stiffness approximately 10^7 lb/in). Figure 14 gives typical results. Above mount readings, typical of measurement of a hard mounted gear, reach

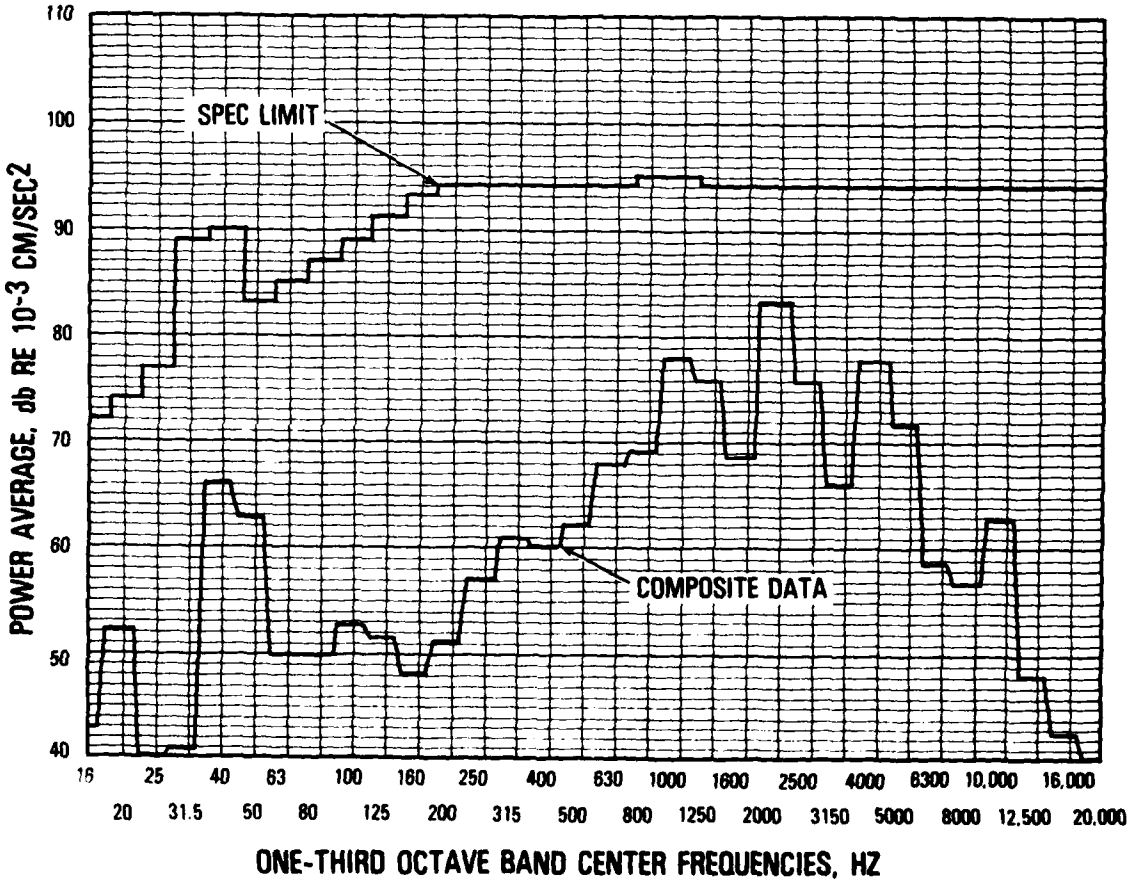

Figure 13. Vertical Structureborne Noise at 2680 RPM ± 3%

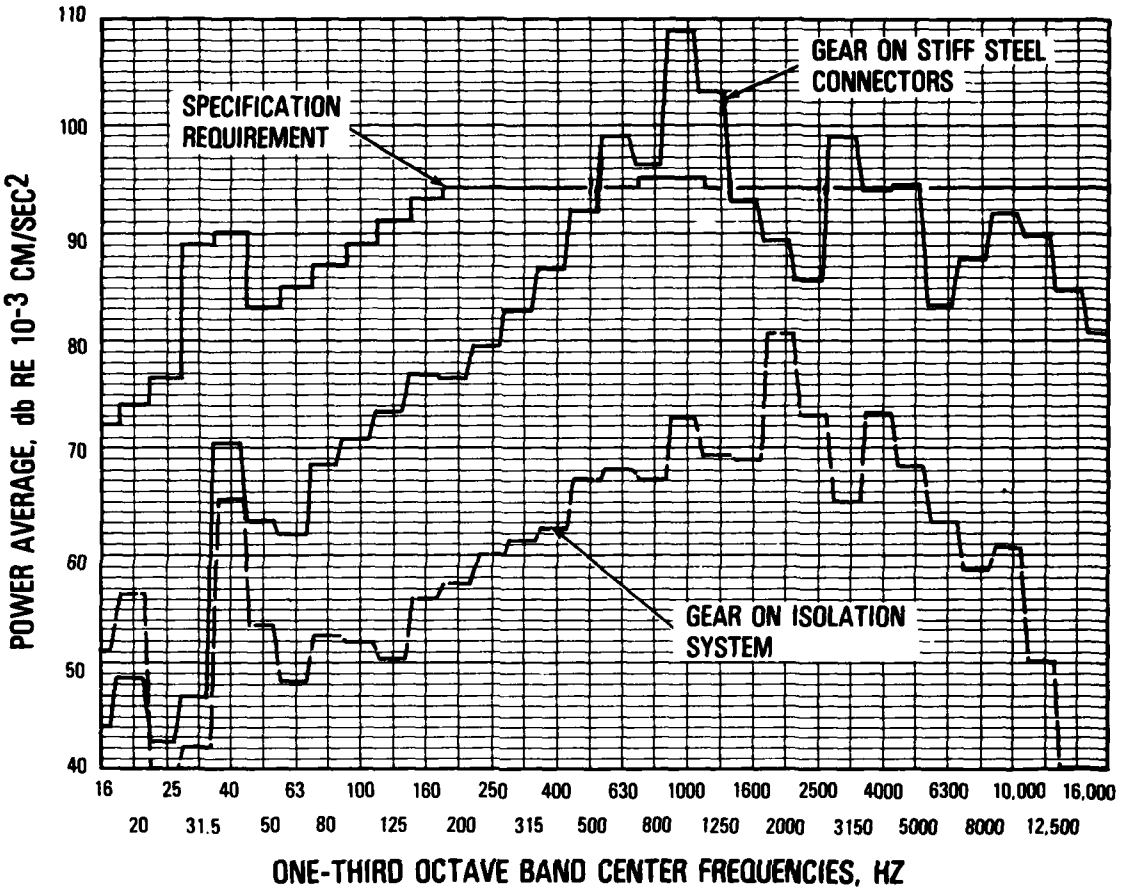

Figure 14. Vertical Structureborne Noise at 2680 RPM

10-15 dB above specification limits. The below isolator data are from a test with the same conditions, but the gear mounted on the isolation system. Figure 15 gives the dB difference between gear flange vibration measured both above the steel connectors and above the vertical isolators. Data are from tests at two different speeds and are power averaged. It can be seen that in the frequency range above approximately 1 KHZ, vibration levels above the steel connections were generally within ±4 dB of the levels above the vertical isolators and the average difference is close to zero. In the frequency range from 1 KHZ down to 250 Hz, the average ratio drops off to approximately -6 dB. In the lowest frequency range, the ratio is quite variable, as may be expected. Thus, there is no large reverberant vibration buildup in the gear due to decoupling from the foundation damping; hence, over most of the frequency range of interest, transmission loss and insertion loss are approximately the same.

Figure 16 gives results of tests at input speeds of 2140 RPM and 2680 RPM. In both cases, power averaged measurements made below the vertical isolators and corrected for terminator impedance are compared to power averaged measurements made above the vertical isolators. Data for above and below isolators were not taken at the same time, and thus lack of repeatability of the vibration, due to imperfect repeat of test conditions, and other uncontrolled events, must have an effect. Despite this, the two test speeds give essentially the same results,

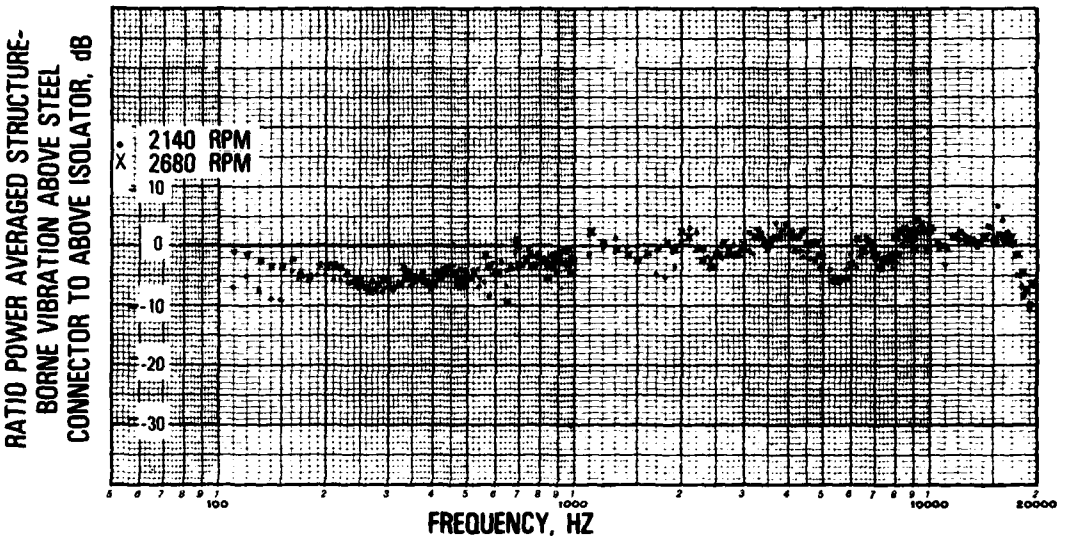

Figure 15. Comparison of Structureborne Noise Data Above Steel Connectors Relative To that Above Vertical Isolators, Power Averaged

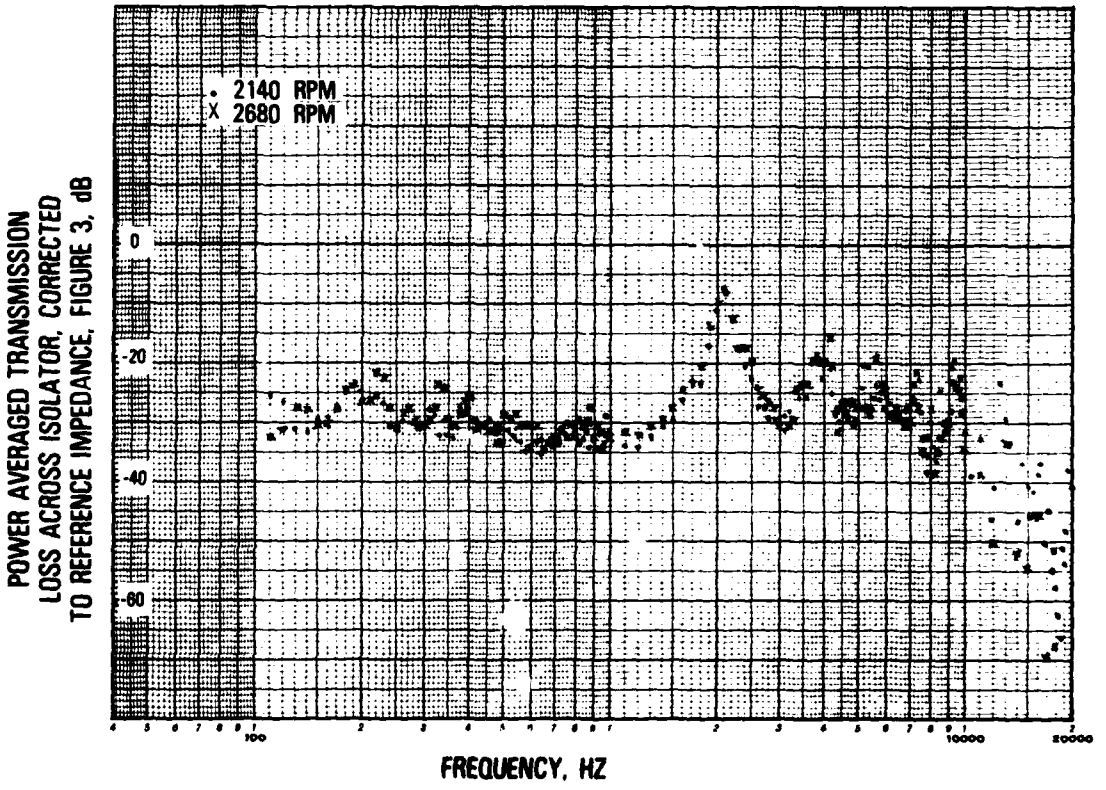

Figure 16. Transmission Loss Across Vertical Isolators

which are in accord with results of mass terminated isolator and isolator on terminator tests and calculations. Basic low frequency transmission loss (approximates insertion loss) is seen to be 30 dB or slightly higher, compared to an estimated 32.3 dB for the design employed in these tests. The first surge frequency stands out at 2100 Hz and gives a transmission loss of about 8 dB. This compares to a calculated surge frequency at 115°F of 2240 Hz (for the initial design) and calculated transmission loss, assuming a dissipative termination, of 15 dB. Since during gear vibration testing the isolators were operated at room temperature rather than the more favorable service (and calculation) temperature, this difference appears reasonable. Higher order surge frequencies evidently are of reduced importance, as theory predicts. The transmission minimums between these surge frequencies approximate 30 dB, whereas 31 dB is predicted by comparing the characteristic column impedance of the isolator with the termination impedance. Above 10 KHZ only the high's and low's of the transmission loss are plotted as it was desired to define general levels only, and the details cannot be interpreted in any case. It appears sufficient to note that good transmission loss holds through the frequency range of interest.

Similar extensive test data are not yet available for the horizontal isolators. However, the fragmentary data that are available tend to give a picture which is very similar to the picture on the vertical isolators. The horizontal isolators being simpler than the vertical isolators, are easier to analyze accurately. On the other hand, the terminators for the horizontal isolators are more complex than those for the vertical isolators and are more difficult to analyze. Experimental evidence to date indicates a more than adequate performance of the isolation system. However, if geometeric constraint were even moderately relaxed in a new design, this type of isolation system could be further improved. Better damping of the vertical isolators will improve performance both at the surge frequencies, and in the low frequency range where rigid body modes occur. Further, low frequency performance could be improved by a closer approach to a 'center of gravity' isolator arrangement, thus minimizing the spread in rigid body modes. Finally, cost could be appreciably reduced by eliminating the 'folded back' vertical isolator design in favor of a design similar to that of the horizontal isolators.

ACKNOWLEDGEMENT

In an extensive effort such as is described herein, many more people make important contributions to the overall result than can be recognized in a paper. In this effort, D. R. McAllister, Manager of DD963/Gear Engineering, and H. W. Semar, Consultant to the Marine Division made particularly outstanding contributions.

THE DESIGN AND MEASUREMENT OF A HIGH IMPEDANCE FOUNDATION TO 20 kHz AND USE OF THE DATA IN CORRECTING NOISE MEASUREMENTS

J.R. Hupton
Westinghouse Electric Corporation
Marine Division
Sunnyvale, California 94088

A foundation (10^6 lb) was designed such that the point impedance of each isolator termination point could be controlled from 14Hz to 20kHz. The objective was to have each termination impedance approximate a reference impedance and then measure each termination point impedance such that the measured structureborne noise of the gear could be corrected to the reference impedance. This reference impedance is itself an approximation of a typical destroyer engine room foundation and was used as a design objective by the shipbuilder for their engine room foundation.

INTRODUCTION

When structureborne noise measurements are made on a component for shipboard use they are normally conducted in accordance with MIL-STD-740B. Under this normal procedure, the component is mounted on some type of Navy standard resilient mount in order to reduce the effects of extraneous shop background noise and to ensure that all the components of a similar nature are tested in similar environmental conditions. The above mount vibration readings are taken at the noisiest foot of the machine. If the foundations to which the resilient mounts are attached differ, the impact on the impedance that the component under test is exposed to is small because the resilient mounts have a relatively small impedance as compared with the foundation.

This procedure is satisfactory as long as the components being tested will be resiliently mounted in service and an acceptance criterion is available for these test conditions. Such a criterion might be based on historical data of like or similar components. However, if such an acceptance criterion is established by means of analytical computations based upon a desired sound pressure level in the water and transfer functions between the water and the component's foundation, then it becomes more desirable to eliminate the isolator as an unknown. This is especially true if the isolator is of a new design and little is known about its insertion loss.

Therefore, below mount measurements are better because they include the isolator's performance as well as set-up variations of the component-isolator combination. They

also eliminate errors in evaluating isolator performance. If the isolators were evaluated separately and then combined with an above mount criterion, the resulting below-mount level would be more difficult to predict, and such an approach would also constrain the isolator design process since it would be judged on a separate performance criterion. Whenever waterborne levels are to be calculated from measured structureborne noise, levels measured on the ship's foundation are better than data measured above the mount.

If the noise measurement method involves making measurements on a rigid foundation for the purpose of comparison with an acceptance criterion, then it is important to know the termination impedance for which the acceptance criterion is intended. And, conversely, the noise measurements made on different foundations must be corrected to a reference impedance for valid comparison.

If a foundation is to be constructed for the purpose of a noise test program, then ideally the point impedances of the attachment points should be equal to the impedance the component will be connected to in normal service. Such equality over a large frequency range is unrealistic, but it is not unrealistic to achieve impedances within 10 to 20 db of a desired reference impedance. Such a test program can be conducted simply by establishing a reference impedance curve (expressing the impedance as a function of frequency) that closely approximates the impedance the component is expected to see in normal service and then by designing and constructing a test foundation whose point impedances closely approximate the reference curve. The noise data that is measured on this foundation beneath the component under test can then be corrected by the ratio of the measured point impedances of the foundation to the reference impedance. Such a procedure requires that the point impedances of each terminating point of the foundation be measured exactly as functions of frequency. The advantage of such a system is that the measured noise data is corrected to a known impedance and thereby represents the exact noise level the foundation with that impedance would have in the ship, assuming that the ship designer designs the ship foundation to meet the reference impedance. It is important that the reference impedance be used as a design objective for both the test foundation and the ship foundation so that there will not be major differences in stiffness between the two. This method of testing is ideal for components that include isolators as part of their design.

REFERENCE IMPEDANCE

In 1971 Westinghouse started design and construction of a shipboard reduction gear that was to provide structureborne noise levels that could not possibly be guaranteed without some form of isolation. Because of the lack of a flexible coupling in the drive shaft system, this isolation had to be designed to eliminate the large excursions that the reduction gear would normally have when mounted on a conventional soft mounted system. Furthermore, the acceptance criterion as agreed to was a structureborne noise level to be measured on a foundation; that is to say, whatever the form of isolation used, it was considered to be part of the gear. This meant that the point impedances of the foundation would have significant impact on the noise measurements made, and, therefore, the customer desired that the acceptance criteria be tied to a reference impedance.

The final reference impedance curve as shown in Figure 1 is the result of technical investigations as well as negotiations between Westinghouse and the customer. The technical investigations included impedance measurements on foundations of similar ships for which historical gear noise data was available. Since the ability to design and manufacture a reduction gear to meet a specific structureborne noise level had to be based upon historical gear noise data, in a similar fashion the impedance from which this historical data was taken was the best criterion in establishing a reference impedance curve. Of course, the impedance measurements made do not follow precisely the curve shown in Figure 1. However, the general trend was similar in that the impedance tended to follow a stiffness line up to 1 to 2 kHz and then to vary sharply with frequency throughout the upper frequency

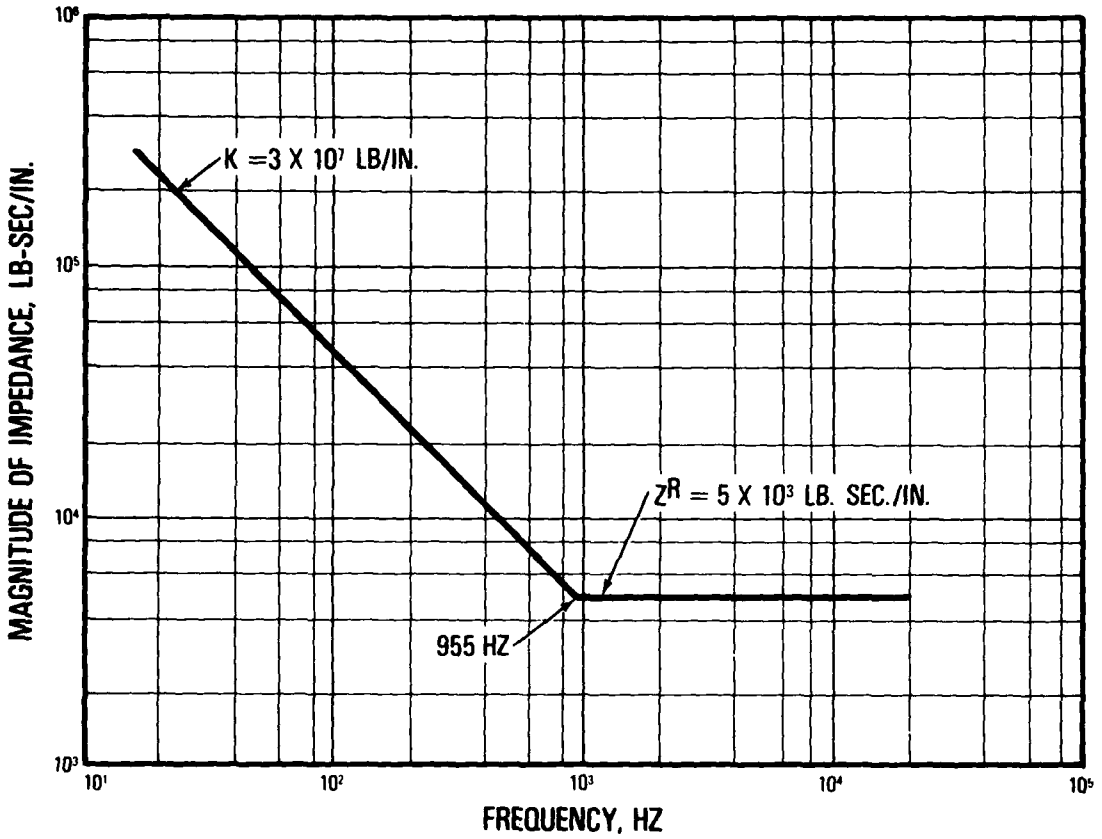

Figure 1. Reference Impedance

range, but it tended to oscillate between resonances and anti-resonances about a constant impedance line of about 5,000 lb. sec/in. The stiffness portion of the measured impedance was consistently in the vicinity of 30 x 10^6 lb/in. Therefore, the reference impedance curve as shown in Figure 1 represents the impedance to which the structureborne noise acceptance criterion was tied, and any differences between the foundation impedance and this reference impedance curve would produce a mathematical correction to the measured structureborne noise on the same foundation. The fact that the curve extends all the way up to 20 kHz illustrates another unorthodox feature of this noise test program in that structureborne noise and impedance were measured to 20 kHz instead of the normal 8 kHz. This feature in itself required that many technical problems in foundation design and instrumentation be overcome.

THE FOUNDATION

The design and construction of a foundation that would support a shipboard reduction gear for test and approximately duplicate the impedance shown on Figure 1 was in itself a major undertaking. The basic approach to achieve this impedance was to mount a large steel "terminator," one for each gear mounting point, in a large common concrete foundation whose size and mass were designed such that its mass line would have the same impedance that a 30 x 10^6 lb/in. stiffness has at a low frequency. The steel terminator had a plunger made of steel separated from the outer steel part of the terminator by a viscoelastic material whose shear stiffness was designed to provide the 30 x 10^6 lb./in. spring.

Figure 2 shows an isometric view of the foundation with the terminators located in the

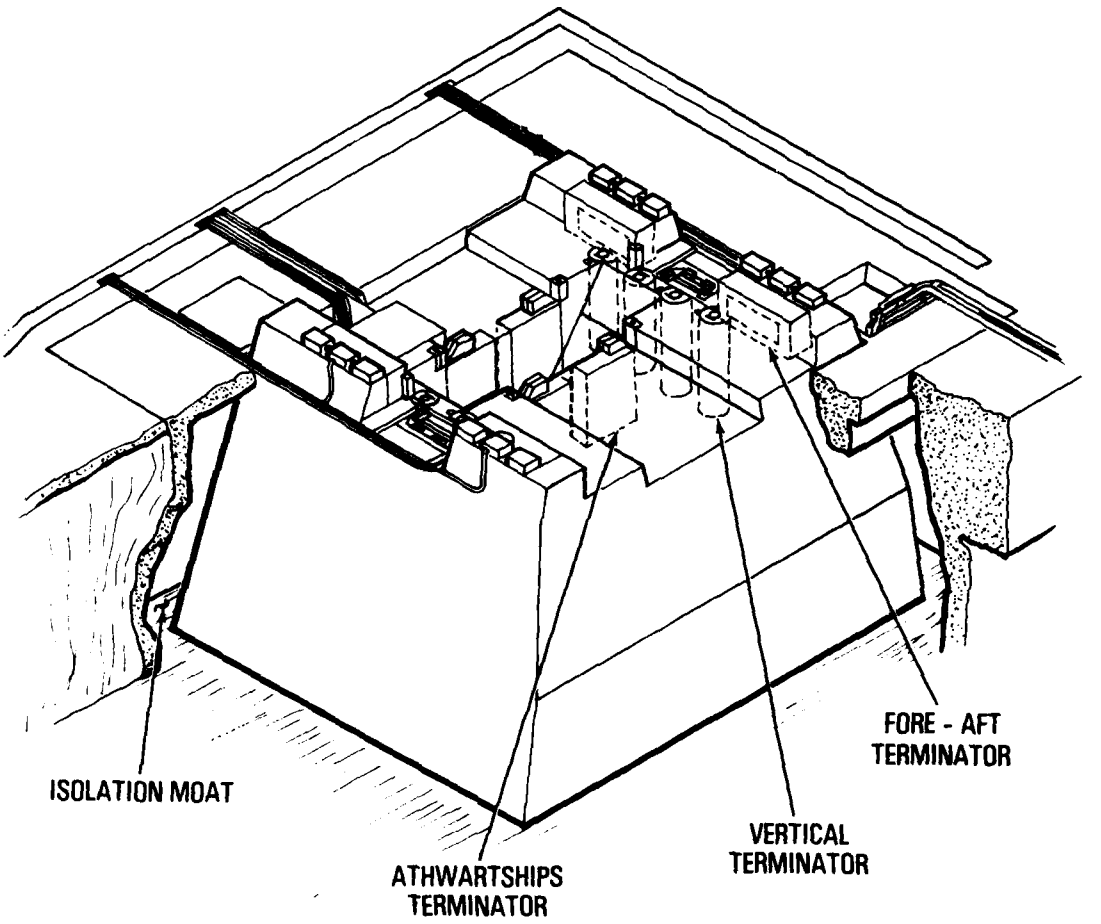

Figure 2. Impedance Block Details

concrete. The design objective was to make each terminator solidly integral with the concrete foundation such that the "mass line" portion of the impedance would be controlled by the one-million-pound foundation. The acceleration response, per unit force, of the foundation is 10^{-6} g's/lb. for frequencies below which the stiffness of the terminator controls the impedance (i.e., mass controlled region). As can be seen from Figure 1, the lower frequency region of the reference impedance curve is equivalent to a spring whose stiffness is 30 x 10^6 lb./in. The frequency at which this impedance intersects the mass line of the foundation calculates to be approximately 17 Hz, which is near the lower limit of the frequency range of interest.

As indicated in Figure 1, the reference impedance levels out at 955 Hz, which is simply the intersection of the 30 x 10^6 lb./in. stiffness curve with a constant impedance of 5,000 lb. sec/in. Both of these curves, the 30 x 10^6 lb./in. stiffness and the constant impedance, were the result of shipboard investigation data.

This reference impedance was the design objective for each type of terminator. The method used to obtain the desired dynamic stiffness up to 955 Hz and then a constant impedance up to 20 kHz was to isolate the termination point from the foundation by means of a visco-elastic material loaded in shear such that its calculated dynamic stiffness

would be 30 x 10^6 lb./in. The termination point itself was a column whose characteristic impedance (ρ ca) was approximately 5,000 lb. sec./in., the nominal design objective. The visco-elastic material was supposed to provide, in addition to the 30 x 10^6 stiffness, sufficient damping in the higher frequency range to minimize the standing wave resonant and anti-resonant swings about the characteristic impedance line. This design is illustrated for the three directions in Figures 3, 4, and 5. In each case the total shear area

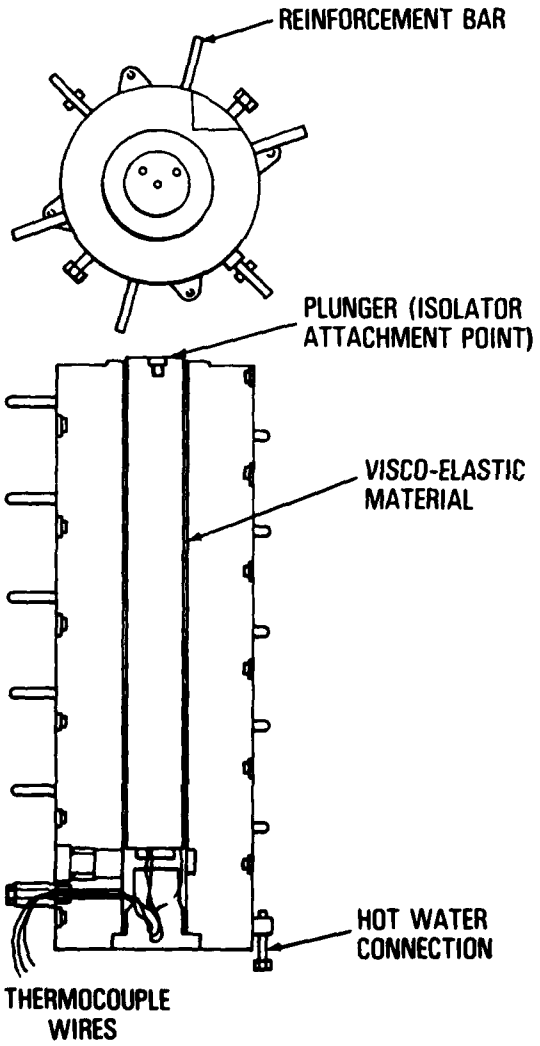

Figure 3. Cross Sectional View of Vertical Terminator

used was based on the desired stiffness and the material properties as published. The basic method of calculating the stiffness and the terminator acceleration response is described in Appendix A.

A similar design method was used for terminators in the fore and aft and athwartships directions. However, the athwartships direction consisted of eight termination points, but only four terminator cases embedded in concrete. As seen in Figure 4, each athwartships terminator consisted of two inner plates separated from the outer body by the visco-elastic material. The large "ears" on top are the termination points for two athwartships isolators. The relative motion between the termination point and the foundation includes rotation in addition to translation, whereas the vertical and fore and aft terminators translate only.

The ability to calculate and predict the impedance of these terminators depends on the predictability of the material properties of the visco-elastic material.

ONE-HALF-SCALE TEST PROGRAM

The material used was CA4OFL, a visco-elastic adhesive material available commercially. The material properties used in the calculations were those published prior to the commencement of this effort. It was not considered necessary to evaluate the material properties since a one-half-scale terminator test was conducted by installing one-half-scale models of the vertical and athwartships terminators in a 30,000 lb. concrete foundation and then evaluating their performance by measuring the point impedance at the termination point. This one-half-scale test program was successful in that it provided sufficient information and data to establish the validity of the design techniques and the general material properties. As a result of this test program, a few minor changes were made to the full-scale design.

One area of concern that helped to justify the half-scale investigation was the question of structureborne noise "cross talk" between termination points. It was desirable to design the foundation such that the vibration on any

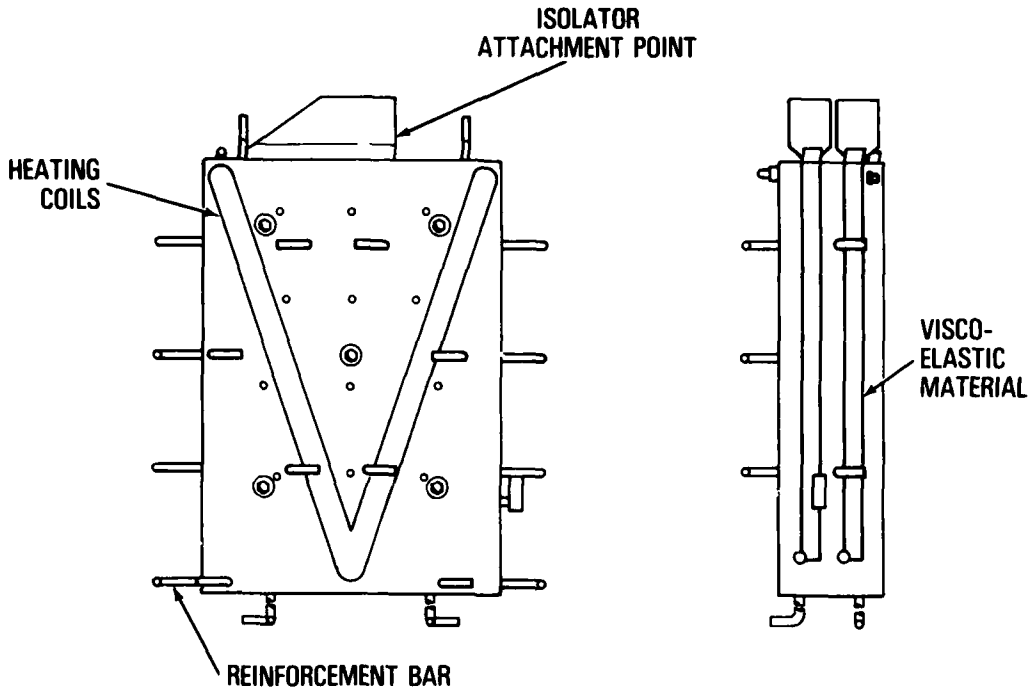

Figure 4. Cross Sectional View of Athwartships Terminator

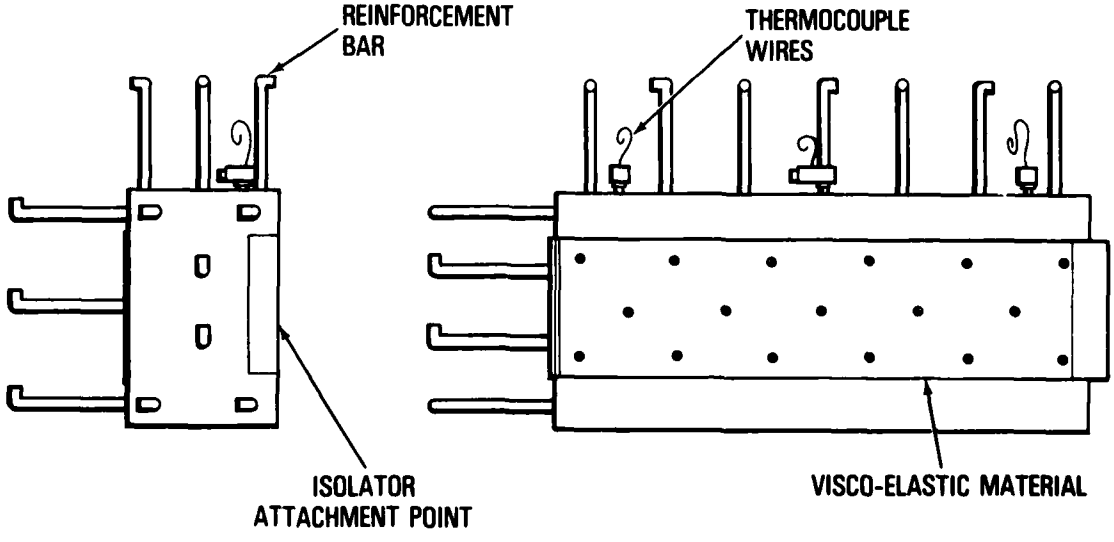

Figure 5. Fore and Aft Terminator

given terminator be controlled, throughout the frequency spectrum, by the force input at that point. If there is significant vibration transmission from one terminator to the next, and if the correction factor is greater than one, then the corrected power summation would be somewhat erroneous because the correction would be made on one terminator for motion that was influenced or controlled by another terminator. During the half-scale test program, an effort was made to determine the transmission from one terminator to another terminator, and it was found that the problem was of negligible magnitude for the vertical terminators but was a serious potential problem for the athwartships terminators. This finding is not surprising since there are two termination points in each of the athwartships terminator cases. Because this potential problem existed, an effort was made to keep the full-scale terminator slightly on the soft side so as to minimize the terminator "cross talk". In general, there is a 10 to 20 db transmission loss between adjacent terminators.

ACCELEROMETER MOUNTING

Concurrent with the one-half-scale test program, efforts were made to develop high frequency measurement techniques, specifically the ability to reliably measure structureborne noise and impedance at frequencies between 10 kHz and 20 kHz. Several things that were learned from this testing eventually had a direct impact on the impedance and noise tests conducted on the full-scale foundation. Most of the lessons learned were the result of the testing of various accelerometers and accelerometer mountings on small blocks whose natural frequencies could be easily calculated. Testing was performed at frequencies as high as 40 kHz. The mounting of the accelerometers was found to be equally as important as their selection, and a technique was devised that incorporated the use of a special ceramic material to provide a satisfactory mounted response to 20 kHz. The ceramic material serves three purposes: First, it provides the necessary electrical isolation and, secondly, it's high modulus (58 x 10^6 psi) combined with its thin size provides a stiff enough layer to keep the mounting frequency as high as possible. Thirdly, the surface finish and flatness of the washer is of high enough quality to prevent high frequency rocking of the accelerometer. Other materials were tried, such as mica, but their lower modulus dictated a thinner washer, and in general the mounting resonance was less consistent because the mica washers had to be split by hand to make them thin enough.

FOUNDATION PERFORMANCE

The theory that the 30 million lb./in. stiffness line intersecting the concrete block mass line on one end and the constant impedance line on the other end ignores the potential problem of resonances within the concrete block or resonances of the contrete block on the earth (i.e., rigid body modes). Therefore, various earth samples were taken prior to the first concrete pour to ascertain the shear modulus and thereby calculate the rigid body modes of the concrete foundation. Then, by using empirical techniques, estimates of damping were made to help determine the responses of the six rigid body modes. This analytical approach was followed up with a testing effort after the foundation was completed by shaking the foundation at various points with a large hydraulic actuator. The resonance response of the six rigid body modes was found to be insignificant, and for all practical purposes, this problem did not have a significant impact on the measured impedance of the terminator.

A series of impedance tests were conducted on the terminators in air before the terminators were installed in the concrete foundation. This was done to serve as a checking procedure on each full-scale terminator to ensure that the dynamic stiffness was within a reasonable tolerance of the 30 x 10^6 lb./in. design objective. To determine the dynamic stiffness, a plot of acceleration divided by input force (i.e., g's/lb.) was made at several temperatures and the dynamic stiffness was then evaluated in the low frequency stiffness controlled frequency range. The data for frequencies above 1 kHz was examined only in a qualitative sense to ensure that its general trend was consistent with the design objective.

The results of these tests indicated that the material properties were inconsistent and tended to vary greatly from terminator to terminator. The dynamic stiffness varied as much as 300 percent at a given temperature and, in general, all the terminators were stiffer than had been predicted from one-half-scale model data. Therefore, prior to installation into the full-scale concrete foundation, the full-scale terminators were modified to incorporate a thicker layer of visco-elastic material in order to reduce the dynamic stiffness.

Figures 6 and 7 show pictures of the vertical and athwartships terminators before the concrete foundation was poured. Illustrated in the figures are the heating coils used to control the temperature of each terminator so as to maintain a specific temperature and thereby keep its impedance from varying during gear testing. This temperature control is necessary because of the strong temperature sensitivity of the visco-elastic material properties.

Figure 8 shows a picture of the completed foundation with the terminators embedded in the concrete. In Figure 8 the actual termination point (i.e., the point to which the isolator attaches) is labeled; this is the point at which the final impedance measurements were made. Also shown in Figure 8 is an accelerometer, which was used for contractual structureborne noise measurements and for the impedance measurements. The method used to obtain the transfer function was to measure acceleration and divide by the measured force. The results were then compared directly with the reference impedance equivalent plotted in g's/lb.

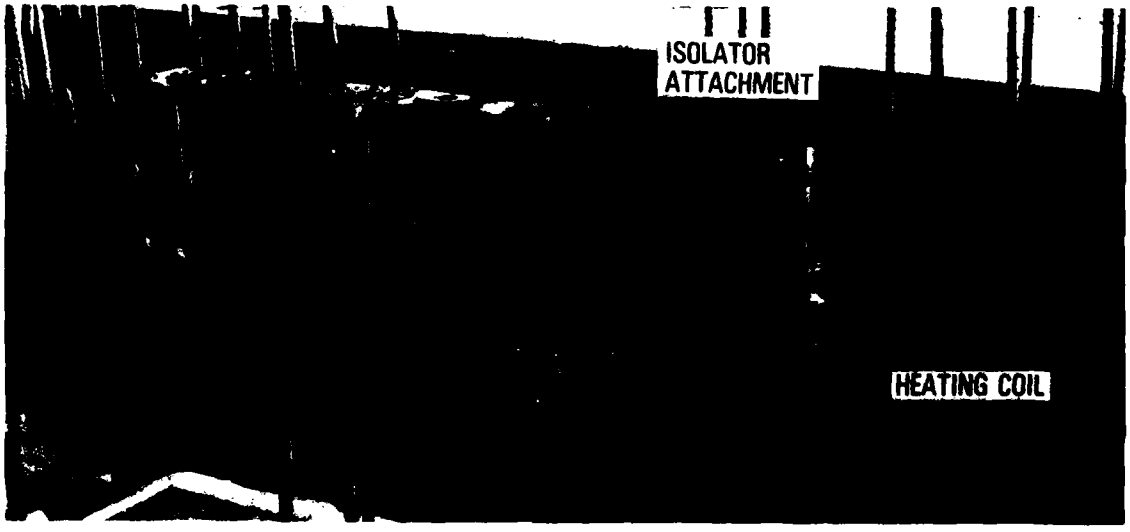

Figure 6. Vertical Terminator

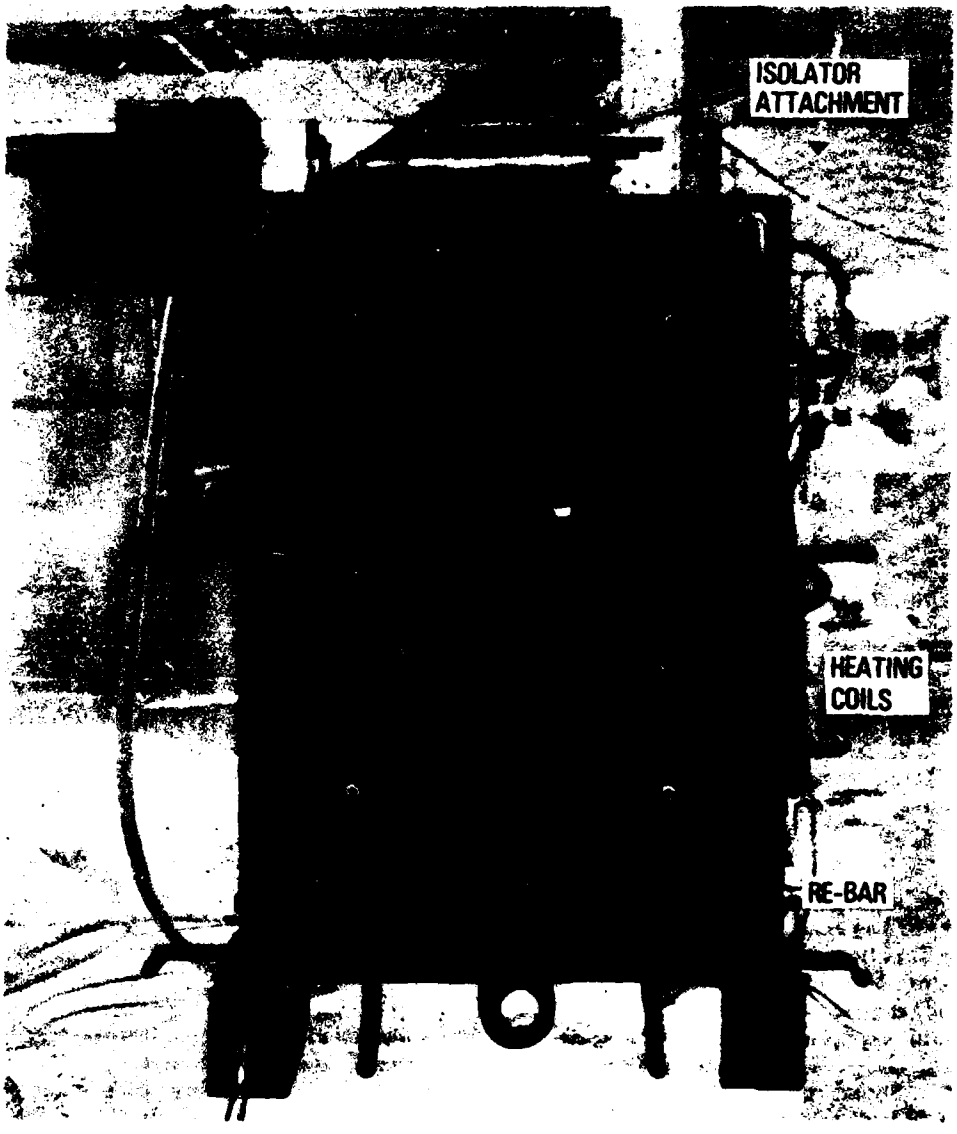

Figure 7. Athwartships Terminator

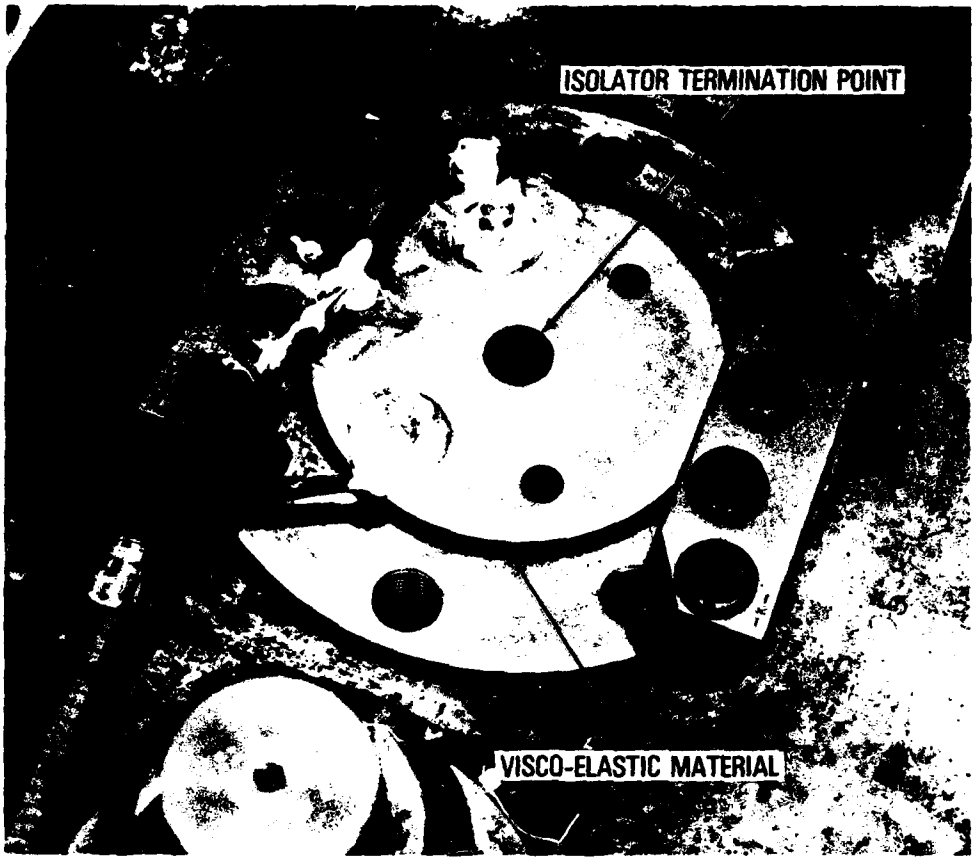

Figure 8. Vertical Terminator in the Foundation

A Fourier analyzer system was used to perform these impedance tests and store 366 transfer function values for each of the 20 terminators. It consisted of a computer, two magnetic digital tape systems, and other peripheral equipment. Figure 9 shows a schematic diagram of a test set-up in which the basic signal used to drive the force shaker was generated in the Fourier analyzer and then supplied to the shaker through a digital-analog converter and a power amplifier. To span the wide range in frequency (14 Hz - 20 kHz), two shakers and accelerometers were used. Use of the Fourier analyzer enabled taking the data at precise frequencies to coincide with specific contractual requirements and also made it possible to drive the shaker at several of the frequencies simultaneously.

Figure 10 shows some typical data taken from one of the vertical terminators and a reference g's/lb. curve. As can be seen from Figure 10, the stiffness portion of the terminator's impedance performed very well. However, this was only after the visco-elastic material thickness had been increased to descrease the stiffness. This change effectively reduced the relative damping, which manifested itself in the form of greater standing wave resonant and anti-rotation response in the upper frequency range. The reason for this is the fact that damping of the visco-elastic material at any given frequency varies inversely with the thickness of the visco-elastic layer. Since the thickness of the layer had been increased by a factor of 2:1 (4:1 over half-scale) to hold down the dynamic stiffness, a 50 percent decrease in relative

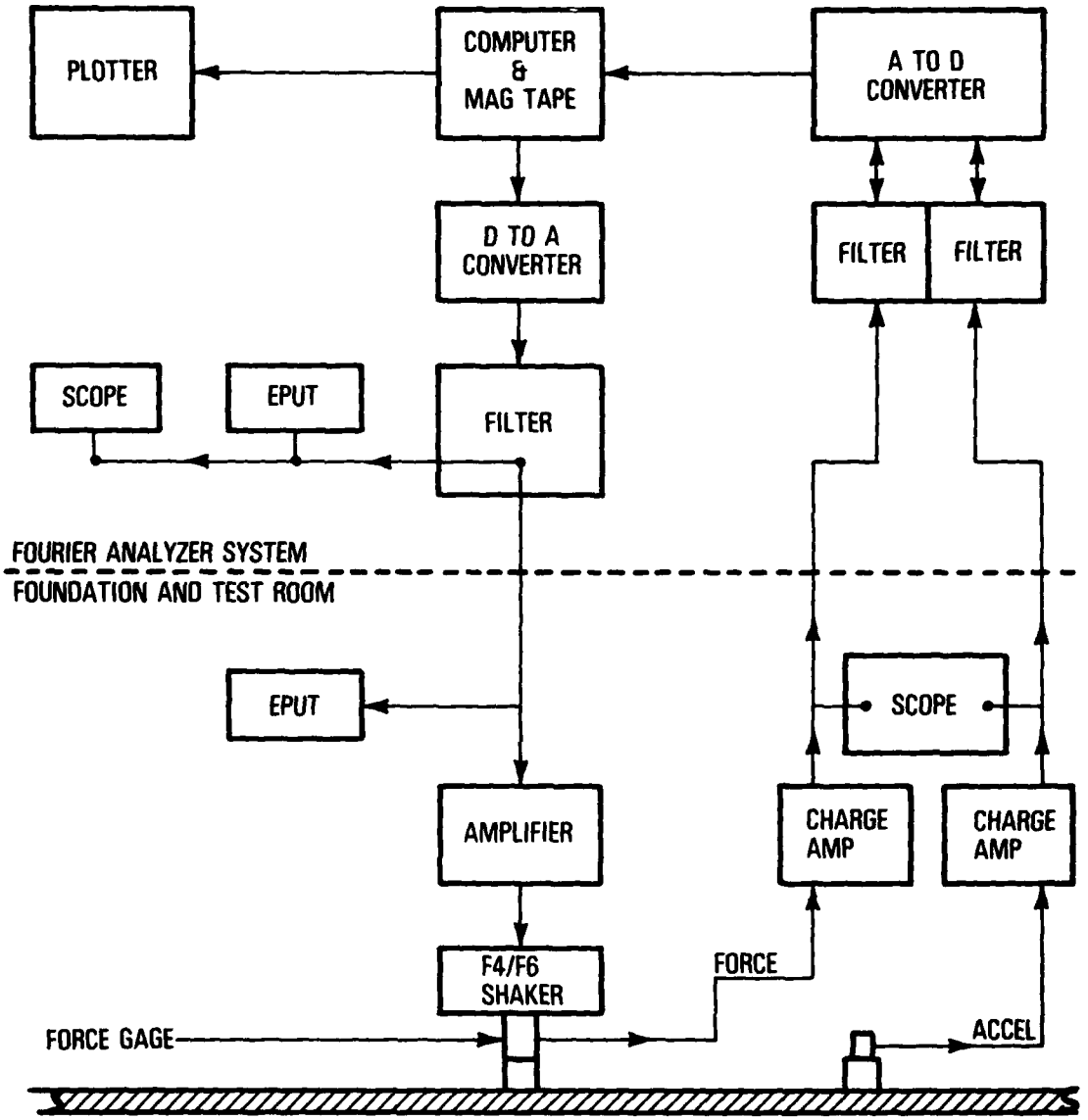

Figure 9. Impedance Test Schematic

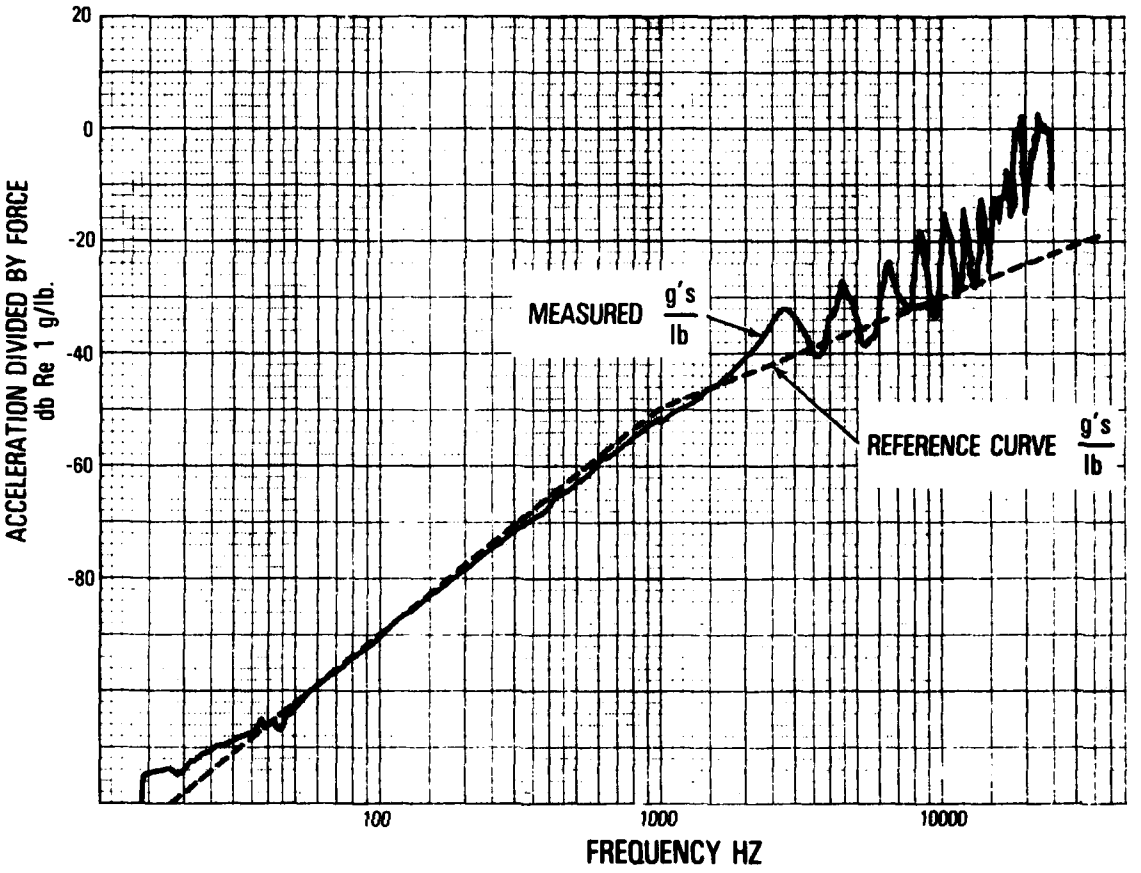

Figure 10. Vertical Terminator Test Data (Final)

damping resulted. This decrease in damping in turn increased the resonant and anti-resonant swings by approximately 6 db. Another factor affecting the resonant response of the plunger, as compared to the response of the half-scale models, is the fact that all of the compressional wave resonant frequencies are only half as high. And since the loss modulus of the visco-elastic material increased with frequency, the result was additional loss in damping at each full-scale resonant frequency. This loss in upper frequency damping is the price that had to be paid for keeping the terminators in the proper stiffness range (20 - 30 million lb./in.). This loss in damping was not considered to be of great consequence, however, since the computerized impedance correction process can easily handle any curve similar to the one shown in Figure 10. The change in thickness was accomplished to reduce the stiffness and thereby help to reduce noise transmission from one terminator to another.

Figure 11 shows a g's/lb. plot of data of the same terminator with a much higher response in the higher frequency range (15 - 25 kHz). This data represents the initial set of tests conducted on the completed foundation, and this noticeably high acceleration response was strongly suspected to be a characteristic of the test fixture. As a result, a series of tests were run on small blocks with the same accelerometer and force gage to ascertain the frequency response of the shaker and force gage combination as well as

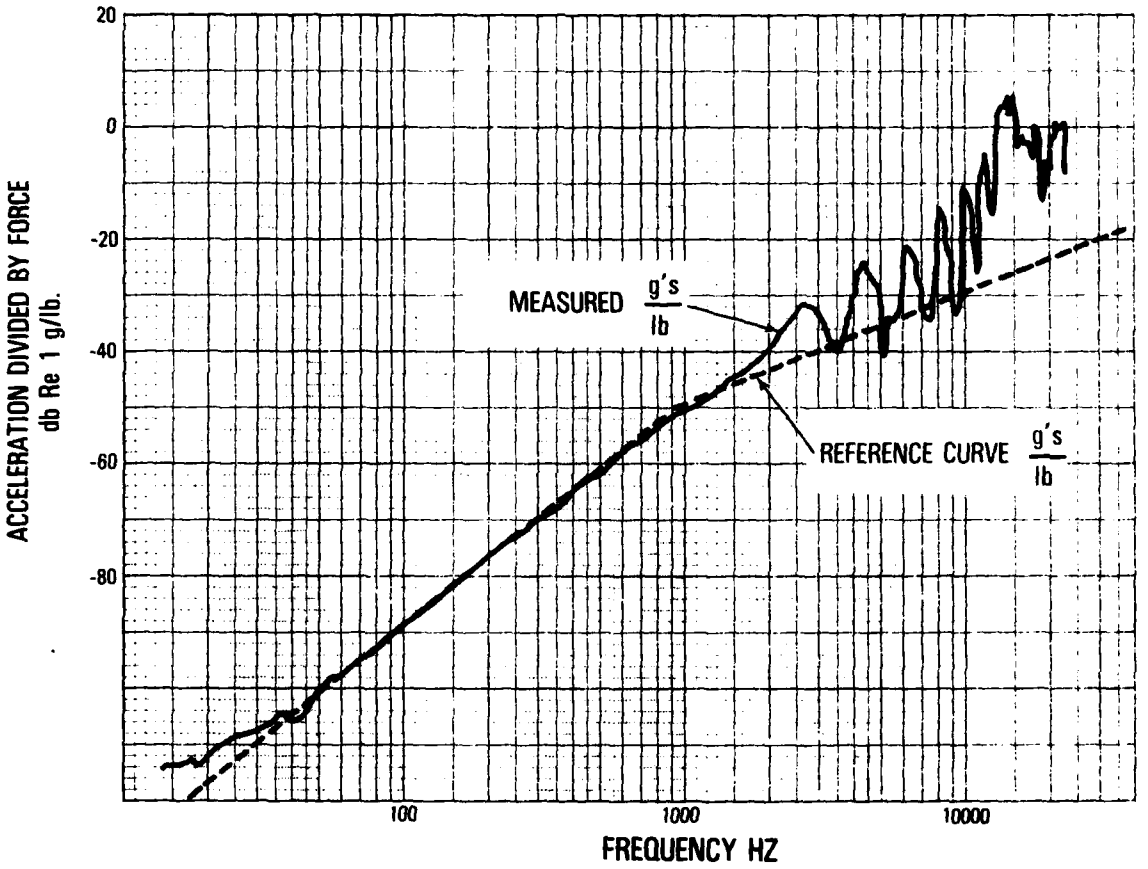

Figure 11. Terminator Response with Excessive High Frequency Resonant Buildup

the driving fixture. Figures 12A and 12B show sketches of the attachment methods used to obtain the data in Figures 10 and 11. Use of the steel adapter shown in Figure 12B provided a significant improvement in frequency response over other drive fixtures in that it maximized the contact stiffness to the terminator. This adapter was held in place by dental cement, which not only provided good adhesion but also acted as a grout to fill the small irregularities in the surface finish of the terminator. Tests conducted with this adapter on small blocks with known characteristics show that the resonance of the mounting was well above 20 kHz. Figure 13 shows the response of a small calibration block being driven by the shaker. As can be seen, the resonant build-up is about 10 db at 20 kHz. The reciprocal of this curve was used to correct the measured g's/lb. curves because this curve, Figure 13, closely approximates all three directional test conditions (i.e., vertical, fore and aft, and athwartships). This correction process is valid only if the apparent mass of the terminator in the frequency range of interest is of the same order of magnitude as the calibration block mass.

This same resonant buildup of the contact stiffness supporting a mass below the force gage is what precluded using any of the standard impedance heads presently on the market.

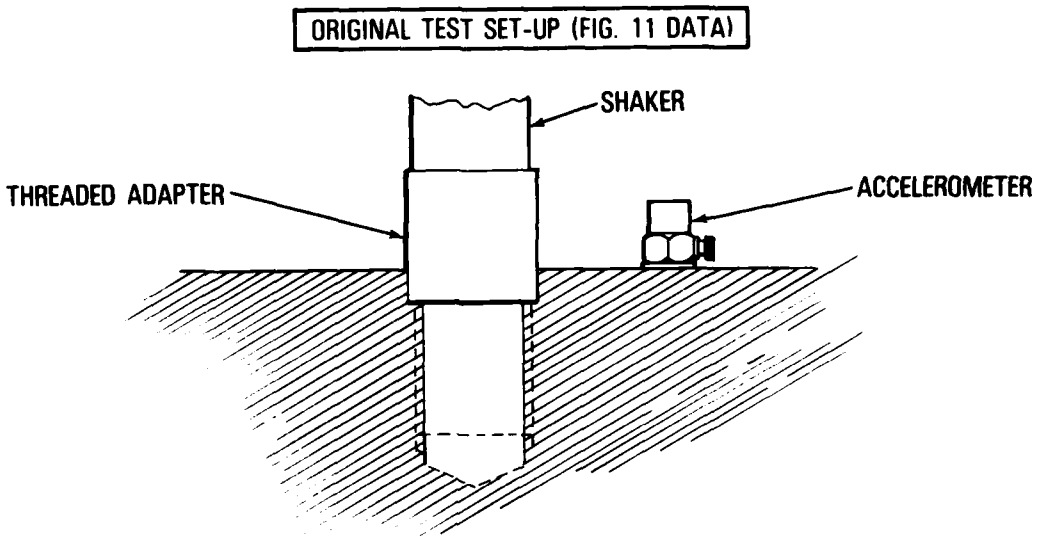

Figure 12A. Transfer Function Test Set-Up

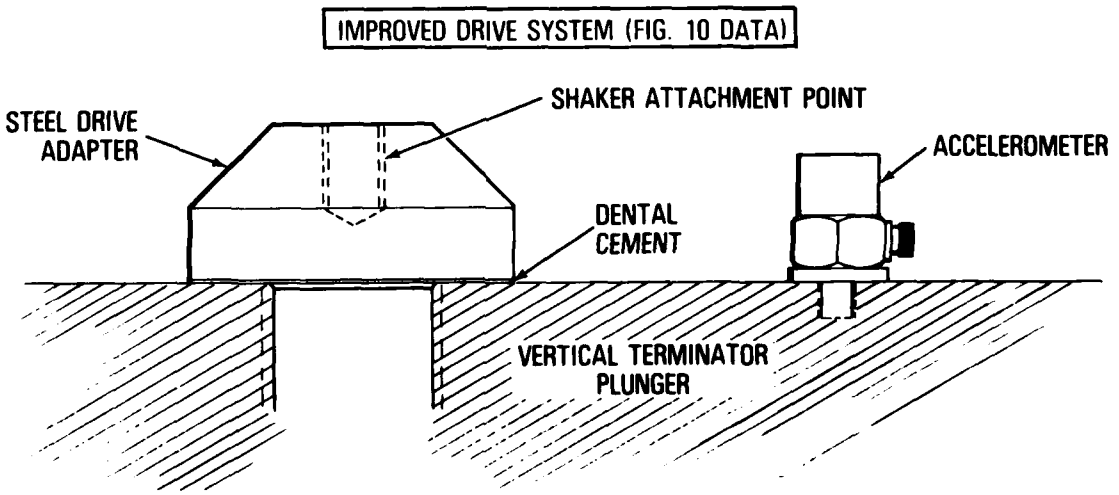

Figure 12B. Transfer Function Test Set-Up

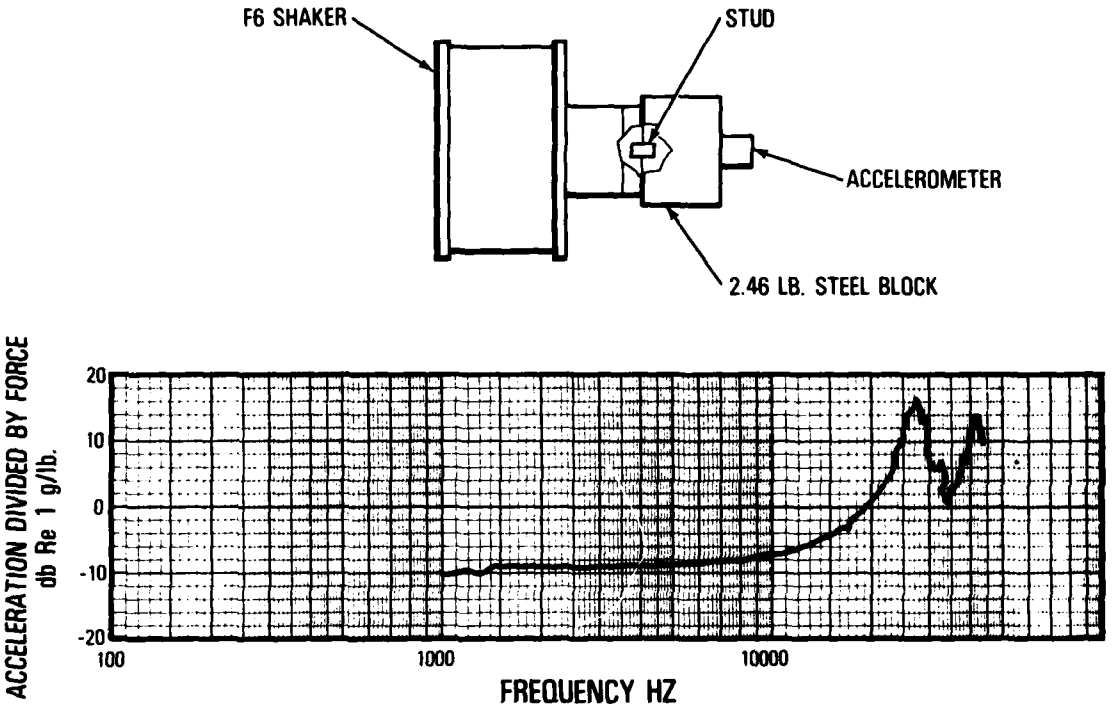

Figure 13. Transfer Function Calibration Curve (2.46 lb. Mass)

After the drive adapter was improved and the resonance on its contact stiffness increased to greater than 20 kHz, the controlling item was the shaker and force gage combination in which the mass between the force gage and drive adapter became resonant on its contact stiffness at about 26 to 28 kHz. Two modifications were made in an effort to up-grade both this limitation and the driving block resonance limitation. First, the driving head of the shaker was changed to a stiffer material and less massive design, and second, special drive blocks were made of Alumina having a modulus of about 58 x 10^6 psi and a density about one-third of the density of steel. The results of these changes are shown in Figure 14, where a calibration block (resonance about 40 kHz) is driven by an Alumina drive adapter that is driven by the modified shaker. A close-up view of the ceramic drive adapter is shown in Figure 15. It was designed specifically to maximize its contact stiffness on the vertical terminator while minimizing its own mass. The use of these drivers was necessary only because of the existing holes in the vertical and athwartships terminators used to attach the isolators. The fore and aft terminators were tested by attaching the shaker directly to the terminator.

USE OF IMPEDANCE DATA

The purpose of measuring each terminator impedance and maintaining a digital record for each frequency was to correct structureborne noise measurements to the reference impedance shown in Figure 1. If the termination impedance is large compared with the source impedance, which is the impedance of the isolator-gear combination, then the acceleration as measured below the isolator varies inversely with the termination impedance. Therefore, during the negotiating phase, it was decided that all structureborne noise measurements made below the isolating mounts would be corrected to

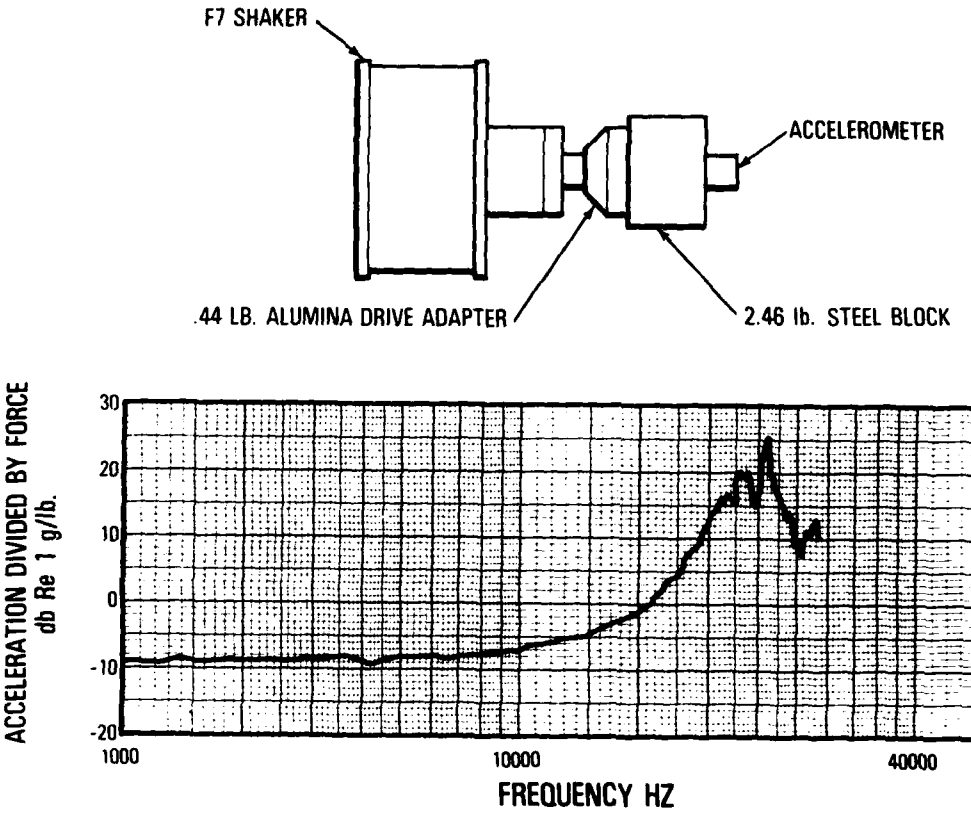

Figure 14. Transfer Function Calibration Using Improved Drive Adapter

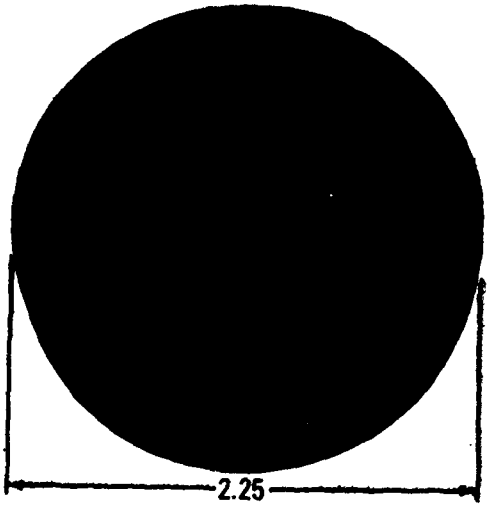

Figure 15. Alumina Drive Adapter

the reference impedance shown in Figure 1 by the following relationship:

$$A_i = 10 \log \sum_{j=1}^{n} \sum_{i=1}^{N} \left\{ A_{ij} \left| \frac{Z^T_{i,j}}{Z^R_i} \right| \right\}^2 - 10 \log n + 60$$

where A_{ij} is the measured acceleration for the i^{th} frequency and j^{th} location in cm/sec^2. A_i is the corrected one-third octave acceleration referenced to 10^{-3} cm/sec^2.

As can be seen from the equation, each frequency measured at each location is corrected to the reference impedance curve by simply multiplying it by the magnitude ratio of the measured impedance to the reference impedance at that frequency and that location. This correction process is valid only if the frequency resolution on which the measurements are made is reasonably narrow. Therefore, the contractual agreement

also specified that A_{ij} and Z_{ij} be measured with a 1 Hz resolution up to 100 Hz, a 10 Hz resolution from 100 to 1 kHz and a 100 Hz resolution from 1 kHz to 20 kHz. An illustration of the correction process can be seen in Figure 10. When the measured g's/lb. is equal to the reference g's/lb. the correction is unity. However, when the measured g's/lb. is higher than the reference g's/lb., then the terminator impedance is lower than the reference impedance, and hence the measured acceleration is higher and the correction factor is less than one.

Making the corrections at all the various terminators and frequencies results in a great number of calculations; therefore, it was necessary to digitize the structureborne data and make all the corrections and one-third octave summations with a mini-computer. Figure 16 shows a schematic diagram of the data acquisition system where all 20 ac-

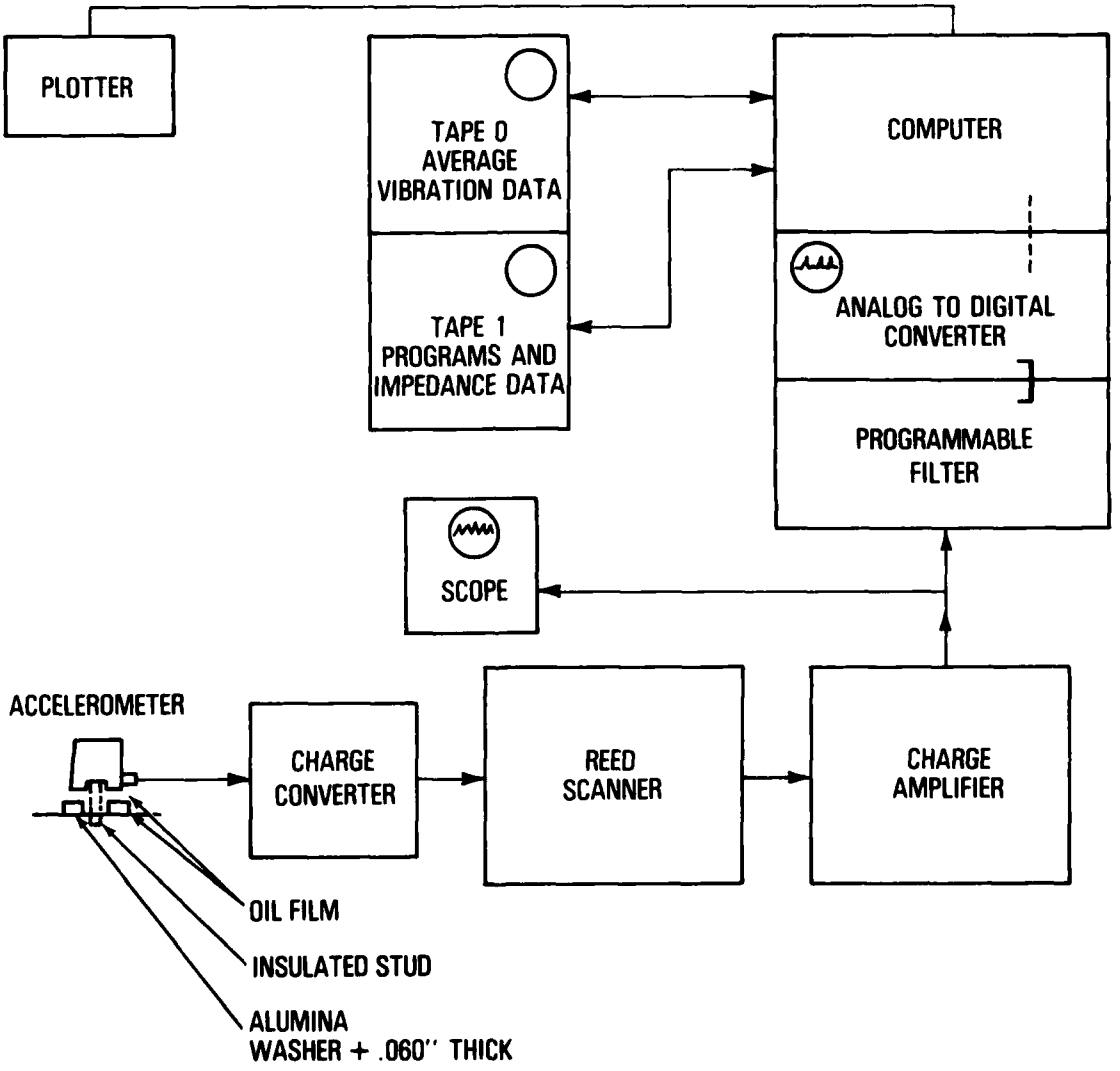

Figure 16. Structureborne Noise and Data Correction Diagram

celerometers (i.e., 20 terminators) feed into a programmable scanner and are digitized through an ADC and then converted into the frequency domain by use of a Fourier transform. The transformed data is then corrected at each frequency and each location by the appropriate correction factor, which is retained on digital tape. Levels of the various vibration components in each one-third octave band are then summed. The one-third octave levels from all the terminators in each direction are summed on a power average basis to produce a power average one-third octave curve corrected to the reference impedance. Figure 17 shows a pair of one-third octave plots of structureborne noise data measured on terminators - one corrected and one uncorrected. The difference between the two curves is a function not only of the correction process but also of the narrow band noise signature. If a given one-third ocatave is controlled by a discrete frequency, then the correction factor at that frequency will mainly determine the difference between the two curves. However, if a one-third octave consists of broad band random noise, then all the correction factors in the band will affect the resulting one-third octave.

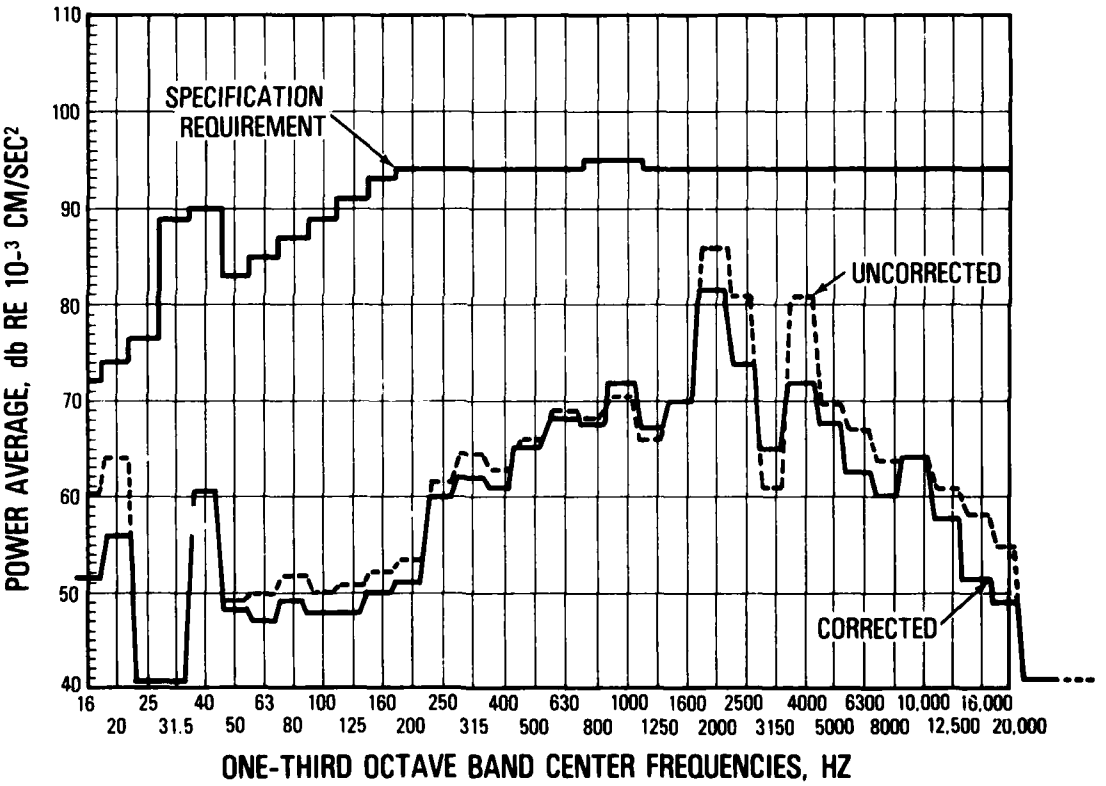

Figure 17. Structureborne Noise Data Comparison - Corrected and Uncorrected

CONCLUSIONS

Although much emphasis was placed on the design and construction of the foundation in an effort to achieve the reference impedance, it is not important to achieve the reference impedances exactly. As previously described, deviations from the reference impedance are easily accounted for in the correction process, and this ability to correct the below-mount structureborne noise to almost any reference impedance is one of the major advantages of the technique. As long as the reference impedance used is reasonably large with respect to the isolator impedance, the correction process is valid. The fact that this correction process can be accomplished so easily with a mini-computer helps to deemphasize the importance of achieving the exact reference impedance. For example, the visco-elastic material used in this case seemed to vary greatly in that the dynamic stiffness of the completed terminators varied by as much as 300 percent from terminator to terminator. Under normal design conditions this variance would be considered unacceptable. However, since the impedance correction process is calculated for each terminator, this variation is easily accounted for in the correction process. This fact leads to the conclusion that the design of a high impedance foundation for component testing in this fashion need not be difficult because irregularities in material performance do not prevent the foundation from serving its design objective. Other findings which reinforce this conclusion are first, the fact that the "cross talk" between terminators failed to manifest itself as a problem, and second, there is no significant amplification at any of the concrete block resonances.

It would have been difficult to recommend a structureborne test procedure incorporating a correction process ten years ago. With today's use of computerized analyzers in which noise data can be easily and extensively processed in the frequency domain, correction processes such as the one described herein can be easily implemented and used advantageously so that structureborne noise data can be made more meaningful and useful.

The structureborne noise data taken during the DD963 gear test program is an example of how corrected below-mount data can be obtained on an energy basis. The sound pressure level in the water is proportional to the power summation of the isolator output forces for any given frequency. This fact

$$\sqrt{\sum_{J=1}^{N} \left| \frac{A_i Z_{ij}}{2\pi f} \right|^2}$$

assumes that the transfer function between the isolator attachment point and the water is the same for all attachment points in a given direction. The transfer functions tend to be different for different directions and, therefore, the acceleration readings in the vertical, fore and aft, and athwartships directions are power summed separately. Therefore, a structureborne specification written as a power average or power sum of all the isolator termination points, in a given direction, is a more realistic method of measuring component structureborne noise than current methods.

ACKNOWLEDGEMENT

In an extensive effort such as is described herein, many more people make important contributions to the overall result than can be recognized in a paper. In this effort, Mr. D.V. Wright, of the Westinghouse Research Lab, made particularly outstanding contributions.

APPENDIX A

ACCELERATION RESPONSE OF TERMINATOR

The acceleration response (g's/lb.) to a sinusoidal force applied at Point A will first respond to the stiffness of the earth by increasing up a stiffness line to the first mode resonance and then into the anti-resonant dip of the one-million-pound block on the terminator stiffness. For example, the vertical mode was calculated to be about 8 Hz, which is below the frequency range of interest. From the earth-block resonance the g's/lb. response follows the block mass line until it intersects the stiffness line of the visco-elastic material around the plunger. The response of the contrete mass as a rigid body varies somewhat from terminator to terminator depending on the nature of the mode (i.e., translation or rotation). However, for the vertical translation case, this intersection of the one-million-pound block with a spring stiffness of 30 x 10^6 lb./in. occurs at about 17 Hz.

The plunger and visco-elastic material stiffness is calculated as shown below. The actual value for the storage modulus is not shown in this example because it varies with frequency and is classified.

When the plunger stiffness begins to control the acceleration response (by providing a lower impedance than the concrete block) the response follows a typical stiffness line until the characteristic impedance of the plunger beings to dominate. The response is affected by a standing-wave-resonant and anti-resonant response of the steel plunger, which is damped by the visco-elastic material. This upper frequency response (beginning at 2020 Hz) varies about the constant characteristic impedance of 4707 $\frac{\text{lb/sec.}}{\text{in.}}$

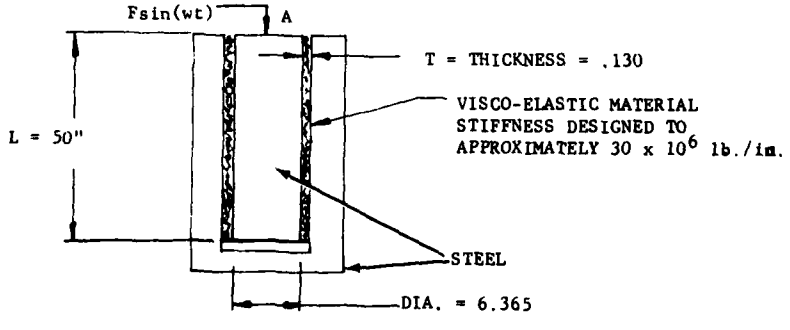

$$K = \frac{G'\pi DL}{T} = \frac{G'\pi[6.365][50]}{.130} = 7690.9\ G' \quad (G' \text{ in PSi})$$

ρCA of Plunger = Characteristic Impedance

$$\rho CA = \frac{7.324}{10^4}\ \frac{\text{lb sec}^2}{\text{in}^4}\ [2.02 \times 10^6\ \text{in/sec}]\left[\frac{6.365}{2}\right]^2 \pi\ \text{in}^2 = 4707\ \frac{\text{lb sec}}{\text{in}}$$

Discussion

Mr. Panaro: (IBM Corporation) What prompted you to use the LD 502 in conjunction with the viscoelastic material?

Mr. Hupton: Let me clarify something first then and try and answer your question. The viscoelastic material that you saw was not the LD 502. The LD 502 was used in the isolators, the material was one that has been used on submarines and other applications and it was recommended to us. We used the LD 502 after we reviewed all of the data that we had from various sources and we previously conducted some other tests using the constrained layer techniques. The LD 502 seemed to have the E- product that we were looking for in the temperature range that we were looking for; that is we knew the temperature of the gear oil and the engine room environment, and we found something that would give us the proper E- product in that temperature range.

Mr. Warner: (Westinghouse Electric Corporation) We had to have good damping at 10 Hertz as well as 2000 Hertz and at 4000 Hertz. This was the only material that had good damping properties over that large a frequency range.

RESPONSE OF THICK STRUCTURES DAMPED BY VISCOELASTIC MATERIAL WITH APPLICATION TO LAYERED BEAMS AND PLATES

M. Lalanne, M. Paulard and P. Trompette
Institut National des Sciences Appliquées,
Villeurbanne, France

A method based on the finite element technique is presented for the prediction of the harmonic response of thick damped structures. Results are given for the application of the method to beams and plates. In order to reduce the large number of degrees of freedom, the response is expressed by a modal series. Calculations take into account the dynamic properties of the viscoelastic materials used, as these vary both with frequency and also with temperature. The agreement between experimental and theoretical results is good. The method can be applied to more complicated systems such as frames, panels and blades.

INTRODUCTION

In many examples of mechanical structures, it is necessary to reduce vibration levels over a wide range of frequencies. For several years, attempts have been made to achieve this objective by utilizing the damping properties of viscoelastic materials.

In this study, the finite element method has been used to predict the harmonic response of three-dimensionnal structures damped with thick layers of viscoelastic material. The structures considered here are beams and plates which consist of three layers - one viscoelastic layer sandwiched between two elastic layers - but the method may be readily extended to more complex geometries.

When a structure is modelled by three-dimensional finite elements the number of degrees of freedom can become very large and the cost of making calculations can become prohibitive. Furthermore, the dynamic properties of the viscoelastic materials, and thus those of the complete structure, vary with frequency. These two problems constitute a major consideration in this study.

RESPONSE OF A DAMPED STRUCTURE TO HARMONIC EXCITATION

Dynamical behaviour of a discretized structure, for the case of viscous damping, may be expressed by the matrix equation :

$$M\ddot{X} + C\dot{X} + KX = F(t) \qquad (1)$$

where M, C, K are the mass, damping and stiffness matrices of the structure respectively, X is a vector of generalized coordinates, and F(t) is a vector of excitation forces. The order of the equations is N.

In general, the response can be obtained either in terms of the generalized coordinates X or in terms of the principal (or modal) coordinates.

Solution in terms of generalized coordinates

For harmonic excitation of frequency ω, we may write :

$$F(t) = F_0 e^{j\omega t} \qquad (2)$$

The response may be written as :

$$X(t) = X_0 e^{j\omega t} = (X_r + j X_i) e^{j\omega t} \qquad (3)$$

Substituting in (1) for F(t) and X(t), we find :

$$\begin{vmatrix} K - \omega^2 M & -\omega C \\ \omega C & K - \omega^2 M \end{vmatrix} \begin{vmatrix} X_r \\ X_i \end{vmatrix} = \begin{vmatrix} F_0 \\ 0 \end{vmatrix} \qquad (4)$$

Thus for a given frequency ω, it is necessary to solve 2N simultaneous equations but this method permits the inclusion of properties which vary with frequency, and thus may be applied directly to a composite viscoelastic structures. However, in the case of three dimensionnal structures, the formulation and the solution of these equations for each value ω becomes long and tedious because of the large number of degrees of

freedom. In addition, when the frequency ranges of interest (i.e. near the resonances) are not known a priori, it becomes necessary to solve the equations for many different values of frequency. For these reasons, this method is not used here.

Solution in terms of modal coordinates

First of all, the lowest n (<< N) modes of the undamped structure are found. If we let ϕ be a matrix (N x n) formed of the lowest n eigenvectors, we may define a set of limited modal coordinates, q, by the equation

$$X = \phi \cdot q \tag{5}$$

Now, premultiplying equation (1) by ϕ^T, we obtain :

$$\phi^T M \phi \ddot{q} + \phi^T C \phi \dot{q} + \phi^T K \phi q = \phi^T F(t) \tag{6}$$

For harmonic motion, and writing :

$$m = \phi^T M \phi \ , \ c = \phi^T C \phi \ , \ k = \phi^T K \phi \ , \ f = \phi^T F \tag{7}$$

equation (6) becomes :

$$(-\omega^2 m + j\omega c + k)\, q_o = f_o \tag{8}$$

where :

$$q = q_o\, e^{j\omega t} = (q_r + j\, q_i)\, e^{j\omega t} \tag{9}$$

and

$$f = f_o\, e^{j\omega t} \tag{10}$$

It may be noted that m and k are diagonal matrices of order n and c is also an n x n matrix but not necessarily diagonal.
The response q is then obtained by solving the reduced equations :

$$\begin{vmatrix} k - \omega^2 m & -\omega c \\ \omega c & k - \omega^2 m \end{vmatrix} \begin{vmatrix} q_r \\ q_i \end{vmatrix} = \begin{vmatrix} f_o \\ 0 \end{vmatrix} \tag{11}$$

which are of order 2n (<< 2N).

The behaviour of a linear viscoelastic material subjected to harmonic excitation can be described by a complex elastic modulus E (1) where :

$$E = E_o(1 + j\eta) \tag{12}$$

E_o is the quantity commonly referred to as Young's modulus, but only for dynamic loading, and η is the damping loss factor.

In this case, the stiffness matrix for a viscoelastic material may be written as :

$$K_V + j\, \eta\, K_V \tag{13}$$

The stiffness matrix of the structure is thus complex and must be written as :

$$K = K_r + j\eta\ K_i \tag{14}$$

It should be noted that the only non-zero terms of K_i are those which are non-zero in K_V. If we neglect damping in the elastic members of the structure, equation (6) becomes :

$$(-\omega^2 \phi^T M \phi + j\eta \phi^T K_i \phi + \phi^T K_r \phi) q_o = f_o \tag{15}$$

Equation (11) may then be written :

$$\begin{vmatrix} \phi^T K_r \phi - \omega^2 \phi^T M \phi & -\eta \phi^T K_i \phi \\ \eta \phi^T K_i \phi & \phi^T K_r \phi - \omega^2 \phi^T M \phi \end{vmatrix} \begin{vmatrix} q_r \\ q_i \end{vmatrix} = \begin{vmatrix} f_o \\ 0 \end{vmatrix} \tag{16}$$

The quantities E_o and η vary with temperature and frequency (2). For a given temperature the modal solution above may not be used directly because the matrices K_r and K_i the loss factor η, and the matrix ϕ are functions of frequency.

Extension of the method for variable characteristics

We suppose here that the characteristics $E_o(\omega)$ and $\eta(\omega)$ are known. If the natural frequencies of the structures are sufficiently separated, one can obtain the modal response in the region of each frequency by using the values of E_o and η at that natural frequency. In practice, however, values of these properties cannot be known until one has found the natural frequencies. For this reason it is necessary to seek a solution in several steps. We begin with two convenient values of E_o - for example E_o' and E_o'' - with which we find two sets of natural frequencies - ω_1', ω_2', ... and ω_1'', ω_2'', ... -. With these values we may examine the variation of each natural frequency as a function of E_o. In effect, this variation is approximately linear, as shown by formula for the Rayleigh's quotient (3) :

$$\Delta\omega_\ell = \frac{1}{\omega_\ell} \frac{\Delta E_o}{E_o} \frac{\phi_\ell^T K_i \phi_\ell}{\phi_\ell^T M \phi_\ell} \tag{17}$$

Where ΔE_o represents the variation in Young's modulus, $\Delta\omega_\ell$ the variation in the natural frequency of the ℓ^{th} mode, and ϕ_ℓ is the ℓ^{th} column of ϕ.

The intersections of the lines A_1B_1, A_2B_2, A_3B_3 (see fig. 1) with the curve of the material characteristic leads to the values of E_o to be used. Having thus obtained values for ϕ, η, K_r, K_i for each frequency, a solution to the equation (16) may be found in the region of each natural frequency in turn by inserting the appropriate values of the those constants.

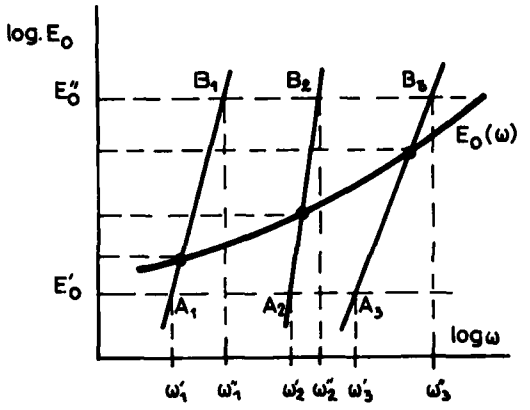

Fig. 1 Young's modulus determination

NUMERICAL CONSIDERATIONS

In the finite element model we have used a thick shell isoparametric element having 16 nodes and 3 degrees of freedom per node (4), as shown in figure 2. However, we have chosen to use a distributed mass matrix in preference to the concentred mass matrix of Wilson. The matrices K and M are partitioned in blocks.

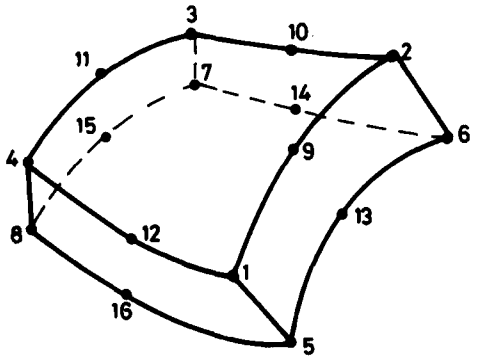

Fig. 2 Thick shell isoparametric element

The lowest natural frequencies and the corresponding modes for the undamped structure are obtained by the method of simultaneous iterations, without reducing the number of degrees of freedom, (5), (6).

In the case of rigid body modes, the stiffness matrix is singular and the frequencies are found by solving :

$$(K + aM)X = (\omega^2 + a)MX \quad \text{with} \quad a > 0 \qquad (18)$$

The greater part of the computation time is spent on finding the natural frequencies and modes. For example, the total computation time to obtain the response curve for the plate using a CDC 6600 is approximately 4 minutes. However, ten natural frequencies have been found.

Several examples have been studied in order to test the performance and the validity of the program. We shown in figure 3 the results obtained for one particular case - that of a three-layer beam (steel - P.V.C. - steel) whose dynamic properties (stiffness and damping) are independent of frequency. The beam was a cantilever and was modelled by 3 x 3 elements.

APPLICATIONS

Before it is possible to apply the method described above it is necessary to determine the viscoelastic characteristics E_O, η functions of frequency. To obtain these values, we have used an indirect method based on measurements, as follows.

Indirect measurement of the characteristics

A thick beam, damped by the viscoelastic material of interest, is studied both by experiment and by calculation for a given temperature.

Determination of $E_O(\omega)$

We begin as in the general method for calculating the two series of frequencies for the free-free composite beam, using two different values for Young's modulus. In this calculations the damping of the viscoelastic layer is neglected. We thus obtain the lines A_1B_1, A_2B_2, ... in figure 4.

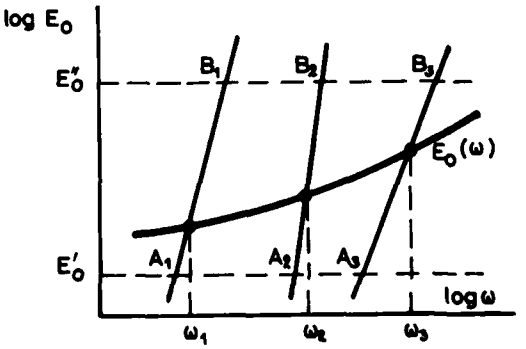

Fig. 4 Variation of Young's modulus with the frequency

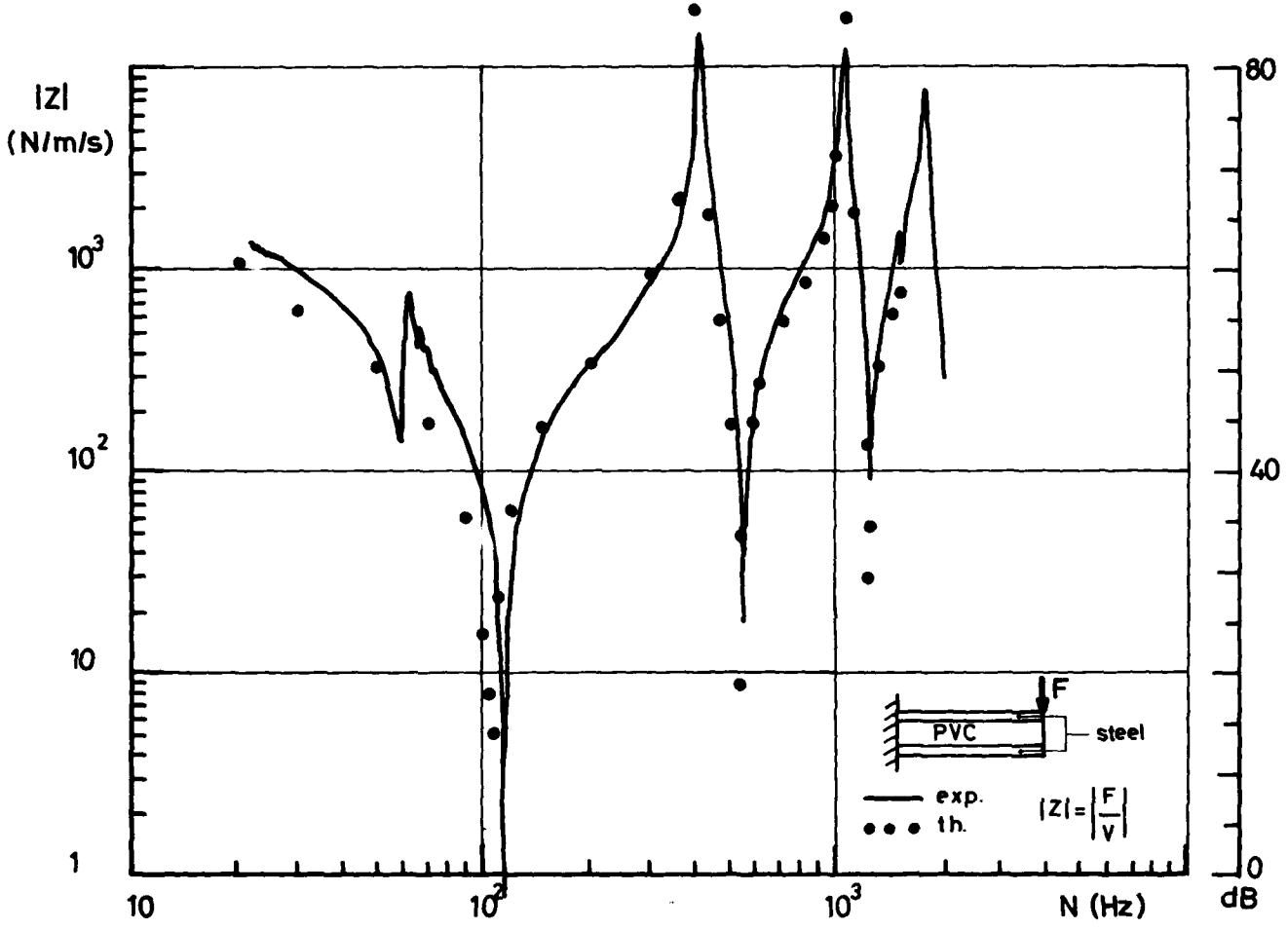

Fig.3 Steel - P.V.C. - Steel beam response

In addition, it is possible to find the natural frequencies and modes of the damped free-free beam by a suitable experiment, for example, by measuring the mechanical impedance.

Several points on the curve of $E_0(\omega)$ against ω may then be deduced from the above calculations and measurements, as shown in figure 4. An error will be introduced by this method because the calculated natural frequencies do not take into account the slight variation which is caused by damping. However, the slopes of the lines A_1B_1, A_2B_2, ... are such that this error is always small.

Determination of $\eta(\omega)$

If we can assume that the modes are well separated, then we can measure the 3dB bandwidth for each resonance from the impedance curve. For the ℓ^{th} resonance, we may write :

$$\alpha_\ell = \frac{1}{2}\frac{\Delta\omega_\ell}{\omega_\ell} = \frac{c_\ell}{2\sqrt{k_\ell m_\ell}} \qquad (19)$$

where c_ℓ, k_ℓ, m_ℓ are the modal damping, stiffness and mass respectively of the ℓ^{th} mode. Using equations (8) and (15), we have in addition :

$$\omega_\ell c_\ell = \eta \phi_\ell^T K_1 \phi_\ell \qquad (20)$$

from which :

$$\eta_\ell = \Delta\omega_\ell \frac{\sqrt{k_\ell m_\ell}}{\phi_\ell^T K_1 \phi_\ell} \quad \text{for frequency } \omega_\ell \qquad (21)$$

Results

In this example we have used a viscoelastic material known as SONECRAN (7). An experimental beam was made by sandwiching a layer of SONECRAN between two identical layers of aluminium. The layers were glued together using CHEMLOCK (8).

An impedance curve was drawn for such a beam having dimensions of 352 mm x 30 mm x 26 mm free-free, excited at its center, and at a constant temperature of 17°C. For this case, it is necessary to model by finite elements only one half of the beam. The number of elements used was again 3 x 3. The results for $E_0(\omega)$ are shown in figure 5, for the first two flexural frequencies.

In addition, it is found that $\eta(\omega)$ is effectively constant at 0.6. Throughout the calculations, Poisson's ratio has been taken at 0.49, as used by other workers (9).

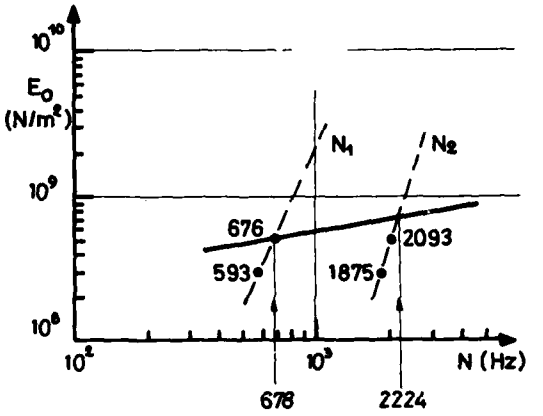

Fig. 5 Sonecran Young's modulus determination

Application of the method

The method has been applied to the calculation of a composite plate - aluminium/Sonecran/aluminium - having dimensions of 272.5 mm x 138.5 mm x 25 mm. The free-free plate was excited at its center and, accordingly, one quarter of the plate was modelled by 3 x 3 x 2 elements, as shown in figure 6, for the calculations.

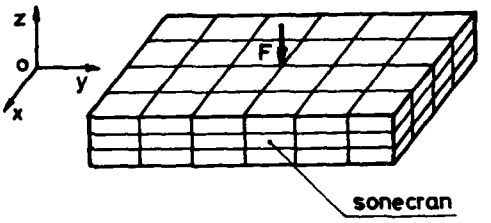

Fig. 6 Aluminium/Sonecran/Aluminium Plate

The initial estimates of E_0 were chosen as those values which applied at 1000 Hz and at 4000 Hz. The results in figure 7 show good agreement between theory and experiment.

In addition, one can see from figure 8 good agreement between theory and experiment over a very wide frequency range, and not just near the resonant frequencies where E_0 and η have been deduced.

For the experiments, we have used a SPECTRAL DYNAMICS system SD 1002, a KISTLER 903 force gauge, and an ENDEVCO 2221 C accelerometer.

CONCLUSION

A method has been developed for predicting the harmonic response of thick, heavily-damped beams and plates. In fact, the method may be applied readily to more complex structures, such as are listed in (10), (11).

ACKNOWLEDGEMENTS

This work (12) was supported by the Direction Generale de la Recherche Scientifique et Technique, under contract 7270867. The authors are indebted to D.G.R.S.T. for permission to publish this paper. Experimental results have been provided by the firm METRAVIB.

REFERENCES

1. J.C. Snowdon, Vibration and shock in damped mechanical systems, pp. 1-20, J. Wiley
2. J.D. Ferry, Viscoelastic Properties of Polymers, chap. 2, J. Wiley
3. S.H. Crandall, R.B. Mc Calley, Shock and Vibration Handbook, Vol. 2, chap. 28
4. K.J. Bathe, E.L. Wilson and F.E. Peterson, Sap IV, Berkeley, June 1973
5. M. Clint and A. Jennings, "The evaluation of eigenvalues and eigenvectors of a real symmetric matrices by simultaneous iterations", Computer J., Vol. 13, Feb. 1970
6. A. Jennings and D.L.R. Orr, "Application of the simultaneous iteration method to undamped vibration problems", Int. J. for num. Meth. in Engineering, Vol. 3, 1971
7. Material Sonecran is manufactured by ERMIA 68, route de Soissons 60800 OISE FRANCE
8. Glue CHEMLOCK 304, two components,AVIQUIPO FRANCE, Route de Service Est, CIDEX 1.128 ORLY FRANCE
9. P. Dunlop and J.M. Ducan, "Development of failure around excavated slopes", J. Soil Mech. Found. Div., ASCE, 96, pp. 471-493, 1970
10. D.I.G. Jones, A.D. Nashif and H. Stargardter, "Vibration in Gas Turbine Blades", ASME paper n° 74-GT-75, 1974
11. C.H. Cannon and D.I.G. Jones, "Controlling the dynamic response levels of jet engine components", to be published in the 45th Shock and Vibration Bulletin
12. M. Lalanne, M. Paulard and P. Trompette, "*Amortissement* des structures par revêtement viscoelastique. Calcul prévisionnel et vérification expérimentale", Rapport D.G.R.S.T., July 1974.

SYMBOLS

M	Mass matrix of the structure
K	Stiffness matrix
C	Damping matrix
X	Vector of generalized coordinates
F(t)	Vector of excitation forces
$\dot{}$	Time derivitive
T	Transpose (of matrix)
ω	Pulsation
$\emptyset$	Lowest n eigenvectors of the undamped structure
q	Modal coordinates
m	Modal mass matrix
c	Modal damping matrix
k	Modal stiffness matrix
E	Complex elastic modulus
E_0	Real part of E
η	Loss factor
K_r	Real part of the stiffness matrix of the structure
K_i	Imaginary part of the stiffness matrix of the structure
a	Positive constant
α_ℓ	3dB bandwidth for the ℓ^{th} resonance.

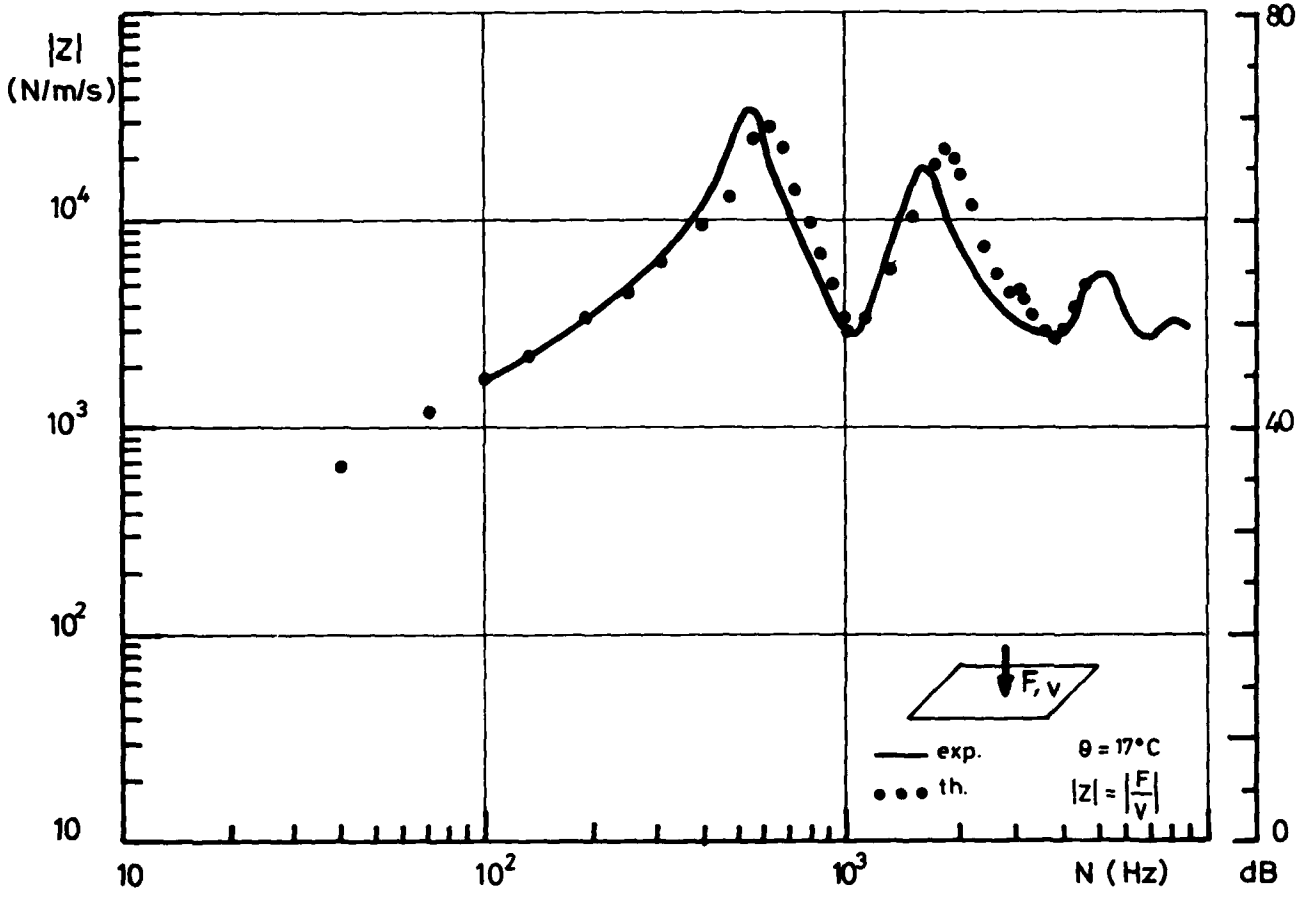

Fig. 7 Aluminium - Sonecran - Aluminium plate response

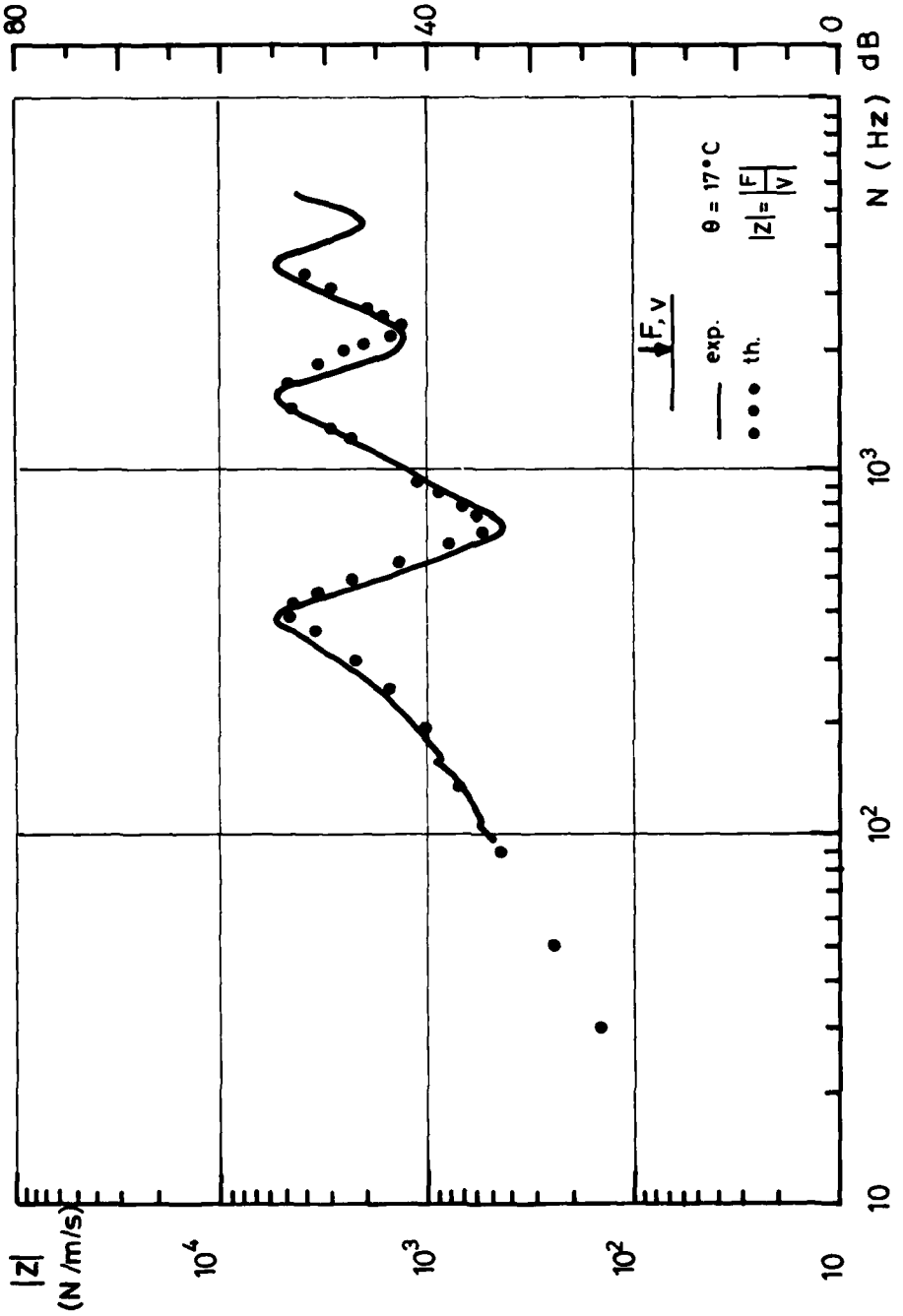

Fig. 8 Aluminium - Sonecran - Aluminium beam response

CONTROLLING THE DYNAMIC RESPONSE OF JET ENGINE COMPONENTS (U)

David I. G. Jones
Air Force Materials Laboratory
Wright-Patterson AFB, Ohio 45433

and

C. M. Cannon and M. L. Parin
University of Dayton
Dayton, Ohio 45469

This paper details recent progress made at the Air Force Materials Laboratory toward developing an alternative approach for controlling high frequency vibration problems in jet engine components such as stator vanes, inlet guide vanes, compressor and turbine blades, combustor liners, at high temperatures. The approach used is the selective application of high temperature enamels or glasses in such a way that energy is dissipated in the enamel or glass as the component deforms cyclically during vibration. In this way, provided that sufficient effort is applied, it is possible that the cumbersome and inefficient mechanical friction devices now used in rotating components such as fan, compressor or turbine blades, can ultimately be eliminated and that the often capricious aerodynamic sources of damping in static components such as stator and inlet vanes can be effectively and consistently supplemented. The specific damping treatments discussed include unconstrained and constrained layer treatments, and tuned damping devices, incorporating enamels in their high damping temperature zones.

INTRODUCTION

(U) Many jet engine components such as turbine blades, compressor blades, stator vanes, inlet guide vanes and combustor liners suffer from vibration induced high stresses under operational conditions. As jet engines become progressively more complex, lighter and more powerful, it will eventually become extremely difficult to design the systems so that these vibration problems are always circumvented by control of blade profiles, stiffnesses and natural frequencies alone, so as to avoid encountering resonant amplification of excitations around integral multiples of the blade passage frequency. As of now, damping techniques to limit such vibration induced stresses to acceptable levels include mechanical friction devices relying on interface slipping for energy dissipation, such as the platforms in turbine blades and the mid-span shrouds in compressor blades, and aerodynamic damping alone in the case of stator vanes and inlet guide vanes. Such approaches are expensive, inefficient and heavy, and aerodynamic damping is capricious, although these approaches are necessary at present.

An alternative approach which, if properly developed, can supplement these current techniques is the use of the energy dissipating properties of certain enamels and glasses when deformed cyclically at high temperatures. The essence of this approach is to properly select the glass or enamel so that its damping capability is high within the operational temperature range, and applying it in a suitable treatment or device according to the vibrational characteristics of the component.

This paper will review the status of two such potential applications, namely the control of vibration induced stresses in a set of

stator vanes by means of an external enamel coating over part of the surface area, and the control of vibrations in a turbine blade by means of a tuned damping device.

DAMPING MATERIAL BEHAVIOR

Room Temperature Damping Material

Since it is difficult to conduct vibration tests on jet engine components at high temperature, because of the necessity to protect the detection and excitation transducers, the initial tests were conducted around room temperature using an elastomeric damping material, having qualitatively similar properties at low temperatures to those of the enamel at high temperatures. The purpose of these tests was to establish the effect of the proposed treatment on the response of the components, thereby establishing the most appropriate approach and indicating the orders of magnitude involved.

The material selected for the room temperature tests was a typical stiff room temperature damping tile [1]. The complex modulus properties of the material were measured by vibrating beam, rocking beam and resonance tests [2,3]. The resulting graphs of Young's Modulus and loss factor versus temperature are shown in Figure 1. The damping material behaves in a qualitatively similar manner to the enamel, as will be seen presently, apart from the different temperature ranges and the somewhat greater stiffness of the enamel. The test systems used for these tests are illustrated in references [2] and [3].

High Temperature Damping Material Behavior

Glasses and enamels exhibit damping properties very similar to those of some high damping elastomers [4]. Experiments show that the peak damping of enamels and glasses occurs near their softening point, and it is therefore necessary to select a glass or enamel whose softening point occurs near the operating temperature range of the component to be damped.

The operating temperature of the stator vane assembly was estimated to be between 800 and 1100°F (427 to 593°C). A particular commercially available porcelain enamel [4,5,6] with an appropriate softening temperature was therefore evaluated. The complex modulus properties of the material were measured using a vibrating beam technique

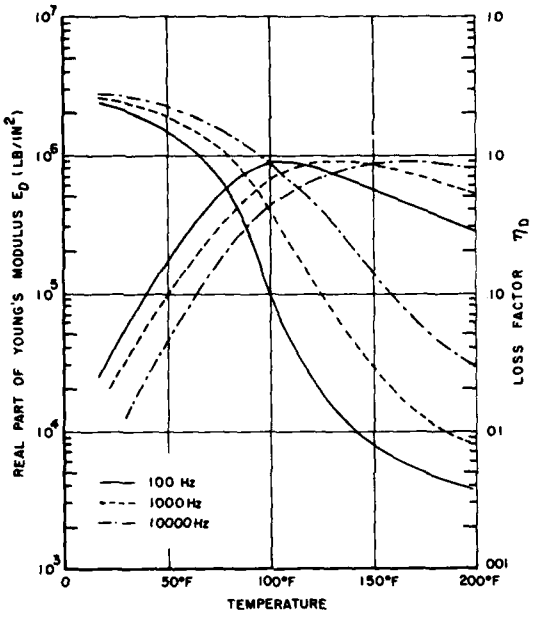

Figure 1. Graphs of E_D and η_D versus temperature for LD-400

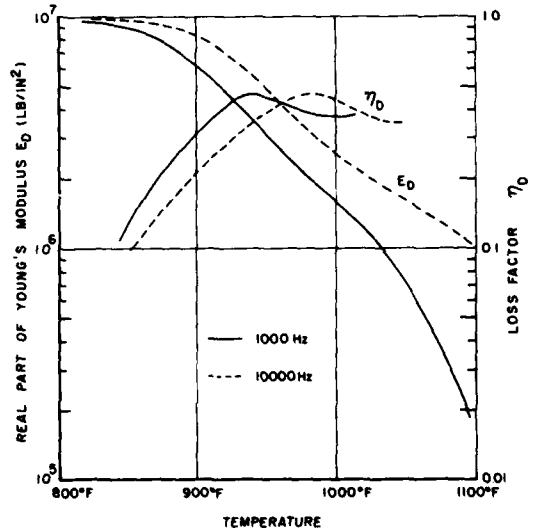

Figure 2. Graphs of E_D and η_D versus temperature for CV-16845

[3,6,7]. Graphs of E_D, the Young's Modulus, and of η_D, the loss factor, versus temperature are shown in Figure 2. It is seen that the material has a high loss factor in the appropriate temperature range, and a high storage modulus E_D near 950°F (510°C).

The turbine blade was estimated to operate at around 1200°F (649°C), and a different commercial enamel was selected [7, 9]. The complex modulus properties of this enamel, measured in the same way, are plotted as graphs of E_D and η_D versus temperature in Figure 3. The test system used to measure the complex modulus properties of the enamels is illustrated in references [6] and [7].

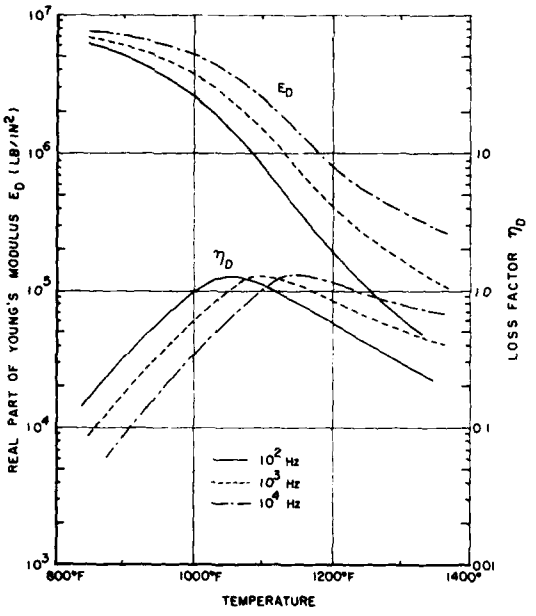

Figure 3. Graphs of E_D and η_D versus temperature for CV-17214

VIBRATION CONTROL IN A STATOR STAGE

Uncoated Vanes

A typical jet engine stator ring segment is illustrated in Figure 4. The vanes are thin, aerodynamically shaped beams welded or brazed to the outer and inner shrouds. The vanes are short, so that the natural frequencies are high, of the order of 2 kHz or higher. The modal damping is usually very low, with modal loss factors of the order of 0.002 or less, because of the lack of any sliding surfaces in the joints. This means that resonant vibration levels can be very high, leading possibly to failure, whenever the aerodynamic damping is low. This occurs, for example, when the vanes are stalled.

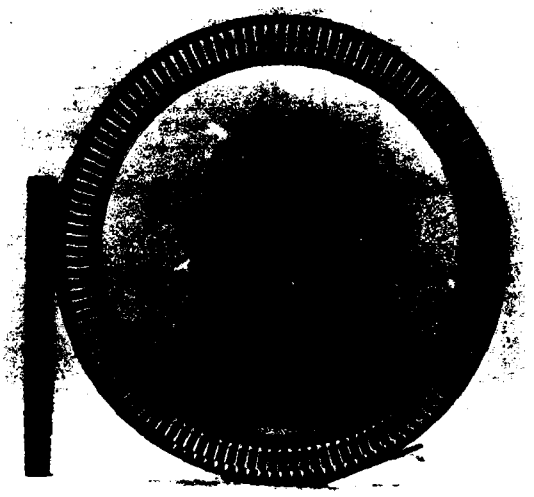

Figure 4. Photograph of typical stator vane

In order to determine the type of response behavior encountered, a typical stator segment was tested using the test system shown in Figures 5 and 6. The stator was excited by a small magnetic transducer and the response picked up by a miniature accelerometer at the points shown in Figure 6. Typical damped and undamped response spectra, consisting of plots of acceleration amplitude versus frequency, are shown in Figure 7. The mode at 2750 Hz is the first bending (1B) mode, while that at 6094 Hz is the first torsion (1T) mode. These modes were identified using laser holographic techniques. The other modes have not been specifically identified to date. In view of the thinness of the vanes, they behaved essentially as thin beams or, more precisely, plates, and a damping treatment consisting of a thin layer of a stiff, highly dissipative, damping material was expected to provide considerable increase in the modal damping. The initial modal damping, and the damping of the coated system, was measured using the "half-power bandwidth" method.

Effect of Room Temperature Damping Treatment on Stator Response

The damping tile was glued to the outer surface of each stator vane, on both sides and at both ends, as illustrated in Figures 6 and 8,

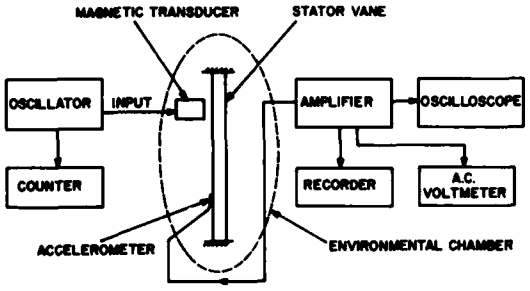

Figure 5. Stator vane test system

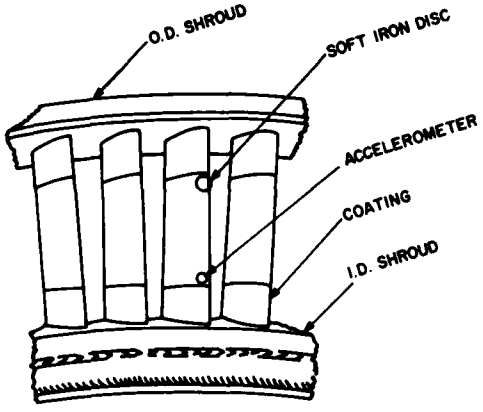

Figure 6. Stator vane pickup and excitation points

and the system was excited in the same way as for the undamped case. The coating width was 0.5 inches (12.7 mm) and two thicknesses were evaluated, namely 0.02 inches (0.508 mm) and 0.04 inches (1.016 mm). Figures 9 to 11 show the variation of the measured modal loss factor (η_s) and resonant frequency (f_n) for the first three modes as a function of temperature. It is seen that the damping was increased considerably by the treatment. Figure 7 shows a typical damped response spectrum, as compared with an undamped spectrum for the same excitation and pickup points.

From the known properties of the damping tile material, it was then straightforward to calculate the ratios η_s/η_D and ω_r/ω_o for the coated versus uncoated vanes and plot these quantities against the modulus ratio E_D/E as in Figure 12. From this figure, it is seen that η_s/η_D is approximately proportional to E_D/E ($10^{-3} \leq E_D/E \leq 10^{-1}$) and to the thickness ratio n ($0 \leq n \leq 0.67$) of coating thickness to maximum vane thickness (0.06 inches or

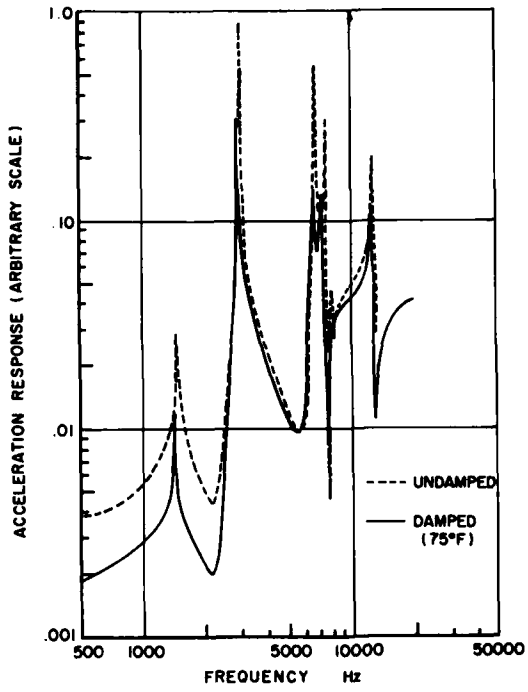

Figure 7. Typical response spectra

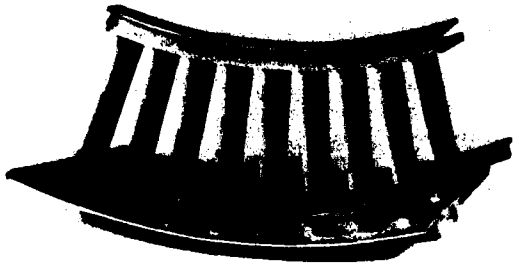

Figure 8. Photograph of stator vane segment with damping tile

1.52 mm). Numerically, in fact, it is readily shown for the first two modes that:

$$\eta_{s1} = 5.61\ \eta_D\ n\ (E_D/E) \qquad (1)$$

$$\eta_{s2} = 9.10\ \eta_D\ n\ (E_D/E) \qquad (2)$$

These approximate relationships are, of course, applicable only to vanes of the particular cross-section geometry tested, as illustrated in Figure 13. From them, we can

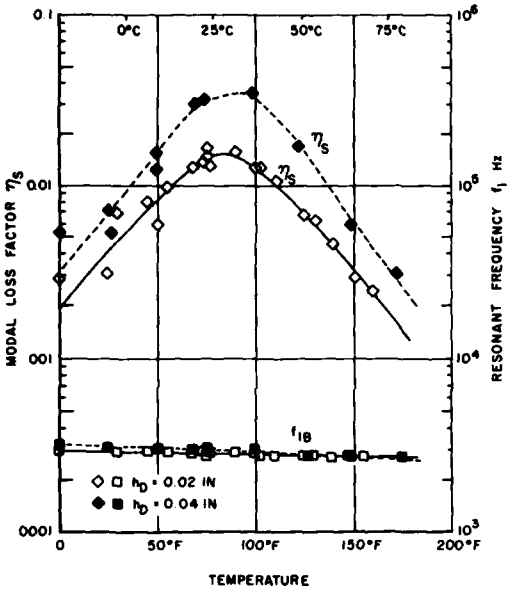

Figure 9. Graphs of η_{s1} and f_1 versus temperature

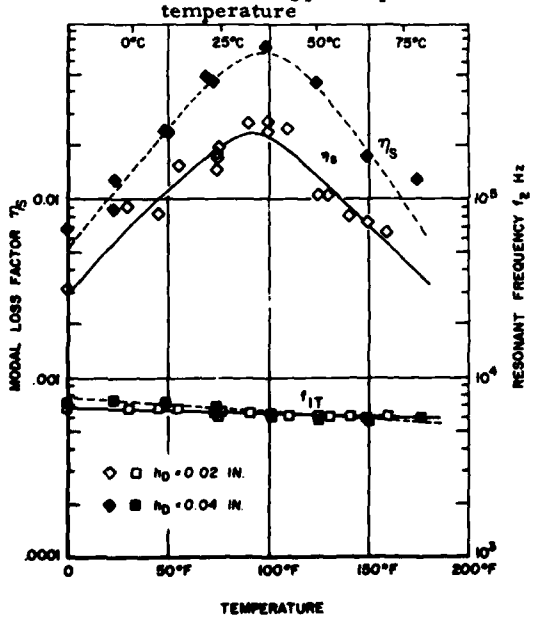

Figure 10. Graphs of η_{s2} and f_2 versus temperature

deduce the effect of any other coating treatment, such as an enamel. For example, consider an enamel coating 0.01 inches (0.254 mm) thick, having a Young's modulus E_D of 4.5×10^6 Lb/in^2 (3.1×10^{10} N/m^2) and loss factor η_D of 0.38 at 2700 Hz and 925°F, as in Figure 2. Then the appropriate value of η_{s1}

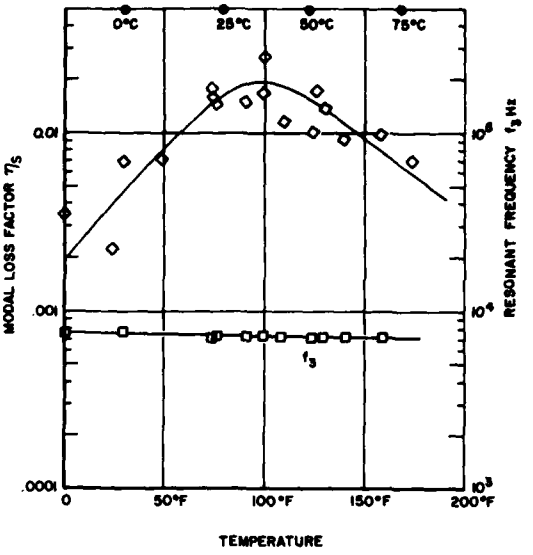

Figure 11. Graphs of η_{s3} and f_3 versus temperature

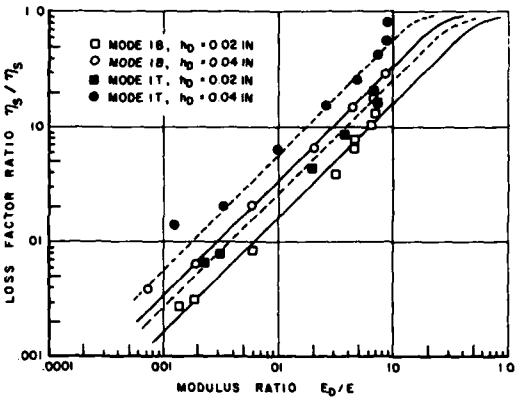

Figure 12. Graphs of η_s/η_D and ω_r/ω_o versus E_D/E

is readily shown from equation 1 to be 0.049. This value can be compared with the measured value in the next section.

Effect of Enamel Coating on Stator Response

Tests were conducted on a single stator vane at high temperature to determine the effect of a free-layer treatment, incorporating a commercially available enamel [5], on the dynamic response and modal damping. The experimental system used is shown in Figure 14. It was not possible at the time to test more than one vane, as in the case of the room temperature tests, because of available space

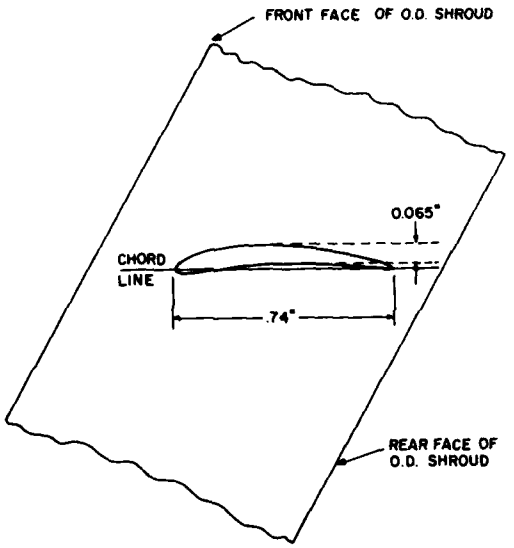

Figure 13. Sketch of stator section

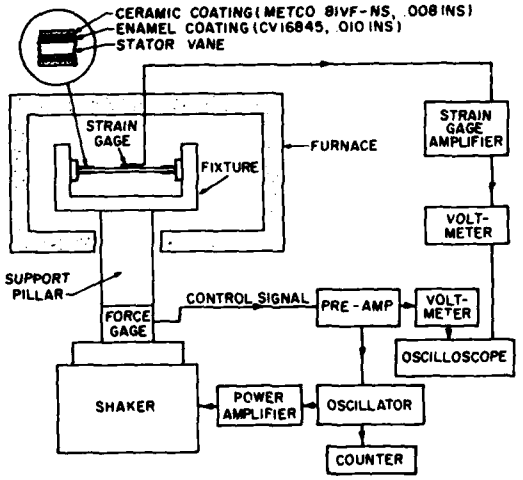

Figure 14. Test system for measuring response of enamel coated stator vanes

in the furnace and difficulties of designing a suitable fixture in such a case. The single vane was mounted in a rigid fixture attached to the top of a stiff column which was, in turn, connected to a shaker table. The response was measured by a high temperature strain gage applied at the center of the vane. Results for the first bending mode are shown in Figure 15, in the form of graphs of modal loss factor versus temperature for the two specific treatment configurations identified. The stator vane was coated at both ends and on both sides,

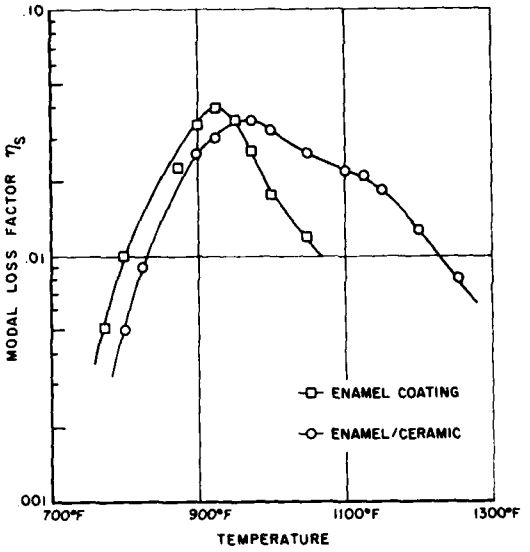

Figure 15. Graphs of η_s and ω_r versus temperature for enamel coated stator vane

with a thickness of enamel of 0.01 inches (0.254 mm) and breadth 0.5 inches (12.7 mm). Because the strain gage was aligned longitudinally on the vane surface, and very close to the node line for the first torsion mode, it was not possible to measure the response in this or any higher modes. Further tests with different strain gage locations were not carried out because of difficulties in strain gage attachment and time limitations.

The ceramic coating (Metco 81VF-NC Chromium Carbide powder) was plasma sprayed to a thickness of about 0.008 inches (0.203 mm) in order to create an abrasion resistant protective coating over the enamel, since early engine tests showed such erosion to occur. The erosion protection is needed to reduce the scouring action of the high velocity hot gases in the jet engine and also to minimize flow of the coating during occasional overheat conditions. The ceramic coating also had the effect of markedly increasing the effective temperature range over which the modal damping was high, probably because it acted as a constraining layer for the enamel as it softened at high temperatures, since the ceramic coating retains its high stiffness to far higher temperatures.

TURBINE BLADE VIBRATION CONTROL

Undamped Blade Response

A typical cooled turbine blade is illustrated in Figures 16 and 17. Again, the initial damping is usually very low and often has to be increased by means of mechanical friction devices. In order to measure the dynamic response behavior of the specimen turbine blade, the system illustrated in Figure 18 was used. The specimen was again excited by a magnetic transducer and the response picked up by a miniature accelerometer. A typical undamped response spectrum, consisting of a graph of acceleration amplitude versus frequency, is shown in Figure 19. Several modes occur in the frequency range examined, the lowest being the first "bending" mode. The response behavior of the turbine blade is very different from that of the stator vane because the turbine blade is very thick whereas the stator vane is thin, and a simple surface coating treatment will not have much effect on the modal damping, as was readily verified. A more appropriate approach is to use a tuned damping device which depends on the peak displacement rather than the peak strain in the blade, as will be discussed in the next section.

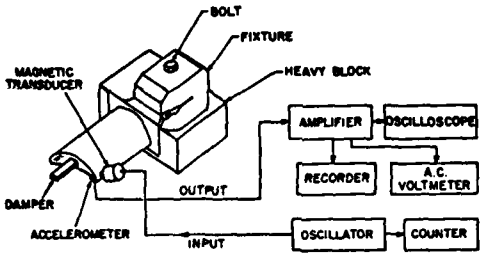

Figure 18. Turbine blade dynamic test system

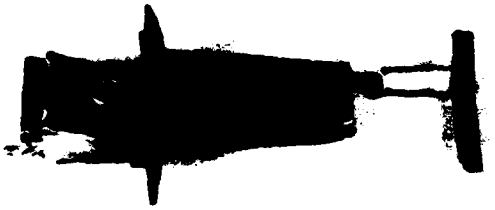

Figure 16. Photograph of turbine blade and damper

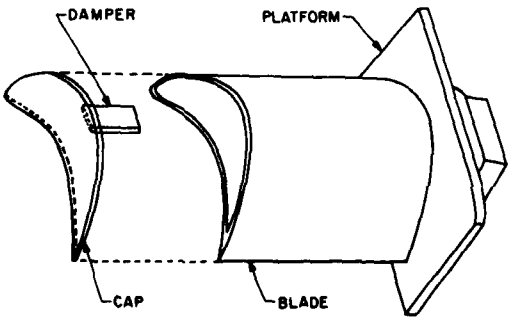

Figure 17. Sketch of turbine blade and damper

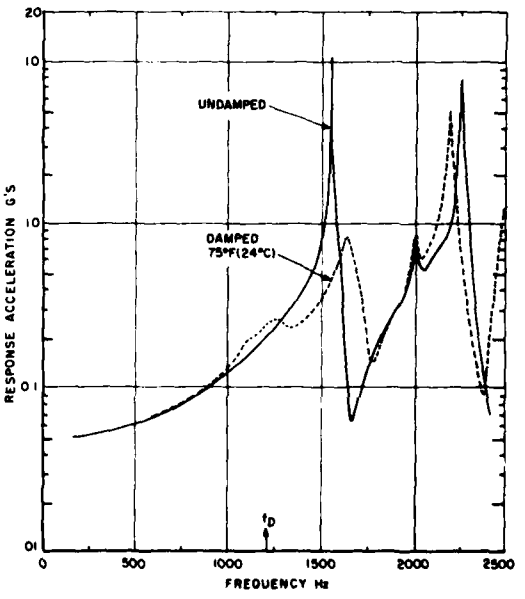

Figure 19. Typical response spectra for turbine blade

Effect of Room Temperature Tuned Damper on Response

It is difficult, by means of a layered damping treatment, to add much damping to the various modes of vibration of the turbine blade because of its exceptionally high stiffness. A very promising approach appeared to be to use a tuned damping device to control the amplitude of the first bending mode, which occurred at about 1600 Hz, by tuning the damper to this frequency. Other modes can be controlled in the same way by appropriately tuning the damper. Many prior investigations [10-12] have demonstrated the effectiveness of tuned dampers and the necessary criteria for proper tuning.

The type of damper examined in this investigation is illustrated in Figure 20. The damper consisted of an enamel or elastomer with a metal coating, i.e. the dissipative material is encapsulated. An electrodeposition technique was used to apply the metal coating. The encapsulated damper has the advantage over an unencapsulated damper that the dissipative material is totally restrained, so that creep resulting from the centrifugal loads can be controlled. Unfortunately, there are also some disadvantages, including the fact that the damping levels in the damper are far lower than for the externally coated damper [9], and the analysis is more complex. In order to verify the levels of damping achievable in practice, as well as to verify the levels of reduction in amplitude which could be achieved in a typical turbine blade, the first tests were carried out around room temperature.

The specific damper tested consisted of a core of room temperature damping tile [1], having a thickness of 0.0676 inches (1.717 mm), with an electroplated copper coating of thickness 0.005 inches (0.127 mm). The effective vibrating length of the damper in the turbine blade was 1.0 inches (25.4 mm). The damper loss factor at room temperature was measured to be about 0.04, the peak value, and the resonant frequency was about 1350 Hz [13]. The damper was glued to the tip of the turbine blade as shown in Figure 19. A typical measured response spectrum at room temperature is illustrated in Figure 19 and compared with the nominally undamped spectrum. It is seen that considerable reductions in vibration amplitude are achievable in the first bending mode, even though the damper loss factor was not very high and the damper was not optimally tuned, having a natural frequency around 1350 Hz instead of 1600 Hz. The higher modes were not significantly changed, as was to be expected unless the damper was tuned to a much higher frequency. It should be noted that the familiar pair of response peaks, well known from classical theory, are clearly discernible in the vicinity of the fundamental frequency.

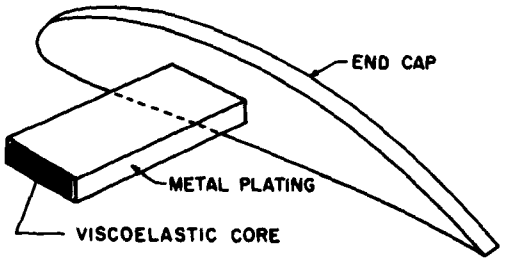

Figure 20. Sketch of damper geometry

High Temperature Response Tests

High temperature tests have been conducted, so far, only for externally coated cantilever beam dampers, using the higher temperature enamel [9]. Reference [9] shows that such a damper can reduce dynamic response levels, when properly tuned, by over an order of magnitude. Efforts to produce encapsulated dampers by electroplating an enamel strip with a thin coating of nickel have been successful on an experimental basis, and further work to produce a damped turbine blade and test it under static and rotating conditions is being planned.

CONCLUSIONS

It has been shown that enamel damping materials can be used very effectively to reduce vibration amplitudes in jet engine components under resonant conditions. The results are illustrated through two specific examples, namely a stator ring and a turbine blade. Considerable engineering effort will be necessary to bring this basic technology to the point of routine practical use, but the corresponding rewards of greater efficiency, cost effectiveness and reliability seem well worth the effort. Some such efforts are now being undertaken and will be reported on in due course.

ACKNOWLEDGMENTS

This investigation was conducted at the Air Force Materials Laboratory under Project No. 7351, Task No. 735106. Thanks are due to G. Buchhalter for assistance with enamel coating application and measurement, D. McCullum for plasma spraying the ceramic coatings and S. Askins for assistance with electronic instrumentation. Thanks are due to Lt. J. McBain of the Air Force Aero Propulsion Laboratory for conducting holographic studies of stator vane mode shapes and to J. Davis of the Air Force Flight Dynamics Laboratory for applying high temperature strain gages. Particular thanks are due to R. Barrett and H. Stargardter of Pratt and Whitney Aircraft, East Hartford, for bringing the problems to the authors' attention and assisting with specimens and technical information.

REFERENCES

1. LD-400 damping tile, made by Lord Mfg. Co., Erie, Pa.

2. Jones, D. I. G., "An Alternative System for Measuring Complex Dynamic Moduli of Damping Materials", Shock and Vibration Bulletin 45, 1975.

3. Nashif, A. D., "A New Method for Determining Damping Properties of Viscoelastic Materials", Shock and Vibration Bulletin 36, Part 4, 37-47, 1967.

4. Nashif, A. D., "Damping of Glass-Like Materials at High Temperatures", Proc. SEECO 73, Soc. of Environmental Engineers Symposium, Imperial College, London, 1973.

5. CV-16845 enamel frit, supplied by Chicago Vitreous Corp., Chicago, Illinois.

6. Nashif, A. D., "Materials for Vibration Control in Engineering", Shock and Vibration Bulletin 43, Part 4, 145-157, 1973.

7. Jones, D. I. G., "Temperature-Frequency Dependence of Dynamic Properties of Damping Materials", Journal of Sound and Vibration, 33(4), 451-470, 1974.

8. CV-17214 enamel frit, supplied by Chicago Vitreous Corp., Chicago, Illinois.

9. Jones, D. I. G., Nashif, A. D. and Stargardter, H., "Vibrating Beam Dampers for Reducing Vibrations in Gas Turbine Blades", ASME Paper No. 74-GT-95, Journal of Engineering for Power, 1974.

10. Jones, D. I. G., "Response and Damping of a Simple Beam With Tuned Dampers", Journal of the Acoustical Society of America, 42(1), 50-53, 1967.

11. Snowdon, J. C., "Vibrati[illegible]s of Cantilever Beams to Which Dy[illegible]amic Absorbers are Attached", Journal of the Acoustical Society of America, 39, 878-886, 1966.

12. Jones, D. I. G. and Nashif, A. D., "Damping of Blade-Like Structures", Shock and Vibration Bulletin 39, Part 4, 19-29, 1969.

13. Jones, D. I. G. and Parin, M. L., "Encapsulated Tuned Dampers for Jet Engine Component Vibration Control", Accepted for Publication in the Journal of Aircraft, 1975.

NOMENCLATURE

E	Young's modulus of stator material
E_D	Real part of Young's modulus of damping material
f_i	ith resonant frequency (i = 1, 2, 3, --)
f_{1B}	Resonant frequency of first bending mode (= f_1)
f_{1T}	Resonant frequency of first torsion mode (= f_2)
h	Maximum cross section thickness of stator vane
h_D	Thickness of damping layer
n	Thickness ratio h_D/h
η_D	Loss factor of damping material
η_s, η_{si}	Modal loss factor of damped stator system
ω_r	Resonant frequency of damped system
ω_o	Resonant frequency of undamped system

Discussion

Mr. Warner:(Westinghouse Marine Division) You used the word enamel which scares me. What are the mechanical properties that would enable that coating to last and how long do you think it should last?

Mr. Jones: That unfortunately is one of the fine questions and that is one that we have asked ourselves. If you take an enamel up into a temperature range where it starts to soften it tends to get somewhat viscous, that is a term that is qualitative only I would not try verifying it, and in fact if you get sufficiently high overheating, or if you get considerably very large forces applied to it, it would certainly creep and move; in the case of rotating components you have the worry of creep and I would not address this here. As applied to a stator vane there are two ways to look upon this particular problem. At 950 degrees F, the material stiffness had not dropped too much for the particular material that we used; at about 1200 degrees F it starts to become very soft and it starts melting, and at that point it would just spread all over the engine. So if there is some accidental overheating you have a problem. There is a way of solving this problem, and that is to coat the enamel with a thin layer of nickel or of some ceramic material, which in itself does not melt. We currently have some tests in progress in which we have put a very thin layer of an aircraft engine specification type of a ceramic coating which we hope is designed to prevent erosion and to prevent any adverse effects from overheating; but the purpose of this particular investigation was to verify that in fact it would work.

Mr. Russo: (Air Force Materials Laboratory) Some of the alloys in these engines are extremely tempermental and different variations of trace elements anyplace can drastically affect just the basic properties of the material. So this is one of the things we will have to investigate pretty heavily when you talk about applying these types of enamel, or what ever word you would rather use for them, to damp out vibration.

Mr. Sen Gupta: (The Boeing Company) I'm not quite sure if you applied the damping treatment on the whole stator blade or just near the root.

Mr. Jones: Only near the root.

Mr. SenGupta: Why didn't you apply it to the entire blade?

Mr. Jones: In the case of the thirteenth stage it would only be a quarter inch out from the root and you would leave the rest of the blade uncoated to satisfy the aerodynamicists mainly. We would prefer to coat all of it but the aerodynamicists say they would much rather have nothing on the blade.

Mr. SenGupta: Because the activity was bending, would you expect the damping material to be more effective by having it near the center?

Mr. Jones: That was our intuition we have not been able to verify it and I think a finite element analysis, or perhaps a transfer matrix analysis would be necessary before we could really verify this. We have not made any stress measurements.

Mr. Butzel: (The Boeing Company) What is the long term purpose of increasing the damping in these blades, to get longer life?

Mr. Jones: I understand the question. As with all questions it is difficult to give just a simple answer. The purpose, as far as we are concerned, is to increase life to an acceptable level and obviously you would not apply damping to a system which is working perfectly well. But this particular system was not,the life of the stator was much less than the normal replacement cycle. So any time you have a component which is subjected to excessive stresses and it is not convenient for any reason to redesign it, as in this particular instance because this was an existing engine in the inventory, in a case like that you would apply damping since it would be expensive to go back and retool and remake.

Mr. Butzel: Are you also thinking in terms of future designs? That is, if you can increase the damping in these blades will it influence the design of future stators?

Mr. Jones: Absolutely, and I think some of the engine manufacturers are inclined to agree with us although the question of how to do it is just in its infancy. If you could in fact increase the damping to a significant level without any other unsatisfactory side effects you would simplify the design considerably because if you are not bothered by one multiple of the rotational frequency you may be bothered by another.

AN INVESTIGATION OF THE RESPONSE OF A DAMPED STRUCTURE USING DIGITAL TECHNIQUES

M. L. Drake
University of Dayton Research Institute, Dayton, Ohio
and
J. P. Henderson
Air Force Materials Laboratory, Wright-Patterson Air Force Base, Ohio

I. INTRODUCTION

The design of effective damping treatments for the control of resonant structural vibrations necessitates the making of engineering trade-off decisions based on the dynamic characteristics of the vibrating structure, and the effect of environmental factors on the properties of the damping materials. It is for this reason that the Air Force Materials Laboratory, in conjunction with the University of Dayton Research Institute, is in the process of completing an experimental program to develop vibration damping treatments for possible application in the reduction of sonic fatigue in structures such as the aft fuselage of the B-1 aircraft. Although it is not anticipated that there will be a sonic fatigue problem with the B-1 aircraft, the development of damping treatments to work effectively in the unique combination of operational environments seen by this structure represents a challenge that will have to be met by the aerospace industry sooner or later. These environments include temperatures up to 300°F, sound pressure levels in excess of 168 db and, since the damping treatment would be inside a fuel tank, there is the added complication that it must be unaffected by long term exposure to fuel.

This investigation is divided into essentially four stages:

1. Measurement of natural frequencies and mode shapes in an undamped specimen representative of the full scale structure.
2. Evaluation of effects of elevated temperature, fuel exposure, and water environment on the performance of candidate damping materials.
3. Measurement of the effect of room temperature damping materials on the response of the structural specimen.
4. Measurement of the effects of high temperature on the undamped specimen, and evaluation of candidate damping materials in damping treatment configurations on the test specimen at high temperature.

This paper describes the structural response measurement and room temperature damping portions of this investigation, including the application of impact testing techniques utilizing digital fast Fourier analysis. Digital techniques for rapidly determining resonant frequencies, mode shapes and structural damping are discussed and results compared with sine sweep techniques.

II. IMPACT TESTING FOR DIGITAL TRANSFER FUNCTIONS

Fourier analysis of vibrating systems is not a new idea in the shock and vibration area but the advent of the digital fast Fourier analyzer has made this method of analyzing experimental data far more readily available to the engineer than ever before. In this study, an impact testing method was used, with the Fourier analyzer system shown schematically in Figure 1, to determine transfer functions. These transfer functions, which represent the frequency response of the structure at some point due to a unit excitation at either the same point (driving point transfer function) or another point (cross transfer function), provide information which include resonant frequencies, mode shapes and modal damping. The impact technique used was a very straight-forward process in which a "hammer", instrumented with a piezoelectric force transducer, was used to excite the structure. Frequency content of the excitation impulse could be controlled, to some extent, by using hammer

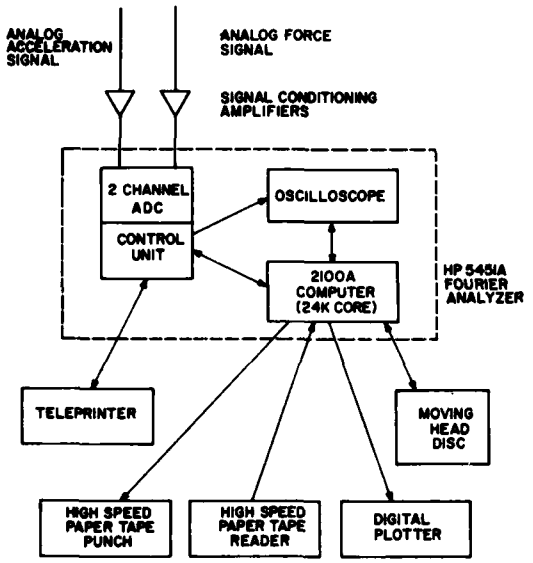

Figure 1. Diagram of Digital Test System

heads of different materials, the "harder" head giving a higher maximum frequency than the "softer" heads. The response of the structure was measured using a piezoelectric accelerometer. The digital transfer functions were obtained by simultaneously measuring, and digitally storing, the time histories of impact force and acceleration response. These time-domain signals were then analyzed using the fast Fourier analyzer system, thereby calculating, in the frequency domain, the acceleration auto power spectrum Gyy, the force auto power spectrum Gxx, the cross power spectrum Gyx, and the transfer function H (iω) where:

$$H(i\omega) = \frac{\overline{Gyx}}{\overline{Gxx}}, \quad (1)$$

and the coherence function δ^2 where

$$\delta^2(i\omega) = \frac{\left|\overline{Gyx}\right|^2}{\overline{Gxx}\;\overline{Gyy}}, \quad 0 \le \delta^2 \le 1. \quad (2)$$

The coherence function used here is a measure of the "quality" of the data, since a coherence value of 1 indicates that the "output" (acceleration) is completely causally related to the input (force), whereas a coherence value of zero indicates that the acceleration signal is due entirely to some other input [1]. Thus, problems in the signal conditioning system, such as bad cables or ground loops, as well as spurious excitation by ambient acoustic noise, or nonlinearities in the structural response, become immediately apparent in terms of a low value of the coherence function. This gives the test engineer the advantage of immediately being able to recognize and reject bad data, at the time that the test is being run, as opposed to attempting to recognize unreasonable final results, caused by bad data, which can occur when utilizing analog sine sweep techniques.

* — indicates average over several samples.

III. COMPARISON OF ANALOG AND DIGITAL TECHNIQUES

As with any relatively new test technique, it was considered desirable to obtain a quantitative comparison between the data obtained using impact test techniques, with digital data processing, and the data obtained using more conventional analog sine sweep techniques. For comparative purposes, it was decided to examine the response of a stiffening strap (shown in Figure 2) within the frequency range around its fundamental resonance, which occurred at about 240 Hz. Transfer functions were measured using both analog (sine sweep) and digital (impact) methods for the undamped structure and for the structure when damped with various room temperature damping treatments.

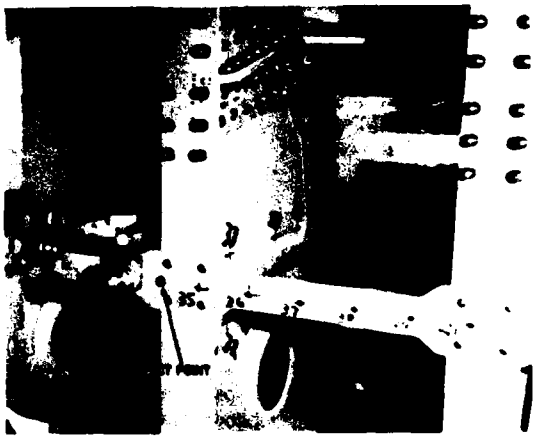

Figure 2. Photo of Sine-Sweep Set Up Used to Collect Data for Digital to Analog Comparison

The sine sweep experimental system utilized a magnetic transducer** for excitation, and a very small accelerometer*** for response pickup,as shown in Figure 2. With this method of excitation, it is necessary to attach a small ferromagnetic disk to the structure, and this disk is then driven by the oscillating component of the magnetic field of the transducer. The mass loading effects are negligible in most aerospace type structures. In these analog tests, the excitation point was located on the stiffening strap at a point near the frame, and the response was picked up by an accelerometer near the center of the strap. The force signal at the transducer was used as a control feedback to maintain a constant force amplitude as the frequency was swept, therefore the plots of measured acceleration versus frequency, of which a typical example is shown in Figure 3, are directly comparable with plots of the magnitude of an acceleration transfer function. The resonant frequency was determined from the location of the peak in the acceleration plot, and the damping was determined by measuring the "half-power bandwidth" of this peak. Table 1 contains a summary of fundamental mode resonant frequencies and structural loss factors measured by sine sweep techniques.

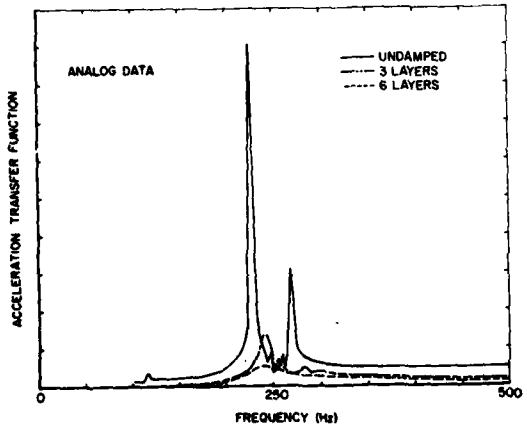

Figure 3. Analog Transfer Function Data Used in Comparison

The impact tests were accomplished using the same pickup point, but a slightly different excitation point was used, because one problem encountered with impact testing is that when one impacts a flexible structure, the usable frequency range for a transient force input is limited to relatively low frequencies, since the upper frequency limit depends on the local structural stiffness at the point of impact. In these tests, because of the relatively low local stiffness, it was necessary to move the excitation point closer to the frame as shown in Figure 2, to excite the resonant frequencies of interest.

** Bruel and Kjaer MM0002 Transducer

*** Endevco 22 Accelerometer

TABLE I

COMPARISON OF DIGITAL TO ANALOG DATA

	Sine Sweep	Digital Nyquist Plot
UNDAMPENED		
Res. Freq.	236.2	235.75
Loss Factor	.006	.006
DAMPENED 3 LAYERS		
Res. Freq.	243.5	246.5
Loss Factor	.038	.037
DAMPENED 6 LAYERS		
Res. Freq.	243.9	243.5
Loss Factor	.090	.082

Three digital transfer functions are shown in Figure 4, which are compared to the analog response functions shown in Figure 3. Resonant frequencies can be

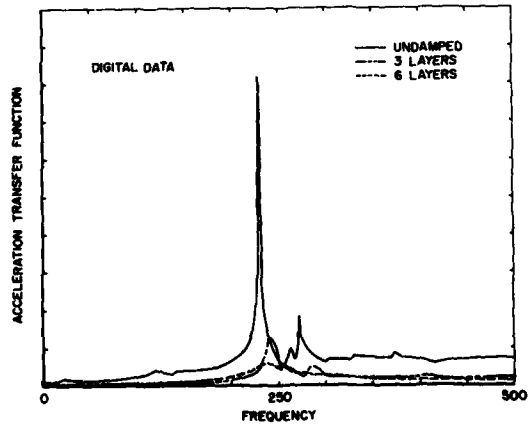

Figure 4. Digital Transfer Function Data Used in Comparison

determined from transfer function data by identifying the frequencies at which the imaginary part of the transfer function becomes a maximum and the real part is small, or the magnitude becomes a maximum and the phase angle is approximately 90°. Modal damping can be obtained from a Nyquist plot, which is simply a plot of the imaginary part of the transfer function against the real part, in the frequency range around a single resonance. In this investigation, Nyquist plots were obtained utilizing both digital and analog methods. The analog set-up used to obtain Nyquist plots utilizing Spectral Dynamics tracking filters and a CO-Quad unit. Examples of Nyquist plots obtained through both analog and digital techniques are shown in Figures 5 and 6 respectively.

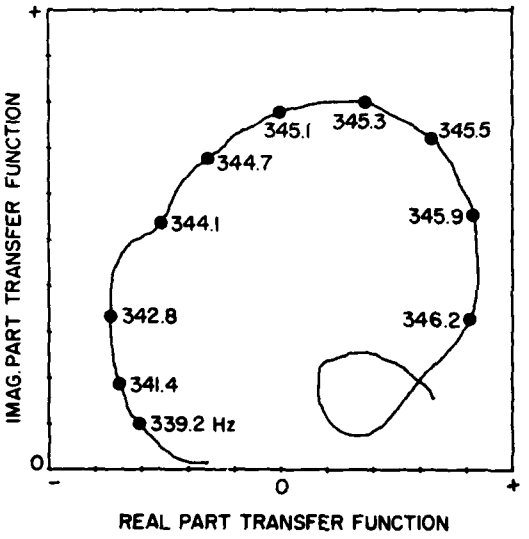

Figure 5. Analog Nyquist Plot

Fitting a circle, using a least square technique, to a Nyquist plot of measured transfer function data near a resonance can provide all of the modal parameters necessary to define a complex normal mode, except in the case of nearly coincident resonant frequencies [2]. For instance, the resonant frequency occurs at the point where the rate of change of arc length with respect to frequency, ds/df, is a maximum. In the case of a discrete Fourier transform, where data is taken only at specific frequency intervals Δf, resonance occurs at a point between the frequencies which mark the end points of the interval of maximum arc length, Δs_{max}, of

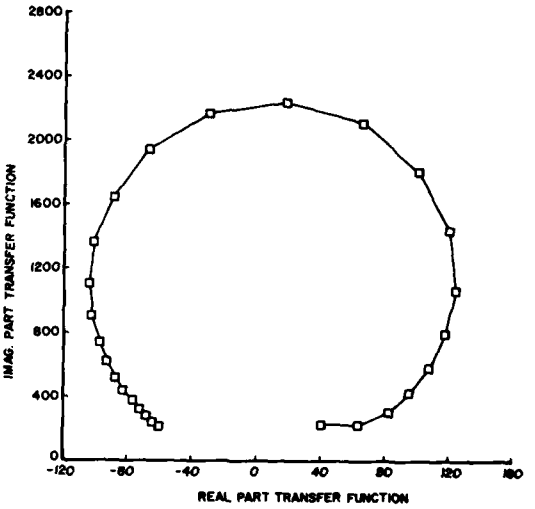

Figure 6. Digital Nyquist Plot

the circle. Furthermore, it can be shown that if hysteretic damping is assumed to be the dominant mechanism, then the structural loss factor, η_s, can be determined at a resonant frequency, f_n, from the relationship

$$\eta_s = 4R/[f_n(\Delta f/\Delta s_{max})] \qquad (3)$$

where R is the radius of the circle.

There are several advantages to be obtained from using Nyquist plots obtained by digital techniques. One advantage is the speed of data acquisition, since all the data required for Nyquist plots are automatically obtained and stored during the process of measuring the digital transfer functions. A typical time interval for processing this data from a single impact, in this investigation, was found to be about 6 seconds for a 2048 point transfer function. The analog method, however, generally required a separate test for each transfer function, with several minutes of slow frequency sweep and also a lengthy set-up and calibration procedure. A second advantage of digital data acquisition techniques lies in the fact that the data are already digitized at the outset, and are in a form that can be rapidly processed by the mini computer, using a Fortran program for least squares fitting of the data to a circle and for immediate calculation of resonant frequency and damping. Graphical techniques examined in this

investigation, in conjunction with the analog Nyquist plots, proved to be too cumbersome to be practical, and damping was far more readily determined from direct band-width measurements of the analog response data.

Data obtained through analog and digital techniques are shown in Figures 3 through 6 and are compared in Figure 7 and Table I. The excellent agreement obtained in these tests went a long way toward verifying the validity and convenience of the digital test techniques. The digital techniques were therefore utilized in the remainder of this investigation.

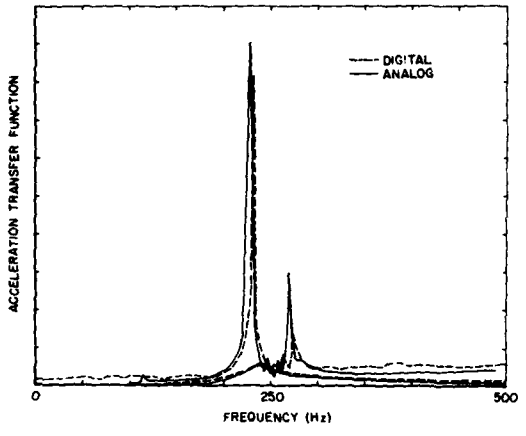

Figure 7. Plot of the Digital Data vs Analog Data

IV. MEASUREMENTS OF RESONANT FREQUENCIES AND MODE SHAPES

The structure examined in this investigation is typical of a segment of the proposed aft fuselage area of the B-1 aircraft, near fuselage station 1475. Figure 8 shows the particular structural specimen used and the three zones chosen to characterize structural response for different average radii of curvature. The specimen is shown in a side view, with zone 3 representing the relatively flat bottom of the fuselage, and zones 1 and 2 representing side sections with decreased radii of curvature. The basic construction is of titanium skin stiffened by perpendicular frames, with the inside frame caps interconnected by straps. This construction, which combines a chem-milled titanium skin of varying curvature and thickness, and a complex system of frame webs (shown in Figure 9) having varying thicknesses of frame caps and straps,

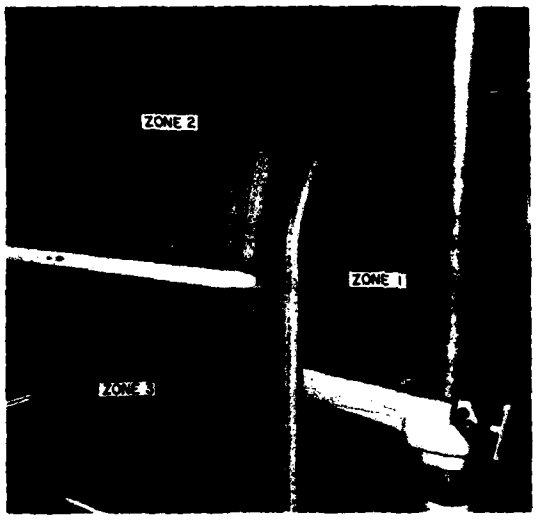

Figure 8. Overall External View of Test Specimen

Figure 9. Internal View of Test Specimen

resulted in extremely complicated vibrational response characteristics. Resonant frequencies, identified from transfer function measurements, occurred in several frequency bands of high modal density. Typically these occurred between 250-350 Hz and 500-600 Hz in zones 1 and 3, and at somewhat higher frequencies in zone 2. This high modal density is evident in Figure 10. The primary

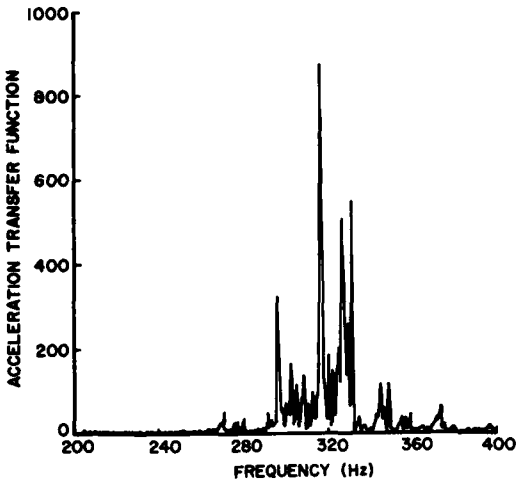

Figure 10. Undamped Transfer Function

frequency range of interest was the low frequency band, 250-350 Hz, which was identified as having high 1/3-octave band strain levels by Rockwell International during their sonic fatigue tests.

A detailed understanding of typical mode shapes is necessary for proper design of damping treatments. One analog sine-excitation method of obtaining mode shapes is to excite the structure with a discrete frequency force, at one point, and move a lightweight accelerometer to various points in a grid pattern, measuring and plotting the acceleration at each point at each resonant frequency. This method is very cumbersome and time consuming, because the system must be re-swept for each point and is difficult to use for closely spaced resonances because of modal coupling.

Impulse testing and digital data processing can, however, often be used to rapidly and conveniently acquire mode shape data. The process involves obtaining several transfer functions, representing the frequency response of the structure at several points, due to excitation at a single point. This can be done either by impacting the structure at a single point and moving the accelerometer to each response point, as for the analog method, or by using Maxwell's Law of Reciprocity [3], leaving the accelerometer at a single point and impacting the structure at each point where mode shape data is required [4].

Mode shape information can then be compiled by examining the amplitude of the imaginary part of the transfer function, at each resonant frequency, for each response point measured on the structure. In the case where there are several closely spaced resonant frequencies, and structural damping is low, small errors in identifying resonant frequencies, resulting from the limited frequency resolution, can cause large errors in the measured mode shapes. In some cases, this problem can be alleviated by employing a special time window [5] which causes the observed force and acceleration time samples to decay with time.* This windowing process smooths the calculated transfer function and therefore can provide more accurate determination of mode shapes. Obviously, however, since the special time window adds apparent damping of the transfer function, it must not be used when the transfer function data is used to calculate modal damping. Two test techniques were used in this investigation to obtain mode shape data, namely: (1) a fairly straight-forward method which produces two-dimensional mode shapes, and (2) a more sophisticated method which generates animated three-dimensional mode shapes on the oscilliscope screen.

The two dimensional technique involves determination of each resonant frequency from observation of a "windowed" transfer function, such as that shown in Figure 11. As can be

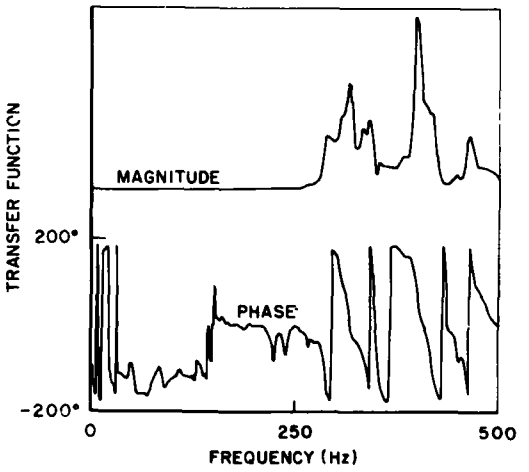

Figure 11. Time Windowed Undamped Transfer Function

*The time window used in this investigation was an exponentially decaying function, with an arbitrary rate of decay.

seen, the special window produces a transfer function which is considerably smoother than those taken without the window, such as those shown in Figure 10. Resonant peaks in the transfer function are characterized by a peak in the magnitude, and a 90 degree phase angle between force and acceleration, such as occurs at 295 Hz in Figure 11. Once a resonant frequency has been identified, a transfer function measurement is then made for each point on the structure at which mode shape information is desired. For a two-dimensional mode shape display these structural coordinate points are usually selected to lie in a pattern of straight lines. The two dimensional mode shape computer program used in this investigation [6] then determines and displays, on the oscilliscope, the amplitude of the imaginary part of the transfer function, not only at the designated resonant frequency, but also at four additional frequencies, namely the two frequency steps immediately above the resonant frequency and the two frequency steps immediately below the designated resonance. With this method, slight shifts in the frequency at which maximum quadrature amplitude is observed do not affect the measured mode shape significantly. Typical outputs of this program are shown in Figures 12 and 13, with a peak displayed at each point representing a structural coordinate; thus the mode shape is taken to be the envelope of these peaks. Figure 13 shows a mode shape of a skin panel, along a line parallel to the frames. Figure 14 shows a mode shape of the same panel measured along a line perpendicular to the frames. With these plots, and a little imagination, the three dimensional mode shape of a simple panel can be visualized.

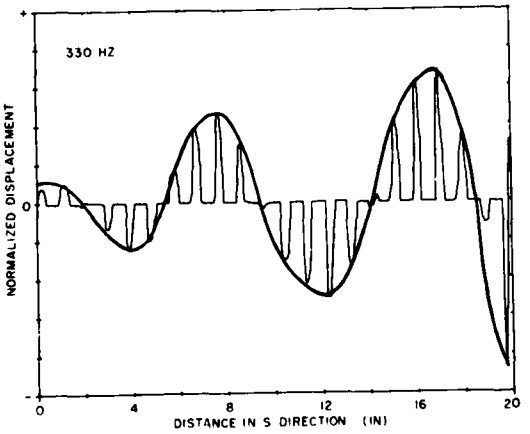

Figure 12. Typical Skin Panel Mode Shape at 330 Hz

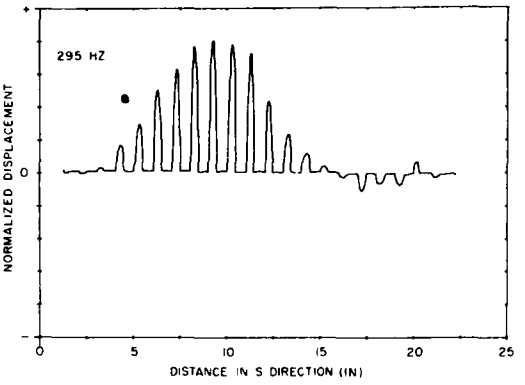

Figure 13. Typical Skin Panel Mode Shape at 295 Hz in S Direction

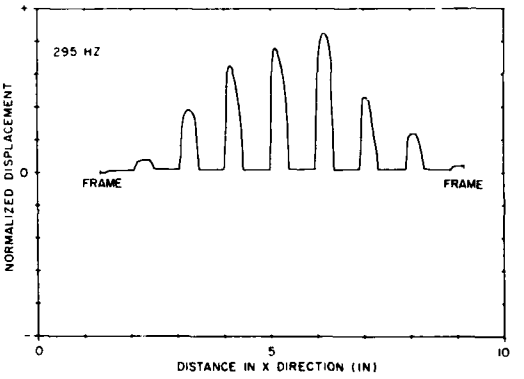

Figure 14. Typical Skin Panel Mode Shape at 295 Hz in X Direction

However, with a more complicated structural geometry, it becomes increasingly difficult to visualize 3-D mode shapes by viewing a collection of 2-D mode shape sections. For example, using the above 2-D mode shape procedure, it would be extremely tedious to attempt to visualize the modes involving coupled motions of the skin, frames and straps. Yet it is exactly this type of information which is needed for the proper design and placement of damping treatments on this structure. Therefore, the 3-D mode shape computer program which produces an orthogonal projection of the structure with a superimposed animation of the mode shape, having a capability of selecting any viewing angle, is a very powerful aid to engineers faced with designing effective damping treatments.

Perhaps the best way to explain how the 3-D mode program works is through an example. Consider the structure shown in Figures 2, 15, and 16. The portion of structure under consideration consists of a skin panel, two stiffening frames, and a connecting strap. The structure is then represented by a finite number of points in space. In this case 50 points were chosen with 25 points on the skin, 9 points on alternate sides of a stiffner on one of the frames, 6 points on the strap, and 10 additional points on alternate sides of a stiffener on the other frame. This grid pattern, representing the structure, is shown in Figure 17. The spatial coordinates of each point, along with the direction of impact or acceleration measurement, is stored by the computer in a geometry file. A cross transfer function is then measured for every point on the grid relative to the single impact (or pick-up) point, and each of these transfer functions is stored on the disc. These transfer functions can be taken with the special time window previously discussed or, if modal damping measurements are required, stored without windowing on the disc and then, if desired, smoothed later by applying the window to data. The computer software can then calculate the 3-D mode shapes from the stored transfer function data and the information in the geometry file for a number of resonant frequencies selected and identified by the test engineer. These mode shapes can be displayed in a slow motion animated fashion superimposed on orthogonal projection of the points representing the structure. Furthermore this 3-D view of the mode shape can be viewed from any point in space selected by the test engineer. Photos of different mode shapes are shown in Figures 18-22.

Figure 15. Skin Area Used in Three Dimensional Mode Shape Program

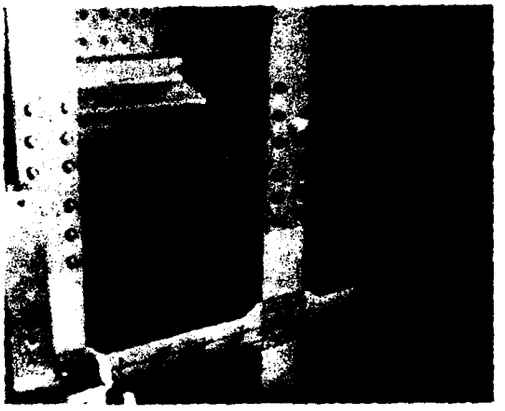

Figure 16. Right Frame Area Used in Three Dimensional Mode Shape

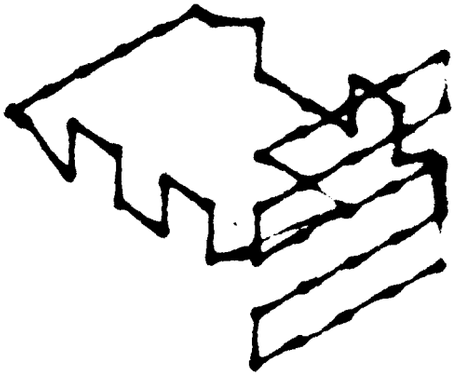

Figure 17. Undeformed Three Dimensional Mode Shape Model

At first glance one might assume that this is an interesting gimmick, of little technical value, but in reality this 3-D mode shape display is a very powerful tool for under-

standing the modes of complex structures.

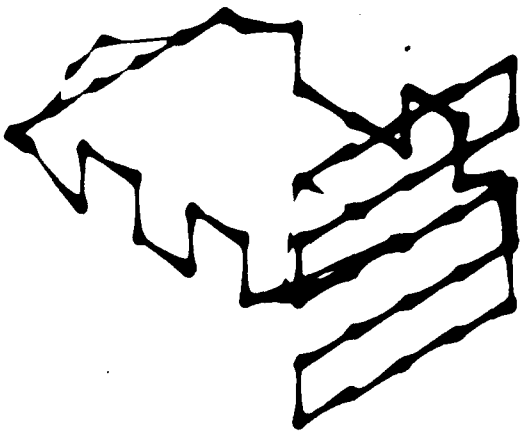

Figure 18. First Bending Mode of the Strap at 237 Hz

Figure 20. Edge View of Skin and Strap Mode at 295 Hz

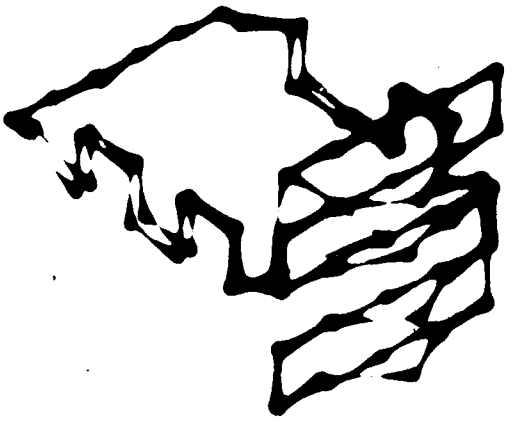

Figure 19. Mode Shape at 295 Hz

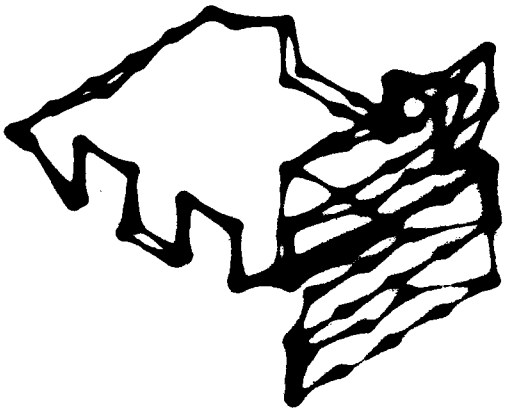

Figure 21. Mode Shape at 354 Hz

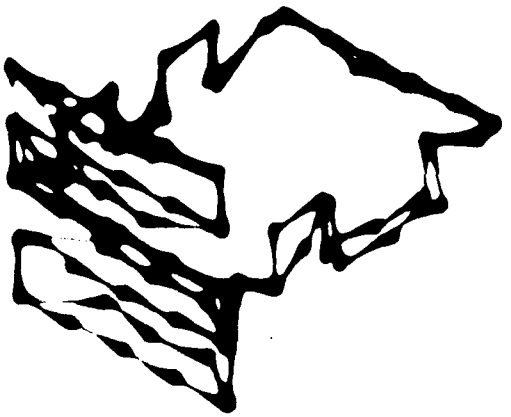

Figure 22. Rotated View Showing Right Frame at 354 Hz

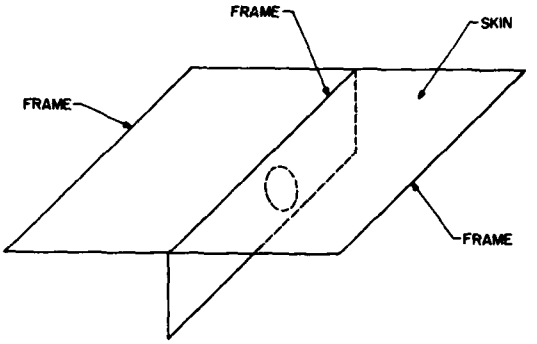

Figure 23. Structure Construction to which Damping Treatment was Applied

V. DAMPED AND UNDAMPED RESPONSE MEASUREMENTS

The transfer function and mode shape data previously discussed led into an experimental study to determine the effect of the placement of various room temperature damping treatments on the vibrational response of the aft section of the B-1 structure. The object of the study was two fold; namely, (1) to determine the effect of skin-frame modal coupling on the damped vibration response of the structure; and, (2) to establish the parts of the structure, found from the 3-D mode shape data, to which the damping treatments should be applied in order that they may be used in the most efficient manner.

The areas of the B-1 structure investigated were two adjacent skin panels and the frame between them. Figure 23 illustrates the construction of the structure. The blocked-off section in Figure 24 shows the skin area to which the damping treatments were applied and the pickup location for the frame area is illustrated in Figure 9.

Two types of damping treatment were applied successively and independently to the structure, namely constrained layer damping treatments and tuned dampers. Each layer of the constrained layer damping treatment consisted of 0.002 in. of a pressure sensitive adhesive and 0.005 in. aluminum backing, as in Figure 25. The tuned dampers were single

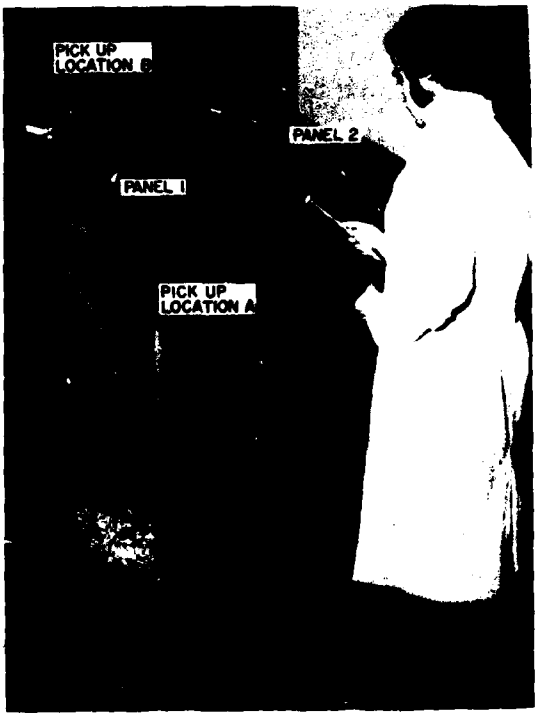

Figure 24. Skin Area of B-1 Structure to which Damping Treatments were Applied.

degree-of-freedom spring-mass systems with a Dow Corning fluorosilicone sealant as the viscoelastic spring and were designed to have a resonance frequency of 280 Hz. The frequency corresponds to one of the resonances of the structure.

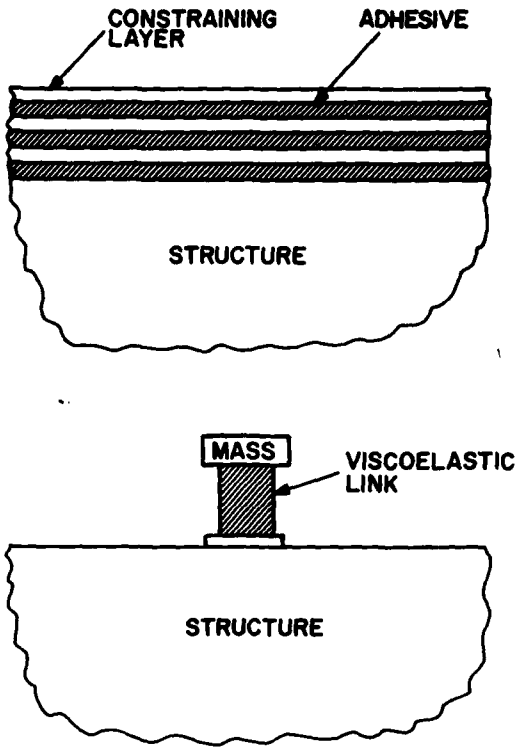

Figure 25. Configuration of Damping Treatments Applied

The damping treatments examined and their placement on the structure are listed in Table II. The resulting effect of each damping treatment was determined by measuring the transfer function at positions A, B, and C and comparing this to the undamped transfer function. The reduction of peak amplitude is a measure of the effectiveness of the damping treatment and its location. These results are shown in Table III. Nyquist plot determinations of damping for this system was not feasible because of the closely spaced modes encountered in the structures. Closely spaced modes cause the Nyquist circle of one resonance to distort the circle of adjacent resonances. This distortion ruins the Nyquist plot circle fit method of determining damping!

Transfer functions for each damped configuration listed in Table III, at position B, are shown in Figures 10 and 26-29. The results indicate that the most effective way to add damping to a specific area is to directly apply the treatment there. However, the coupled nature of the motion observed in the three-dimensional mode shape analysis is illuminated by the reduction in amplitude observed in the frame as a result of the damping on the skin and vice versa. Because of this coupling, the greatest amount of damping is added by applying damping to both the skin and the frame.

TABLE II

TYPES OF DAMPING TREATMENTS AND THE PART OF STRUCTURE APPLIED TO

Treatment No.	Type of Treatment and Part of Structure to Which it Was Applied
0	Undamped
1	Six layers of the constrained layer treatment applied to frame web only.
2	Three layers of the constrained layer treatment applied to both adjacent skin panels.
3	Three layers of the constrained layer treatment applied to both skin panels and six layers applied to frame web.
4	Four tuned dampers applied to the frame web number 3. (See Figure 30 for location on frame.)

TABLE III

TREATMENT NUMBER AND PEAK TRANSFER FUNCTION RESULTS

Location of Pickup	Treatment Number and Applitude of Maximum Peak in Transfer Function Below 350 Hz				
A	0-320	1-112	2-63	3-11	4-90
B	0-850	1-118	2-20	3-11	4-540
C	0-1400	1-100	2-520	3-110	4-500

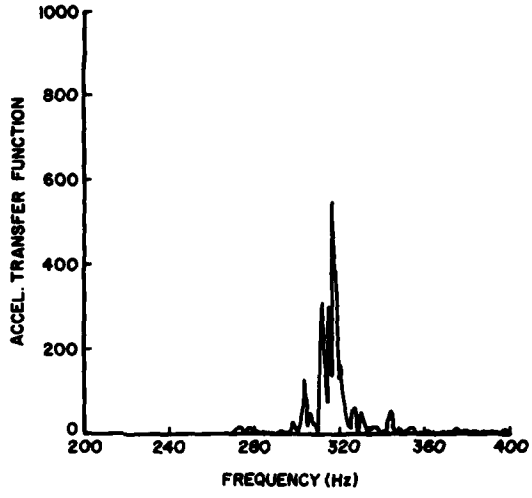

Figure 26. Transfer Function with Damping Treatment No. 1 Applied

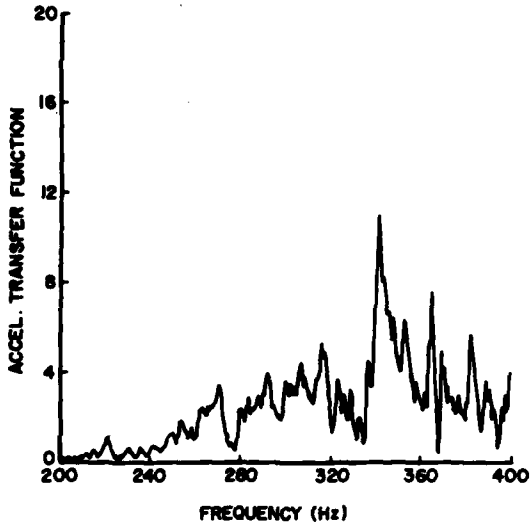

Figure 28. Transfer Function with Damping Treatment No. 3 Applied

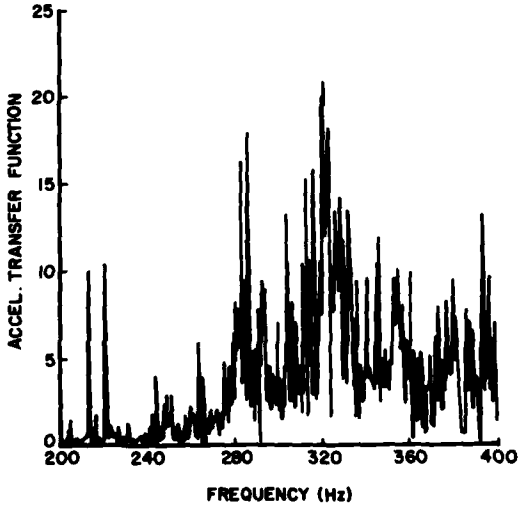

Figure 27. Transfer Function with Damping Treatment No. 2 Applied

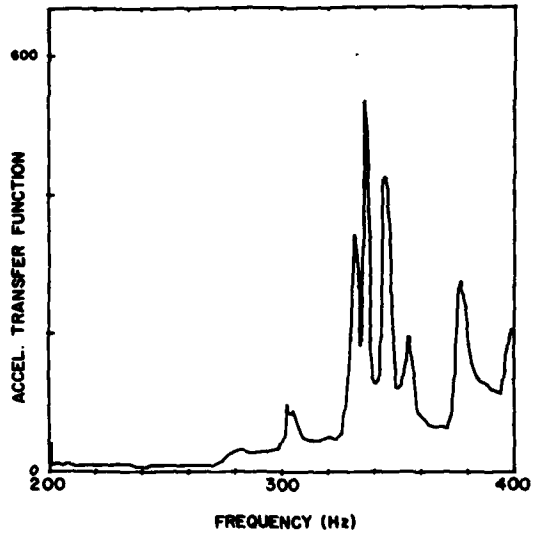

Figure 29. Transfer Function with Damping Treatment No. 4 Applied

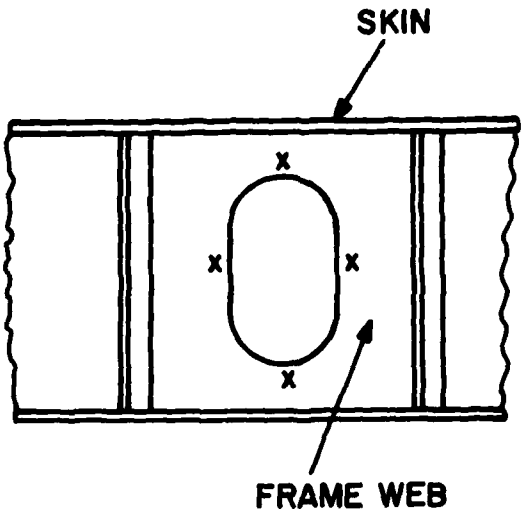

Figure 30. Placement of Tuned Dampers

VI. SUMMARY AND CONCLUSIONS

The results obtained, to date, during this on-going investigation demonstrate some of the advantages of using impact testing techniques, with digital data processing, through a Fourier analyzer consisting of a minicomputer and appropriate software to conduct discrete fast Fourier transform and modal analysis. Comparisons of data obtained utilizing digital techniques with data obtained from sine sweep tests show that measured resonant frequencies and modal damping are essentially the same for either method. Digital techniques have the advantage of being much faster, coupled with a capability of being able to immediately evaluate the quality of the measured data through observation of the coherence function. In addition, two and three dimensional mode shape information can be rapidly obtained and conveniently displayed. It was found that three dimensional animated mode shapes were of great value in determining where, and which type, of damping treatments are most appropriate for effective damping of structures having fairly complex geometry.

Test results, to date, indicate that the most effective way to damp the modes of this structure, which are of interest from a sonic fatigue standpoint, is to have damping treatments applied to the skin, to the frame webs, and to the straps. This necessitates three different material systems, since each of these components is expected to have different operating temperature ranges. Tests are presently underway to evaluate appropriate damping treatments for each temperature range. Different damping materials, as well as highly efficient graphite-epoxy constraining layers and appropriate adhesive systems, are being investigated for their damping effectiveness at the expected temperature, and possible degradation resulting from long term exposure to fuel and moisture environments.

ACKNOWLEDGEMENTS

This work was sponsored by the Metals Behavior Branch of the Air Force Materials Laboratory, in part under Contract AF33615-73-C-5028 with the University of Dayton Research Institute. The authors wish to acknowledge inputs from several individuals including assistance with the software by Mr. Al Peter and Mr. Ray Zimmerman of Structural Dynamics Research Corporation, as well as assistance with the experiments by Mr. Charles Cannon of the University of Dayton Research Institute and Mr. Robert Gordon, formerly with Air Force Materials Laboratory, now with Air Force Flight Dynamics Laboratory. Dr. David I. G. Jones assisted with the editing of the manuscript. Manuscript was typed by Louise Farren.

REFERENCES

1. Bendat, J.A., and Piersol, A.G., Measurement and Analysis of Random Data, John Wiley and Sons, New York, 1966.

2. Klosterman, A.L., "On the Experimental Determination and Use of Modal Representations of Dynamic Characteristics," Ph.D. dissertation, University of Cincinnati, 1971.

3. Langhaar, H.L., Energy Methods in Applied Mechanics, John Wiley and Sons, New York, pp 138, 1962.

4. Morse, I.E., Shapton, W.R., and Brown, D.L., "Applications of Pulse Testing for Determining Dynamic Characteristics of Machine Tools," presented at 13th International Machine Tool Design and Research Conference, University of Birmingham, Birmingham, England, 1972; published as part of Application Note 140-3, Hewlett-Packard Company.

5. Informal communication with D.L. Brown, Mechanical Engineering Department, University of Cincinnati, 1973.

6. Peter, A.F., "Impact Transfer Function and Mode Shape Keyboard Program for the Hewlett-Packard 5451A Digital Fourier Analyzer," Structural Dynamics Research Corporation, Cincinnati, Ohio, 1972.

7. "Animated Three Dimensional Mode S Shape Program for 4551A Digital Fourier Analyzer," Structural Dynamics Research Corporation, Cincinnati, Ohio, 1973.

Discussion

Mr. Caruso: (Westinghouse Product Qualification Laboratory) Was all of your testing done using a sinusoidal input?

Mr. Drake: No the testing was done with impact. We have what we call a "calibrated hammer" with a force gage; we would impact the structure at one point and simultaneously measure the acceleration output and the force input during the impact, digitize this data, and fourier transform it which would then put you into the frequency domain. We use no sine sweep testing at all, other than for a comparison to see that our digital data was accurate.

Mr. Caruso: We have a similar system at the lab now that we have been using and we have been running some modal analyses primarily of our vibration test fixtures, as well as a couple of systems. We have been running some tests mostly as a selling point to designers engineers and we are trying to show that the random testing and sinusoidal testing are equivalent using some of the digital techniques.

Mr. Drake: We have found that to be true. We have run comparisons where we use what they call the "DAK", which is a Digital to Analog Output, and we can control shakers. We have run Digital to Analog Output (DAK) tests, the typical magnetic transducer or shaker type sinusoidal sweep tests, and impact tests; we have compared the data and the comparison is unbelievable.

Mr. Caruso: Were the data that you obtained from the sine sweep and the random burst tests virtually equivalent?

Mr. Drake: Yes.

Mr. Stroud: (Lockheed Missiles & Space Co.) The response plots indicated that your modes were well isolated which simplified determining the mode shapes. What kind of luck have you had with this technique in dealing with multiple mode response, where the modes were closely spaced?

Mr. Henderson: You are right, the technique for fitting a circle in the nyquist plot will not work if your modes are closely coupled. We have resorted to a comparison of a level of the transfer function for the evaluation of the effectiveness of the damping treatment on the more complicated structures in this particular investigation; there are techniques available for curve fitting closely coupled modes to various mathematical models and we have tried some of these. The most successful techniques that we are aware of use a complex normal mode analysis. They curve fit the transfer function data to a number of complex normal modes in order to synthesize the behavior, they use this to derive the modal damping; this is the only way that I am aware of that you can obtain the modal damping if you have really closely coupled modes. This technique works if we can obtain something like eight data points around a resonance that we can curve fit, and those frequency points are typically separated by either 1 Hz or ½ Hz, so that we can handle fairly closely coupled modes; but if they are really closely coupled, or if the system is highly damped, you cannot sort out the modal damping with this nyquist plot.

Mr. Drake: I think we are missing part of your question about the mode shapes. I picked out something that was very simple and clean in

the transfer function data that I have shown and it only had one mode; but in the mode shapes that you have seen, I didn't make it as evident as I should have, we had nine modes between 212 Hz and 354 Hz. I don't know if you consider that closely packed modes or not, but for the closely packed modes it doesn't really make too much difference, for the mode shapes alone because if you are interested in a particular resonant frequency, and if there are modes or frequencies that are two or three Hz apart, you can examine them individually.

Mr. Stroud: You would need a sufficient number of data points between the resonances such as the eight points that you mentioned.

Mr. Drake: This is for damping. I don't think you would need that many data points for the mode shapes.

Mr. Stroud: Then you wouldn't use the quadrature response you would plot the diameter of the circle.

Mr. Henderson: The quadrature response has a tendency to decouple this. The quadrature response on coupled modes is closer to a normal mode than the actual magnitude of the complex response. There are some very good treatments of this subject, Dave Brown at the University of Cincinnati has been discussing this lately. We are also looking at the quadrature response mode shapes.

Mr. Stroud: What did you use for displaying the mode shapes?

Mr. Drake: The display was just an ordinary oscilloscope.

Voice: Do you expect the third mode involving frame twisting to be symmetrical?

Mr. Drake: I think if you had an ideal structure it would be, but I have never seen one put together so that its motion was symmetrical.

Mr. Caruso: I just wanted to make a quick point in response to the gentleman's question on isolating very closely spaced modes. We have a setup similar to yours and just from the visual interpretations end of it you can pick out modes as closely as you want by limiting the test and analysis frequency bands. Without going into specific equipment terms we have been able to visually isolate modes that are ½ Hz and 1 Hz apart; the numerical data would be in the form of a printout but you can go as close as you want. You would be limited by the quality of your data, I think, with that type of digital set up.

AN ALTERNATIVE SYSTEM FOR MEASURING COMPLEX DYNAMIC MODULI OF DAMPING MATERIALS (U)

David I. G. Jones
Air Force Materials Laboratory
Wright-Patterson AFB, Ohio 45433

In this paper, a simple technique for measuring complex dynamic moduli of damping materials is described and evaluated. The system consists of a rigid rod supported at both ends by two metallic flexural springs, with the damping material specimen placed between the center of the rod and a rigid surface. The rod is then excited horizontally, and the effect of the material specimen on the dynamic response behavior measured. Results obtained by this technique are compared with those obtained using the well established vibrating beam techniques. The results indicate that this "rocking beam" technique can be used to accurately measure Young's moduli of the specimen material from over 10^6 Lb/in^2 (6.87×10^9 N/m^2) to less than 10^4 Lb/in^2 (6.87×10^7 N/m^2), possibly as low as 10^3 Lb/in^2 (6.87×10^6 N/m^2).

INTRODUCTION

(U) The well established vibrating beam techniques [1-4] have been used for many years to measure complex extensional moduli of elastomeric materials. The normal range over which reliable data is readily obtainable is from a modulus of 10^7 Lb/in^2 (6.87×10^{10} N/m^2) to 10^5 Lb/in^2 (6.87×10^8 N/m^2), while moduli of less than 10^4 Lb/in^2 (6.87×10^7 N/m^2) can be measured on occasion if extreme care is taken. Values below this cannot be regarded as valid in general, even if the results appear to be self consistent. The advantages of the vibrating beam techniques are simplicity and the fact that data for several frequencies can be obtained for a single specimen at each test temperature. One major disadvantage is that for low moduli of the damping material, error magnifications are large so that apparently consistent but nevertheless erroneous data is then readily obtained. It is not easy to overcome this difficulty, and other techniques are then resorted to [3, 5-7]. Another disadvantage of the vibrating beam technique is the fact that the excitation and pickup transducers must be close to the beam in order to interact effectively. This limits the temperature range over which data can be obtained, especially at the high temperature end.

The technique being evaluated in this paper does not overcome all of these difficulties, and even loses the advantage of obtaining data for several frequencies at each temperature because it is essentially a single degree of freedom system. However, the specimen can be heated to any degree within the limitations of the materials used, while the pickup and excitation transducers are safely outside. The tests reported herein involved a relatively low temperature damping material, so that no special protective measures had to be taken in regard to the transducers. However, for tests on very high temperature enamels, epoxies and elastomers, such protection would be essential. The tests conducted on this low temperature material show that satisfactory results can be obtained by the technique over a wide range of conditions and that the accept/reject criteria for reliable data are simple to apply.

ANALYSIS

The test system being analyzed is illustrated in Figure 1. The rigid metal rod is supported and restrained at each end by a flexible metal spring and the material specimen being evaluated is placed between the center of the rod and a rigid surface. The rod is then excited at one end and the response picked

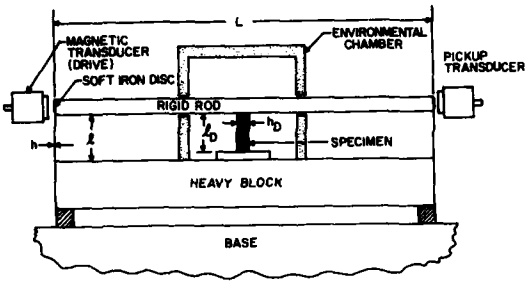

Figure 1. Rocking beam test system

up at the other. In this way, the excitation and pickup transducers are well separated and are, or can be, kept outside the environmental chamber or furnace so that the specimen can be taken to higher temperatures than the transducers can normally withstand. This is a most significant advantage.

Consider, now, the deformation of the system in the longitudinal direction, as illustrated in Figure 2. The flexural stiffness of

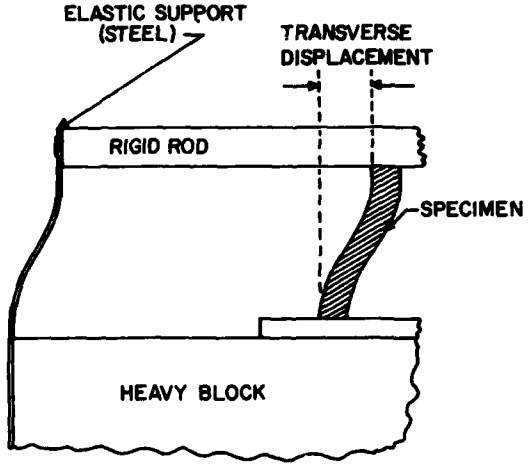

Figure 2. Deformed specimen

each end spring provides an equivalent spring opposing the motion of the rod, of magnitude $12EI/\ell^3$ according to classical beam theory under static conditions [8]. The specimen stiffness, by the same token, is $12E_D^*I_D/S\ell_D^3$, where S is a shape factor to account for the fact that the specimen may not be a thin beam in the classical sense. S has yet to be determined, but can be expected to be unity for $h_D/\ell_D \ll 1$ and increase rapidly as the specimen becomes thicker. The net stiffness of the system in the longitudinal direction is, therefore:

$$k^* = 24EI/\ell^3 + 12E_D^*I_D/S\ell_D^3 \qquad (1)$$

The net mass of the system is equal to the sum of the mass of the rod, m_r, and the equivalent mass m_e of each end spring. The specimen mass may usually be neglected unless the rod is very light; indeed the mass of the end springs may also be neglected in many cases. The effective mass of each end spring can be calculated by first calculating the static deformation at each point along the flexural spring for zero displacement and slope at the lower end and zero slope but finite displacement at the other end and, secondly, calculating the total kinetic energy and comparing terms. The result is:

$$m_e = (13/35)\, m_b \qquad (2)$$

where m_b is the actual mass of the length ℓ of the flexural spring and m_e is the equivalent mass if all were concentrated at the rod end. Since the system behaves, to a degree of approximation, as a single degree of freedom system, we may write the equation for the resonant frequency in the form $\omega^2 = \mathrm{Re}(k^*)/m$. Hence, for the undamped system:

$$\omega_o^2 = 24EI/\ell^3 m \qquad (3)$$

and, for the damped system:

$$\omega_D^2 = 24EI/m\ell^3 + 12E_DI_D/mS\ell_D^3 \qquad (4)$$

where $m = m_r + (26/35)\, m_b$. Therefore:

$$Z^2 = (\omega_D/\omega_o)^2$$

$$= 1 + (E_D/E)(I_D/I)(\ell/\ell_D)^3/2S \qquad (5)$$

$$\therefore E_D = m\omega_o^2(\ell_D/h_D)^3\, S\,(Z^2 - 1) \qquad (6)$$

where $I_D = bh_D^3/12$ and $I = bh^3/12$. From equation 1, the loss factor η_s is deduced by taking the ratio of the imaginary to the real part of the stiffness k^*:

$$k^* = 24EI/\ell^3 + 12E_DI_D/S\ell_D^3$$

$$+ 12iE_D\eta_DI_D/S\ell_D^3$$

$$\therefore \eta_s = (12E_D\eta_DI_D/S\ell_D^3)/(24EI/\ell^3 + 12E_DI_D/S\ell_D^3)$$

$$\therefore \eta_D = \eta_s/(1 - 1/Z^2) \qquad (7)$$

using equation 5. From the measured resonant frequencies ω_D and ω_o, and the measured loss factor η_s, one can therefore use equations 6 and 7 to determine the material modulus E_D and loss factor η_D. η_s can be measured using the "half-power bandwidth" method.

The shape factor S can be calculated for a particular section by finite element techniques or, approximately, by means of classical two-dimensional elasticity theory. While exact results are not readily available in the literature, the limiting case of a very thick specimen, for which shear effects are dominant, is [9]. In this reference, a correction factor is given for a shear specimen to allow for bending effects, which is valid for h_D/ℓ_D ratios as low as 1.0. Transposing this correction into a correction for bending instead of shear is then easily shown to give:

$$S = 3(h_D/\ell_D)^2 (1 + 2h_D^2/\ell_D^2) \qquad (8)$$

This result is valid for $h_D/\ell_D \geq 1.0$, i.e. for a square cross-section specimen. For $h_D/\ell_D < 1.0$, bending effects become progressively more important and S approaches the limiting value of 1.0 for $h_D/\ell_D = 0$. Comparison with experimental results will be discussed in the next section.

EXPERIMENTAL INVESTIGATIONS

Vibrating Beam Tests

In order to establish the validity and usefulness of the "rocking-beam" technique, it was necessary to compare the results with those obtained by a well established technique, such as the vibrating cantilever beam with the damping material coated symmetrically on both sides as shown in Figure 3 [2]. The beam was excited by a magnetic transducer near the root. Typical measured loss factor and resonant frequency data for the first three modes is shown in Table I, for thickness ratio $n = h_D/\ell_D = 0.449$ of a typical room temperature range damping material [10]. The beam was 7 inches long (177.8 mm), 0.078 inches thick (1.98 mm) and 0.45 inches wide (11.43 mm). The data was reduced in the usual manner, by means of the equations [2]:

$$E_D = E(Z_o^2 - 1)/(8n^2 + 12n + 6) \qquad (9)$$

$$\eta_D = \eta_s/(1 - 1/Z_o^2) \qquad (10)$$

Some of the results are shown in Figures 4 and 5, as graphs of E_D and η_D versus frequency at several temperatures, based on interpolated

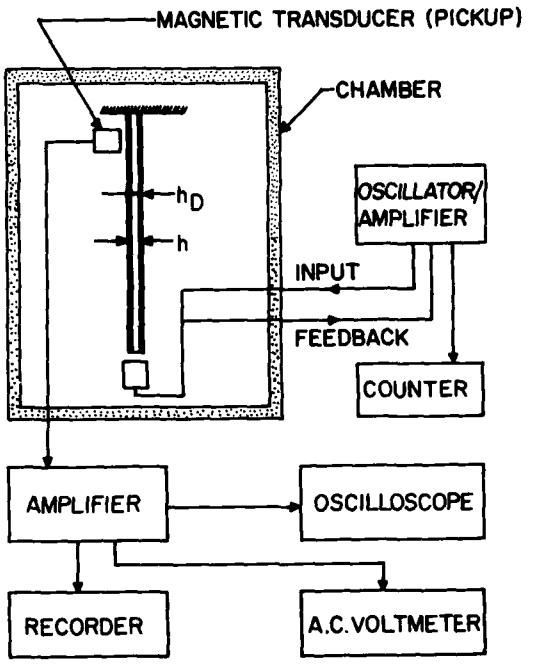

Figure 3. Vibrating beam test system

values of ω_D, ω_o and η_s from Table I. The data was subject to the limitation that when $Z_o^2 - 1$ becomes equal to or less than 0.1 the results are unreliable [2]. For this reason, no data was obtained for the higher temperatures.

Static Deformation Tests to Determine S

In order to determine S, the simple test system illustrated in Figure 6 was used. The length ℓ_D of the soft rubber specimen was varied from 1.0 inches (25.4 mm) to 0.25 inches (6.35 mm), by successively cutting the specimen and re-gluing. The load was applied in successive steps, and then released by the same steps, and the process repeated several times. Typical results are shown in Figure 7, as graphs of load versus deformation. Since the same specimen material was used in each test, the values of S were readily derived from the observed stiffnesses. If it is assumed that S = 1.0 for the longest specimen, ℓ_D = 1.0 inches (25.4 mm), then it is easily shown that S = 1.09 for ℓ_D = 0.5 inches (12.7 mm) and S = 1.46 for ℓ_D = 0.25 inches (6.35 mm). These results are plotted as a graph of S versus h_D/ℓ_D in Figure 8, along with the limiting values discussed in the analysis.

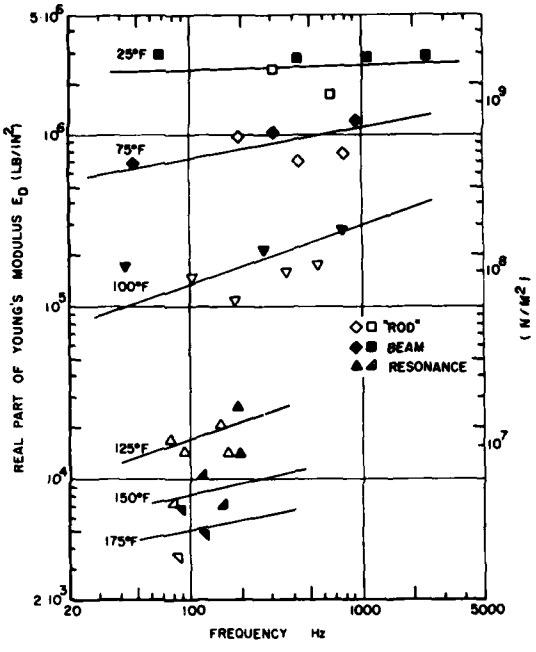

Figure 4. Graphs of E_D versus frequency at various temperatures

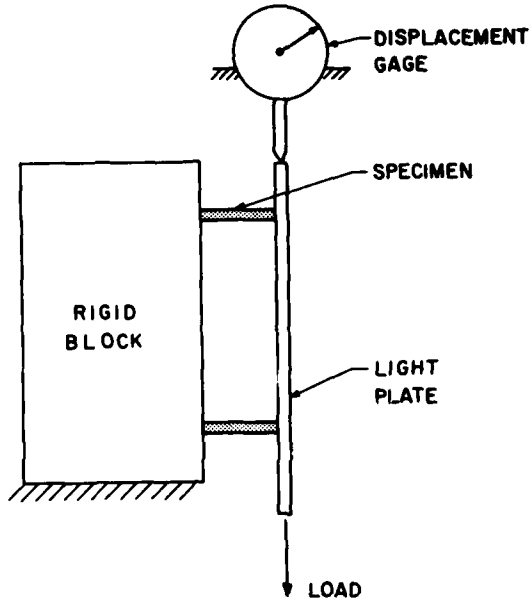

Figure 6. Static test system for measuring shape factor

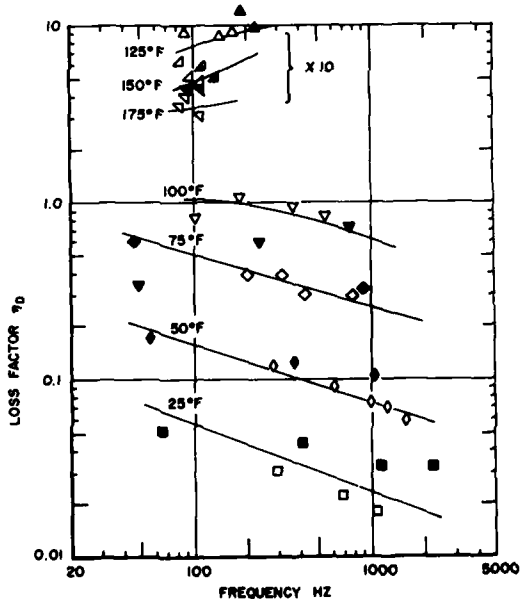

Figure 5. Graphs of η_D versus frequency at various temperatures

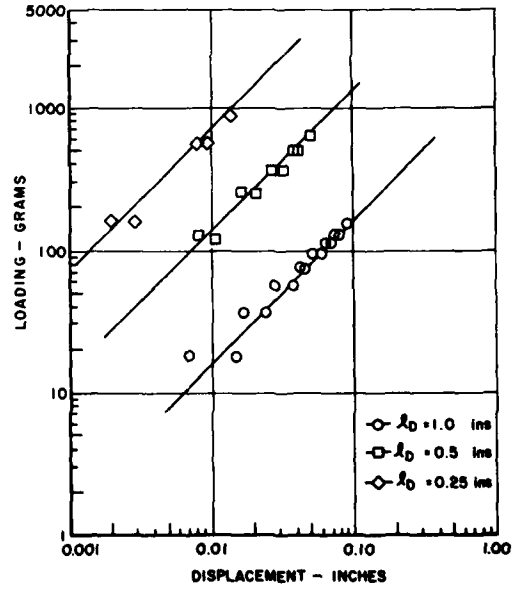

Figure 7. Load-deformation curves

TABLE I

Vibrating Beam Test Results

Temp °F	Mode	η_s	f_r (HZ)	f_o (HZ)
0	1	0.017	67.7	50.0
	2	0.013	416.8	312.7
	3	0.011	1168.5	876.9
25	1	0.032	65.8	49.8
	2	0.026	406.9	310.9
	3	0.020	1147.5	872.0
50	1	0.087	57.9	49.4
	2	0.067	370.0	308.9
	3	0.057	1061.6	866.3
75	1	0.172	47.5	49.1
	2	0.143	316.8	306.8
	3	0.133	914.1	860.5
100	1	0.033	41.8	48.7
	2	0.067	264.1	304.2
	3	0.105	753.4	853.2
125	1	0.013	41.4	48.1
	2	0.017	258.0	300.6
	3	0.033	715.8	843.2

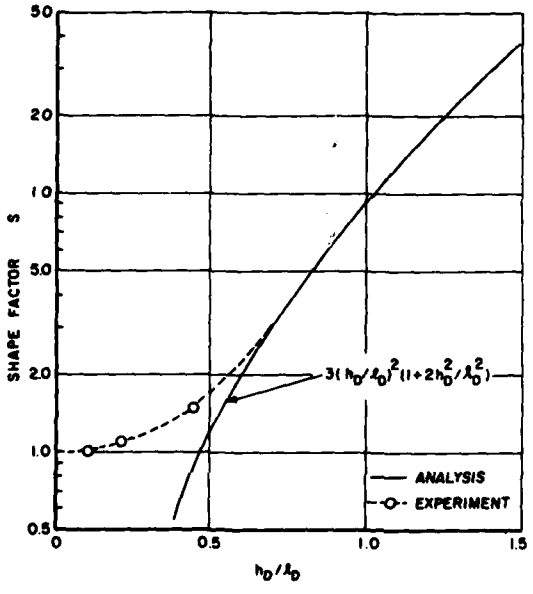

Figure 8. Graph of shape factor S versus h_D/ℓ_D

Rocking Beam Tests

In order to evaluate the effectiveness of the "rocking beam" test technique, it was necessary to restrict attention to specific specimen dimensions. After some trial and error, the following dimensions were found to be most convenient for the initial investigations; h = 0.01 inches (0.254 mm), ℓ = 7/8 inch (22.23 mm), b = 0.5 inches (12.7 mm), m_r = 43.03 grams and the thickness h_D of the specimen was varied from 0.077 inches (1.96 mm) to 0.454 inches (11.53 mm). Figure 9 illustrates the test system. Figure 10 shows the measured variation of η_s, f_D and f_o with temperature for the various values of h_D. From equations 6 and 7, it was then straightforward to calculate η_D and E_D, using the values of S obtained earlier. The results are shown in Figures 4 and 5. It is seen that the two techniques give comparable results over the entire temperature range over which reliable results are obtainable by both techniques. Figure 11 shows a typical undamped and a typical damped response spectrum.

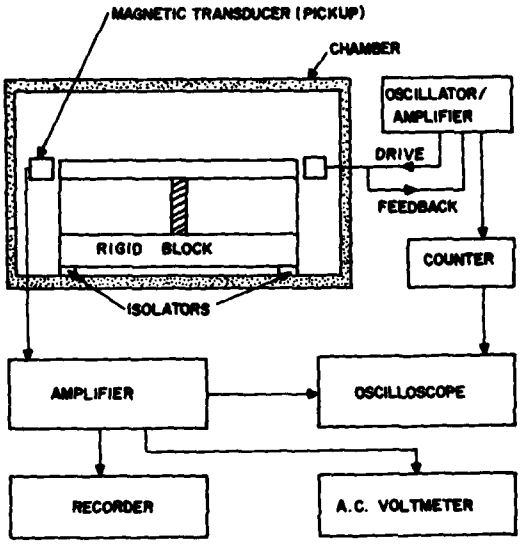

Figure 9. Rocking beam test system

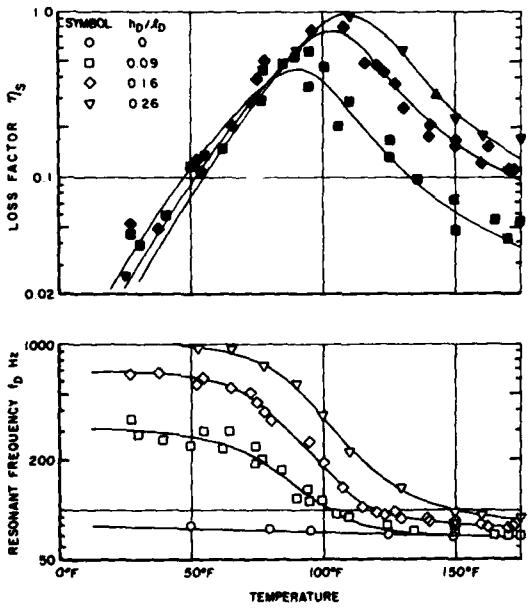

Figure 10. Graphs of η_s and f_D versus temperature

Resonance Tests

In order to complete the investigation, the complex modulus properties of the damping tile were also measured at high temperature using a simple resonance technique [3], utilizing the setup illustrated in Figure 12.

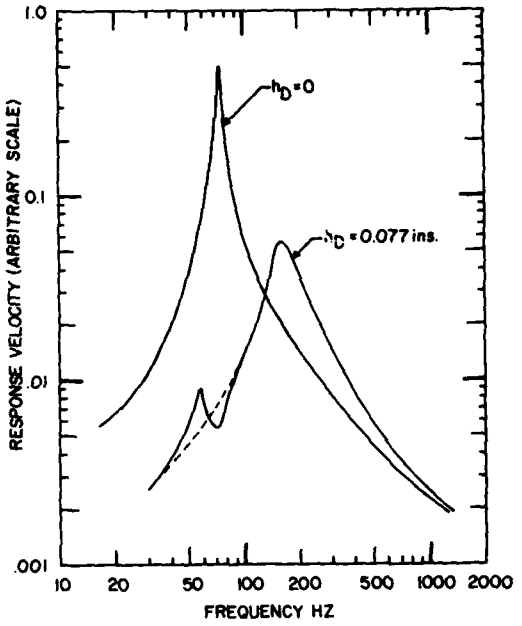

Figure 11. Typical dynamic response spectra

The values of E_D and η_D of the damping material were determined from the measured resonant frequency of the specimen and the system loss factor was determined by the half-power bandwidth method. The dimensions of the specimen were ℓ = 1.75 inches (44.5 mm), h_D = 0.085 inches (2.16 mm) and b = 0.5 inches (12.7 mm). Values of E_D and η_D were obtained at 125°F, 150°F and 175°F. The results are shown in Figures 4 and 5. It is seen that the resonance and rocking beam test results are in good agreement in the range where data is obtainable using both techniques.

Temperature-Frequency Reduction of Test Data

Following the procedure of reference [3], the data shown in Figures 4 and 5 has been reduced to graphs of E_D and η_D versus reduced frequency $f\alpha_T$ and of the shift factor α_T versus temperature, as shown in Figures 13 and 14. This procedure completes the characterization of the complex modulus properties of the particular elastomer tested utilizing three separate measurement techniques, and the results illustrate the consistency of the data obtained.

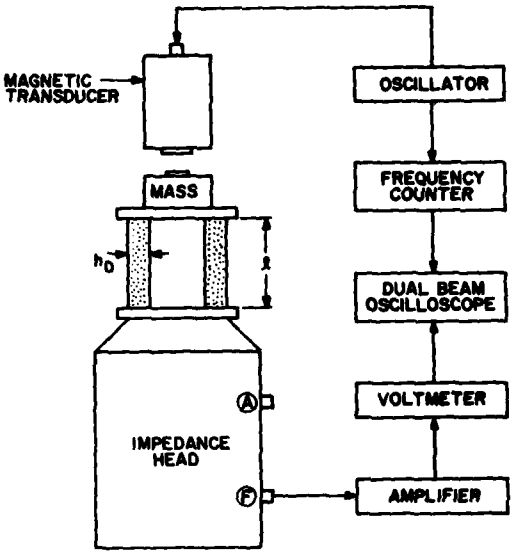

Figure 12. Resonance test system

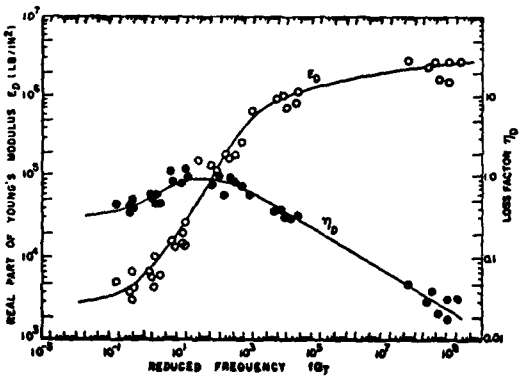

Figure 13. Graphs of E_D and η_D versus $f\alpha_T$

CONCLUSIONS

The tests described in this paper show that the rocking-beam technique represents a feasible approach toward accurately measuring the complex dynamic moduli of damping materials over a wide range of magnitudes. The method is easy to use over very broad temperature ranges, utilizes very simple electronic instrumentation, and does not require mass-cancellation circuitry as do some of the mechanical impedance and vibrating beam techniques for high temperature testing.

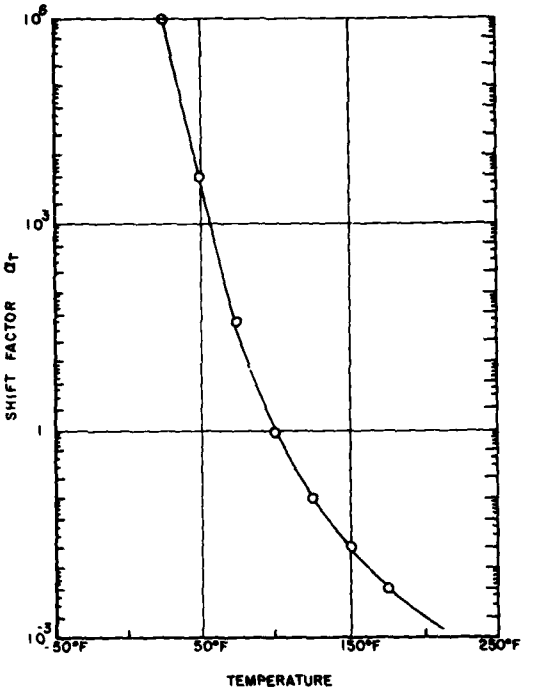

Figure 14. Graph of a_T versus temperature

ACKNOWLEDGMENTS

This effort was conducted under Project No. 7351, Task No. 735106 at the Air Force Materials Laboratory. Thanks are due to S. Askins for assistance with the electronic instrumentation, Sally Lindsay for typing the manuscript and Mr. DeMarey for preparing the figures.

REFERENCES

1. Oberst, H. and Frankenfeld, K., "Uber die Dampfung dunner Bleche durch Festhaltende Belage", Acustica, Vol. 2, Leaflet 4, 181-194, Part 1, 1952 and Part 2, 433, 1954.

2. Nashif, A. D., "New Method for Determining Damping Properties of Viscoelastic Materials", Shock and Vibration Bulletin 36, Part 4, 37-47, 1967.

3. Jones, D. I. G., "Temperature-Frequency Dependence of Dynamic Properties of Damping Materials", J. Sound and Vibration, 33(4), 451-470, 1974.

4. Dudék, T. J., "Damping-Material Effectiveness Measured by the Geiger-Plate

and Composite-Beam Tests", J. Acoustical Soc. of America, 46, 1384-1386, 1969.

5. Edwards, J. L. and Hicks, D. R., Useful Range of a Mechanical Impedance Technique for Measurement of Dynamic Properties of Materials", J. Acoustical Soc. of America, 3, Part 2, 1053-1056, 1971.

6. Eller, S. A. and Cohen, L., "Investigation of the Vibration Damping Properties of Viscoelastic Materials Using a Delay Angle Technique", Shock and Vibration Bulletin 35, 159-168, 1966.

7. Adkins, R. L., "Design Considerations and Analysis of a Complex Modulus Apparatus", Experimental Mechanics, 1966.

8. Bishop, R. E. D. and Johnson, D. C., "The Mechanics of Vibration", Cambridge University Press, 1960.

9. Seely, F. B. and Smith, J. C., Advanced Mechanics of Materials, John Wiley and Sons Inc., New York, 1952.

10. LD-400 damping tile, made by Lord Manufacturing Company, Erie, Pa.

NOMENCLATURE

b	Breadth of springs (uniform)
E_D	Real part of complex Young's modulus of damping material
E	Young's modulus of beam-like end springs
E_D^*	Complex Young's modulus of damping material $[= E_D(1+i\eta_D)]$
f_D	Resonant frequency of damped system
f_r	Resonant frequency of damped beam
f_o	Resonant frequency of undamped system
h	Thickness of end springs in rocking beam system or thickness of metal beam in vibrating beam system
h_D	Thickness of damping material
i	$\sqrt{-1}$
I	Flexural rigidity $(bh^3/12)$ of end-springs
I_D	Flexural rigidity of beam-like viscoelastic specimen $(bh_D^3/12)$
k^*	Complex stiffness of system
ℓ	Length of end springs
ℓ_D	Length of specimen
m	Effective mass of system
m_r	Mass of rod
m_e	Effective mass of end spring
m_b	Actual mass of end spring
n	Thickness ratio for beam specimen (h_D/h)
S	Shape factor
Z	Frequency ratio for rocking beam (ω_D/ω_o)
Z_o^2	Frequency parameter for vibrating beam $[= (\omega_r/\omega_o)^2 (1+\rho_D h_D/\rho h)]$
η_s	Loss factor of damped system
η_D	Loss factor of damping material
ρ_D	Density of damping material
ρ	Density of beam material
ω_o	Resonant frequency of undamped systems
ω_D	Resonant frequency of damped rocking beam system
ω_r	Resonant frequency of vibrating beam system in rth mode

DYNAMIC ANALYSIS

NONLINEAR VIBRATION OF CYLINDRICAL SHELLS UNDER RADIAL LINE LOAD

Steven S. Tang
Member of Technical Staff, B-1 Division
Rockwell International Corporation
Los Angeles, California

The nonlinear responses of a thin, cylindrical shell under radial line load sinusoidally distributed around the circumference is investigated using the large deflection theory for cylindrical shells given by Mushtari (1).

The equations of motion for the line load problem are solved by the series expansion technique in conjunction with Galerkin method. By taking a two-term periodic solution, the shell problem is transformed to a set of nonlinear equations of the Duffing type for a two-degrees-of-freedom system. The harmonic balance method (7, 8) is then applied to derive the frequency responses.

In accordance with Floquet theory (4), the stability of the solutions is investigated by the perturbation method (12, 13). The problem then reduces to the type of Mathieu equation from which the stability criteria are determined.

Numerical solutions for a specific cylindrical shell are presented graphically to demonstrate the application of various procedures of the analysis.

NOMENCLATURE

a = radius of cylinder

a_i = amplitude of response x_1, $i = 1,2,\ldots,n$, Eq. (31)

a'_j = amplitude of perturbed motion, $j = 0,1,2$, Eq. (49)

A_{mn} = response amplitude in radial direction for mode mn

$A_1 = A_{11}$

$A_2 = A_{12}$

b_j = amplitude of response x_2, $j = 0,1,2$, Eq. (31)

b'_i = amplitude of perturbed motion, $i = 1,2$, Eq. (49)

B_0 = parameter defined by Eq. (36)

B_{mn} = amplitude of stress function for mode mn

c_1, c_2, c_3 = geometric parameters defined by Eq. (28)

C = loading constant defined by Eq. (22)

$D = \frac{Eh^3}{12(1-\nu^2)}$ = flexual rigidity of shell

E = modulus of elasticity

f_{mn} = linear natural frequency of shell mode mn in cps

$f_{mn}(x, \Phi)$ = modal function of stress function defined by Eq. (12)

F = stress function defined by Eq. (5)

F_0 = equivalent additional force defined by Eq. (29)

F_i = amplitude of excitation $\bar{P}_i$, Eq. (30)

$\bar{F}_1 = F_1/\omega_1^2$

G = shear modulus

h = shell thickness

i = integers, 1 and 2, unless otherwise specified

k = integers, 1, 2,...,n = number of circumferential full waves of excitation; also $k = 1 - (c_2^2/\omega_1^2 c_3)$ in Eq. (85)

k_0, K_1, K_2 = shell geometric parameters defined by Eq. (22)

K = shell geometric parameter defined by Eq. (25)

L = shell length

m = mode number = number of half-sine waves in axial direction

$m_1 = 1 + \dfrac{c_2}{\omega_1^2}\left(1 - \dfrac{c_2}{c_3}\right)$ in Eq. (95)

$m_2 = \dfrac{2c_2}{\omega_1^2\sqrt{\epsilon'_2}}$ in Eq. (95)

M_β, M_x, M_Φ = bending moments

$M_{x\Phi}$ = twist moments

n = mode number = number of circumferential full waves

N_x, N_Φ = membrane forces

$N_{x\Phi}$ = inplane shearing forces

p = maximum value of m

p' = coefficient in the cubic equation (82)

p_i = coefficient in the stability characteristic Eq. (56)

P_z = external load in z-direction

P = amplitude of P_z, Eq. (8)

P_m = time function of external load

= coefficient of Fourier series, Eq. (17)

$\bar{P}_i$ = forcing function defined by Eq. (25)

q = maximum value of n, also coefficient in Eq. (74)

q' = coefficient in Eq. (82)

q_i = constant term in stability characteristic equation (56)

Q = geometric constant defined by Eq. (25)

Q_x, Q_Φ = normal shearing forces

r = ω_2/ω_1 = natural frequency ratio

R = ω/ω_1 = forcing frequency ratio

s = $a\phi$ = circumferential coordinate of cylindrical shell

S = surface area of shell

t = time

u,v,w = displacements of shell middle surface

W_{mn} = shell modes in Eq. (10)

x = axial coordinate of cylindrical shell

x_i = shell responses defined by Eq. (31)

X_i = response amplitudes in Eq. (32)

$\bar{X}_1 = \sqrt{\epsilon'_1}\, X_1$, Eq. (78)

$X'_i = \sqrt{\epsilon'_i}\, X_i$, Eq. (79)

z = radial coordinate of shell

α, β = phase angles of x_1 and x_2 with respect to forcing function

α_m, β_n = frequency parameters in Eq. (27)

$\delta(x-x_0)$ = Dirac delta function in Eq. (8)

δf_{mn} = variation of the stress function f_{mn}

δx_i = variation of response x_i

δW_{mn} = variation of mode W_{mn}

$\epsilon_1, \epsilon_2, \gamma_{12}$ = bending and shear strains of shell middle surface

$\bar{\epsilon}_1 = c_1/\omega_1^2$

$\epsilon_1' = \left(3c_1 + c_3/r^2\right)/\omega_1^2$

$\epsilon_2' = \left(3c_1 r^2 + c_3\right)/\omega_1^2 = r^2 \epsilon_1'$

ζ = characteristic exponent of perturbed motion in Eq. (49)

μ = mass per unit area of shell

ν = Poisson's ratio

$\tau = \omega t$

Φ = angular coordinate of cylindrical shell

$\phi(t), \psi(t)$ = periodic function of time in Eq. (31)

$\lambda_1, \lambda_2, \gamma_{1c}, \gamma_{1s}, \gamma_{2c}, \gamma_{2s}, \eta_c, \eta_s, \psi, \sigma_c,$

σ_s, ξ_c, ξ_s = stability parameters in Eq. (47)

$\bar{\lambda}_1 = \lambda_1 - 1$

$\bar{\gamma}_1^2 = \gamma_{1c}^2 + \gamma_{1s}^2$

$\eta^2 = \eta_c^2 + \eta_s^2$

$\chi_1, \chi_2, \chi_{12}$ = changes of curvature of shell middle surface, Eq. (3)

ω = angular forcing frequency

ω_i = natural frequency of shell

$$\bar{\omega}_1 = \left[\omega_1^2 - \frac{c_2^2}{c_3}\right]^{1/2}$$

INTRODUCTION

Thin cylindrical shells are often used as substructures or components of aerospace vehicles. In some cases, these shell structures, serving as fuel or gas tanks, are installed inside a large shell. During various operational or test conditions, vibratory motions may be excited in the primary structure. The radial component of the vibration will then transmit inward through ring frames or bulkhead supports to the internal shell in the form of radial excitation which is periodic around the circumference of the internal shell. This constitutes the dynamic problem of a thin elastic cylindrical shell under radial line load sinusoidally distributed around the circumference. This paper presents an analytical solution to the forced response of the shell under such a dynamic line load.

LARGE DEFLECTION OF CYLINDRICAL SHELLS

Since the shell is thin, the radial deflection under this type of load may not be small in comparison with the shell thickness. Therefore, the large deflection theory for elastic shells (1, 2) is used for the analysis.

The basic assumptions are the following:

1. The shell is made of linear elastic material. Hooke's law holds for the stress-strain relationship.

2. The small quantities of the transverse shear deformation and the stress normal to the middle surface of the shell are neglected, in accordance with Kirchhoff-Love hypothesis.

For a cylindrical shell with its geometry and coordinates as shown in Fig. 1, the large deflection theory gives the following equations:

Strain components of a lamina at a distance z from the middle surface,

$$\epsilon_x = \epsilon_1 + z\chi_1$$

$$\epsilon_\Phi = \epsilon_2 + z\epsilon_2$$

$$\gamma_{x\Phi} = \gamma_{12} + 2z\chi_{12} \qquad (1)$$

a = radius of the cylinder

L = length of the cylinder

x = axial coordinate

Φ = angular coordinate

s = a Φ = circumferential coordinate

z = radial coordinate, positive outward

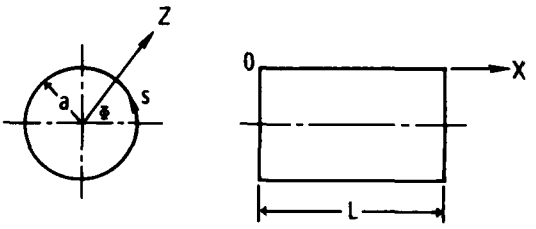

Fig. 1 - Geometry and coordinates of a cylindrical shell

Strain components of the middle surface,

$$\epsilon_1 = \frac{\partial u}{\partial x} + \frac{1}{2}\left(\frac{\partial w}{\partial x}\right)^2$$

$$\epsilon_2 = \frac{\partial v}{a\,\partial \Phi} + \frac{w}{a} + \frac{1}{2}\left(\frac{\partial w}{a\,\partial \Phi}\right)^2$$

$$\gamma_{12} = \gamma_{21} = \frac{\partial v}{\partial x} + \frac{\partial u}{a\,\partial \Phi} + \frac{1}{a}\frac{\partial w}{\partial x}\frac{\partial w}{\partial \Phi} \qquad (2)$$

Changes of curvature of the middle surface,

$$\chi_1 = -\frac{\partial^2 w}{\partial x^2}, \qquad \chi_2 = -\frac{\partial^2 w}{a^2 \partial \Phi^2},$$

$$\chi_{12} = -\frac{\partial^2 w}{a\,\partial x \partial \Phi} \qquad (3)$$

The relations between the membrane forces and strains, and between the moments and curvatures are the same as those for the linear case (3).

Based on Vlasov's engineering theory for shallow cylindrical shells, the equations of equilibrium are

$$\frac{\partial N_x}{\partial x} + \frac{\partial N_{x\Phi}}{a\,\partial \Phi} = 0$$

$$\frac{\partial N_{x\Phi}}{\partial x} + \frac{\partial N_\Phi}{a\,\partial \Phi} = 0$$

$$D\nabla^4 w - N_x \frac{\partial^2 w}{\partial x^2} - \frac{2}{a} N_{x\Phi} \frac{\partial^2 w}{\partial x \partial \Phi} - N_\Phi \left(\frac{\partial^2 w}{a^2 \partial \Phi^2} - \frac{1}{a}\right) - P_z = 0 \qquad (4)$$

where

$$\nabla^4 = \left(\frac{\partial^2}{\partial x^2} + \frac{\partial^2}{a^2 \partial \Phi^2}\right)^2$$

By introducing a stress function F defined in such a way that

$$N_x = \frac{\partial^2 F}{a^2 \partial \Phi^2}, \quad N_\Phi = \frac{\partial^2 F}{\partial x^2},$$

$$N_{x\Phi} = N_{\Phi x} = -\frac{\partial^2 F}{a\,\partial x \partial \Phi} \qquad (5)$$

the equations of equilibrium can be transformed into two nonlinear differential equations in terms of F and w.

$$D\nabla^4 w - \frac{\partial^2 F}{a^2 \partial \Phi^2}\frac{\partial^2 w}{\partial x^2} + \frac{2}{a^2}\frac{\partial^2 F}{\partial x \partial \Phi}\frac{\partial^2 w}{\partial x \partial \Phi} - \frac{\partial^2 F}{\partial x^2}\left(\frac{\partial^2 w}{a^2 \partial \Phi^2} - \frac{1}{a}\right) = P_z$$

$$\nabla^4 F - Eh\left[\left(\frac{\partial^2 w}{a\,\partial x \partial \Phi}\right)^2 - \frac{\partial^2 w}{\partial x^2}\left(\frac{\partial^2 w}{a^2 \partial \Phi^2} - \frac{1}{a}\right)\right] = 0 \qquad (6)$$

The second equation is the condition of the compatibility of deformations derivable from Eqs. (2), (3), and (5) in conjunction with the force, moment, and strain relations.

EQUATIONS OF MOTION

The equations of motion for a cylindrical shell under a radial dynamic load $P_z(t)$ can be obtained by replacing the static load P_z in Eq. (6) by the combined inertia and external load.

$$D\nabla^4 w - \frac{\partial^2 F}{a^2 \partial \Phi^2}\frac{\partial^2 w}{\partial x^2} + \frac{2}{a^2}\frac{\partial^2 F}{\partial x \partial \Phi}\frac{\partial^2 w}{\partial x \partial \Phi} - \frac{\partial^2 F}{\partial x^2}\left(\frac{\partial^2 w}{a^2 \partial \Phi^2} - \frac{1}{a}\right) + \mu \frac{\partial^2 w}{\partial t^2} = P_z(t)$$

$$\nabla^4 F - Eh\left[\left(\frac{\partial^2 w}{a\,\partial x \partial \Phi}\right)^2 - \frac{\partial^2 w}{\partial x^2}\left(\frac{\partial^2 w}{a^2 \partial \Phi^2} - \frac{1}{a}\right)\right] = 0 \qquad (7)$$

The radial line load applied to the cylindrical shell is defined as

$$P_z(x, \Phi, t) = P(t)\delta(x-x_0)\sum_{k=1}^{n} \cos k\Phi \qquad (8)$$

where

$P(t)$ = load amplitude, a function of time

$k = 1, 2, 3, \ldots, n$ = number of circumferential waves

x_0 = axial location of loading

$\delta(x-x_0)$ = Dirac delta function having the following property:

$$\int \delta(x-x_0)dx = \begin{cases} 1, & \text{if } x = x_0 \\ 0, & \text{if } x \neq x_0 \end{cases}$$

This forcing function is sinusoidally distributed around the circumference of the cylinder. Its amplitude, P(t), having the dimension of force per unit length, varies with time periodically.

Rewriting Eq. (7) and making use of Eq. (8), the equations of motion are as follows:

$$D\nabla^4 w - \frac{\partial^2 F}{a^2 \partial \Phi^2}\frac{\partial^2 w}{\partial x^2} + \frac{2}{a^2}\frac{\partial^2 F}{\partial x \partial \Phi}\frac{\partial^2 w}{\partial x \partial \Phi} - \frac{\partial^2 F}{\partial x^2}\left(\frac{\partial^2 w}{a^2 \partial \Phi^2} - \frac{1}{a}\right) + \mu \frac{\partial^2 w}{\partial t^2} - P(t)\delta(x-x_0)\sum_{k=1}^{n} \cos k\Phi = 0$$

$$\nabla^4 F - Eh\left[\left(\frac{\partial^2 w}{a\,\partial x \partial \Phi}\right)^2 - \frac{\partial^2 w}{\partial x^2}\left(\frac{\partial^2 w}{a^2 \partial \Phi^2} - \frac{1}{a}\right)\right] = 0 \qquad (9)$$

SOLUTIONS

The solutions of Eq. (9) can be assumed in the form of a series as

$$w(x, \Phi, t) = \sum_{m}^{\infty}\sum_{n}^{\infty} A_{mn}(t)W_{mn}(x, \Phi)$$

$$F(x, \Phi, t) = \sum_{m}^{\infty}\sum_{n}^{\infty} B_{mn}(t)f_{mn}(x, \Phi) \qquad (10)$$

where

$m, n = 1, 2, 3, \ldots$

$A_{mn}(t)$, $B_{mn}(t)$ = time functions of the response

$W_{mn}(x, \Phi)$ = shell modes

and

$f_{mn}(x, \Phi)$ = stress function depended only on shell coordinates

For practical problems, only a definite number of terms in the series (10) are considered. Hence,

$$w(x, \Phi, t) = \sum_{m}^{p}\sum_{n}^{q} A_{mn}(t)W_{mn}(x, \Phi)$$

$$F(x, \Phi, t) = \sum_{m}^{p}\sum_{n}^{q} B_{mn}(t)f_{mn}(x, \Phi) \qquad (11)$$

where p, q = maximum value of m and n, respectively.

For a cylindrical shell simply supported at both ends, the mode shapes and stress function are assumed as

$$W_{mn}(x, \Phi) = \sin \frac{m\pi x}{L} \cos n\Phi$$

$$f_{mn}(x, \Phi) = \sin \frac{m\pi x}{L} \cos n\Phi \qquad (12)$$

These functions satisfy the following boundary conditions exactly; namely, at both ends, $x = 0$ and $x = L$,

$$w = 0, \quad v = 0, \quad N_x = 0, \text{ and } M_x = 0 \qquad (13)$$

But they do not satisfy the equations of motion (9). In order to solve the problem in an approximate manner, it is convenient to apply the Galerkin method.

According to this method, the following integrations are performed over the entire surface, S, of the shell:

$$\int_S \int [\text{Equation (9a)}]\, \delta W_{mn} dS = 0$$

$$\int_S \int [\text{Equation (9b)}]\, \delta f_{mn} dS = 0 \qquad (14)$$

where $dS = ad\Phi dx$; δW_{mn} and δf_{mn} are the variations of the mode shape and stress function, respectively, and are defined as

$$\delta W_{mn} = \frac{\partial w}{\partial A_{mn}} = W_{mn}(x, \Phi)$$

$$= \sin \frac{m\pi x}{L} \cos n\Phi$$

$$\delta f_{mn} = \frac{\partial F}{\partial B_{mn}} = f_{mn}(x, \Phi)$$

$$= \sin \frac{m\pi x}{L} \cos n\Phi \qquad (15)$$

The forcing function (8) must be transformed to series form before substitution into Eq. (14).

$$P_z(x, \Phi, t) = \sum_m^p \sum_n^q P_m(t) \sin \frac{m\pi x}{L} \cos n\Phi \qquad (16)$$

where the time function $P_m(t)$ is determined by the following equation:

$$P_m(t) = \frac{\int_S \int P_z(x, \Phi, t)\, W_{mn}(x, \Phi)\, dS}{\int_S \int W_{mn}^2(x, \Phi)\, dS}$$

or

$$P_m(t) = \frac{P(t) \int_0^{2\pi} \int_0^L \sin \frac{m\pi x}{L} \delta(x - x_0) \sum_k^n \cos k\Phi \cos n\Phi\, dx d\Phi}{\int_0^{2\pi} \int_0^L \sin^2 \frac{m\pi x_0}{L} \cos^2 n\Phi\, dx d\Phi}$$

$$= \frac{2}{L} P(t) \sin \frac{m\pi x_0}{L} \qquad (17)$$

By substituting Eq. (17) into Eq. (16), the forcing function becomes

$$P_z(x, \Phi, t) = \frac{2}{L} P(t) \sum_m^p \sum_n^q \sin \frac{m\pi x_0}{L} \sin \frac{m\pi x}{L} \cos n\Phi \qquad (18)$$

By using Eqs. (9), (11), (12), (15), and (18), the integration of Eq. (14) can be carried out. Then a set of two nonlinear algebraic equations will be obtained for each m, n with A_{mn} and B_{mn} as unknown functions of time. However, due to the nonlinear terms existing in the integrands, no general solutions are obtainable for the foregoing integrations. For the problem under investigation, p and q are limited to the following:

$$p = 1 \quad \text{and} \quad q = 2.$$

Physical interpretation of these is that the lateral mode shape along the axial length of the cylinder is assumed to be the first mode with only one half-sine elastic wave, while the radial mode shapes around the circumference of the cylinder consist of the first two modes with one and two full-sine waves ($n = 1$ and 2).

The wave number k of the forcing function (8) has the same value as n (1 and 2) so that the radial excitation around the cylinder is corresponding to the first and second modes of free vibration. The time function P(t) is degenerated into $P_1(t)$ and $P_2(t)$ corresponding to $n = 1$ and 2, respectively.

The assumption of a two-term solution is, of course, only an approximation. Due to the complexity of the nonlinear problem as shown

later on, no attempt is made to include more terms in the series. The approximate solution to be derived for this special case serves to demonstrate a useful and practical way for solving such a nonlinear vibration problem.

From Eq. (11), the assumed two-term solutions for displacement and stress function are

$$w(x,\Phi,t) = A_{11}(t)W_{11}(x,\Phi) + A_{12}(t)W_{12}(x,\Phi)$$

$$F(x,\Phi,t) = B_{11}(t)f_{11}(x,\Phi) + B_{12}(t)f_{12}(x,\Phi) \tag{19}$$

where

$$W_{11}(x,\Phi) = f_{11}(x,\Phi) = \sin\frac{\pi x}{L}\cos\Phi$$

$$W_{12}(x,\Phi) = f_{12}(x,\Phi) = \sin\frac{\pi x}{L}\cos 2\Phi \tag{20}$$

By using Eqs. (19) and (20), the integrations of Eq. (14) are carried out, and the resulting four equations are as follows:

$$D\left(\frac{aL}{\pi}\right)^2\left[\left(\frac{\pi}{L}\right)^2+\frac{1}{a^2}\right]^2 A_{11} - \frac{4}{\pi}(A_{11}B_{12} + A_{12}B_{11}) - aB_{11} + \left(\frac{aL}{\pi}\right)^2\mu\ddot{A}_{11} = 2L\left(\frac{a}{\pi}\right)^2\sin\frac{\pi x_0}{L}P_1(t)$$

$$D\left(\frac{aL}{\pi}\right)^2\left[\left(\frac{\pi}{L}\right)^2+\frac{4}{a^2}\right]^2 A_{12} - \frac{4}{\pi}A_{11}B_{11} - aB_{12} + \left(\frac{aL}{\pi}\right)^2\mu\ddot{A}_{12} = 2L\left(\frac{a}{\pi}\right)^2\sin\frac{\pi x_0}{L}P_2(t)$$

$$\left(\frac{aL}{\pi}\right)^2\left[\left(\frac{\pi}{L}\right)^2+\frac{1}{a^2}\right]^2 B_{11} + \frac{Eh}{\pi}A_{11}(4A_{12} + \pi a) = 0$$

$$\left(\frac{aL}{\pi}\right)^2\left[\left(\frac{\pi}{L}\right)^2+\frac{4}{a^2}\right]^2 B_{12} + \frac{Eh}{\pi}(2A_{11}^2 + \pi aA_{12}) = 0 \tag{21}$$

By introducing some new notations,

$$k_0 = \left(\frac{aL}{\pi}\right)^2$$

$$K_1 = k_0\left[\left(\frac{\pi}{L}\right)^2+\frac{1}{a^2}\right]^2$$

$$C = 2L\left(\frac{\pi}{L}\right)^2\sin\frac{\pi x_0}{L}$$

$$K_2 = k_0\left[\left(\frac{\pi}{L}\right)^2+\frac{4}{a^2}\right]^2 \tag{22}$$

the foregoing four equations can be simplified as follows:

$$DK_1A_{11} - \frac{4}{\pi}(A_{11}B_{12} + A_{12}B_{11}) - aB_{11} + k_0\mu\ddot{A}_{11} = CP_1(t)$$

$$DK_2A_{12} - \frac{4}{\pi}A_{11}B_{11} - aB_{12} + k_0\mu\ddot{A}_{12} = CP_2(t)$$

$$K_1B_{11} + \frac{Eh}{\pi}A_{11}(4A_{12} + \pi a) = 0$$

$$K_2B_{12} + \frac{Eh}{\pi}\left(2A_{11}^2 + \pi aA_{12}\right) = 0 \tag{23}$$

From the last two equations of Eq. (23), B_{11} and B_{12} can be solved in terms of A_{11} and A_{12}.

$$B_{11} = -\frac{Eh}{K_1}A_{11}\left(\frac{4}{\pi}A_{12} + a\right)$$

$$B_{12} = -\frac{Eh}{K_2}\left(\frac{2}{\pi}A_{11}^2 + aA_{12}\right) \tag{24}$$

Substituting Eq. (24) into the first two equations of Eq. (23), two nonlinear differential equations in terms of A_{11} and A_{12} are obtained.

$$\ddot{A}_{11} + (1/k_0\mu)A_{11} \left\{ \left(DK_1 + a^2Eh/K_1\right) + \left[\frac{8Eh}{\pi^2} A_{11}^2/K_2 + 2A_{12}^2/K_1 + \frac{\pi}{2}\left(\frac{2}{K_1} + \frac{1}{K_2}\right) aA_{12}\right]\right\} = \frac{C}{K_0\mu} P_1(t)$$

$$\ddot{A}_{12} + \frac{1}{k_0\mu} A_{11} \left\{\left(DK_2 + \frac{a^2Eh}{K_2}\right) + \frac{2Eh}{\pi^2}\left(\frac{A_{11}}{A_{12}}\right)^2 \left[8A_{12}^2/K_1 + (2/K_1 + 1/K_2)\, aA_{12}\right]\right\} = \frac{C}{k_0\mu} P_2(t)$$

Further simplification of these two equations can be achieved by introducing the following notations:

$$\omega_{11}^2 = \frac{1}{k_0\mu}\left(DK_1 + a^2\, Eh/K_1\right)$$

$$\omega_{12}^2 = \frac{1}{k_0\mu}\left(DK_2 + a^2\, Eh/K_2\right)$$

$$Q = \frac{2Eh}{\pi^2 k_0\mu},$$

$$K = \frac{\pi}{2}\,(2/K_1 + 1/K_2),$$

$$\bar{P}_{1,2}(t) = \frac{C}{k_0\mu} P_{1,2}(t) \tag{25}$$

Thus,

$$\ddot{A}_{11} + A_{11}\left[\omega_{11}^2 + 4Q\left(A_{11}^2/K_2 + 2A_{12}^2/K_1 + KaA_{12}\right)\right] = \bar{P}_1(t)$$

$$\ddot{A}_{12} + A_{12}\left[\omega_{12}^2 + 2Q\,(A_{11}/A_{12})^2\left(4A_{12}^2 + KaA_{12}\right)\right] = \bar{P}_2(t) \tag{26}$$

Eq. (26) gives the two equations of motion of the system. The quantities ω_{11} and ω_{12} given by Eq. (25) are the first two linear, angular natural frequencies corresponding to the normal modes, W_{11} and W_{12}. The general expression of the natural frequency is

$$\omega_{mn}^2 = \frac{1}{\mu} D\,(\alpha_m + \beta_n)^2 + \frac{Eh\,\alpha_m^2}{a^2(\alpha_m + \beta_n)^2} \tag{27}$$

where

$$\alpha_m = (m/L)^2$$

$$\beta_n = (n/a)^2$$

For an aluminum thin shell with a = 18 in., L = 72 in., and h = 0.05 in., Eq. (27) is evaluated for m = 1,2,...,5, and n = 1,2,...,20. The computed natural frequences $f_{mn} = \omega_{mn}/2\pi$ in cps are tabulated in Table 1 and plotted in Fig. 2.

TABLE 1
Natural Frequencies of Cylindrical Shell (CPS)

$E = 10^6$, $h = 0.05$, $a = 18$, $\nu = 0.3$, $L = 72$, $m = 5$, $n = 20$

n \ m	1	2	3	4	5
1	663.1	1,236.8	1,472.8	1,578.2	1,632.4
2	232.3	663.2	1,010.3	1,237.0	1,380.4
3	112.4	374.3	663.4	909.5	1,098.1
4	68.9	233.8	448.8	664.2	854.3
5	56.1	161.2	319.0	494.6	665.7
6	61.0	124.8	240.0	380.0	526.6
7	75.6	112.2	194.0	303.8	426.6
8	95.9	116.6	172.0	256.1	356.9
9	112.0	132.3	168.6	230.8	311.6
10	147.4	155.4	179.3	223.9	287.0
11	177.9	183.7	200.0	231.8	279.9
12	211.4	216.0	227.8	250.9	287.3
13	247.9	251.8	260.9	278.4	306.1
14	287.3	290.8	298.3	312.1	333.8
15	329.7	332.9	339.4	350.8	368.5
16	374.9	378.0	383.9	393.8	408.7
17	423.1	426.1	431.6	440.4	453.4
18	474.3	477.2	482.4	490.5	502.1
19	528.3	531.1	536.2	543.8	554.5
20	585.3	588.1	593.0	600.3	610.4

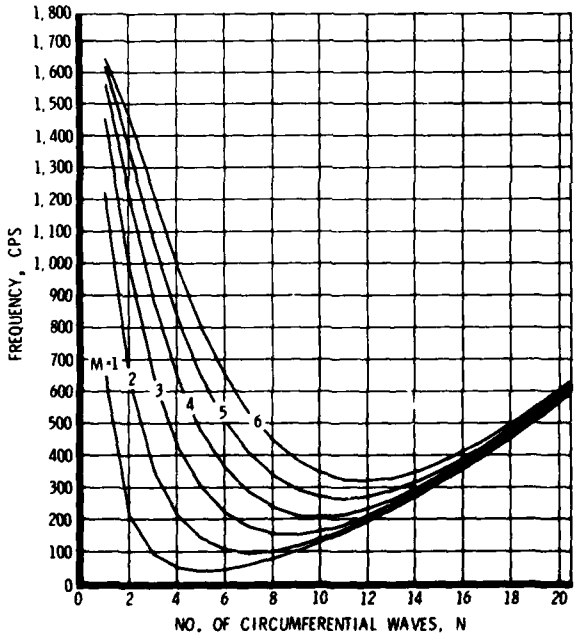

Fig. 2 - Natural frequencies of a cylindrical shell

For simplicity in further analysis, the first subscript 1 will be dropped from the notations A_{11}, A_{12}, ω_{11}, and ω_{12} hereafter. They become now A_1, A_2, ω_1, and ω_2, respectively.

Eq. (26) is then written in another form:

$$\ddot{A}_1 + \omega_1^2 A_1 + c_1 A_1^3 + 2c_2 A_1 A_2 + c_3 A_1 A_2^2 = \bar{P}_1(t)$$

$$\ddot{A}_2 + \omega_2^2 A_2 + c_2 A_1^2 + c_3 A_1^2 A_2 = \bar{P}_2(t) \qquad (28)$$

where

$$c_1 = 4Q/K_2$$

$$c_2 = 2QKa$$

$$c_3 = 8Q/K_1$$

By introducing two variables,

$$x_1 = A_1$$

$$X_2 = A_2 + c_2/c_3$$

Eq. (28) is transformed to the following form:

$$\ddot{x}_1 + \bar{\omega}_1^2 x_1 + c_1 x_1^3 + c_3 x_1 x_2^2 = \bar{P}_1(t)$$

$$\ddot{x}_2 + \omega_2^2 x_2 + c_3 x_1^2 x_2 = \bar{P}_2(t) + F_0 \qquad (29)$$

where

$$\bar{\omega}_1^2 = \omega_1^2 - c_2^2/c_3$$

and

$$F_0 = \omega_2^2 c_2/c_3$$

It is noted that, by this transformation, the second-degree nonlinear terms in Eq. (28) have been eliminated. Eq. (29) becomes the standard Duffing equations with only odd order nonlinear terms. The right side of the second equation includes a frequency-dependent constant F_0 which is equivalent to an additional constant force input.

Various methods had been used in the past by many investigators (4-11) to solve the nonlinear vibration problems of a single-degree-of-freedom system. These include the phase plane technique, the perturbation approach, equivalent linearization, numerical iteration, averaging method, and harmonic balance. However, for a multidegree-of-freedom system as the present case, the harmonic balance method (7, 8) is found to be the most direct and convenient approach. Therefore, in the following analysis, this method will be employed for finding the steady-state response of the nonlinear system represented by Eq. (29).

The forcing functions in Eq. (29) are assumed to be harmonic with a period $T = 2\pi/\omega$, namely,

$$\bar{P}_1(t) = F_1 \cos \omega t$$

$$\bar{P}_2(t) = F_2 \cos \omega t \qquad (30)$$

where

F_1, F_2 = amplitudes of excitation

ω = forcing frequency

The steady-state responses are not merely harmonic in this case. They may consist of harmonic motion, superharmonic motion, and subharmonic motion depending upon the system characteristics - damping force, restoring force, and external load. Mathematically, the responses can be expressed in series form as follows:

$$x_1(t) = \sum_i a_i \Phi_i(t)$$

$$x_2(t) = \sum_i b_i \psi_i(t) \qquad (31)$$

where

$i = 1, 2, \ldots, n$

a, b = constants to be determined

$\Phi(t)$, $\psi(t)$ = periodic function of time

For the present case, only the first approximation of a two-term harmonic solution is sought. The appropriate form of the responses can be assumed as

$$x_1(t) = X_1 \cos(\omega t - \alpha)$$

$$x_2(t) = b_0 + X_2 \cos(\omega t - \beta) \qquad (32)$$

where

b_0 = constant

X_1, X_2 = response amplitudes

α, β = phase angles

As pointed out by Hayashi (7), the constant b_0 is required for balancing the harmonics and accounts for the response of zero frequency due to the existence of the constant force F_0 in Eq. (29).

According to the principle of harmonic balance, Eqs. (30) and (32) are substituted into Eq. (29). By equating to zero separately the constant terms, the coefficients of $\cos \omega t$ and $\sin \omega t$ terms, the following six equations are obtained:

$$c_3 b_0 X_1 X_2 \cos(\alpha - \beta) = 0$$

$$b_0 \left(\omega_2^2 + \frac{1}{2} c_3 X_1^2\right) = F_0$$

$$\bar{\omega}_1^2 - \omega^2 + c_3 b_0^2 + \frac{3}{4} c_1 X_1^2 + \frac{1}{4} c_3 X_2^2 \left[2 + \frac{\cos(2\beta - \alpha)}{\cos \alpha}\right] = \frac{F_1}{X_1 \cos \alpha}$$

$$X_1 \sin\alpha \left\{ \bar{\omega}_1^2 - \omega^2 + c_3 b_0^2 + \frac{3}{4} c_1 X_1^2 + \frac{1}{4} X_2^2 \left[2 + \frac{\sin(2\beta - \alpha)}{\sin\alpha} \right] \right\} = 0$$

$$\omega_2^2 - \omega^2 + \frac{1}{4} c_3 X_1 \left[2 + \frac{\cos(2\alpha - \beta)}{\cos\beta} \right] = \frac{F_2}{X_2 \cos\beta}$$

$$X_2 \sin\beta \left\{ \omega_2^2 - \omega^2 + \frac{1}{4} c_3 X_1^2 \left[2 + \frac{\sin(2\alpha - \beta)}{\sin\beta} \right] \right. = 0 \tag{33}$$

For nontrivial solutions, the first equation gives

$$\cos(\alpha - \beta) = 0$$

or

$$\alpha - \beta = \pm \pi/2 \tag{34}$$

This means that, for nonvanishing X_1 and X_2, the two phase angles are 90 degrees out of phase.

From the second equation of Eq. (33), the constant b_0 can be solved.

$$b_0 = \frac{F_0}{\omega_2^2 + \frac{1}{2} c_3 X_1^2} = \frac{\omega_2^2 c_2}{c_3 \left(\omega_2^2 + \frac{1}{2} c_3 X_1^2 \right)} \tag{35}$$

or

$$b_0 = \frac{c_2}{c_3 \left(1 + \frac{c_3}{2\omega_2^2} X_1^2 \right)}$$

By introducing a new notation

$$B_0 = c_3 b_0^2 - \frac{c_2^2}{c_3} = c_3 \left[\frac{c_2}{c_3 \left(1 + \frac{c_3}{2\omega_2^2} X_1^2 \right)} \right]^2 - \frac{c_2^2}{c_3} \tag{36}$$

or

$$B_0 = \frac{c_2^2}{c_3} \left[\frac{1}{\left(1 + \frac{c_3}{2\omega_2^2} X_1^2 \right)^2} - 1 \right]$$

the remaining four equations with four unknowns, X_1, X_2, α and β, are transformed as follows:

$$\omega_1^2 - \omega^2 + B_0 + \frac{3}{4} c_1 X_1^2 + \frac{1}{4} c_3 X_2^2 \left[2 + \frac{\cos(2\beta - \alpha)}{\cos\alpha} \right] = \frac{F_1}{X_1 \cos\alpha}$$

$$\omega_1^2 - \omega^2 + B_0 + \frac{3}{4} c_1 X_1^2 + \frac{1}{4} c_3 X_2^2 \left[2 + \frac{\sin(2\beta - \alpha)}{\sin\alpha} \right] = 0$$

$$\omega_2^2 - \omega^2 + \frac{1}{4} c_3 X_1^2 \left[2 + \frac{\cos(2\alpha - \beta)}{\cos\beta} \right] = \frac{F_2}{X_2 \cos\beta}$$

$$\omega_2^2 - \omega^2 + \frac{1}{4} c_3 X_1^2 \left[2 + \frac{\sin(2\alpha - \beta)}{\sin\beta} \right] = 0$$

They can be rearranged in another form:

$$\left(\frac{\omega}{\omega_1} \right)^2 = 1 + \frac{1}{\omega_1^2} \left| B_0 + \frac{3}{4} c_1 X_1^2 + \frac{1}{4} c_3 X_2^2 \left[2 + \frac{\cos(2\beta - \alpha)}{\cos\alpha} \right] - \frac{F_1}{X_1 \cos\alpha} \right|$$

$$\left(\frac{\omega}{\omega_1} \right)^2 = 1 + \frac{1}{\omega_1^2} \left| B_0 + \frac{3}{4} c_1 X_1^2 + \frac{1}{4} c_3 X_2^2 \left[2 + \frac{\sin(2\beta - \alpha)}{\sin\alpha} \right] \right|$$

$$\left(\frac{\omega}{\omega_2} \right)^2 = 1 + \frac{1}{\omega_2^2} \left| \frac{1}{4} c_3 X_1^2 \left[2 + \frac{\cos(2\alpha - \beta)}{\cos\beta} \right] - \frac{F_2}{X_2 \cos\beta} \right|$$

$$\left(\frac{\omega}{\omega_2}\right)^2 = 1 + \frac{1}{4\omega_2^2} c_3 X_1^2 \left[2 + \frac{\sin(2\alpha - \beta)}{\sin\beta}\right] \tag{38}$$

For any given forcing functions with amplitudes F_1 and F_2 and frequency ω, the steady-state responses X_1 and X_2 and the phase angles α and β can be solved from the foregoing equations.

By observation of Eqs. (35) and (36), it is apparent that, for a large frequency ω_2, the constant b_0 approximately equals to c_2/c_3, and the other constant B_0 approaches zero. In general, the second natural frequency of a thin shell is quite high. Therefore, the constant B_0 will be neglected hereafter. The system of equations then becomes the following:

$$\left(\frac{\omega}{\omega_1}\right)^2 = 1 + \frac{1}{\omega_1^2}\left\{\frac{3}{4}c_1 X_1^2 + \frac{1}{4}c_3 X_2^2\left[2 + \frac{\cos(2\beta - \alpha)}{\cos\alpha}\right] - \frac{F_1}{X_1\cos\alpha}\right\}$$

$$\left(\frac{\omega}{\omega_1}\right)^2 = 1 + \frac{1}{\omega_1^2}\left\{\frac{3}{4}c_1 X_1^2 + \frac{1}{4}c_3 X_2^2\left[2 + \frac{\sin(2\beta - \alpha)}{\sin\alpha}\right]\right\}$$

$$\left(\frac{\omega}{\omega_2}\right)^2 = 1 + \frac{1}{\omega_2^2}\left\{\frac{1}{4}c_3 X_2^2\left[2 + \frac{\cos(2\alpha - \beta)}{\cos\beta}\right] - \frac{F_2}{X_2\cos\beta}\right\}$$

$$\left(\frac{\omega}{\omega_2}\right)^2 = 1 + \frac{1}{4\omega_2^2} c_3 X_1^2 \left[2 + \frac{\sin(2\alpha - \beta)}{\sin\beta}\right] \tag{39}$$

Eq. (39) can be further simplified by substituting the phase angles relation, Eq. (34), into the bracket terms in Eq. (39) and noting that the second term inside the bracket involving sine and cosine functions in each equation reduces to (-1). The resulting equations are as follows:

Case 1: For $\alpha = 0, \pi$; $\beta = \pm\pi/2$

$$\left(\frac{\omega}{\omega_1}\right)^2 = 1 + \frac{1}{\omega_1^2}\left(\frac{3}{4}c_1 X_1^2 + \frac{1}{4}c_3 X_2^2 \mp \frac{F_1}{F_2}\right) \tag{40}$$

$$\left(\frac{\omega}{\omega_1}\right)^2 = r^2\left(1 + \frac{1}{4\omega_2^2} c_3 X_1^2\right) \tag{41}$$

where

$$r = \omega_2/\omega_1$$

The upper sign for the last term of Eq. (40) stands for $\alpha = 0$, and the lower sign for $\alpha = \pi$.

Case 2: For $0 < \alpha < \pi/2$ and $\pi/2 < \alpha < \pi$; $\beta = \alpha \pm \pi/2$

$$\left(\frac{\omega}{\omega_1}\right)^2 = 1 + \frac{1}{\omega_1^2}\left(\frac{3}{4}c_1 X_1^2 + \frac{1}{4}c_3 X_2^2 - \frac{F_1}{X_1\cos\alpha}\right) \tag{42}$$

$$\left(\frac{\omega}{\omega_1}\right)^2 = r^2\left(1 + \frac{1}{4\omega_2^2} c_3 X_1^2 - \frac{F_2}{X_2\cos\beta}\right) \tag{43}$$

These simplified equations then can be evaluated numerically to investigate the nonlinear behavior of the system.

Stability of the Solutions

Due to the presence of the nonlinear terms, Eq. (39) may yield more than one set of solutions. Similar to the single-degree-of-freedom system of the Duffing type (4), there may exist more than one set of solutions for a certain range of the exciting frequencies. These multiple solutions are not all physically stable. Therefore, it is essential to determine the stability of each solution so that a better prediction of the nonlinear response of the system can be accomplished.

The physical stability of a steady-state solution can be determined by investigating the nature of the frequency response curves in the

vicinity of the steady-state solution according to Floquet theory (4, 7, 8) and by the application of the perturbation method (12, 13).

Let $x_{1s}(t)$ and $x_{2s}(t)$ be the steady-state solutions in the form of Eq. (32), and $\delta x_1(t)$ and $\delta x_2(t)$ be the small variations of x_1 and x_2, respectively. Then, the total responses after the disturbance are

$$x_1(t) = x_{1s}(t) + \delta x_1(t)$$
$$x_2(t) = x_{2s}(t) + \delta x_2(t) \qquad (44)$$

Substitution of Eq. (44) into the equations of motion (29) and retaining only the first degree terms of δx yield the following two variational differential equations:

$$\delta\ddot{x}_1 + \left(\bar{\omega}_1^2 + 3c_1x_{1s}^2 + c_3x_{2s}^2\right)\delta x_1 + 2c_3x_{1s}x_{2s}\delta x_2 = 0$$
$$\delta\ddot{x}_2 + \left(\omega_2^2 + c_3x_{1s}^2\right)\delta x_2 + 2c_3x_{1s}x_{2s}\delta x_1 = 0 \qquad (45)$$

By substituting the steady-state solutions given by Eq. (32) in the foregoing equations and letting $\tau = \omega t$, a new set of linear differential equations in δx_1 and δx_2 is obtained.

$$\delta\ddot{x}_1 + \left\{\bar{\omega}_1^2 + 3c_1X_1^2\cos^2(\tau-\alpha) + c_3\left[b_0 + X_2\cos(\tau-\beta)\right]^2\right\}\delta x_1 + 2c_3X_1\cos(\tau-\alpha)\left[b_0 + X_2\cos(\tau-\beta)\right]\delta x_2 = 0$$

$$\delta\ddot{x}_2 + \left[\omega_2^2 + c_3X_1^2\cos^2(\tau-\alpha)\right]\delta x_2 + 2c_3X_1\cos(\tau-\alpha)\left[b_0 + X_2\cos(\tau-\beta)\right]\delta x_1 = 0 \qquad (46)$$

These are two Hill-type equations of two-degrees-of-freedom system with periodic coefficients. They can be transformed to the standard Mathieu equations as follows:

$$\frac{d^2(\delta x_1)}{d\tau^2} + (\lambda_1 + \gamma_{1c}\cos 2\tau + \gamma_{1s}\sin 2\tau + \eta_c\cos\tau + \eta_s\sin\tau)\,\delta x_1 + (\psi + \sigma_c\cos 2\tau + \sigma_s\sin 2\tau + \xi_c\cos\tau + \xi_s\sin\tau)\,\delta x_2 = 0$$

$$\frac{d^2(\delta x_2)}{d\tau^2} + (\lambda_2 + \gamma_{2c}\cos 2\tau + \gamma_{2s}\sin 2\tau)\,\delta x_2 + (\psi + \sigma_c\cos 2\tau + \sigma_s\sin 2\tau + \xi_c\cos\tau + \xi_s\sin\tau)\,\delta x_1 = 0 \qquad (47)$$

where

$$\lambda_1 = \left(\bar{\omega}_1^2 + c_3b_0 + \frac{3}{2}c_1X_1^2 + \frac{1}{2}c_3X_2^2\right)/\omega^2$$
$$\lambda_2 = \left(\omega_2^2 + \frac{1}{2}c_3X_1^2\right)/\omega^2$$
$$\gamma_{1c} = \left(3c_1X_1^2\cos 2\alpha + c_3X_2^2\cos 2\beta\right)/2\omega^2$$
$$\gamma_{2c} = c_3X_1^2\cos 2\alpha/2\omega^2$$
$$\gamma_{1s} = \left(3c_1X_1^2\sin 2\alpha + c_3X_2^2\sin 2\beta\right)/2\omega^2$$
$$\gamma_{2s} = c_3X_1^2\sin 2\alpha/2\omega^2$$
$$\eta_c = 2c_3b_0X_2\cos\beta/\omega^2$$
$$\eta_s = 2c_3b_0X_2\sin\beta/\omega^2$$
$$\psi = c_3X_1X_2\cos(\alpha-\beta)/\omega^2$$
$$\sigma_c = c_3X_1X_2\cos(\alpha+\beta)/\omega^2$$
$$\sigma_s = c_3X_1X_2\sin(\alpha+\beta)/\omega^2$$
$$\xi_c = 2c_3b_0X_1\cos\alpha/\omega^2$$
$$\xi_s = 2c_3b_0X_1\sin\alpha/\omega^2$$

It is noted that, in the foregoing notations, on the left of the equal sign the subscript 1 or 2 indicates to which equation of Eq. (47), the first or the second, the coefficient belongs. The subscript c or s indicates that the coefficient involves only cosine or sine function of the phase angles.

Eq. (47) gives the basic equations for the investigation of nonlinear stability of the original system, Eq. (29). Similar to the Mathieu equation of the single-degree-of-freedom system, the stability criterion for the present case is to determine whether the solutions, δx_1 and δx_2, of Eq. (47) are bounded for $t > 0$.

The perturbed motions are assumed to be harmonic, having the same frequency as the forcing function, which relates to the natural frequencies of the shell as follows:

$$\omega = \omega_1 \simeq 3\omega_2 \tag{48}$$

According to the Floquet theory (4, 7, 8, 12), the solutions of Eq. (47) can be assumed as

$$\delta x_1(\tau) = e^{\zeta\tau}\,(a_0' + a_1' \cos\tau + b_1' \sin\tau)$$

$$\delta x_2(\tau) = e^{\zeta\tau}\left(a_2' \cos\frac{\tau}{3} + b_2' \sin\frac{\tau}{3}\right) \tag{49}$$

where ζ is a characteristic exponent; a_0', a_1', b_1', a_2', b_2' are arbitrary, small constants depending on the initial conditions of perturbation. Similar to the steady-state solution, the constant a_0' is necessary for balancing the harmonics.

The assumption of Eq. (49) as the approximate solutions of Eq. (47) is based on two observations: (1) The two equations are coupled only through small terms in comparison with the uncoupled terms; (2) The periodicity of the solutions of the uncoupled equations depends mainly on the parameters λ_1 and λ_2 rather than on the other small periodic coefficients. From the notations after Eq. (47), it is seen that

$$\lambda_1 \approx (\omega_1/\omega)^2 = 1$$

and

$$\lambda_2 \approx (\omega_2/\omega)^2 = (1/3)^2 = 1/9$$

The periodicities are approximately 2π and 6π for δx_1 and δx_2, respectively. In fact, Eq. (49) represents the harmonic solutions of the uncoupled equations derived by dropping all coupled terms in Eq. (47).

By substituting Eq. (49) into Eq. (47) in accordance with the method of harmonic balance, the following two sets of equations for the determination of the amplitudes of δx_1 and δx_2 are obtained:

$$\left(\zeta^2 + \lambda_1\right)a_0' + \frac{1}{2}\eta_c a_1' + \frac{1}{2}\eta_s b_1' = 0$$

$$\eta_c a_0' + \left(\zeta^2 + \lambda_1 - 1 + \frac{1}{2}\gamma_{1c}\right)a_1' + \left(2\zeta + \frac{1}{2}\gamma_{1s}\right)b_1' = 0$$

$$\eta_s a_0' - \left(2\zeta - \frac{1}{2}\gamma_{1s}\right)a_1' + \left(\zeta^2 + \lambda_1 - 1 - \frac{1}{2}\gamma_{1c}\right)b_1' = 0$$

$$\psi a_2' = 0$$

$$\psi b_2' = 0 \tag{50}$$

$$\psi a_0' + \frac{1}{2}\xi_c a_1' + \frac{1}{2}\xi_s b_1' = 0$$

$$\xi_c a_0' + \left(\psi + \frac{1}{2}\sigma_c\right)a_1' + \frac{1}{2}\sigma_s b_1' = 0$$

$$\xi_s a_0' + \frac{1}{2}\sigma_s a_1' + \left(\psi - \frac{1}{2}\sigma_c\right)b_1' = 0$$

$$\left(\zeta^2 + \lambda_2 - \frac{1}{9}\right)a_2' + \frac{2}{3}\zeta b_2' = 0$$

$$-\frac{2}{3}\zeta a_2' + \left(\zeta^2 + \lambda_2 - \frac{1}{9}\right)b_2' = 0 \tag{51}$$

These equations clearly indicate that the perturbed motions, δx_1 and δx_2, are completely uncoupled. Their solutions lead to the following two possible cases for stability analysis:

Case 1: $\delta x_1 \neq 0$, $\delta x_2 = 0$ (52)

Case 2: $\delta x_1 = 0$, $\delta x_2 \neq 0$ (53)

The characteristic equations are derived from the first three equations of Eq. (50) and the last two equations of Eq. (51) as follows:

For Case 1,

$$\Delta_1(\zeta_1) \equiv \begin{vmatrix} \left(\zeta_1^2+\lambda_1\right) & \eta_c/2 & \eta_s/2 \\ \eta_c & \left(\zeta_1^2+\lambda_1-1+\frac{1}{2}\gamma_{1c}\right) & \left(2\zeta_1+\frac{1}{2}\gamma_{1s}\right) \\ \eta_s & -\left(2\zeta_1-\frac{1}{2}\gamma_{1s}\right) & \left(\zeta_1^2+\lambda_1-1-\frac{1}{2}\gamma_{1c}\right) \end{vmatrix} = 0 \tag{54}$$

For Case 2,

$$\Delta_2(\zeta_2) \equiv \begin{vmatrix} \left(\zeta_2^2+\lambda_2-\frac{1}{9}\right) & \frac{2}{3}\zeta_2 \\ -\frac{2}{3}\zeta_2 & \left(\zeta_2^2+\lambda_2-\frac{1}{9}\right) \end{vmatrix} = 0 \tag{55}$$

where the subscripts for ζ indicate the case number corresponding to Eqs. (52) and (53); $\Delta_1(\zeta_1)$ and $\Delta_2(\zeta_2)$ are determinants of the coefficients of a's and b's of Eqs. (50) and (51), respectively.

Expanding the determinants and omitting the sixth degree term due to its smallness in comparison with other quantities, the following equation is obtained:

$$\zeta_i^4 + P_i\zeta_i^2 + q_i = 0 \tag{56}$$

where i = 1, 2

$$P_1 = \left[3\lambda_1^2 + 1 - \frac{1}{4}\left(\gamma_{1c}^2 + \gamma_{1s}^2\right) - \frac{1}{2}\left(\eta_c^2 + \eta_s^2\right)\right] \Big/ (3\lambda_1 + 2)$$

$$q_1 = \left\{\lambda_1\left[(\lambda_1 - 1)^2 - \frac{1}{4}\left(\gamma_{1c}^2 + \gamma_{1s}^2\right)\right] - \frac{1}{2}\left[\eta_c^2\left(\lambda_1 - 1 - \frac{1}{2}\gamma_{1c}\right) + \eta_s^2\left(\lambda_1 - 1 + \frac{1}{2}\gamma_{1c}\right)\right]\right\} \Big/ (3\lambda_1 + 2)$$

$$P_2 = 2\left(\lambda_2 + \frac{1}{9}\right)$$

$$q_2 = \left(\lambda_2 - \frac{1}{9}\right)^2 \tag{57}$$

The characteristic exponent then can be solved as

$$\zeta_i^2 = \frac{1}{2}\left[-p_i \pm \sqrt{p_i^2 - 4q_i}\right] \tag{58}$$

Since ζ_i appears in $\pm$ pairs, no asymptotic stability is possible. The only condition for a stable solution is that all roots ζ_i as computed by Eq. (58) are purely imaginary. This requires that

$$\zeta_i^2 < 0 \tag{59}$$

In terms of p_i and q_i, the stability criteria for a stable system are

$$q_i > 0 \tag{60}$$

and

$$p_i > +2\sqrt{q_i} \tag{61}$$

For each ζ, there exists a set of values of a_0', a_1', a_2', b_1' and b_2' obtainable from Eqs. (50) and (51). The perturbed motions δx_1 and δx_2 are then determined by Eq. (49). As stated earlier, however, these solutions can physically exist only if they are stable. Therefore, it is unnecessary to obtain the solutions of δx_1 and δx_2. Instead, it will be necessary to study the stability criteria of Eqs. (60) and (61). If they are satisfied, the steady-state solutions of the original system of Eq. (29) will have infinitesimal stability. The nonlinear response behavior of the system then can be analyzed according to Eq. (39) by graphical method.

From the assumption that the forcing frequency is the same as the natural frequency of X_1, Eq. (48), and from the decoupling effect of the stability Eqs. (50) and (51), it can be seen that the response X_2 will not attain appreciable amplitude due to the direct excitation of F_2. Thus, the system is equivalent to one with a single excitation F_1 acting upon the first degree of freedom. The response X_2 of the second degree of freedom may not vanish due to the nonlinear coupling of X_1.

Corresponding to Eqs. (52) and (53), the cases of stability analysis are restated as follows:

Case 1: $F_1 \neq 0$, $F_2 = 0$; $X_1 \neq 0$; and $X_2 = 0$

Case 2: $F_1 \neq 0$, $F_2 = 0$; $X_1 \neq X_2 \neq 0$

Under these two conditions, the set of equations for analyzing the nonlinear responses and stability behaviors of the system can be summarized as follows:

1. Free vibration loci

   a. Only X_1 mode is considered.

$$\left(\frac{\omega}{\omega_1}\right)^2 = 1 + \frac{3}{4\omega_1^2} c_1 X_1^2 \qquad (62)$$

   This equation is derived from Eq. (40) by letting $F_1 = X_2 = 0$.

   b. Both modes, X_1 and X_2, are considered.

$$\left(\frac{\omega}{\omega_1}\right)^2 = 1 + \frac{1}{\omega_1^2}\left(\frac{3}{4} c_1 X_1^2 + \frac{1}{4} c_3 X_2^2\right) \qquad (63)$$

   This equation is obtained by vanishing the forcing function F_1 in Eq. (40). By assuming that the vibration amplitudes are inversely proportional to the natural frequencies, i.e.,

$$X_1/X_2 = \omega_2/\omega_1 = r$$

or

$$X_1 = rX_2$$

$$X_2 = X_1/r \qquad (64)$$

Eq. (63) is transformed to the following forms with only one mode involved in each equation:

$$\left(\frac{\omega}{\omega_1}\right)^2 = 1 + \frac{1}{4\omega_1^2}\left(3c_1 + \frac{c_3}{r^2}\right) X_1^2 \qquad (65)$$

$$\left(\frac{\omega}{\omega_1}\right)^2 = 1 + \frac{1}{4\omega_1^2}\left(3c_1 r^2 + c_3\right) X_2^2 \qquad (66)$$

2. Frequency response loci

   a. Only X_1 mode is excited. Eq. (40) is reduced to the following form for $X_2 = 0$:

$$\left(\frac{\omega}{\omega_1}\right)^2 = 1 + \frac{1}{4\omega_1^2} c_1 X_1^2 \mp \frac{F_1}{\omega_1^2 X_1} \qquad (67)$$

   b. Both modes, X_1 and X_2, are excited directly or indirectly by F_1. The response equation is the same as Eq. (40).

$$\left(\frac{\omega}{\omega_1}\right)^2 = 1 + \frac{1}{\omega_1^2}\left(\frac{3}{4} c_1 X_1^2 + \frac{1}{4} c_3 X_2^2 \mp \frac{F_1}{X_1}\right) \qquad (68)$$

   Using the relations of Eq. (64), Eq. (68) is transformed into two equations each of which involves only one mode.

$$\left(\frac{\omega}{\omega_1}\right)^2 = 1 + \frac{1}{4\omega_1^2}\left(3c_1 + \frac{c_3}{r^2}\right) X_1^2 \mp \frac{F_1}{\omega_1^2 X_1} \qquad (69)$$

$$\left(\frac{\omega}{\omega_1}\right)^2 = 1 + \frac{1}{4\omega_1^2}\left(3c_1 r^2 + c_3\right) X_2^2 \mp \frac{F_1}{r\omega_1^2 X_2} \qquad (70)$$

3. Jump point loci

   These are the vertical tangents of response equations Eqs. (67), (69), and (70).

   a. For Eq. (67):

$$\left(\frac{\omega}{\omega_1}\right)^2 = 1 + \frac{9}{4\omega_1^2} c_1 X_1^2 \qquad (71)$$

b. For Eqs. (69) and (70):

$$\left(\frac{\omega}{\omega_1}\right)^2 = 1 + \frac{3}{4\omega_1^2}\left(3c_1 + \frac{c_3}{r^2}\right) X_1^2 \qquad (72)$$

$$\left(\frac{\omega}{\omega_1}\right)^2 = 1 + \frac{3}{4\omega_1^2}\left(3c_1 r^2 + c_3\right) X_2^2 \qquad (73)$$

4. Stability criteria

The stability boundaries between the stable and unstable regions are obtained from Eqs. (60) and (61).

$$q_i = 0, \text{ and } p_i = \pm 2\sqrt{q_i} \qquad (74)$$

where i = 1, 2.

In terms of the parameters of Eq. (47), the two sets of stability boundaries are the following:

a. Case 1

From Eq. (74) with i = 1 and using Eq. (57).

$$\lambda_1\left(\bar{\lambda}_1^2 - \frac{1}{4}\bar{\gamma}_1^2\right) - \frac{1}{2}\left[\eta_c^2\left(\bar{\lambda}_1 - \frac{1}{2}\bar{\gamma}_{1c}\right) + \eta_s^2\left(\bar{\lambda}_1 + \gamma_{1c}\right)\right] = 0 \qquad (75)$$

$$\left[3\lambda_1^2 + 1 - \frac{1}{4}\bar{\gamma}_1^2 - \frac{1}{2}\bar{\eta}^2\right]^2 = 4\,(3\lambda_1 + 2)\left\{\lambda_1\left(\bar{\lambda}_1^2 - \frac{1}{4}\bar{\gamma}_1^2\right) - \frac{1}{2}\left[\eta_c^2\left(\bar{\lambda}_1 - \frac{\gamma_{1c}}{2}\right) + \eta_s^2\left(\bar{\lambda}_1 + \frac{\gamma_{1c}}{2}\right)\right]\right\} \qquad (76)$$

where

$$\bar{\gamma}_1 = \gamma_1 - 1$$

$$\bar{\gamma}_1^2 = \gamma_{1c}^2 + \gamma_{1s}^2$$

$$\bar{\eta}^2 = \eta_c^2 + \eta_s^2$$

b. Case 2

From Eq. (74) with i = 2 and using Eq. (57),

$p_2 = 2\,(\lambda_2 + \frac{1}{9})$, and

$q_2 = (\lambda_2 - \frac{1}{9})^2 > 0$

It is obvious, in this case, that $p_2 > +2\sqrt{q_2}$. Therefore, according to Eq. (61), the perturbed motion δx_2 is stable at all frequencies while $\delta x_1 = 0$. The stable motion of the original system is represented by Eq. (68) or Eq. (69) and (70).

Numerical Evaluation

The various nonlinear response equations are evaluated numerically for a cylindrical shell specified in Table 1. Computer programs are utilized whenever necessary. It is assumed that there is only one forcing function F_1 acting with $\bar{F}_1 = F_1/\omega_1^2 = 1$. The forcing frequency ω is assumed to be the same as ω_1. However, for graphical presentation, it is treated as a variable so that the plots of the equations cover a frequency range of $R = \omega/\omega_1 = 0.7$ to 1.4.

From Table 1, the first two computed natural frequencies are:

$f_1 = 663.1$ cps

$f_2 = 232.3$ cps

$\omega_1 = 4166.4$ rad/sec

$\omega_2 = 1459.6$ rad/sec

$$r = \frac{\omega_2}{\omega_1} = \frac{f_2}{f_1} = 0.3503 \approx \frac{1}{3}$$

The computed geometric parameters are as follows:

$$c_1 = 5326$$

$$c_2 = 1.303 \times 10^6$$

$$c_3 = 86{,}852$$

$$\bar{\epsilon}_1 = c_1/\omega_1^2 = 0.0003068$$

$$\sqrt{\bar{\epsilon}_1} = 0.017516$$

$$\epsilon_1' = \left(3c_1 + \frac{c_3}{r^2}\right) \Big/ \omega_1^2 = 0.04595$$

$$\sqrt{\epsilon_1'} = 0.21436$$

$$\epsilon_2' = \left(3c_1 r^2 + c_3\right) \Big/ \omega_1^2 = r^2 \epsilon_1' = 0.0051056$$

$$\epsilon_2' = 0.071453 \qquad (77)$$

Calculations for the response equations are also carried out. The results are plotted and discussed as follows:

1. Free vibration loci

   a. $X_1 \neq 0, F_1 = X_2 = 0$

   Eq. (62) represents the free vibration of this case. By noting $R = \omega/\omega_1$ and using the notations of Eq. (77), this equation is converted to the following form for evaluation:

   $$R^2 = 1 + \frac{3}{4} \bar{X}_1^2 \qquad (78)$$

   where $\bar{X}_1 = \sqrt{\bar{\epsilon}_1} X_1$

   Eq. (78) is then plotted as curve 1 in Fig. 3. The curve bends to the right side of the graph and is similar to the free vibration of a single-degree-of-freedom system with a nonlinear, hard spring.

   b. $X_1 \neq X_2 \neq 0, F_1 = 0$

   The free vibration of this case are given by Eqs. (65) and (66), which can be reduced to a single equation by using Eq. (77).

$$R^2 = 1 + \frac{1}{4} X_i'^2 \qquad (79)$$

where $X_i' = \sqrt{\epsilon_i'} X_i$, $i = 1, 2$

This equation is plotted as curve 1 in Fig. 4, which is also similar to the vibration of a nonlinear, hard spring system.

2. Frequency response loci

   a. $X_1 \neq F_1 \neq 0, X_2 = 0$

   Using Eq. (77), the response equation Eq. (67) is transformed as

   $$R^2 = 1 + \frac{3}{4} \bar{X}_1^2 \mp \frac{\sqrt{\bar{\epsilon}_1} \bar{F}_1}{\bar{X}_1} \qquad (80)$$

   In another form,

   $$\bar{X}_1^3 + p\bar{X}_1 \mp q = 0 \qquad (81)$$

   where $p = \frac{4}{3}\left(1 - R^2\right)$, and

   $$q = \mp \frac{4}{3} \sqrt{\bar{\epsilon}_1} \bar{F}_1$$

   The solutions of this cubic equation, obtained by a computer program, represent the forced response of the first degree of freedom when the second degree of freedom is not excited. The equation is plotted as curve 2 in Fig. 3, which resembles the frequency response of the Duffing equation.

   b. $X_1 \neq X_2 \neq 0, \quad F_1 \neq 0$

   The frequency responses of this case are given by Eqs. (69) and (70). They can be reduced to a single equation by using Eqs. (77) and (79).

   $$X_i'^3 + p' X_i' + q' = 0, \quad i = 1, 2 \qquad (82)$$

   where

   $$p' = 4\left(1 - R^2\right)$$

   $$q' = \mp 4 \sqrt{\epsilon_1'} F_1 = \mp \frac{4}{r} \sqrt{\epsilon_2'} F_1$$

The solution of this equation is plotted as curve 2 in Fig. 4, which represents the forced response of either X_1' or X_2'. Although there is no direct excitation for the second degree of freedom (since $F_2 = 0$), the response X_2' exists due to the nonlinear coupling of the two modes.

3. Jump point loci

a. Eq. (71) is the jump point locus of Eq. (67). By using Eq. (77), it can be simplified as

$$R^2 = 1 + \frac{9}{4}\,\bar{X}_1^2 \tag{83}$$

This equation is then plotted as curve 3 in Fig. 3.

b. Eqs. (72) and (73) are the two jump point loci for Eqs. (69) and (70). They are reduced to a single equation by using the parameters in Eq. (77) together with Eq. (79).

$$R^2 = 1 + \frac{3}{4}\,X_i'^2, \quad i = 1, 2 \tag{84}$$

This equation is plotted as curve 3 in Fig. 4.

These two equations, Eqs. (83) and (84), are the loci of the vertical tangents of the nonlinear response curves for frequency ratio $R > 1$. Similar to the peridic solution of the Duffing equation, these curves represent the critical points at which an abrupt jump of the motion will occur during a frequency sweep.

4. Stability criteria

The stability boundaries for Case 1, Eqs. (75) and (76), are evaluated under the previously stated two conditions:

a. $X_1 \neq 0$, $F_1 \neq 0$, $X_2 = F_2 = 0$

Since there is only one excitation and one response in this undamped system, the phase angle α of x_1 must be zero or π. Then the stability parameters of Eq. (47) can be reduced to the following forms:

$$\lambda_1 = \frac{1}{\omega^2}\left(\omega_1^2 - \frac{c_2^2}{c_3} + \frac{3}{2}c_1\bar{X}_1^2\right)$$

$$= \frac{1}{R^2}\left(k + \frac{3}{2}\bar{X}_1^2\right)$$

$$\bar{\gamma} = \gamma_{1c} = \frac{3}{2}\frac{c_1}{\omega^2}\bar{X}_1^2$$

$$= \frac{3}{2R^2}\bar{X}_1^2$$

$$\gamma_{1s} = \eta_c = \eta_s = 0 \tag{85}$$

where $k = 1 - \dfrac{c_2^2}{\omega_1^2 c_3}$

By eliminating the zero terms in Eq. (75), the stability boundary equation is reduced to the following form:

$$\lambda_1\left(\lambda_1^2 - \frac{1}{4}\gamma_{1c}^2\right) = 0 \tag{86}$$

or

$$\lambda_1^3 - 2\lambda_1^2 + \lambda_1 - \frac{1}{4}\lambda_1\gamma_{1c}^2 = 0 \tag{87}$$

Substituting Eq. (85) into Eq. (87) and neglecting the higher degree terms of $\bar{X}_1$ other than the second, the stability boundary for $q_1 = 0$ is obtained.

$$(R^4 - 4kR^2 + 3k^3)\,\bar{X}_1^2 + \frac{2}{3}k\,(R^4 - 2kR^2 + k^2) = 0 \tag{88}$$

This equation then can be plotted as curve 4 in Fig. 3. The other stability boundary, $p_1 = \pm\sqrt{q_1}$, can be derived from Eq. (76) by eliminating the zero terms according to Eq. (85).

$$\left(3\lambda_1^2 + 1 - \frac{1}{4}\gamma_{1c}^2\right)^2 = 4\lambda_1(3\lambda_1 + 2)\left(\bar{\lambda}_1^2 - \frac{1}{4}\gamma_{1c}^2\right) \quad (89)$$

Since γ_{1c}^2 involves small quantity of $\bar{X}_1^4$, the preceding equation can be reduced to

$$(3\lambda_1^2 + 1)^2 = 4\lambda_1(3\lambda_1 + 2)(1 - \lambda_1)^2 \quad (90)$$

or

$$3\lambda_1^4 - 16\lambda_1^3 - 10\lambda_1^2 + 8\lambda_1 = 0 \quad (91)$$

Substituting Eqs. (85) into (91) and neglecting the higher degree terms of $\bar{X}_1$, the stability boundary for this case is obtained.

$$6(2R^6 - 5kR^4 - 12k^2R^2 + 5k^3)\bar{X}_1^2 = R^8 - k(8R^6 - 10kR^4 - 16k^2R^2 + 3k^3) \quad (92)$$

This equation is plotted as curve 5 in Fig. 3.

b. $X_1 \neq X_2 \neq F_1 \neq 0,\ F_2 = 0$

According to Eq. (54), the two-phase angles have the following values:

$$\alpha = 0, \pi$$

$$\beta = \pm\pi/2$$

The stability parameters then can be simplified as

$$\lambda_1 = \frac{1}{\omega^2}\left(\omega_1^2 + c_3 b_0 + \frac{3}{2}c_1 X_1^2 + \frac{1}{2}c_3 X_2^2\right)$$

$$\gamma_{1c} = \frac{1}{2\omega^2}\left(3c_1 X_1^2 - c_3 X_2^2\right) \quad (93)$$

$$\gamma_{1s} = \eta_c = 0,\ \bar{\gamma}_1 = \gamma_{1c}$$

$$\eta_s = \pm 2c_3 b_0 X_2/\omega^2,\ \bar{\eta} = \eta_s$$

Using Eqs. (35) and (64),

$b_0 \approx c_2/c_3$, and $X_1 = rX_2$,

the parameters in Eq. (93) can be expressed in terms of either X_1 or X_2 alone.

$$\lambda_1 = \frac{1}{\omega^2}\left[\bar{\omega}_1^2 + c_2 + \frac{1}{2}\left(3c_1 + \frac{c_3}{r^2}\right)X_1^2\right] = \frac{1}{R^2}\left(m_1 + \frac{1}{2}X_1'^2\right)$$

$$= \frac{1}{\omega^2}\left[\bar{\omega}_1^2 + c_2 + \frac{1}{2}\left(3c_1 r^2 + c_3\right)X_2^2\right] = \frac{1}{R^2}\left(m_1 + \frac{1}{2}X_2'^2\right) \quad (94)$$

$$\lambda_{1c} = \frac{1}{2\omega^2}\left(3c_1 - \frac{c_3}{r^2}\right)X_1^2 = \frac{1}{2R^2}X_1'^2$$

$$= \frac{1}{2\omega^2}\left(3c_1 r^2 - c_3\right)X_2^2 = \frac{1}{2R^2}X_2'^2$$

$$\bar{\eta} = \eta_s = \pm\frac{2}{r\omega^2}c_2 X_1 = \pm\frac{1}{R^2}m_2 X_1'$$

$$= \pm\frac{2}{\omega^2}c_2 X_2 = \pm\frac{1}{R^2}m_2 X_2' \quad (95)$$

where

$$m_1 = 1 + \frac{c_2}{\omega_1^2}\left(1 - \frac{c_2}{c_3}\right),$$

$$m_2 = \frac{2c_2}{\omega_1^2\sqrt{\epsilon_2'}}$$

The stability boundary Eq. (75) for $q_1 = 0$ is reduced to the following form by eliminating the zero quantities of Eq. (93):

$$\lambda_1\left(\bar{\lambda}_1^2 - \frac{1}{4}\gamma_{1c}^2\right) - \frac{1}{2}\eta_s^2\left(\bar{\lambda}_1 + \gamma_{1c}\right) = 0 \tag{96}$$

or

$$\lambda_1^3 - 2\lambda_1^2 + \lambda_1 - \frac{1}{4}\lambda_1\gamma_{1c}^2 - \frac{1}{2}\lambda_1\eta_s^2 + \frac{1}{2}\eta_s^2 - \frac{1}{2}\gamma_{1c}\eta_s^2 = 0 \tag{97}$$

Substituting Eqs. (94) and (95) into (97) and neglecting the higher degree terms of X_1' and X_2' the stability boundary becomes

$$\left[R^4 + \left(m_2^2 - 4m_1\right)R^2 - m_1\left(m_2^2 - 3m_1\right)\right]X_i'^2 + 2m_1\left(R^4 - 2m_1R^2 + m_1^2\right) = 0 \tag{98}$$

where $i = 1, 2$

This equation is then plotted as curve 4 in Fig. 3. The other stability boundary, $p_1 = \pm 2\sqrt{q_1}$, with $X_1 \neq X_2 \neq 0$ is derived from Eq. (76) by eliminating the zero terms according to Eq. (93).

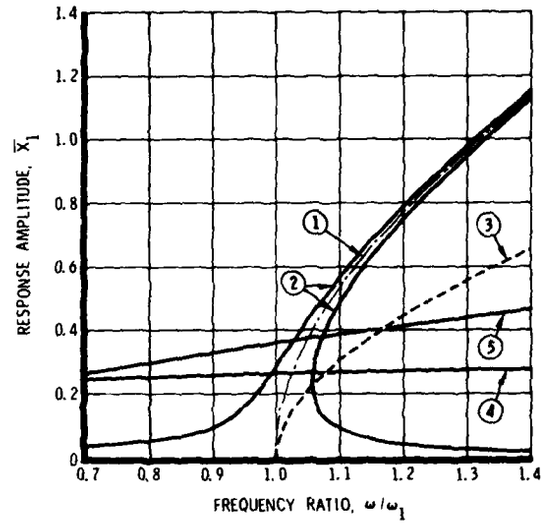

$X_1 \neq 0$, $F_1 \neq 0$; $X_2 = F_2 = 0$

1. Free vibration locus
2. Forced vibration locus
3. Jump point locus
4. Stability boundary $q_1 = 0$
5. Stability boundary $p_1 = \pm 2\sqrt{q_1}$

Fig. 3 - Frequency response of shell with only first mode excited

$$\left(3\lambda_1^2 + 1 - \frac{1}{2}\eta_s^2\right)^2 = 4(3\lambda_1 + 2)\left(\lambda_1\bar{\lambda}_1^2 - \frac{1}{2}\bar{\lambda}_1\eta_s^2\right) \tag{99}$$

or

$$3\lambda_1^4 - 16\lambda_1^3 - 10\lambda_1^2 + 8\lambda_1 - 1 + \eta_s^2\left(2\lambda_1 - 3\lambda_1^2 + 5 - \frac{1}{4}\eta_s^2\right) = 0 \tag{100}$$

Substituting Eqs. (94) and (95) into (100) and neglecting the higher degree of terms of X_1' the stability boundary becomes

$$\left[4R^6 + 5(m_2^2 - 2m_1)R^4 + 2m_1(m_2^2 - 12m_1)R^2 - 3m_1^2(m_2^2 - 2m_1)\right] X_i'^2 = R^8 - m_1(8R^6 - 10m_1R^4 - 16m_1^2R^2 + 3m_1^3) \quad (101)$$

Eq. (101) is plotted as curve 5 in Fig. 4.

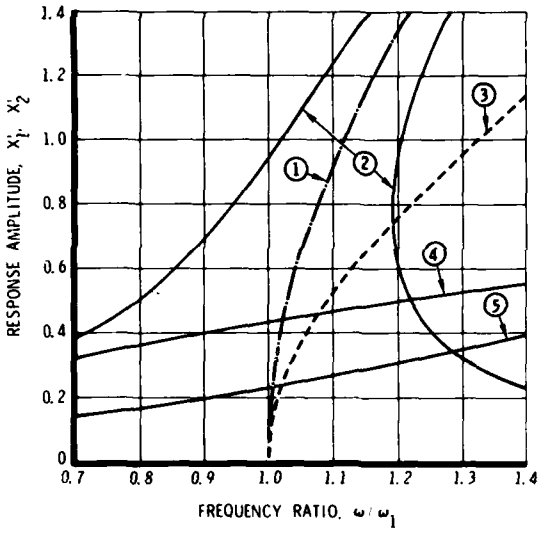

$X_1 \neq X_2 \neq 0$; $F_1 \neq 0$, $F_2 = 0$

1. Free vibration locus
2. Forced vibration locus
3. Jump point locus
4. Stability boundary $q_1 = 0$
5. Stability boundary $p_1 = \pm 2\sqrt{q_1}$

Fig. 4 - Frequency responses of shell with first two modes coupled and only mode 1 directly excited

CONCLUSIONS

The problem of nonlinear responses of cylindrical shells under radial line load has been investigated. A general procedure for solving the problem was presented. Because of its complexity, no exact solutions can be derived. Instead, a two-term series approximation was used to develop the frequency responses and the stability criteria. For the purpose of demonstration of the methods of analysis, the approximate solutions are seen to be adequate.

It is interesting to observe from the analyses and the response plots that the nonlinear shell problem under dynamic, sinusoidal line load can be treated systematically as a nonlinear vibration problem of a mechanical system. The application of the study results will enable one to derive solutions with sufficient accuracy for other shell problems of similar nature.

In engineering practice, one may be interested in finding the stresses in the shell. This would pose no difficulty as far as mathematics is concerned. Once a stable solution of displacement is found, it is only necessary to trace back step by step the formulas in the previous paragraphs to calculate all unknown quantities. The problem is then completely solved.

REFERENCES

1. K. M. Mushtari, "Nonlinear Theory of Thin Elastic Shells," (English Translation), NASA TT-F62,1961

2. S. S. Tang, and D. Y. Konishi, "Large Deflection of Circular Cylindrical Shell Under Circumferential Radial Line Load," North American Aviation Report NA-64-961, September 1964

3. V. A. Vlasov, "A General Theory of Shells," (English Traslation), NASA TT-F99, April 1964

4. J. J. Stoker, "Nonlinear Vibrations," Interscience, New York, 1950

5. K. Klotter, "Nonlinear Oscillations," Appl. Mech. Revs., 10, 1957, pp. 495-498

6. L. S. Jacobsen, and R. S. Ayre, "Engineering Vibrations," McGraw-Hill, New York, 1958

7. C. Hayashi, "Nonlinear Vibration in Physical Systems," McGraw-Hill, New York 1964

8. C. Hayashi, "Forced Oscillation in Nonlinear Systems," Nippon Print. & Publ. Co., Osaka, Japan, 1953

9. M. L. Cartwright, "Forced Oscillation in Nonlinear Systems, Contributions to the Theory of Nonlinear Oscillations," Vol. 1, Princeton Univ. Press. New Jersey, 1950, p. 149

10. K. Klotter, and E. Pinney, "A Comprehensive Stability Criterion for Forced Vibrations in Nonlinear Systems," J. Appl. Mech., Vol. 20, 1953, pp. 9-12

11. K. Klotter, "Nonlinear Vibration Problems Treated by the Averaging Method of W. Ritz," Proc. 1st U.S. Natl. Congr. Appl. Mech., 1951, pp. 125-131

12. G. J. Efstathiades, and C. J. H. Williams, "Vibration Isolation Using Nonlinear Springs," International J. Mech. Sci., Vol. 9, Pergamon Press, England, 1967, pp. 27-44

13. C. J. Efstathiades, "Subharmonic Instability in Nonlinear Two-degree-of-freedom Systems," Int. J. Mech. Sci., Vol. 10, Pergamon Press. England, 1948, pp. 829-847

DETERMINATION OF THE ELASTIC MODES AND FREQUENCIES WHEN RIGID BODY MODES EXIST

J. W. Straight, Associate Professor
Mechanical Engineering
Christian Brothers College
Memphis, Tennessee

A technique for the determination of the elastic mode shapes and natural frequencies of an unrestrained structure is proposed. The original equations of motion are transformed into a set of equations that possess symmetric and non-singular inertia and stiffness matrices. The eigenvalues and eigenvectors of these equations are determined by conventional iteration procedures. The eigenvectors are then transformed back to the original co-ordinates as the elastic mode shapes.

INTRODUCTION

The difficulty of determining the natural frequencies and mode shapes of a multi-degree-of-freedom system is increased whenever rigid body modes (and their zero eigenvalues) are present. The classical solution [1], [2][1] which involves determining the roots of the characteristic equation is usable for systems with few degrees of freedom, but becomes far too cumbersome for systems with many degrees of freedom.

The usual iteration solution [3] uses the inverse of the stiffness matrix. However, for systems with rigid body modes, the stiffness matrix is singular and cannot be inverted. Although the iteration form requiring the inverse of the mass matrix can be used, it is undesirable to do so in most instances since that form determines the high frequency modes first.

Anderson [2] uses the property of orthgonality to alter the equations of motion to a form that has a non-singular stiffness matrix. Although useful, this technique is laborious in that it requires inverting a different stiffness matrix for each successive mode. In addition, conventional sweeping techniques cannot be used with the modified equations since the modified stiffness matrix is not symmetric. A biorthogonal sweeping system [4] could be used but that technique requires twice the computation time of a conventional system.

[1] Numbers in brackets designate References at end of paper.

Complete co-ordinate transformation of the types proposed by Newman and Ojalvo [5] and Craig and Bampton [6] leads to reduced equations that may be solved by conventional techniques. Their primary disadvantage is the difficulty involved in the determination of the transformation matrix. The transformation used by Meirovitch [7] and by Bishop, Gladwell and Michaelson [8] also leads to well conditioned reduced equations and is not overly complex. However, the transformation does require writing a constraint equation based on conservation of momentum.

The technique proposed in this paper overcomes these objections by using a simple, easily obtained transformation matrix to modify the equations of motion to a form that has symmetric and nonsingular mass and stiffness matrices. As a result, the natural frequencies and mode shapes may be determined by conventional iteration and sweeping procedures.

While for clarity of presentation, the development in this paper will be limited to systems with one rigid body mode, the technique can easily be extended to systems with several rigid body modes.

ANALYSIS

The homogeneous equations of motion for an n degree-of-freedom system can generally be written as

$$[M]\{\ddot{x}\} + [K]\{x\} = \{0\} \qquad (1)$$

where $[M]$ is an $n \times n$ intertia matrix and $[K]$ is an $n \times n$ stiffness matrix. Typically, the

solution to Eqs. (1) is written in terms of the natural mode shape matrix and the uncoupled normal co-ordinates as

$$\{x\} = [\phi]\{q\} \tag{2}$$

where $[\phi]$ is the modal matrix composed of the mode shape columns and $\{q\}$ is the normal co-ordinate vector.

The determination of $[\phi]$ is difficult any time a rigid body mode exists, but once it is known $[\phi]$ can be used to uncouple Eqs. (1) in terms of the normal co-ordinates.

Generally, the existence of rigid body modes and the mode shapes associated with them can be determined by observation.

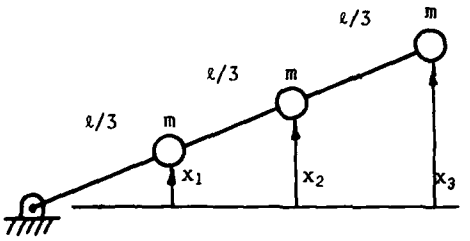

Fig. 1 *System with rigid body mode*

For example, the rigid body mode for the system shown in Fig. 1 is

$$\begin{Bmatrix} x_1 \\ x_2 \\ x_3 \end{Bmatrix} = \begin{Bmatrix} 1/3 \\ 2/3 \\ 1 \end{Bmatrix} q_1$$

The mode shape is therefore

$$\begin{Bmatrix} \phi_{11} \\ \phi_{21} \\ \phi_{31} \end{Bmatrix} = \begin{Bmatrix} 1/3 \\ 2/3 \\ 1 \end{Bmatrix} \tag{3}$$

The rigid body mode shape forms the basis for the co-ordinate transformation.

$$\{x\} = [A]\{y\} \tag{4}$$

where $\{x\}$ is the original co-ordinate vector, $\{y\}$ is the new co-ordinate vector and $[A]$ is the transformation matrix. The first column of this transformation matrix is simply $\{\phi\}_1$ and the lower right hand submatrix is a unity matrix. The general form of the transformation is

$$[A] = \left[\begin{array}{c|ccc} \phi_{11} & 0 & \cdots & 0 \\ \hline \cdot & 1 & 0 & \cdots \\ \cdot & 0 & 1 & \cdots \\ \cdot & \cdot & & \cdot \\ \cdot & \cdot & & \cdot \\ \cdot & \cdot & & 0 \\ \phi_{n1} & 0 & \cdots & 0\ 1 \end{array}\right] \tag{5}$$

For the system shown in Fig. 1, the transformation matrix is

$$[A] = \begin{bmatrix} 1/3 & 0 & 0 \\ 2/3 & 1 & 0 \\ 1 & 0 & 1 \end{bmatrix} \tag{6}$$

After the co-ordinate transformation is performed, the equations of motion are premultiplied by the transpose of the transform matrix. The result is

$$[A]^T[M]\,[A]\{\ddot{y}\} + [A]^T[K][A]\{y\} = \{0\} \tag{7}$$

Since $[M]$ and $[K]$ are symmetric, $[A]^T[M][A]$ and $[A]^T[K][A]$ will also be symmetric. For simplicity, Eqs. (7) can be rewritten in the form

$$[B]\{\ddot{y}\} + [S]\{y\} = \{0\} \tag{8}$$

by letting

$$[B] = [A]^T[M][A]$$

and

$$[S] = [A]^T[K][A]$$

The transformation is based on the rigid body mode shape and because the generalized stiffness associated with that mode is zero, the matrix $[S]$ will have the form

$$[S] = \left[\begin{array}{c|c} 0 & 0 \\ \hline & \\ 0 & SR \end{array}\right] \tag{9}$$

where $[SR]$ is of order (n-1) x (n-1) and is merely $[S]$ without the first row and column. Thus the first equation of Eqs. (8) is

$$B_{11}\ddot{y}_1 = -B_{12}\ddot{y}_2 \cdots B_{1n}\ddot{y}_n$$

or

$$\ddot{y}_1 = -\frac{1}{B_{11}}[B_{12} \cdots B_{1n}] \begin{Bmatrix} \ddot{y}_2 \\ \cdot \\ \cdot \\ \cdot \\ \ddot{y}_n \end{Bmatrix} \tag{10}$$

The remainder of Eqs. (8) can be written as

$$\begin{Bmatrix} B_{21} \\ \cdot \\ \cdot \\ \cdot \\ B_{n1} \end{Bmatrix} \ddot{y}_1 + [BR] \begin{Bmatrix} \ddot{y}_2 \\ \cdot \\ \cdot \\ \cdot \\ \ddot{y}_n \end{Bmatrix}$$

$$+ [SR] \begin{Bmatrix} y_2 \\ \cdot \\ \cdot \\ \cdot \\ y_n \end{Bmatrix} = 0 \qquad (11)$$

where $[BR]$ is $[B]$ without the first row and column. The first term of this equation can be expanded by using Eq. (10) as

$$\begin{Bmatrix} B_{21} \\ \cdot \\ \cdot \\ \cdot \\ B_{n1} \end{Bmatrix} \ddot{y}_1 = -\frac{1}{B_{11}} \begin{Bmatrix} B_{21} \\ \cdot \\ \cdot \\ \cdot \\ B_{n1} \end{Bmatrix} \lfloor B_{12} \cdots B_{1n} \rfloor \begin{Bmatrix} \ddot{y}_2 \\ \cdot \\ \cdot \\ \cdot \\ \ddot{y}_n \end{Bmatrix} \qquad (12)$$

The resulting coefficient matrix on the right hand side is symmetric. The combination and simplification of Eqs. (11) and (12) gives

$$[\bar{M}] \begin{Bmatrix} \ddot{y}_2 \\ \cdot \\ \cdot \\ \cdot \\ \ddot{y}_n \end{Bmatrix} + [\bar{K}] \begin{Bmatrix} y_2 \\ \cdot \\ \cdot \\ \cdot \\ y_n \end{Bmatrix} = 0 \qquad (13)$$

where

$$[\bar{M}] = [BR] - \frac{1}{B_{11}} \begin{Bmatrix} B_{21} \\ \cdot \\ \cdot \\ \cdot \\ B_{n1} \end{Bmatrix} \lfloor B_{12} \cdots B_{1n} \rfloor$$

and $[\bar{K}] = [SR]$

Both $[\bar{M}]$ and $[\bar{K}]$ are symmetric, nonsingular, and of order n-1.

The modified equations of motion in the form of Eqs. (10) can be iterated for eigenvectors and eigenvalues using conventional iteration and sweeping techniques. The eigenvalues will be the natural frequencies of the system but the eigenvectors will not be the natural mode shapes.

The true natural mode shapes may be obtained from the eigenvectors through simple transformations. The system motion can be written in the form

$$\begin{Bmatrix} y_2 \\ \cdot \\ \cdot \\ \cdot \\ y_n \end{Bmatrix} = [\gamma] \begin{Bmatrix} q_2 \\ \cdot \\ \cdot \\ \cdot \\ q_n \end{Bmatrix} \qquad (14)$$

where $[\gamma]$ is the matrix of eigenvectors and

$\begin{Bmatrix} q_2 \\ \cdot \\ \cdot \\ \cdot \\ q_n \end{Bmatrix}$ is the matrix of elastic generalized co-ordinates

Hence, Eq. (10) can be written as

$$\ddot{y}_1 = -\frac{1}{B_{11}} \lfloor B_{12} \cdots B_{1n} \rfloor [\gamma] \begin{Bmatrix} \ddot{q}_2 \\ \cdot \\ \cdot \\ \cdot \\ \ddot{q}_n \end{Bmatrix}$$

Motion in any one of the elastic modes, which are represented by the normal coordinates q_2 through q_n is sinusoidal and thus

$$\ddot{q}_i = -\omega_i^2 q_i \quad \text{for} \quad 1 < i \leq n$$

Consequently, the elastic response in y_1 can be written

$$y_1 = -\frac{1}{B_{11}} \lfloor B_{12} \cdots B_{1n} \rfloor [\gamma] \begin{Bmatrix} q_2 \\ \cdot \\ \cdot \\ \cdot \\ q_n \end{Bmatrix} \qquad (15)$$

Eqs. (14) can thus be expanded to include y_1 as

$$\begin{Bmatrix} y_1 \\ \cdot \\ \cdot \\ \cdot \\ y_n \end{Bmatrix} = [\bar{\gamma}] \begin{Bmatrix} q_2 \\ \cdot \\ \cdot \\ \cdot \\ q_n \end{Bmatrix} \qquad (16)$$

Where $[\bar{\gamma}]$ is $[\gamma]$ augmented by an additional row at the top. That row is given by Eq. (15) as

$$\lfloor \bar{\gamma}_{11} \cdots \bar{\gamma}_1 \rfloor = -\frac{1}{B_{11}} \lfloor B_{12} \cdots B_1 \rfloor [\gamma]$$

It should be noted that $[\bar{\gamma}]$ is of order n x (n-1). The transformation back to the original co-ordinates is then

$$\begin{Bmatrix} x_1 \\ \cdot \\ \cdot \\ \cdot \\ x_n \end{Bmatrix} = [A]\,[\bar{\gamma}] \begin{Bmatrix} q_2 \\ \cdot \\ \cdot \\ \cdot \\ q_n \end{Bmatrix} \qquad (17)$$

The n x (n-1) product of $[A]\,[\bar{\gamma}]$ is the matrix of vibratory mode shapes. Thus

$$[\phi]_{vib} = [A]\,[\bar{\gamma}] \qquad (18)$$

The complete mode shape matrix is obtained by simply including the rigid body modal column. Hence

$$[\phi] = \left[\begin{array}{c|c} & \\ \phi_{RB} & \phi_{vib} \\ & \end{array}\right] \qquad (19)$$

EXAMPLE

The equations of motion for the system shown in Fig. 1 are

$$m \begin{bmatrix} 1 & 0 & 0 \\ 0 & 1 & 0 \\ 0 & 0 & 1 \end{bmatrix} \begin{Bmatrix} \ddot{x}_1 \\ \ddot{x}_2 \\ \ddot{x}_3 \end{Bmatrix} + \frac{54EI}{5\ell^3} \begin{bmatrix} 24 & -21 & 6 \\ -21 & 24 & -9 \\ 6 & -9 & 4 \end{bmatrix} \begin{Bmatrix} x_1 \\ x_2 \\ x_3 \end{Bmatrix} = \begin{Bmatrix} 0 \\ 0 \\ 0 \end{Bmatrix}$$

The rigid body mode shape is given by Eqs. (3) and the transformation matrix, [A], is given by Eqs. (6). The transformed equations become

$$m \begin{bmatrix} 1.555 & .666 & 1 \\ .666 & 1 & 0 \\ 1 & 0 & 1 \end{bmatrix} \begin{Bmatrix} \ddot{y}_1 \\ \ddot{y}_2 \\ \ddot{y}_3 \end{Bmatrix} + \frac{54EI}{5\ell^3} \begin{bmatrix} 0 & 0 & 0 \\ 0 & 24 & -9 \\ 0 & -9 & 4 \end{bmatrix} \begin{Bmatrix} y_1 \\ y_2 \\ y_3 \end{Bmatrix} = \begin{Bmatrix} 0 \\ 0 \\ 0 \end{Bmatrix} \qquad (20)$$

The first of these equations gives

$$\ddot{y}_1 = -.4286\,\ddot{y}_2 - .6428\,\ddot{y}_3 \qquad (21)$$

Substituting this value of $\ddot{y}_1$ into the remainder of Eqs. (20) yields two equations in the unknowns y_2 and y_3:

$$m \begin{bmatrix} .7143 & -.4286 \\ -.4286 & .357 \end{bmatrix} \begin{Bmatrix} \ddot{y}_2 \\ \ddot{y}_3 \end{Bmatrix} + \frac{54EI}{5\ell^3} \begin{bmatrix} 24 & -9 \\ -9 & 4 \end{bmatrix} \begin{Bmatrix} y_2 \\ y_3 \end{Bmatrix} = \begin{Bmatrix} 0 \\ 0 \end{Bmatrix}$$

These equations, which have symmetric and nonsingular coefficient matrices, can be iterated to their eigenvalues and eigenvectors by using conventional methods. The results are

$$[\gamma] = \begin{bmatrix} .341 & 1.141 \\ 1 & 1 \end{bmatrix}$$

and $\omega_2^2 = 47.66 \dfrac{EI}{m\ell^3}$

and $\omega_3^2 = 513.93 \dfrac{EI}{m\ell^3}$

These results can be used to write the y vector in terms of the normal co-ordinates as

$$\begin{Bmatrix} y_2 \\ y_3 \end{Bmatrix} = \begin{bmatrix} .341 & 1.141 \\ 1 & 1 \end{bmatrix} \begin{Bmatrix} q_2 \\ q_3 \end{Bmatrix}$$

Eq. (21) can be used to determine y_1 by

$$y_1 = -\begin{bmatrix} .4286 & .6428 \end{bmatrix} \begin{bmatrix} .341 & 1.141 \\ 1 & 1 \end{bmatrix} \begin{Bmatrix} q_2 \\ q_3 \end{Bmatrix}$$

Thus the complete y vector becomes

$$\begin{Bmatrix} y_1 \\ y_2 \\ y_3 \end{Bmatrix} = \begin{bmatrix} -.7889 & -1.1318 \\ .341 & 1.141 \\ 1 & 1 \end{bmatrix} \begin{Bmatrix} q_2 \\ q_3 \end{Bmatrix}$$

The y vector is easily transformed back to the x co-ordinates by

$$\begin{Bmatrix} x_1 \\ x_2 \\ x_3 \end{Bmatrix} = \begin{bmatrix} 1/3 & 0 & 0 \\ 2/3 & 1 & 0 \\ 1 & 0 & 1 \end{bmatrix} \begin{bmatrix} -.7889 & -1.1318 \\ .341 & 1.141 \\ 1 & 1 \end{bmatrix} \begin{Bmatrix} q_2 \\ q_3 \end{Bmatrix}$$

Thus

$$\begin{Bmatrix} x_1 \\ x_2 \\ x_3 \end{Bmatrix} = \begin{bmatrix} -1.25 & 2.861 \\ -.877 & -2.93 \\ 1 & 1 \end{bmatrix} \begin{Bmatrix} q_2 \\ q_3 \end{Bmatrix}$$

Addition of the rigid body mode as the first column completes the modal matrix as

$$[\phi] = \begin{bmatrix} .333 & -1.25 & 2.861 \\ .666 & -.877 & -2.93 \\ 1 & 1 & 1 \end{bmatrix}$$

CONCLUSION

A method has been presented for finding the mode shapes and natural frequencies of a multi-degree-of-freedom system which has a rigid body mode. The technique has the primary advantage of employing a simple transformation matrix that is easily obtained in terms of the rigid body mode. The transformed equations have symmetric and non-singular inertia and stiffness matrices. As a result, conventional computer-oriented iteration and sweeping procedures can be used for the determination of frequencies and mode shapes.

Although the necessary transformations appear complicated, they are operationally quite simple and can be easily programmed for computer solution. The majority of the effort involved in the application of this method is expended in the determination of the eigenvalues and eigenvectors of the modified equations as is true of all of the existing methods for the solution to this type of system. The effort is minimized in this case, however, since existing computer programs can be utilized.

The development illustrated has been for a system with one rigid body mode; however, the method can easily be extended to include several rigid body modes.

References

1. Timoshenko, S. P., Vibrations Problems in Engineering, 3rd Ed., D. Van Nostrand Co., New York, 1955, pp 188-194.

2. Anderson, R. A., Fundamentals of Vibrations, Macmillan, New York, 1967, pp 179-182, pp 207-211.

3. Thomson, W. T., Vibration Theory and Applications, Prentice-Hall, New Jersey, 1965, pp 222-228.

4. Straight, J. W., "Solution to Beam Vibrations Problems with Mixed Response-Excitation Input Information," AIAA Journal, Vol. 7, Jan. 1969, pp 73-77.

5. Newman, M. and Ojalvo, I. U., "Nonzero Free-Free Frequencies of Structures Idealized by Matrix Methods," AIAA Journal, Vol. 7, Dec. 1969, pp 2343-2344.

6. Craig, R. Jr., and Bampton, M. C. C., "On the Iterative Solution of Semi definite Eigenvalue Problems," Aeronautical Journal, Vol. 75, Apr. 1971, pp 287-290.

7. Meirovitch, L., Analytical Methods in Vibrations, Macmillan, New York, 1967, pp 112-115.

8. Bishop, R. E. D., Gladwell, G. M. L., and Michaelson, S., The Matrix Analysis of Vibration, Cambridge University Press, 1965, pp 80-86.

ON THE FORCED VIBRATION OF TRIANGULAR PLATES (U)

H. M. Negm, S. Chander, B. K. Donaldson
Department of Aerospace Engineering
University of Maryland
College Park, Maryland 20742

(U) This article deals with the application of the extended field method of approximate analysis to the forced vibration of thin triangular plates with clamped or simple support boundary conditions. The numerical results show that greater accuracy per degree of freedom can be expected with the extended field method than with any of the presently popular approximate methods of analysis.

INTRODUCTION

(U) Thin triangular plates have relatively few practical uses. Nevertheless, they always have been of particular interest to analysts because of the challenge posed by their geometry. Some exact solutions do exist for some special geometries and special static loadings [1] but there is no general static or sinusoidal vibration solution. Hence analysts must be concerned with approximate solutions. The three most popular methods of approximate structural analysis today are the finite element deflection method, the finite difference method, and the Rayleigh-Ritz method. Each of these three methods can be used to provide good engineering answers, but each has small drawbacks when applied to triangular plates. When deflection finite elements are used to model a triangular plate, it is of course necessary to employ triangular plate elements. The popular Clough triangle [2] tends to be overly stiff, so a non-compatible rectangular element would be a reasonable choice for the majority of the model as shown in Figure 1. This figure shows that there is the small problem of the aspect ratios of the rectangles varying across the field. This causes one side of the triangular plate to be slightly less stiff in one direction, while the other side of the triangular plate is slightly less stiff in the perpendicular direction. A finite difference solution would have to accept three different grid spacings in order to place grid points exactly on the triangular plate boundary. The Rayleigh-Ritz method is also a bit awkward when dealing with a triangular field. It is not certain which coordinate system and which set of functions would produce the simplest integrations. Again, while each of the above three methods can produce good deflection results, none of the three is without some small complication. Furthermore, as is cautioned for example in reference [3], ". . . a finite difference solution requires an advance to one or more finer meshes so that convergence may be examined, (and) a series solution requires investigation of the effect of including additional terms." Therefore it is worthwhile to consider new approximate methods of solution.

This paper deals with a new approximate method of analysis called the extended field method of analysis. The purpose of this paper is to report on the first application of the extended field method to thin triangular plates. These plates will be taken to be Hookean, homogeneous, isotropic, and of constant thickness. The specific problem considered is one of forced sinusoidal vibration.

A detailed explanation of the extended field method and some of its applications can be found in References [3, 4, and 5]. However, because of its newness, a very brief description of the method follows. The extended field method, as applied to the forced vibration of thin plates, begins with a rectangular plate which is not loaded over its surface, but is forced to vibrate due to applied edge moments and shears along just one side of the plate. The other three sides are taken to be simply supported. The deflecting edge conditions are described ordinarily in terms of the resulting edge vertical deflection and normal slope amplitudes. These amplitudes are in turn described in terms of Fourier sine series. A Lévy series solution

is easily obtained in terms of those Fourier series coefficients. This Lévy solution and three similar ones for the other three sides of the rectangle are then superimposed on the Navier solution for a simply supported rectangular plate subjected to a surface pressure which has an arbitrary spatial distribution, but has the same vibration frequency as the edge loads. The result of this superposition is the extended plate (or extended field). The plate to be analyzed, called the actual plate, is geometrically located within the boundaries of the extended plate in a convenient manner. Then the simple, arbitrary boundary conditions of the extended plate, which are at the disposal of the analyst, are used to achieve the otherwise intractable boundary conditions of the actual plate. Since the pressure amplitude over the extended plate is chosen to coincide with that of the actual plate within the boundaries of the actual plate, then the extended field solution is also the actual plate solution within the boundaries of the actual plate.

It proved possible to apply the extended field method to triangular plates in several different ways. The most significant ways are discussed below. Right angle triangular plates are discussed first, and the lessons learned from that application are used in the analysis of triangular plates of general geometry.

THE RIGHT ANGLE TRIANGULAR PLATE

To locate a triangular actual plate within a rectangular extended plate requires, of course, that one or more of the triangular plate boundaries be oblique to the boundaries of the rectangular extended plate. In the case of a right angle triangular plate, the simplest arrangement is as shown in Figure 2 when $f = b$ and $g = 0$. For the sake of simplicity, let the triangular plate boundary conditions be such that the oblique edge is clamped, and the other two edges are simply supported. Hence it will be called a CSS triangular plate. In the extended field method, simply supported edges which are coincident with extended field edges are obtained by just omitting from the total extended field solution those Lévy solutions that correspond to the simply supported edges. Thus the only equations that need be written are those that require that the vertical deflection amplitude and the normal slope amplitude along the oblique edge be zero; i. e.

$$W\left(\frac{a}{\ell}\xi, -\frac{b}{\ell}\xi + b\right) = 0 \tag{1a}$$

$$W_{,z}\left(\frac{a}{\ell}\xi, -\frac{b}{\ell}\xi + b\right) = 0 \tag{1b}$$

where W is the deflection amplitude, $x = (a/\ell)\xi$, $y = -(b/\ell)\xi + b$, and a subscripted independent variable following a comma indicates partial differentiation with respect to that subscript. These symbols are those of Reference [4], and are explained in Appendix I. Using the chain rule, the second of the above equations is rewritten for convenience as

$$(b/a)W_{,x} + W_{,y} = 0 \tag{1c}$$

Equations (1a) and (1c) are put into a form convenient for numerical calculation by application of the Galerkin technique which renders the error in approximating the boundary conditions orthogonal, in this case, to an uninterrupted, finite set of sine functions. That is, after multiplying by $(2/\ell)\sin(m\pi\xi/\ell)$ and integrating over ξ from 0 to ℓ, the oblique edge boundary conditions become

$$\begin{aligned}
&\sum_{n=1}^{N} [(U_{9,m,n}E_{1,n} - U_{10,m,n}E_{2,n})h_{1,n} \\
&+ (U_{9,m,n}E_{3,n} - U_{10,m,n}E_{4,n})k_{1,n} \\
&+ (U_{11,m,n}E_{5,n} - U_{12,m,n}E_{6,n})h_{2,n} \\
&+ (U_{11,m,n}E_{7,n} - U_{12,m,n}E_{8,n})k_{2,n}] = -P_{9,m}
\end{aligned} \tag{2a}$$

$$\begin{aligned}
&\frac{f-g}{a}\sum_{n=1}^{N} [-(U_{17,m,n}E_{17,n} - U_{18,m,n}E_{18,n})h_{1,n} \\
&- (U_{17,m,n}E_{19,n} - U_{18,m,n}E_{20,n})k_{1,n} \\
&+ (U_{19,m,n}E_{21,n} - U_{20,m,n}E_{22,n})h_{2,n} \\
&+ (U_{19,m,n}E_{23,n} - U_{20,m,n}E_{24,n})k_{2,n}] \\
&+ \sum_{n=1}^{N} [(U_{13,m,n}E_{9,n} - U_{14,m,n}E_{10,n})h_{1,n} \\
&+ (U_{13,m,n}E_{11,n} - U_{14,m,n}E_{12,n})k_{1,n} \\
&+ (U_{15,m,n}E_{13,n} - U_{16,m,n}E_{14,n})h_{2,n} \\
&+ (U_{15,m,n}E_{15,n} - U_{16,m,n}E_{16,n})k_{2,n}] \\
&= -\frac{f-g}{a}P_{11,m} - P_{10,m}
\end{aligned} \tag{2b}$$

for $m = 1,2,\ldots,I$. These are the same as Equations (50) and (51) of Reference [4], but with $f = b$ and $g = 0$, and the inclusion of a minus sign erroneously omitted in that reference. The quantities $h_{1,n}$, $k_{1,n}$, $h_{2,n}$, and $k_{2,n}$, where $n = 1,2,\ldots,N$, are the extended plate edge Fourier series coefficients, and, as such, they

are the only unknown quantities in Equations (2). Thus there are four sets of unknown quantities and just two sets of equations. This situation had not been encountered previously.

The most successful way of resolving the disparity between the number of sets of unknowns and the number of sets of equations turned out to be simply requiring the error of approximation to be orthogonal to twice as many sine functions as there are Fourier series coefficients in any one of the four sets of unknowns; i.e. setting I = 2N. Typical numerical results are shown in Table 1, for which the following values were input

$$E = 1.05 \times 10^{7} \text{psi}$$

$$\rho = 2.609 \times 10^{-3} \text{ lbs-sec/in}^4$$

$$\mu = 0.3$$

$$a = 20.0 \text{ in.}$$

$$b = 20.0 \text{ in.}$$

$$d = 0.25 \text{ in.}$$

$$\omega = 100 \text{ rad/sec}$$

The amplitude of the applied load was a constant 1.0 psi, which causes its Fourier series coefficient $p_{m,n}$ to have the value $(16/\pi^2 mn)$ when m and n are both odd, and the value zero otherwise. (This choice of loading is neither advantageous nor disadvantageous.) The last unchanging item of input was the maximum value for the dummy indices of the loading series $P_{9,n}$; $P_{10,n}$, and $P_{11,n}$. A value of 85 was sufficient. As further explanation of Table 1, note that each value of N indicates a new finite series solution, in this case, using 4N unknown quantities. Presentation of the results to eight significant figures is justified by the fact that all computations were performed using double precision arithmetic.

The accuracy of the numerical results shown in Table 1 was checked by using the NASTRAN finite element program. The finite element model is shown in Figure 3, and because of symmetry, the model involves only 65 unconstrained degrees of freedom. The numerical results obtained for the point (14,16) were $W = 3.665 \times 10^{-3}$ in., $W,x = -7.037 \times 10^{-5}$ and $W,y = 3.911$. Taking into account the differences in sign convention, these results differ from those of Table 1 by less than 2%, and thus substantiate the correctness of the extended field method digital computer program.

Table 2 shows similar numerical results when the plate aspect ratio is changed so that a = 20.0 in. and now b = 10.0 in. with all other input quantities unchanged. The numerical results again show truly excellent convergence, but not quite as good as when a/b = 1. Similar results were obtained when a/b had a value of three. At all aspect ratios there was no significant change in convergence as the point at which amplitudes were calculated was shifted from place to place within the actual plate.

A somewhat less successful extended field analysis involved dividing the hypotenuse at the arbitrary point $\xi = q\ell$ and writing 2N equations for one segment, and 2N equations for the other segment, and then solving for the 4N unknown Fourier series coefficients. As might be expected, the quality of convergence varied considerably with the selection of the arbitrary dividing point on the hypotenuse of the triangular plate. Again the quality of convergence varied slightly with plate aspect ratio, but not with forcing frequency or with the point at which amplitudes were calculated. Table 3 shows typical results. For an optimum choice of q, seven digit convergence can be obtained with just sixty degrees of freedom. However a non-optimum, but still reasonable choice of q can drop the quality of convergence to just three significant figures. The optimum choice of q varies with the plate aspect ratio and it is possible to present a graph of optimum q versus (a/b). However, the first approach discussed seems to be preferable even when an optimum q is used in the second approach. Before leaving the discussion of this approach note that the results shown in Table 2 and the best results of Table 3 provide mutual confirmation.

A third approach to the right angle triangular plate was to simply assign arbitrary constants of proportionality, α and β, between similar extended plate edge amplitude Fourier series coefficients; i.e. write

$$h_{2,n} = \alpha h_{1,n}$$

$$k_{2,n} = \beta k_{1,n} \qquad (3)$$

for n = 1,2,...,N. This of course, reduces the number of unknown quantities, and therefore the number of required equations, to 2N. The value (a/b) was the best discovered for α and β, but using this value never produced convergence beyond three significant figures within the use of thirty unknowns, i.e. at an N equivalent to 7 or 8 for the previously discussed work. Thus this approach was deemed to be a poor one.

THE TRIANGULAR PLATE OF GENERAL GEOMETRY

As shown in Figures 4 and 5, CSC boundary conditions were chosen for the general triangular plate to be investigated. As before, this choice of simple support and clamped boundary conditions simplifies the analysis somewhat by requiring only 6N, as opposed to 8N, unknown Fourier series coefficients. This in turn shortens somewhat lengthy equations. This choice also avoids free edges, which when they are

adjacent to each other and thus producing a free corner, make satisfactory convergence of the series solution difficult to achieve. An isosceles triangular plate with its one axis of symmetry was chosen so as to use the symmetry to provide a check on the digital computer program solution. It is worth reiterating, however, that the extended field method in no way relies upon symmetry.

Two approaches to triangular plates of general geometry were investigated. They both are based on the previous success with right angle triangular plates. The first approach here is just a variation on the first approach of the previous section. That is, the oblique line of Figure 2 was used with two different inclinations in the same extended plate to produce a triangular actual plate. The two ways that this can be accomplished are indicated in Figures 4 and 5. In the algebraic solution the y-coordinates of the end points of the upper oblique line are called f and g as before, while those of the lower oblique line are named $\bar{f}$ and $\bar{g}$. Quantities calculated from f and g then also receive a distinguishing upper bar.

Using a second oblique line requires the addition to the situation of Figure 2 of forcing extended plate edge displacement amplitudes along the edge y = b. The Fourier series coefficients associated with those amplitudes are $h_{4,n}$ and $k_{4,n}$ for vertical deflection and normal slope, respectively. Note in passing that if other than simple support boundary conditions were to be selected for the third side, x=a, similar Fourier series coefficients $h_{3,n}$ and $k_{3,n}$ would also be necessary. The equations that produce clamped boundary conditions along the upper oblique line are Equations 4a and 4b. The Fourier series coefficients $h_{3,n}$ and $k_{3,n}$, and their factors, have been included in these equations for the sake of completeness. Of course, $h_{3,n}$ and $k_{3,n}$ were set equal to zero for the present numerical calculations.

$$\sum_{n=1}^{N} [(U_{9,m,n}E_{1,n}-U_{10,m,n}E_{2,n})h_{1,n} + (U_{9,m,n}E_{3,n}-U_{10,m,n}E_{4,n})k_{1,n} + (U_{11,m,n}E_{5,n}-U_{12,m,n}E_{6,n})h_{2,n} + (U_{11,m,n}E_{7,n} - U_{12,m,n}E_{8,n})k_{2,n} + (U_{21,m,n}E_{1,n}-U_{22,n}E_{2,n})h_{3,n} - (U_{21,m,n}E_{3,n}-U_{22,m,n}E_{4,n})k_{3,n} + (U_{23,m,n}E_{5,n}-U_{24,m,n}E_{6,n})h_{4,n} (- U_{23,m,n}E_{7,n}-U_{24,m,n}E_{8,n})k_{4,n}] = - P_{9,m} \quad (4a)$$

$$(\frac{f-g}{a}) \sum_{n=1}^{N} [-(U_{17,m,n}E_{17,n}-U_{18,m,n}E_{18,n})h_{1,n} - (U_{17,m,n}E_{19,n}-U_{18,m,n}E_{20,n})k_{1,n} + (U_{19,m,n}E_{21,n}-U_{20,m,n}E_{22,n})h_{2,n} + (U_{19,m,n}E_{23,n}-U_{20,m,n}E_{24,n})k_{2,n} + (U_{25,m,n}E_{17,n}-U_{26,m,n}E_{18,n})h_{3,n} - (U_{25,m,n}E_{19,n}-U_{26,m,n}E_{20,n})k_{3,n} + (U_{29,m,n}E_{21,n}-U_{30,m,n}E_{22,n})h_{4,n} - (U_{29,m,n}E_{23,n}-U_{30,m,n}E_{24,n})k_{4,n}] + \sum_{n=1}^{N} [(U_{13,m,n}E_{9,n}-U_{14,m,n}E_{10,n})h_{1,n} + (U_{13,m,n}E_{11,n}-U_{14,m,n}E_{12,n})k_{1,n} + (U_{15,m,n}E_{13,n}-U_{16,m,n}E_{14,n})h_{2,n} + (U_{15,m,n}E_{15,n} - U_{16,m,n}E_{16,n})k_{2,n} + (U_{27,m,n}E_{9,n} - U_{28,m,n}E_{10,n})h_{3,n} - (U_{27,m,n}E_{11,n} - U_{28,m,n}E_{12,n})k_{3,n} + (U_{32,m,n}E_{14,n} - U_{31,m,n}E_{13,n})h_{4,n} - (U_{32,m,n}E_{16,n} - U_{31,m,n}E_{15,n})k_{4,n}] = - \frac{f-g}{a} P_{11,m} - P_{10,m} \quad (4b)$$

for m = 1,2, . . ., I. The equations that clamp the lower oblique line have exactly the same form as those above except that the U and P factors are replaced by $\bar{U}$ and $\bar{P}$ factors. Thus there are 6N unknown Fourier series coefficients and 4I equations. Thus, by the first approach, which is simply expanding the number of equations in order to match the number of unknowns, N is required to be even and I must equal 3N/2. Numerical solutions based on this approach and using first the geometry pictured in Figure 4 and then the geometry pictured in Figure 5 produced, for the same actual plate, the results listed in Table 4. All other input data to the solution were the same as that for the right angle triangular plates. Once again the results show remarkable convergence, and engineering accuracy is obtained with just twelve unknowns.

The second approach was to patch back to back two right angle triangular plates by

requiring continuity across their common boundary of vertical deflection, normal slope, moment, and shear amplitudes. Thus the second approach employs two extended fields, one for each of the actual right angle triangular plates. Therefore the second approach requires four (one of which turns out to be trivial) more sets of equations and five more sets of unknown Fourier series coefficients, which is more costly of computer time. See Figure 6. There is an uneveness to the second approach. The total of $7I$ equations to solve for the $11N$ unknowns cannot be equally distributed. The oblique edges get twice as many equations per boundary condition as does the common boundary per continuity equation. The numerical solutions obtained with the second approach ranged from excellent (six figure convergence) to just satisfactory (nearly three figure convergence) at 110 degrees of freedom. Perhaps more effort could bring up the rear, but the extensive work that was done clearly indicated certain trends. The quality of convergence decreased as the ratio of the triangle height to base increased, and was worse in the immediate vicinity of the common boundary. Thus for the particular problem of triangular plates, a combination of the oblique line equations within a single extended field produces the best numerical results.

In conclusion, the extended field method can be successfully applied to any triangular plate with clamped or simple support boundary conditions. Furthermore, with the extended field method, the accuracy that is obtained per degree of freedom is greater than that which can be expected using finite element techniques. Other experience shows that the same can be said for the finite difference and Rayleigh-Ritz methods.

REFERENCES

1. S. Timoshenko and S. Woinowsky-Krieger 1957 Theory of Plates and Shells. New York: McGraw-Hill Book Co., Second Edition.

2. R.W. Clough and J.L. Tocher 1965 Proceedings of Conference on Matrix Methods in Structural Mechanics. AFFDL-TR-66-80. pp. 515-545 Finite Element Stiffness Matrices for Analysis of Plate Bending.

3. L.S.D. Morley 1965 Skew Plates and Structures. New York: The Macmillan Co.

4. B.K. Donaldson 1973 Journal of Sound and Vibration 30, 397-417. A New Approach to the Forced Vibration of Thin Plates.

5. B.K. Donaldson 1973 Journal of Sound and Vibration 30, 419-435. A New Approach to the Forced Vibration of Flat Skin-Stringer-Frame Structures.

6. B.K. Donaldson and S. Chander 1973 Journal of Sourd and Vibration 30, 437-444. Numerical Results for Extended Field Method Applications.

TABLE 1

Deflection and slope amplitudes at the point x = 14 in. and y = 16 in. on the CSS right angle triangular plate of Figure 1, where a = b = f = 20.0 in., and g = 0.

N	W ($\times 10^{-2}$ in.)	$W_{,x}(\times 10^{-4})$	$W_{,y}(\times -10^{-3})$
1	.42188387	.56624721	.47820823
2	.37131614	.71969010	.38567137
3	.37014838	.70354928	.38471381
4	.37015225	.70248466	.38464112
5	.37015138	.70247251	.38463696
6	.37015143	.70246985	.38463677
7	.37015143	.70246988	.38463676
8	.37015143	.70246987	.38463676
9	.37015143	.70246987	.38463676
10	.37015143	.70246987	.38463676

TABLE 2

Deflection and slope amplitudes at the point (15,7) on the CSS triangular plate of Figure 1 where a = 20.0 in, b = f = 10.0 in., and g = 0.

N	$W(\times 10^{-3}$ in.)	$W_{,x}(10^{-4})$	$W_{,y}(\times -10^{-4})$
1	.70867714	.49412800	.04026906
2	.73318264	.60272816	.21260135
3	.72648866	.58495714	.15358350
4	.72719485	.57746950	.15654686
5	.72720480	.57832247	.15699536
6	.72719720	.57833070	.15687139
7	.72719889	.57831298	.15688012
8	.72719918	.57831674	.15688320
9	.72719925	.57831734	.15688276
10	.72719930	.57831739	.15688288
11	.72719932	.57831749	.15688296
12	.72719933	.57831754	.15688297
13	.72719934	.57831757	.15688299
14	.72719934	.57831758	.15688299

TABLE 3

The vertical deflection amplitude at the point (15,7) on the CSS triangular plate of Figure 1, where a = 20.0 in, b = f = 10.0 in., g = 0, as calculated using a divided hypotenuse.

N	W (x 10^{-3} in.)		
	q = 0.52	q = 0.42	q = 0.371
1	.82327238	.76376977	.73759322
2	.73542778	.74006897	.74097488
3	.72592877	.72624329	.72656214
4	.72880698	.72745690	.72717270
5	.72668159	.72717189	.72720557
6	.72754232	.72722576	.72720548
7	.72700265	.72718869	.72719656
8	.72732688	.72720436	.72719986
9	.72711372	.72719673	.72719886
10	.72725957	.72720063	.72719942
11	.72715539	.72719859	.72719923
12	.72723244	.72719974	.72719936
13	.72717373	.72719910	.72719931
14	.72721963	.72719948	.72719935
15	.72718270	.72719926	.72719934

TABLE 4

Deflection amplitude at point A of the C$C triangular plate of Figs. 4 and 5.

N	W_A(x10^{-2}in.)	
	Scheme of Fig. 4	Scheme of Fig. 5
2	.16932157	.16197112
4	.16693520	.16655533
6	.16685213	.16685281
8	.16685047	.16685010
10	.16685059	.16685060
12	.16685067	.16685068
14	.16685069	.16685072
16	.16685070	.16685071

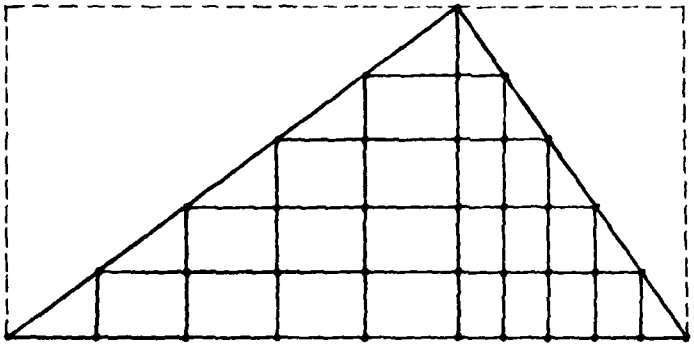

Figure 1. Typical finite element layout or finite difference grid for a general triangle.

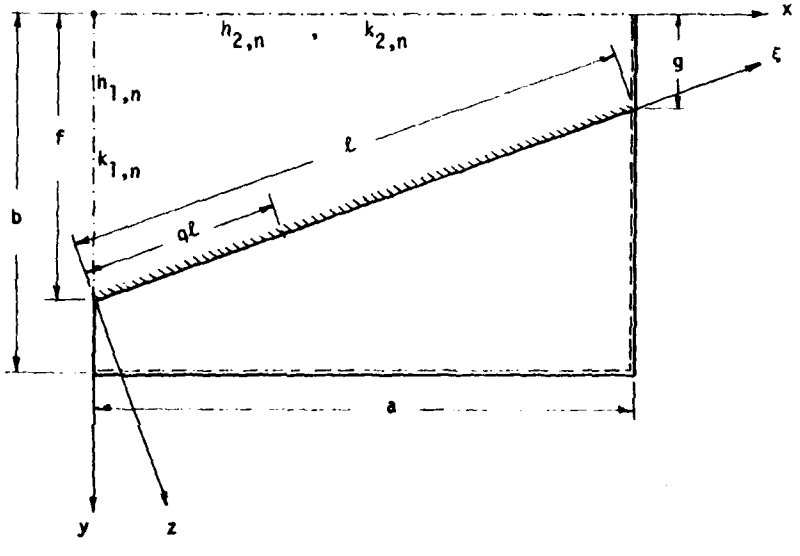

Figure 2. Extended field Fourier series coefficients and geometric quantities needed to imbed a right angle triangular plate within a rectangular extended field.

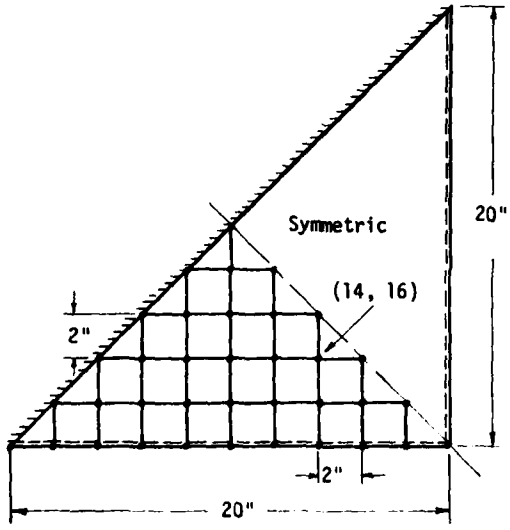

Figure 3. Division scheme for symmetric CSS triangular plate for NASTRAN finite element analysis.

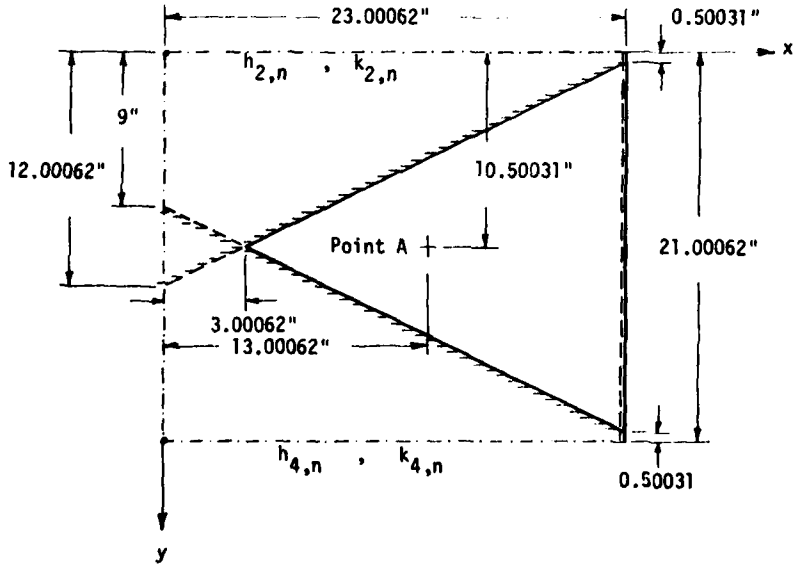

Figure 4. An extended field arrangement for an isosceles triangular actual plate with a twenty inch height and base.

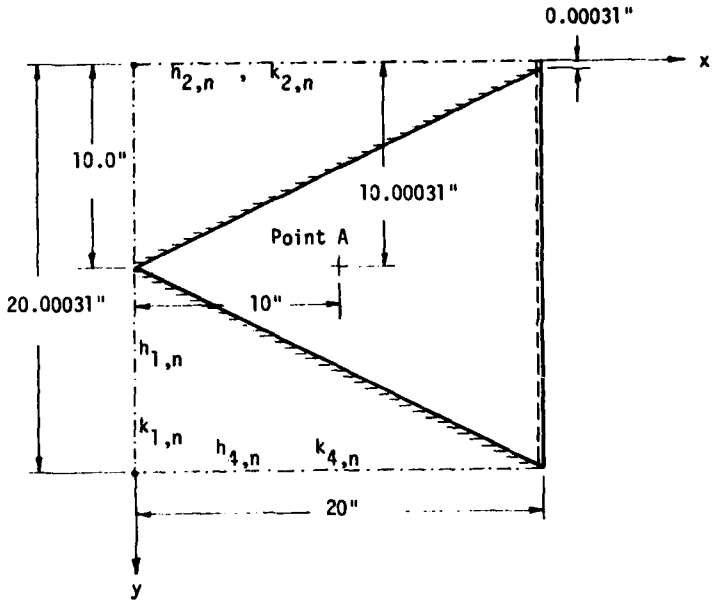

Figure 5. Another extended field arrangement for an isosceles triangular actual plate with a twenty inch height and base.

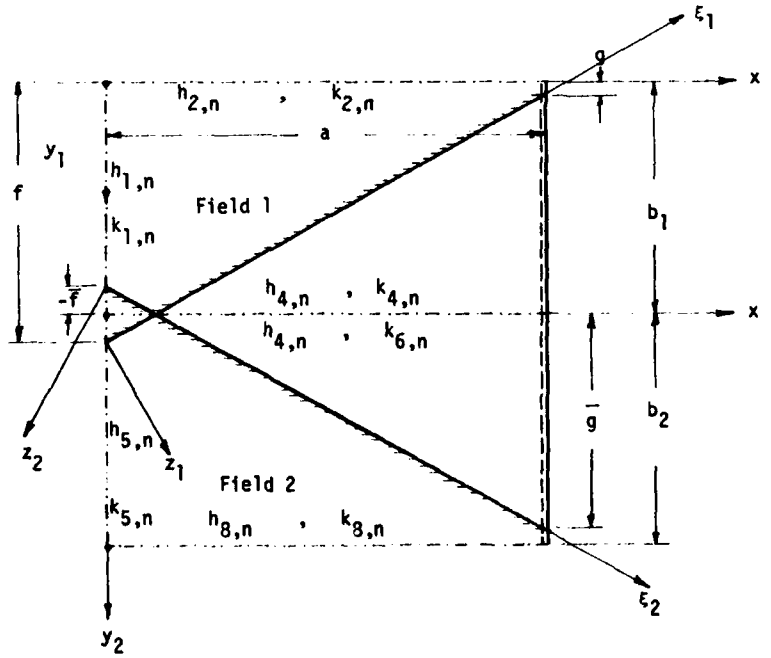

Figure 6. Geometrical arrangement and Fourier series coefficients for the analysis of a general CSC triangular plate by use of two separate extended fields.

APPENDIX I

Symbols

a	extended plate length in x-coordinate direction
b	extended plate length in y-coordinate direction
d	plate thickness
$f,g,\bar{f},\bar{g}$	y-coordinates of the end points of an oblique cut in an extended plate
$h_{j,n}$	nth Fourier series coefficient of the vertical deflection amplitude on the jth extended plate edge
$k_{j,n}$	nth Fourier series coefficient of the normal slope on the jth extended plate edge
ℓ	length of an oblique cut in an extended plate
m,n,p	summation indices
$\hat{n}$	$\frac{b}{\pi}\left[\frac{\rho\omega^2 d}{D}\right]^{1/4}$
$\tilde{n}$	$\frac{a}{\pi}\left[\frac{\rho\omega^2 d}{D}\right]^{1/4}$
$P_{m,n}$	double Fourier series coefficient of the pressure amplitude function on the extended plate
r_n	$\left[\left(\frac{n\pi}{b}\right)^2 + \left(\frac{\rho\omega^2 d}{D}\right)^{1/2}\right]^{1/2}$
s_n	$\left[\left(\frac{n\pi}{b}\right)^2 - \left(\frac{\rho\omega^2 d}{D}\right)^{1/2}\right]^{1/2}$ if $n > \hat{n}$; $\left[-\left(\frac{n\pi}{b}\right)^2 + \left(\frac{\rho\omega^2 d}{D}\right)^{1/2}\right]^{1/2}$ if $n < \hat{n}$
u_n	$\left[\left(\frac{n\pi}{a}\right)^2 + \left(\frac{\rho\omega^2 d}{D}\right)^{1/2}\right]^{1/2}$
v_n	$\left[\left(\frac{n\pi}{a}\right)^2 - \left(\frac{\rho\omega^2 d}{D}\right)^{1/2}\right]^{1/2}$ if $n > \tilde{n}$; $\left[-\left(\frac{n\pi}{a}\right)^2 + \left(\frac{\rho\omega^2 d}{D}\right)^{1/2}\right]^{1/2}$ if $n < \tilde{n}$
x,y	plate Cartesian coordinates
z	coordinate normal to an oblique cut
D	plate stiffness factor, $Ed^3/12(1-\mu^2)$
E	Young's modulus
$E_{j,n}$	constant coefficients of plate edge deflection equations; see Appendix II
M,N,I	maximum values for the indices
$\hat{N}$	$\mathrm{sgn}(n-\hat{n})$
$\tilde{N}$	$\mathrm{sgn}(n-\tilde{n})$
$P_{j,n},\bar{P}_{j,n}$	constants of the pressure loading defined in Appendix II
$U_{j,m,n},\bar{U}_{j,m,n}$	constant coefficients defined in Appendix II
W	plate lateral deflection amplitude
μ	Poisson's ratio
ξ	coordinate along oblique portion of an extended plate
ρ	mass density
ω	circular frequency of forced vibration
$\Pi_{m,n}$	$\frac{P_{m,n}}{D\left(\left[\left(\frac{m\pi}{a}\right)^2 + \left(\frac{n\pi}{b}\right)^2\right]^2 - \frac{\rho\omega^2 d}{D}\right)}$

and

$$\sin(h)s_n a = \begin{cases} \sin s_n a & \text{if } n < \hat{n} \\ \sinh s_n a & \text{if } n > \hat{n} \end{cases}$$

etc.

$$\cos(h)v_n b = \begin{cases} \cos v_n b & \text{if } n < \tilde{n} \\ \cosh v_n b & \text{if } n > \tilde{n} \end{cases}$$

APPENDIX II

Definitions:

$$D_{1,m,n} = \left\{\left(\left[\frac{n\pi}{b}(g-f) - m\pi\right]^2 + r_n^2 a^2\right)\left(\left[\frac{n\pi}{b}(g-f) + m\pi\right]^2 + r_n^2 a^2\right)\right\}^{-1}$$

$$D_{2,m,n} = \left\{\left(\left[\frac{n\pi}{b}(g-f) - m\pi\right]^2 + \hat{N}s_n^2 a^2\right)\left(\left[\frac{n\pi}{b}(g-f) + m\pi\right]^2 + \hat{N}s_n^2 a^2\right)\right\}^{-1}$$

$$D_{3,m,n} = \left\{\left[(m-n)^2\pi^2 + (g-f)^2 u_n^2\right]\left[(m+n)^2\pi^2 + (g-f)^2 u_n^2\right]\right\}^{-1}$$

$$D_{4,m,n} = \left\{\left[(m-n)^2\pi^2 + \tilde{N}(g-f)^2 v_n^2\right]\left[(m+n)^2\pi^2 + \tilde{N}(g-f)^2 v_n^2\right]\right\}^{-1}$$

$$E_{1,n} = J_n s_n \cos(h)\, s_n a$$

$$E_{2,n} = J_n r_n \cosh r_n a$$

$$E_{3,n} = J_n \sin(h)\, s_n a$$

$$E_{4,n} = J_n \sinh r_n a$$

$$E_{5,n} = L_n v_n \cos(h)\, v_n b$$

$$E_{6,n} = L_n u_n \cosh u_n b$$

$$E_{7,n} = L_n \sin(h)\, v_n b$$

$$E_{8,n} = L_n \sinh u_n b$$

$$E_{9,n} = \frac{n\pi}{b} E_{1,n}$$

$$E_{10,n} = \frac{n\pi}{b} E_{2,n}$$

$$E_{11,n} = \frac{n\pi}{b} E_{3,n}$$

$$E_{12,n} = \frac{n\pi}{b} E_{4,n} \qquad E_{19,n} = r_n E_{3,n}$$

$$E_{13,n} = v_n E_{6,n} \qquad E_{20,n} = s_n E_{4,n}$$

$$E_{14,n} = u_n E_{5,n} \qquad E_{21,n} = \frac{n\pi}{a} E_{5,n}$$

$$E_{15,n} = v_n E_{8,n} \qquad E_{22,n} = \frac{n\pi}{a} E_{6,n}$$

$$E_{16,n} = u_n E_{7,n} \qquad E_{23,n} = \frac{n\pi}{a} E_{7,n}$$

$$E_{17,n} = r_n E_{1,n} \qquad E_{24,n} = \frac{n\pi}{a} E_{8,n}$$

$$E_{18,n} = s_n E_{2,n}$$

$$J_n = [s_n \sinh r_n a \cos(h) s_n a - r_n \cosh r_n a \sin(h) s_n a]^{-1}$$

$$L_n = [v_n \sinh u_n b \cos(h) v_n b - u_n \cosh u_n b \sin(h) v_n b]^{-1}$$

$$P_{9,n} = \begin{cases} \sum_{m}^{M} \Pi_{n,m} \sin \frac{m\pi f}{b} & \text{if } n = p \text{ and } g = f \\ \pm \frac{1}{2} \sum_{p}^{M} \sum_{m}^{M} \Pi_{p,m} \sin \frac{m\pi f}{b} & \text{if } (n-p)b = \pm (g-f)m \text{ and } g \neq f \\ -\frac{1}{2} \sum_{p}^{M} \sum_{m}^{M} \Pi_{p,m} \sin \frac{m\pi f}{b} & \text{if } (n+p)b = (g-f)m \text{ and } g \neq f \\ \frac{4}{\pi} \sum_{m}^{M} \sum_{p}^{M} \Pi_{p,m} \dfrac{mnp\, b^3 (g-f)\left[(-1)^{n+p} \cos \frac{m\pi a}{b} - \cos \frac{m\pi f}{b}\right]}{[(n-p)^2 b^2 - m^2 (g-f)^2][(n+p)^2 b^2 - m^2 (g-f)^2]} & \text{otherwise} \end{cases}$$

$$P_{10,n} = \begin{cases} \sum_{m}^{M} \frac{m\pi}{b} \Pi_{n,m} \cos \frac{m\pi f}{b} & \text{if } n = p \text{ and } g = f \\ \pm \frac{1}{2} \sum_{m}^{M} \sum_{p}^{M} \frac{m\pi}{b} \Pi_{p,m} \cos \frac{m\pi f}{b} & \text{if } (n-p)b = \pm (g-f)m \text{ and } g \neq f \\ -\frac{1}{2} \sum_{p}^{M} \sum_{m}^{M} \frac{m\pi}{b} \Pi_{p,m} \cos \frac{m\pi f}{b} & \text{if } (n+p)b = (g-f)m \text{ and } g \neq f \\ 4 \sum_{m}^{M} \sum_{p}^{M} \Pi_{p,m} \dfrac{nm^2 pb^2 (g-f)\left[\sin \frac{m\pi f}{b} - (-1)^{n+p} \sin \frac{m\pi g}{b}\right]}{[(n-p)^2 b^2 - m^2 (g-f)^2][(n+p)^2 b^2 - m^2 (g-f)^2]} & \text{otherwise} \end{cases}$$

$$P_{11,n} = \begin{cases} 0 & \text{if } n = p \text{ and } g = f \\ \pm \frac{1}{2} \sum_{p}^{M} \sum_{m}^{M} \frac{p\pi}{a} \Pi_{p,m} \cos \frac{m\pi f}{b} & \text{if } (n-p)b = \pm (g-f)n \\ \frac{1}{2} \sum_{p}^{M} \sum_{m}^{M} \frac{p\pi}{a} \Pi_{p,m} \cos \frac{m\pi f}{b} & \text{if } (n+p)b = (g-f)m \\ 2 \sum_{p}^{M} \sum_{m}^{M} \Pi_{p,m} \frac{npb^2[(n^2-p^2)b^2 - (g-f)^2m^2][\sin \frac{m\pi f}{b} - (-1)^{n+p} \sin \frac{m\pi g}{b}]}{a[b^2(n-p)^2 - m^2(g-f)^2][b^2(n+p)^2 - m^2(g-f)^2]} & \end{cases}$$

The constants $P_{j,m}$ are obtained by replacing f by $\bar{f}$ and replacing g by $\bar{g}$. Where j = 9, 10, 11.

$$U_{9,m,n} = \frac{2}{\ell} \int_0^{\ell} \sinh r_n a(1 - \frac{\xi}{\ell}) \sin \frac{n\pi}{b} (f + \frac{g-f}{\ell} \xi) \sin \frac{m\pi\xi}{\ell} d\xi$$

$$= D_{1,m,n} \left\{ \frac{4mn\pi^2}{b} (g-f) r_n a [\cosh r_n a \cos \frac{n\pi f}{b} - (-1)^m \cos \frac{n\pi g}{b}] \right.$$

$$\left. -2m\pi [(\frac{n\pi}{b})^2 (g-f)^2 - m^2\pi^2 - r_n^2 a^2] \sinh r_n a \sin \frac{n\pi f}{b} \right\}$$

$$U_{10,m,n} = D_{2,m,n} \left\{ \frac{4mn\pi^2(g-f)}{b} s_n a [\cos(h) s_n a \cos \frac{n\pi f}{b} - (-1)^m \cos \frac{n\pi g}{b}] \right.$$

$$\left. -2m\pi [(\frac{n\pi}{b})^2(g-f)^2 - m^2\pi^2 - \hat{N} s_n^2 a^2] \sin(h) s_n a \sin \frac{n\pi f}{b} \right\}$$

$$U_{11,m,n} = \begin{cases} \sinh u_n(b-g) & \text{if } m = n \text{ and } g = f \\ D_{3,m,n} \{4mn\pi^2(g-f) u_n [\cosh u_n(b-f) - (-1)^{m+n} \cosh u_n (b-g)]\} & \end{cases}$$

$$U_{12,m,n} = \begin{cases} \sin(h) v_n(b-g) & \text{if } m = n \text{ and } g = f \\ D_{4,m,n} \{4mn\pi^2(g-f) v_n [\cos(h) v_n(b-f) - (-1)^{m+n} \cos(h) v_n(b-g)]\} & \end{cases}$$

$$U_{13,m,n} = D_{1,m,n} \left\{ \frac{4mn\pi^2(g-f)}{b} r_n a [(-1)^m \sin \frac{n\pi g}{b} - \cosh r_n a \sin \frac{n\pi f}{b}] \right.$$

$$\left. -2m\pi [(\frac{n\pi}{b})^2(g-f)^2 - m^2\pi^2 - r_n^2 a^2] \sinh r_n a \cos \frac{n\pi f}{b} \right\}$$

$$U_{14,m,n} = D_{2,m,n}\left\{\frac{4mn\pi^2(g-f)}{b}\ s_n a\ [(-1)^m \sin\frac{n\pi g}{b} - \cos(h)\ s_n a \sin\frac{n\pi f}{b}]\right.$$

$$\left.-2m\pi\ [(\frac{n\pi}{b})^2\ (g-f)^2 - m^2\pi^2 - \hat{N}\ s_n^2 a^2]\ \sin(h)\ s_n a \cos\frac{n\pi f}{b}\right\}$$

$$U_{15,m,n} = \begin{cases} \cos(h)\ v_n(b-f) & \text{if } m = n \text{ and } g = f \\ D_{4,m,n}\ \{4mn\pi^2(g-f)\ \tilde{N}\ v_n\ [\sin(h)\ v_n(b-f) - (-1)^{m+n}\ \sin(h)\ v_n(b-f)]\} & \end{cases}$$

$$U_{16,m,n} = \begin{cases} \cosh\ u_n(b-f) & \text{if } m = n \text{ and } f = g \\ D_{3,m,n}\ \{4mn\pi^2(g-f)\ u_n\ [\sinh\ u_n(b-f) - (-1)^{m+n}\ \sinh\ u_n(b-g)]\} & \end{cases}$$

$$U_{17,m,n} = D_{1,m,n}\left\{\frac{4mn\pi^2(g-f)}{b}\ r_n a\ [\sinh\ r_n a \cos\frac{n\pi f}{b}\right.$$

$$\left.-2m\pi\ [(\frac{n\pi}{b})^2(g-f)^2 - m^2\pi^2 - r_n^2 a^2][\cosh\ r_n a \sin\frac{n\pi f}{b} - (-1)^m \sin\frac{n\pi g}{b}]\right\}$$

$$U_{18,m,n} = D_{2,m,n}\left\{\frac{4mn\pi^2(g-f)}{b}\ \hat{N}\ s_n a\ [\sin(h)\ s_n a \cos\frac{n\pi f}{b}]\right.$$

$$\left.-2m\pi\ [(\frac{n\pi}{b})^2(g-f)^2 - m^2\pi^2 - \hat{N}\ s_n^2 a^2][\cos(h)\ s_n a \sin\frac{n\pi f}{b} - (-1)^m \sin\frac{n\pi g}{b}]\right\}$$

$$U_{19,m,n} = \begin{cases} 0 & \text{if } (m+n) = \text{even and } g = f \\ D_{3,m,n}\ \{2m\pi[(m^2-n^2)\pi^2 + (g-f)^2\ u_n^2][\sinh\ u_n(b-f) - (-1)^{m+n}\ \sinh\ u_n(b-g)]\} & \end{cases}$$

$$U_{20,m,n} = \begin{cases} 0 & \text{if } (m+n) = \text{even and } g = f \\ D_{4,m,n}\ \{2m\pi[(m^2-n^2)\pi^2 + \tilde{N}\ (g-f)^2\ v_n^2][\sin(h)\ v_n(b-f) - (-1)^{m+n}\ \sin(h)\ v_n(b-g)]\} & \end{cases}$$

$$U_{21,m,n} = \begin{cases} 2m\pi D_{1,m,n}\{2n\pi r_n a(\frac{g-f}{b})[(-1)^m \cosh r_n a \cos\frac{n\pi g}{b} \\ -\cos\frac{n\pi f}{b}] - [(r_n a)^2 + (m\pi)^2 - (n\pi)^2(\frac{g-f}{b})^2]\ (-1)^m\ \sinh r_n a\ \sin\frac{n\pi g}{b}\} & \end{cases}$$

$$U_{22,m,n} = \begin{cases} 2m\pi D_{2,m,n}\{2n\pi s_n a(\frac{g-f}{b})[(-1)^m \cos(h) s_n a \cos\frac{n\pi g}{b} - \cos\frac{n\pi f}{b}] - [(s_n a)^2\hat{N} + (m\pi)^2 \\ -(n\pi)^2(\frac{g-f}{b})^2]\ (-1)^m \sin(h) s_n a \sin\frac{n\pi g}{b}\} & \end{cases}$$

$$U_{23,m,n} = \begin{cases} \sinh\ u_n f & \text{if } m+n = \text{even and } g = f \\ 4mn\pi^2\ u_n(g-f)D_{3,m,n}[(-1)^{m+n}\ \cosh u_n g - \cosh u_n f] & \text{otherwise} \end{cases}$$

$$U_{24,m,n} = \begin{cases} \sin(h)v_n f & \text{when } m+n = \text{even and } g = f \\ 4mn\pi^2 v_n(g-f)D_{4,m,n}[(-1)^{m+n}\ \cos(h)v_n g - \cos(h)v_n f] & \text{otherwise} \end{cases}$$

$$U_{25,m,n} = \begin{cases} 2m\pi D_{1,m,n}\{2n\pi r_n a(\frac{g-f}{b})(-1)^m \sinh r_n a \cos\frac{n\pi g}{b} - [(r_n a)^2 + (n\pi)^2 \\ - (n\pi)^2(\frac{g-f}{b})^2][(-1)^m \cosh r_n a \sin\frac{n\pi g}{b} - \sin\frac{n\pi f}{b}]\} \end{cases}$$

$$U_{26,m,n} = \begin{cases} 2m\pi D_{2,m,n}\{2n\pi s_n a(\frac{g-f}{b})(-1)^m \sin(h)s_n a \cos\frac{n\pi g}{b} - [(s_n a)^2\hat{N} + (m\pi)^2 \\ - (n\pi)^2(\frac{g-f}{b})^2][(-1)^m \cos(h)s_n a \sin\frac{n\pi g}{b} - \sin\frac{n\pi f}{b}]\} \end{cases}$$

$$U_{27,m,n} = \begin{cases} -2m\pi D_{1,m,n}\{2n\pi r_n a\ (\frac{g-f}{b})\ [(-1)^m \cosh r_n a \sin\frac{n\pi g}{b} - \sin\frac{n\pi f}{b}] \\ + [(r_n a)^2 + (m\pi)^2 - (n\pi)^2(\frac{g-f}{b})^2]\ (-1)^m \sinh r_n a \cos\frac{n\pi g}{b}\} \end{cases}$$

$$U_{28,m,n} = \begin{cases} -2m\pi D_{2,m,n}\{2n\pi s_n a\ (\frac{g-f}{b})\ [(-1)^m \cos(h)s_n a \sin\frac{n\pi g}{b} - \sin\frac{n\pi f}{b}] \\ + [(s_n a)^2\hat{N} + (m\pi)^2 - (n\pi)^2(\frac{g-f}{b})^2]\ (-1)^m \sin(h)s_n a \cos\frac{n\pi g}{b}\} \end{cases}$$

$$U_{29,m,n} = \begin{cases} 0 & \text{if } m+n = \text{even and } g = f \\ -2m\pi[u_n{}^2(g-f)^2 + (m\pi)^2 - (n\pi)^2]D_{3,m,n}\ [(-1)^{m+n}\sinh u_n g - \sinh u_n f] & \text{otherwise} \end{cases}$$

$$U_{30,m,n} = \begin{cases} 0 & \text{if } m+n = \text{even and } g = f \\ -2m\pi[\tilde{N}v_n{}^2(g-f)^2 + (m\pi)^2 - (n\pi)^2]D_{4,m,n}\ [(-1)^{m+n}\sin(h)v_n g - \sin(h)v_n f] & \text{otherwise} \end{cases}$$

$$U_{31,m,n} = \begin{cases} \cos(h)v_n f & \text{if } m+n = \text{even and } g = f \\ 4mn\pi^2 v_n \tilde{N}(g-f)D_{4,m,n}\ [(-1)^{m+n}\sin(h)v_n g - \sin(h)v_n f] & \text{otherwise} \end{cases}$$

$$U_{32,m,n} = \begin{cases} \cosh u_n f & \text{if } m+n = \text{even and } g = f \\ 4mn\pi^2(g-f)u_n D_{3,m,n}\ [(-1)^{m+n}\sinh u_n g - \sinh u_n f] & \text{otherwise} \end{cases}$$

The constants $\bar{U}_{j,m,n}$ are obtained by replacing f by $\bar{f}$ and replacing g by $\bar{g}$. Where j = 9 through 32.

ACKNOWLEDGMENTS

The authors would like to thank the Minta Martin Fund at the University of Maryland for the academic grants which helped make this paper possible. The computer time for this project was jointly supported by the National Aeronautics and Space Administration and the Computer Science Center at the University of Maryland.

EXPERIMENTAL DETERMINATION OF MULTIDIRECTIONAL MOBILITY DATA FOR BEAMS

D. J. Ewins,
Imperial College of Science and Technology,
London, England

and

P. T. Gleeson,
Middlesex Polytechnic and Imperial College,
London, England

When mobility data is to be used for prediction of the vibration properties of coupled structures, it is necessary to consider all the directions of vibration which are significant at each coupling point. In particular, when analysing beam-like structures it is necessary to include both translational and rotational mobilities. Often it is necessary to obtain such data by experiment and although techniques are established for measuring translational vibration, it is difficult to measure rotational mobilities with sufficient accuracy. A method is presented here which enables the required rotational mobilities to be derived from measurements of translational mobilities. Results show that derivation of rotational data is more accurate than direct measurement, especially at low frequencies.

1. INTRODUCTION

When a complete structure is analysed in order to predict its vibration characteristics, it is usually more convenient to break that structure down into its basic component parts. Each of these may then be analysed individually in as much (or as little) detail as its complexity demands. An analytical model of the complete structure may then be generated by combining all the individual component analyses using an impedance or mobility coupling process.

However, it is often found that some of the components in engineering structures are not amenable to (or even defy) theoretical analysis. In this case, in order to make an analysis of the complete structure, recourse may be made to experimental measurement of the necessary data. This situation is often encountered when using non-metallic components (rubber or polymers), or when attaching additional components onto an existing and complex structure such as an air-frame or a bulkhead in a ship. If such a procedure is to be undertaken successfully, very careful consideration must be given to the choice of (a) which mobility data should be measured, and (b) how these may be obtained accurately. The main limitation of conventional mobility or impedance measuring techniques is that they consider motion in one translational direction only, while practical structures usually vibrate in several directions simultaneously (translational and rotational).

Previous work (1) has illustrated this basic problem and presented a method for measuring the type of multi-directional mobility data which may be required. The results were encouraging, although not perfect, but the measurement method was difficult and relatively lengthy. Another, similar, method for measuring such comprehensive mobility data has been reported (2), but this also is fairly complex.

Further work has now been undertaken with the objectives of developing the measurement technique described in (1): (a) by applying it to a wider variety of structures, in particular to smaller ones; (b) by improving the accuracy of the measured data; and (c) by simplifying the procedure so that it may be undertaken with conventional impedance testing equipment.

The present paper describes this development.

2. CASE STUDY

As previously, a specific example was chosen with which to test and demonstrate the various aspects of the measurement method. A very simple structure was selected - a uniform steel beam, C, which was formed by joining two different uniform beams A and B, end to end. The experiment consisted of:

(i) measuring the tip mobility data for beam A;

(ii) measuring similar data for beam B;

(iii) using the above data to predict the properties of the combined beam C, and then comparing these with the actual properties.

The underlying philosophy of this experiment was that unless such a simple system as that described above could be measured and analysed successfully, there was little point in attempting to apply such techniques to more complex practical structures.

Chosen Beams

It was decided to use steel beams of rectangular cross section for the test pieces so that the theoretical mobility values could be readily calculated. Steel was selected because of its availability and also because, being very lightly damped, it would offer a wide dynamic range of response and thus tax the measurement system. Several considerations were made in deciding upon the dimensions of the two beams. As mentioned above, one object of this study was to test the basic multi-directional mobility measurement technique on smaller components than previously. Also, there were frequency constraints to be imposed in order to keep within the range in which accurate measurements could be reliably expected. This range had a lower bound of 50 Hz (mains frequency) and an upper one of about 1000 Hz, above which transducers and drive rods can begin to cause problems. Thus the decade 80 - 800 Hz was selected as the 'central' frequency range.

The beams were to be tested in a free-free configuration; this having boundary conditions which can be most closely achieved in an experiment. The longer of the two beams was chosen with a section of 25 mm x 31 mm and a length of 1.4 m. For bending vibration in its stiffer plane (i.e. with 31 mm as the thickness), this beam has calculated natural frequencies at 86, 237, 464 and 767 Hz. The shorter beam was chosen to have the same cross section and a length of 0.65 m. This beam has its first two natural frequencies at 399 and 1100 Hz, deliberately chosen so as not to coincide with those of the long beam.

3. DIRECT MEASUREMENT OF MOBILITY DATA

Basic Measurement Method

The response of the test piece to a harmonic input force and a harmonic couple M, applied at point P, are the velocity $\dot{X}$ and the angular velocity $\dot{\theta}$.

These are related by the mobility equation:-

$$\begin{Bmatrix} \dot{X} \\ \dot{\theta} \end{Bmatrix} = \begin{bmatrix} \frac{\dot{X}_f}{F} & \frac{\dot{X}_m}{M} \\ \frac{\dot{\theta}_f}{F} & \frac{\dot{\theta}_m}{M} \end{bmatrix} \begin{Bmatrix} F \\ M \end{Bmatrix} = \begin{bmatrix} Y_{xx} & Y_{x\theta} \\ Y_{\theta x} & Y_{\theta\theta} \end{bmatrix} \begin{Bmatrix} F \\ M \end{Bmatrix}$$

or

$$\{\dot{X}\} = [Y]\{F\} \qquad (1)$$

In general, F and M are complex quantities incorporating both magnitude and phase information of steady-state sinusoids and it follows that $\dot{X}$, $\dot{\theta}$ and all four elements of the mobility matrix, $[Y]$, are also complex.

For measurement of these mobility data, the inputs F and M are applied to the structure by an 'exciting block' which is fixed to the test piece at P and which enables F, M and the responses $\dot{X}$ and $\dot{\theta}$ to be deduced from the outputs of accelerometers mounted symmetrically on the block. See Fig. 1.

The responses $\ddot{X}$ and $\ddot{\theta}$ at point P are related to the accelerations a_A and a_B measured by the accelerometers by the equations:-

$$\ddot{X} = (a_A + a_B)/2, \quad \ddot{\theta} = (a_A - a_B)/2s$$

where s is the distance of offset of each accelerometer from P.

These equations may be expressed as a matrix equation:

$$\begin{Bmatrix} \ddot{X} \\ \ddot{\theta} \end{Bmatrix} = \begin{bmatrix} 1/2 & 1/2 \\ 1/2s & -1/2s \end{bmatrix} \begin{Bmatrix} a_A \\ a_B \end{Bmatrix}$$

or

$$\{\ddot{X}\} = [T]\{a\} \qquad (2)$$

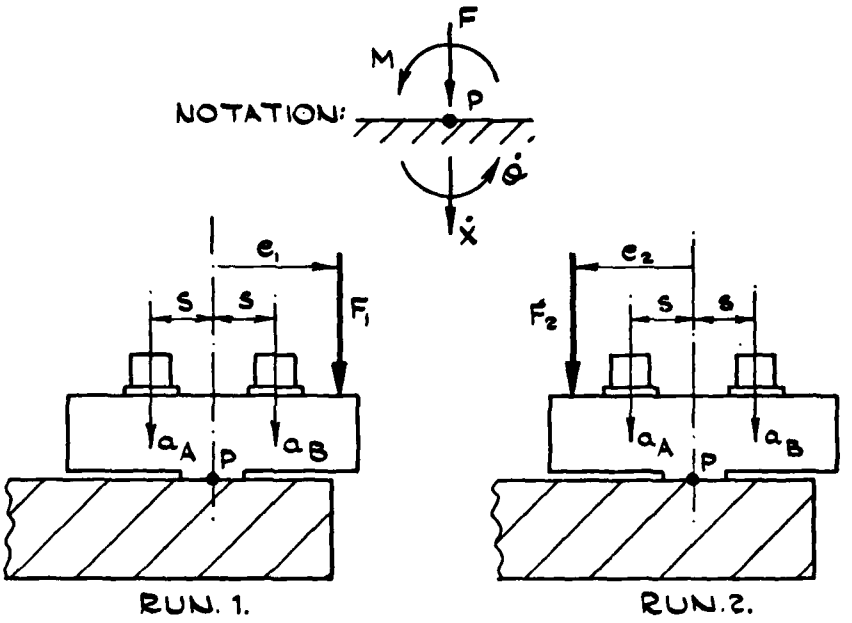

FIG.1. BASIC MEASUREMENT CONFIGURATION.

Data are obtained in each of two test runs at a discrete number of frequencies. In Run 1 a force F_1 is applied to the block at a point offset a distance e_1 from P, and in Run 2 a force F_2 is applied at a point which is a distance e_2 from P. (e_1 and e_2 need not be symmetrical about P).

The coordinate system has X positive downwards and θ positive anti-clockwise. Since F and M are the force and couple inputs applied to the test piece at P, their relationship to F_1 and F_2 can be determined by regarding the exciting block as a free body with an input F_1 or F_2 above the block and -F, -M input at P (see Fig. 1).

Thus, in Run 1, resolving vertical forces:

$$F_1 - F = m \ddot{X}_1$$

and taking moments about P:

$$e_1 F_1 - M = I_p \ddot{\theta}_1$$

where m is the mass of the block (including accelerometers) and I_p its moment of inertia about P.

Thus: $$\begin{Bmatrix} F \\ M \end{Bmatrix} = \begin{Bmatrix} F_1 - m \ddot{X}_1 \\ e_1 F_1 - I_p \ddot{\theta}_1 \end{Bmatrix}$$

Equation (1) may now be rewritten as:

$$\begin{Bmatrix} \dot{X}_1 \\ \dot{\theta}_1 \end{Bmatrix} = [Y] \begin{Bmatrix} F_1 - m \ddot{X}_1 \\ e_1 F_1 - I_p \ddot{\theta}_1 \end{Bmatrix}$$

Dividing through by F_1 and writing $\ddot{X}/j\omega = \dot{X}$; $\ddot{\theta}/j\omega = \dot{\theta}$ we get:

$$1/j\omega \begin{Bmatrix} (\ddot{X}/F)_1 \\ (\ddot{\theta}/F)_1 \end{Bmatrix} = [Y] \begin{Bmatrix} 1 - m (\ddot{X}/F)_1 \\ e_1 - I_p (\ddot{\theta}/F)_1 \end{Bmatrix} \quad (3)$$

Similarly for Run 2:

$$1/j\omega \begin{Bmatrix} (\ddot{X}/F)_2 \\ (\ddot{\theta}/F)_2 \end{Bmatrix} = [Y] \begin{Bmatrix} 1 - m (\ddot{X}/F)_2 \\ e_2 - I_p (\ddot{\theta}/F)_2 \end{Bmatrix} \quad (4)$$

Combining (3) and (4):

$$1/j\omega \begin{bmatrix} (\ddot{X}/F)_1 & (\ddot{X}/F)_2 \\ (\ddot{\theta}/F)_1 & (\ddot{\theta}/F)_2 \end{bmatrix} =$$

$$[Y]\left(\begin{bmatrix}1 & 1\\ e_1 & e_2\end{bmatrix}-\begin{bmatrix}m & 0\\ 0 & I_p\end{bmatrix}\begin{bmatrix}(\ddot{X}/F)_1 & (\ddot{X}/F)_2\\ (\ddot{\theta}/F)_1 & (\ddot{\theta}/F)_2\end{bmatrix}\right) \quad (5)$$

We may write $\begin{bmatrix}1 & 1\\ e_1 & e_2\end{bmatrix}=[T]$, a transformation matrix.

and $\begin{bmatrix}m & 0\\ 0 & I_p\end{bmatrix}=[M]$, a matrix of block inertial properties

Using equation (2), we have:

$$\begin{bmatrix}(\ddot{X}/F)_1 & (\ddot{X}/F)_2\\ (\ddot{\theta}/F)_1 & (\ddot{\theta}/F)_2\end{bmatrix}$$

$$=[T]\begin{bmatrix}(a_A/F)_1 & (a_A/F)_2\\ (a_B/F)_1 & (a_B/F)_2\end{bmatrix}$$

$$\text{or} \quad [In]=[T][In_m] \quad (6)$$

where $[In]$ is a matrix of Inertance quantities

and $[In_m]$ is the matrix of those Inertance quantities which are measured experimentally.

Thus equation (5) may be rewritten:-

$$1/j\omega[T][In_m]=[Y]([\tau]-[M][T][In_m])$$

$$\text{and so } [Y]=1/j\omega[T][In_m]([\tau]-[M][T][In_m])^{-1} \quad (7)$$

The required matrix of mobility parameters is obtained here in terms of $[T]$, $[\tau]$ and $[M]$ which are constant for a given test configuration, together with $[In_m]$ which incorporates data measured at angular frequency ω in the two test runs. The resulting mobility data, $[Y]$, has thus been fully corrected to account for the mass and inertia of the added block and transducers.

Measuring System

The experiments reported here were carried out using a digital transfer function analyser (DTFA) interfaced with a mini-computer, together constituting a system capable of handling the large amount of data and computation involved. The peripheral equipment consisted of a teletype with a read/write facility together with a high-speed punch, a high-speed reader and an X - Y plotter.

The oscillator of the DTFA supplied a conventional shaker via a power amplifier. The coupling of the shaker to the force transducer mounted on the exciting block was made through a short flexible push rod made of steel 1 mm diameter and 25 mm long. This allowed the test structure to rotate slightly when the applied force did not pass through its centre of gravity without being restrained by an unknown couple.

During Run 1 the force was input at a distance e_1 from P and the inertance data at each of the test frequencies were stored on tape. The force input was then moved to a distance e_2 from P. At each test frequency during Run 2, inertance data were again measured and combined with the corresponding data read from the Run 1 tape. The matrix calculation for the four complex components of the mobility matrix $[Y]$ was carried out and the results printed on the teletype and also punched on tape. Graphs of the mobility data versus frequency were subsequently made from the taped data.

Development of Exciting Blocks

Each exciting block was designed to be used with a Bruel and Kjaer type 8200 Force Transducer and Endevco type 233E Accelerometers.

Based on earlier tests (1), block Mk. 4 was designed to provide the smallest, lightest block which could have two accelerometers on its upper surface, equidistant from the measuring point P, and also have two positions for the force gauge. A drawing of this block is shown in Fig. 2. The foot of the block has dimensions 24 by 32 mm which closely matches the section of the test beam to which it was attached (with adhesive) during the tests.

The results of tests using the Mk.4 block were poor in the measurement of the rotational mobilities, of $(\dot{\theta}/M)$ in particular. It was thought that the measurement of $\ddot{\theta}$ could be improved by increasing s (the accelerometer offset) from 25 mm to 50 mm and the rotational signal level could be increased by shifting the force transducer in Run 1 from 0 to 50 mm. Thus a Mk. 5 block was designed which had the accelerometers and the force transducer mounted back-to-back as shown in Fig. 3. The foot of this block (30 mm by 32 mm) was slightly wider than the test beams but it was thought necessary to ensure adequate stiffness at the ends of the block by making the 'skirts' 6 mm thick.

Block Mk. 5 was used extensively in measuring the four mobility parameters of the beams. As before, the rotational quantities were obtained less accurately

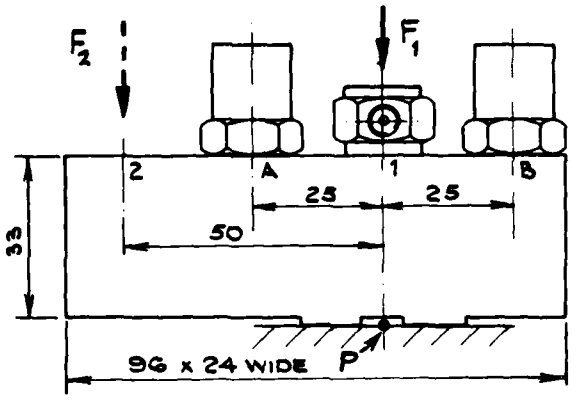

2, A, 1, B, ARE HOLES DRILLED & TAPPED $\frac{10}{32}$ UNF

A & B FOR ACCELEROMETERS ENDEVCO 233E

1 & 2 FOR FORCE GAUGES B&K 8200.

FIG. 2. EXCITING BLOCK. MARK 4.

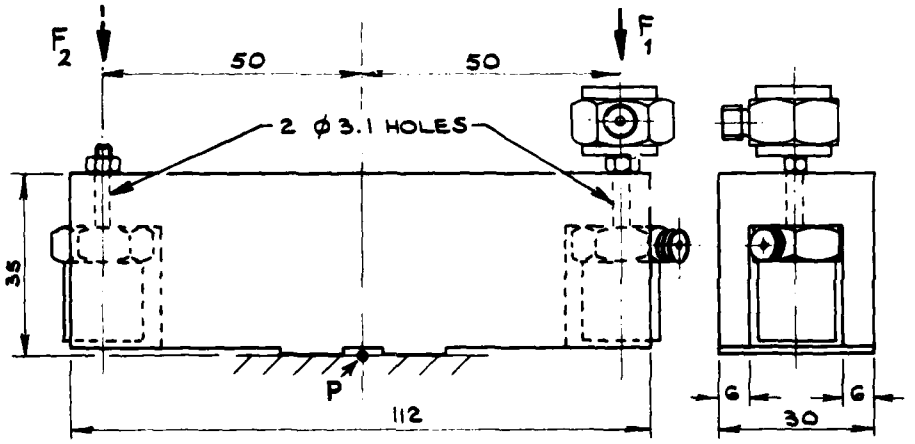

FIG. 3. EXCITING BLOCK. MARK 5.

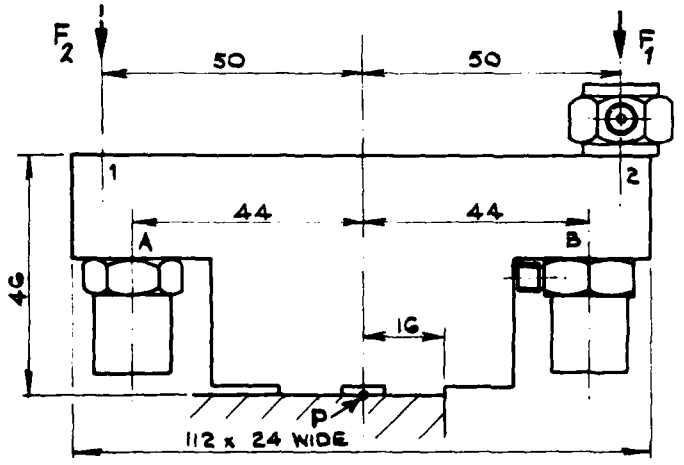

ALL DIMENSIONS IN mm.

FIG. 4. EXCITING BLOCK. MARK 6

than the translational, with ($\dot{\theta}$/M) generally being poor, especially at low frequencies. Two factors were significant:-

(a) The transverse sensitivity of the accelerometers gave rise to signals comparable to the small difference signals associated with θ measurement; and

(b) There appeared to be direct interference between the force gauge and the accelerometer when the transducers shared a common mounting stud.

The first factor was minimised by the use of accelerometers selected to have a transverse sensitivity of less than 1.0%.

The second factor was corrected by the design of block Mk. 6, which has the same essential features as block Mk. 5 but does not use a common mounting stud for both force gauge and accelerometer. This block is shown in Fig. 4: it has no 'skirts' but has a thicker top section to provide sufficient stiffness.

All the measurements reported in this paper were made using block Mk. 6.

Measured Mobilities of Long and Short Beams

In order to measure the mobilities of the long beam, the Mk. 6 exciting block was attached by adhesive to the beam such that the test point, P, was as close as possible (0.016 m) to the tip. Measurements were made at 76 discrete frequencies in the range 31.6 Hz to 1000 Hz and are presented in Fig. 5 in which the continuous line shows the theoretical response for the beam tip, computed using closed-form receptance formulae, and the points are the measured data.

The measured responses for ($\dot{X}$/F), ($\dot{\theta}$/F) and ($\dot{X}$/M) show a little scatter but are accurate to within about 2 dB up to 800 Hz. The ($\dot{\theta}$/M) response is inaccurate below the first response and shows an antiresonance at about 57 Hz whereas the theoretical antiresonance is well below 30 Hz. Above the first resonance at 86 Hz, however, the measured ($\dot{\theta}$/M) response is reasonably accurate. The results of other tests on this beam have very similar features.

A number of corresponding tests were carried out on the short beam and the results are shown in Fig. 6. These show very good correlation between the measured data and the theoretical tip response for the ($\dot{X}$/F), ($\dot{\theta}$/F) and ($\dot{X}$/M) mobilities. The biggest discrepancies are in the location of the antiresonances, but this is probably a result of the measurement point not being quite at the tip of the beam, but 0.016 m inboard. (A theoretical calculation was made for a point 0.016 m along a 0.65 beam. This showed antiresonances exactly coincident with those of the measured data. The resonances of course, were unchanged and remained in close coincidence with the measured data points). The ($\dot{\theta}$/M) response is reasonably accurate above 200 Hz but has a considerable error of about +8 dB below that frequency.

In general, it can be seen that the two rotational responses ($\dot{\theta}$/F) and ($\dot{\theta}$/M) are the more difficult to measure accurately and ($\dot{\theta}$/M), which involves two rotational quantities, is unlikely to be accurate at frequencies below the first resonance. The $\ddot{\theta}$ data depends on the difference between the signals of the 2 accelerometers, which have therefore to be accurately matched and carefully calibrated. Any spurious response which has only a slight effect on the $\ddot{X}$ data (which depends on the sum of the accelerometer signals) will have a major effect on the $\ddot{\theta}$ value. In most cases it is also true to say that the expected values of acceleration due to rotation are much smaller than those due to translation.

4. ANALYSIS OF THE COUPLED BEAMS

Coupling of Components

Components A and B have mobility properties given by:-

$$\{\dot{X}_A\} = [Y_A]\{F_A\} \quad (8)$$

and $$\{\dot{X}_B\} = [Y_B]\{F_B\} \quad (9)$$

Where $[Y]$ is a mobility matrix for the point on the structure which is of interest.

When the components are coupled (to form A + B) their respective motions at the coupling point must be identical:-

$$\{\dot{X}_A\} = \{\dot{X}_B\} = \{\dot{X}_C\} \quad (10)$$

and considering the equilibrium at the point of connection:-

$$\{F_A\} + \{F_B\} = \{F_C\} \quad (11)$$

where $\{F_C\}$ is the net force exerted on the coupled structure.

The mobility of the combination, $[Y_C]$, features in the equation:-

$$\{\dot{X}_C\} = [Y_C]\{F_C\}$$

FIG. 5 MOBILITY PROPERTIES OF THE LONG BEAM: I

—— Theoretical ... Direct Measurements

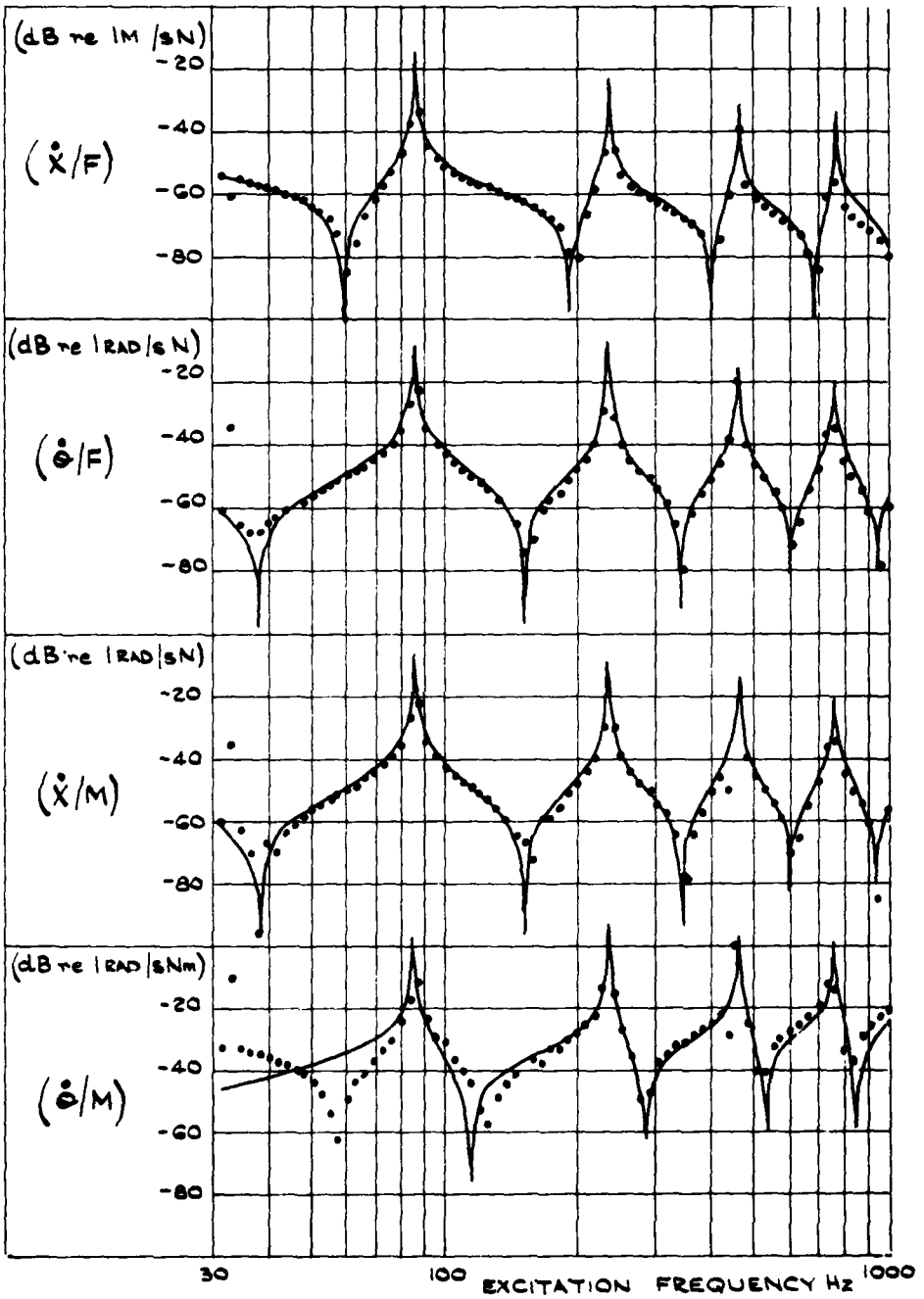

FIG. 6 MOBILITY PROPERTIES OF THE SHORT BEAM: I

——— Theoretical ... Direct Measurements

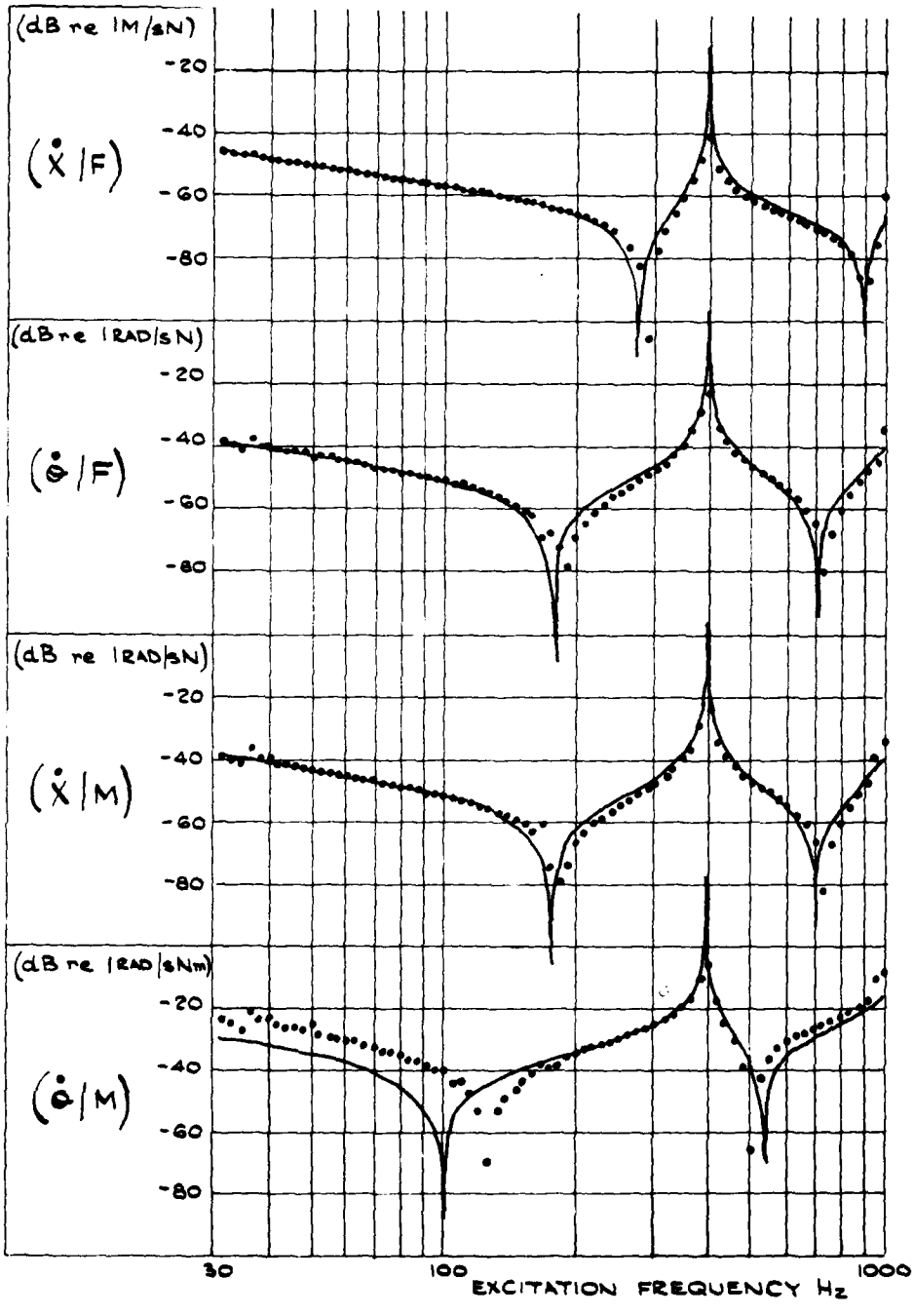

$$= [Y_C] (\{F_A\} + \{F_B\})$$

$$= [Y_C] ([Y_A]^{-1} + [Y_B]^{-1}) \{\dot{X}_C\} \quad (12)$$

$$\therefore [Y_C] = ([Y_A]^{-1} + [Y_B]^{-1})^{-1} \quad (13)$$

Calculation of the mobility matrix of an assembly for any particular frequency thus involves inverting the mobility matrix of each component (for that frequency); adding the two resultant impedance matrices and then re-inverting.

This process has to be carried out at each frequency data point.

Coupled-Beam Analysis Using Raw Data

The measured data used for Fig. 5 and 6 were combined, frequency by frequency, in a calculation of the mobility responses at the point of connection between the long beam (1.4 m) and the short beam (0.65 m). The computation involved reading data simultaneously from two tapes; then inverting and adding two matrices; inverting the result and punching out the data produced. This process took about 30 seconds per resultant data point, the major part of the time being occupied by the teletype reading taped data.

The result of this direct calculation is shown as Fig. 7 together with the theoretical values of the mobility at a point 0.65 m along a 2.05 m beam. The predicted results are extremely poor for all four mobility parameters except in the range 180 Hz to 400 Hz. Examination of the input data shows that this is the only frequency range for which the $(\dot{\theta}/M)$ response of the short beam is accurate. The other seven mobility parameters have wider ranges of reasonable accuracy. Thus it is concluded that if any of the eight input mobility parameters is inaccurate at a particular frequency, the all the calculated mobilities of the combined structure will probably be wrong at that frequency.

The $(\dot{\theta}/M)$ responses were confirmed as the chief sources of error by another calculation in which the raw $(\dot{\theta}/M)$ data of both subsystems were replaced by theoretical $(\dot{\theta}/M)$ data. The result of this exercise is shown in Fig. 8 which illustrates a considerable improvement in accuracy when compared with Fig. 7, especially below 80 Hz. The overall accuracy, however, is still not acceptable since there are ranges where the scatter is considerable, (80 - 100 Hz; 120 - 140 Hz; 400 - 500 Hz, for example).

Improvement in the resultant coupled data could evidently be made first, by smoothing, and second, by improving the accuracy of the rotational mobilities $(\dot{\theta}/F)$ and $(\dot{\theta}/M)$ for the two component subsystems.

5. COUPLED-BEAM ANALYSIS USING SMOOTHED DATA

Smoothing Technique

The first attempt to improve the component data was by a simple smoothing process. In this, the experimental mobility 'curve' is curve-fitted by a suitable equation which thus smoothes out random scatter in the data. The appropriate equation is formed by identifying from the experimental data the main modes of vibration of the test structure. Modal identification provides a simple representation of a system with n resonances as an assembly of n single-degree-of-freedom oscillators, each resonating at one of the n resonant frequencies and weighted by a modal constant. The method of modal identification used here was based on the treatment developed by A. L. Klosterman (3) and is summarised in Appendix 1. There it is shown that the modal constants for a system with n dominant modes can be determined by matrix manipulation involving measured mobility data obtained at n discrete non-resonant frequencies. In the present study, this data could of course be selected from that already measured. Once the n modal constants (e.g. $A_1, A_2 \ldots\ldots A_n$ for $(\dot{X}/F)$) have been determined, the identified frequency response can be regenerated by summing the contribution from each mode in turn at each frequency.

The raw data for the long beam was examined and five resonant frequencies (0, 86, 234, 457 and 758 Hz) estimated. Data measured at the n off-resonant frequencies of 31.6, 69.2, 120, 302 and 724 Hz were taken and used to calculate modal constants from which the smoothed curves of Fig. 9 were calculated. These are seen to be quite similar to the raw data of Fig. 5 except above 758 Hz, the highest resonant frequency used. Above that frequency, the curves approach the 20 dB/decade mobility line of a mass, because the dominant contribution is from the highest mode included in the identification which is mass-like above its resonant frequency.

In the case of the short beam, the resonant frequencies were estimated from the raw data to be 0, 394 and 1100 Hz and data measured at 31.6, 209 and 603 Hz were used in the modal calculations giving the results shown in Fig. 10

FIG. 7 MOBILITY PROPERTIES OF THE COUPLED BEAM: I

——— Theoretical ... Predicted from direct measurements on component beams

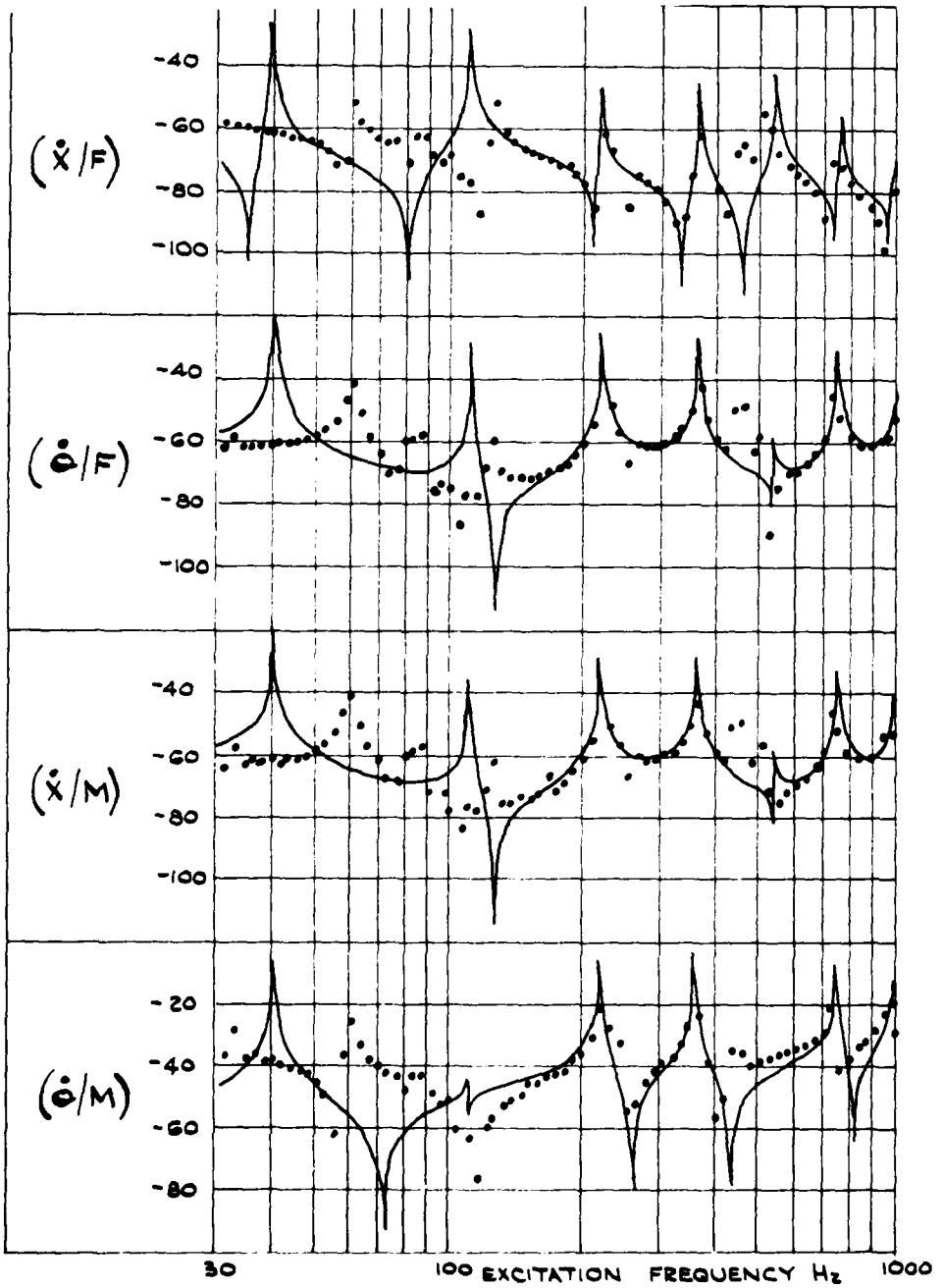

FIG. 8 MOBILITY PROPERTIES OF THE COUPLED BEAM: II

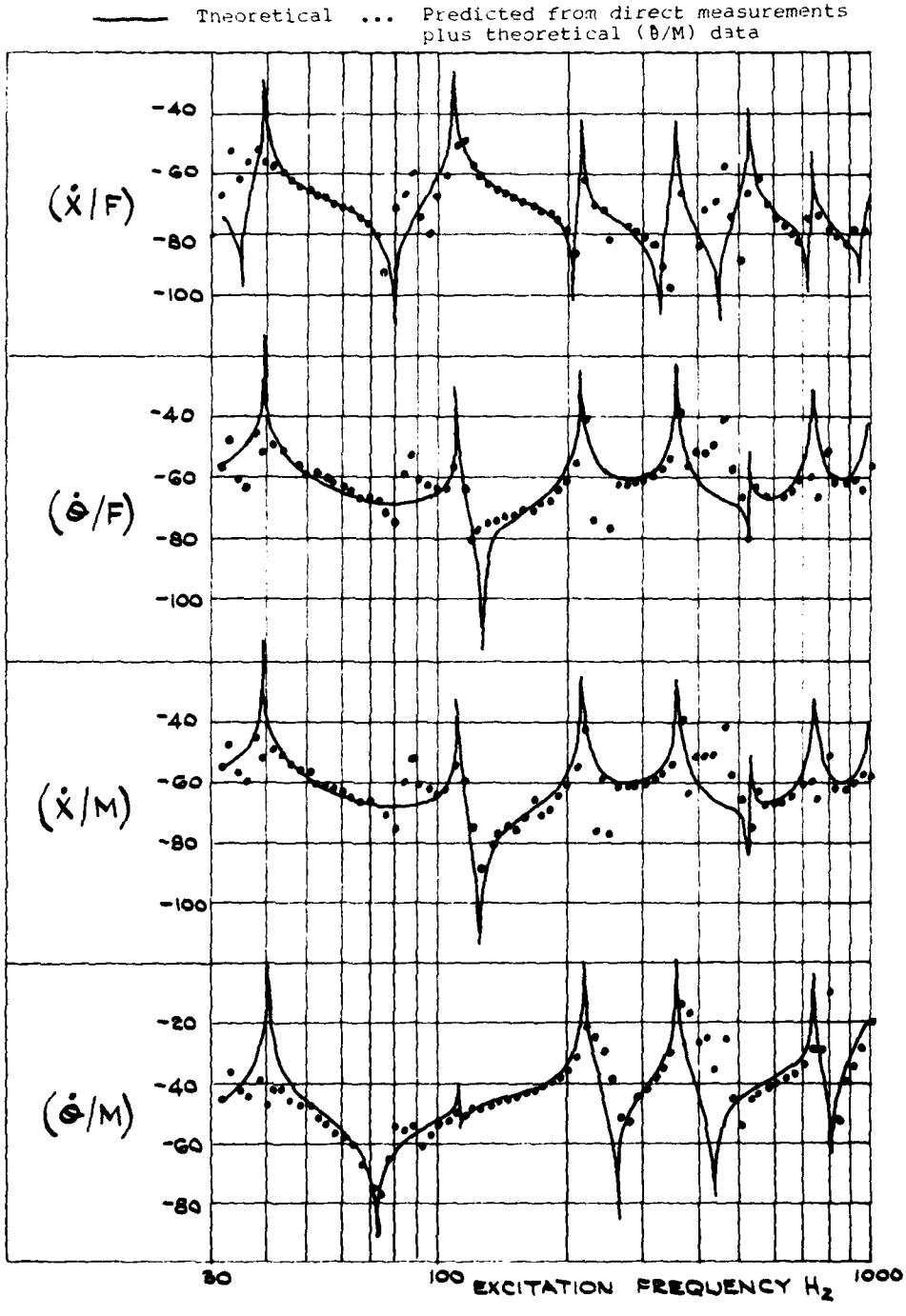

FIG. 9 MOBILITY PROPERTIES OF THE LONG BEAM: II

——— Theoretical ... Smoothed measurements

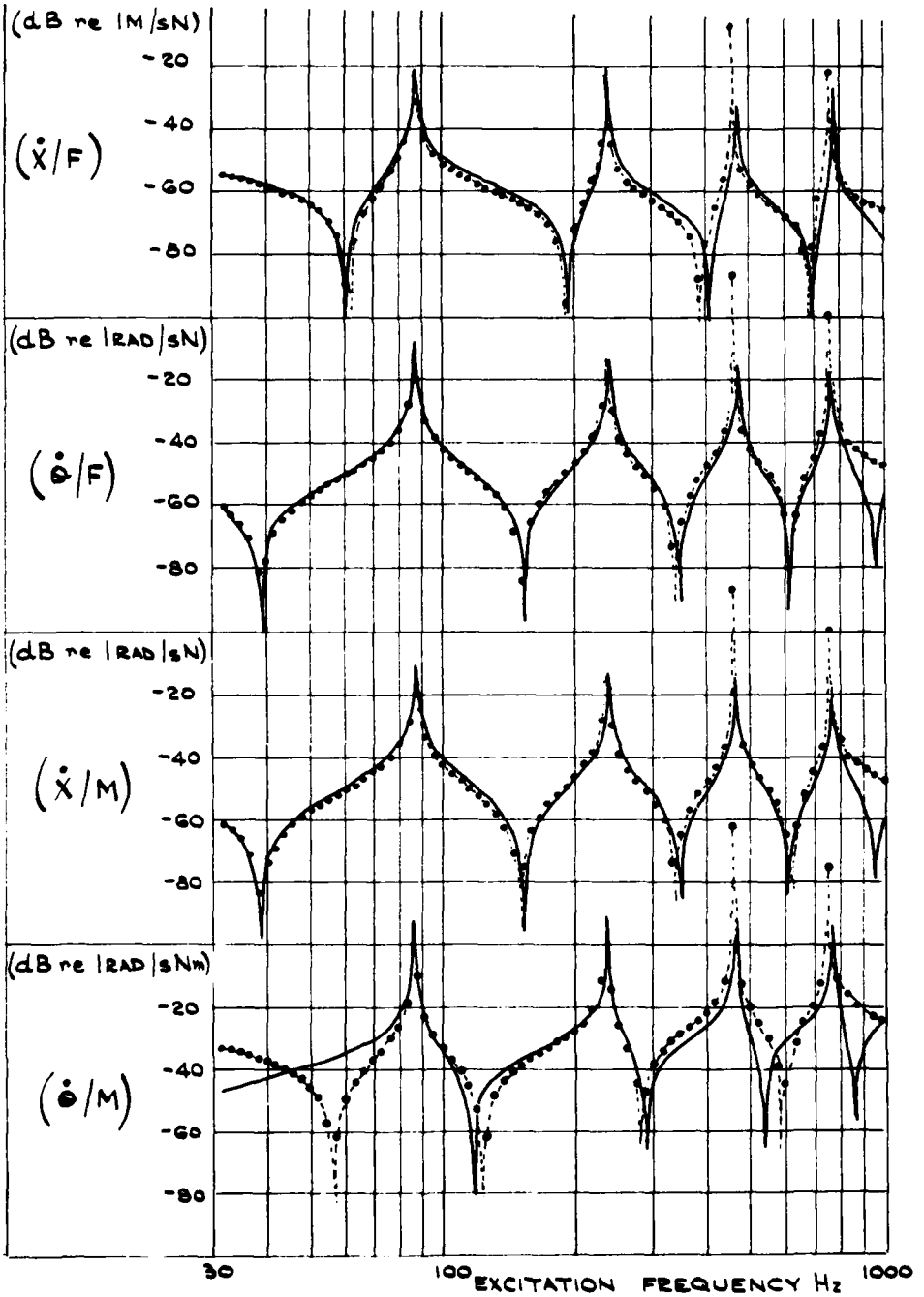

FIG. 10 MOBILITY PROPERTIES OF THE SHORT BEAM: II

——— Theoretical ... Smoothed measurements

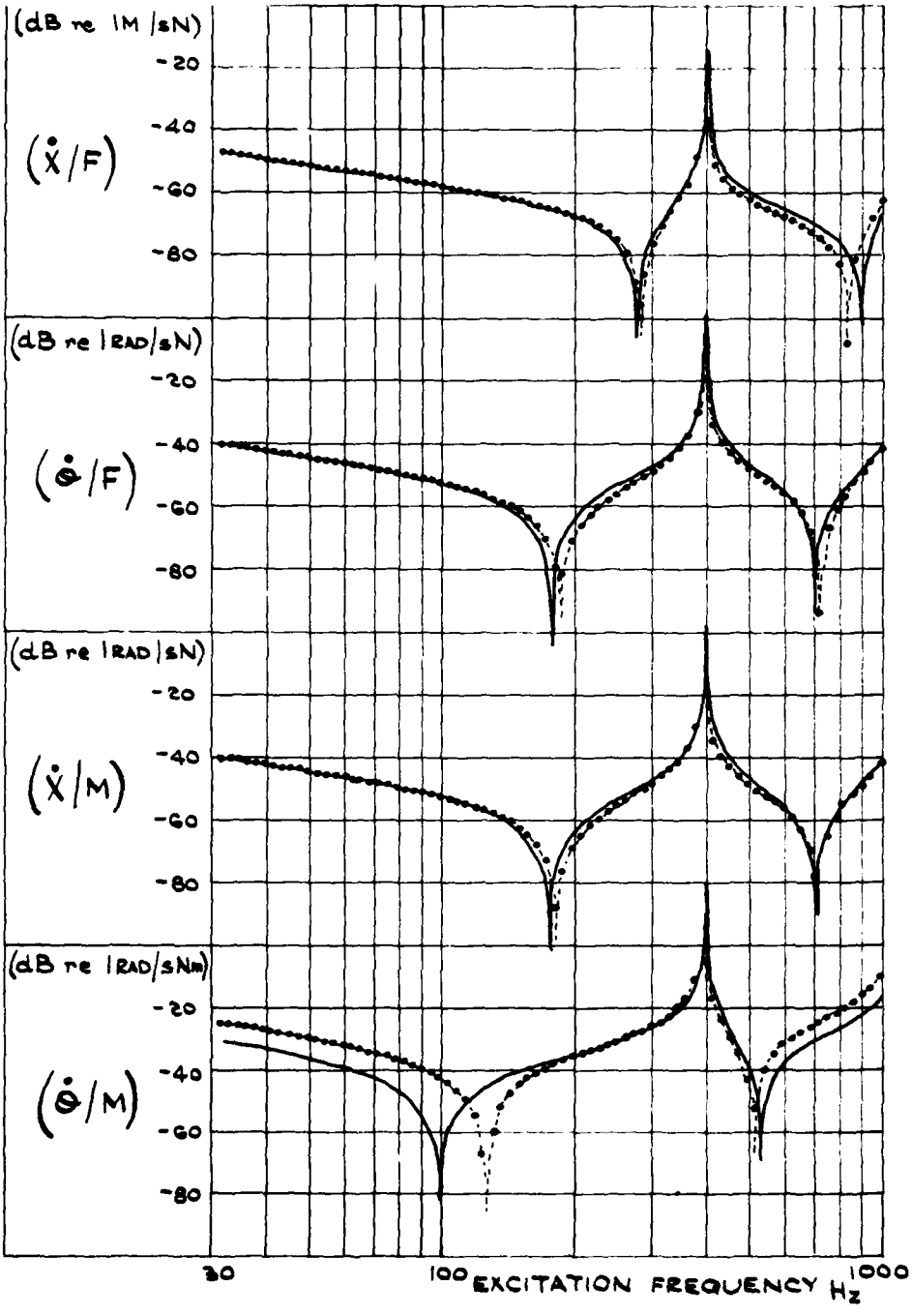

which is recognizably a smoothed version of Fig. 6. There is no high frequency discrepancy on this plot because the highest mode used is at a frequency higher than the range limit of 1000 Hz. In general, smoothing by modal identification gives acceptable accuracy provided that the number of modes identified is one more than the number of modes which lie within the frequency range of interest.

Coupled-Beam analysis using smoothed data

The smoothed data of Fig. 9 and 10 were coupled using exactly the same process as before to produce a predicted set of responses for a 2.05 m beam. The results are presented in Fig. 11 but although having less scatter, they are not otherwise any improvement in the unsmoothed results in Fig. 7.

However, there was one advantage in using smoothed data at this stage, and that was in the computation time which was considerably reduced since much less data needed to be handled. Printing of the output on the teletype took the greater part of the time, the process taking about 12 seconds per resultant data point (compared with 30 seconds previously).

6. ALTERNATIVE METHOD OF DETERMINING ROTATIONAL MOBILITIES

A method was now sought by which the accuracy of $(\dot{\theta}/F)$ and $(\dot{\theta}/M)$ mobility data could be improved. As the rotational motion (θ, $\dot{\theta}$ or $\ddot{\theta}$) is evidently very difficult to measure accurately, some alternative means of deriving the appropriate mobilities was required.

Referring to the modal identification analysis presented in Appendix 1, we find a particularly interesting and useful result. For each mode identified, there are four constants - A_r, B_r, C_r and D_r - which relate to the contribution of the r^{th} mode to the $(\dot{X}/F)(\dot{\theta}/F)$ $(\dot{X}/M)$ and $(\dot{\theta}/M)$ mobilities respectively. Now it is shown in the Appendix that these four constants are very simply related by:

$$B_r = C_r \quad \text{and} \quad D_r = C_r^2/A_r$$

(The special case of the zero-frequency modes possessed by a free-free structure is treated in Appendix 2, resulting in

$$B_1 = C_1 \text{ and } D_1 = C_1^2/(A_1 - 1/m)$$

where m is the mass of the structure).

Because of the greater difficulty in measuring rotation than translations, it is possible to derive more accurate values for A_r and C_r from $(\dot{X}/F)$ and $(\dot{X}/M)$ data than for B_r and D_r. However, it is clear from the above relationships that these latter constants may be immediately determined from A_r and C_r.

Thus the mobilities $(\dot{\theta}/F)$ and $(\dot{\theta}/M)$ can be derived from measurements of $(\dot{X}/F)$ and $(\dot{X}/M)$ using the modal identification techniques, without measuring rotations directly.

Calculations using the relationships between the modal constants developed above were carried out for both beams and the results are shown in Figs. 12 and 13. In these, there are only three distinct responses presented since $(\dot{\theta}/F)$ is now automatically identical to $(\dot{X}/M)$ (since $B_r = D_r$).

When the derived $(\dot{\theta}/M)$ response of Fig. 12 is compared with the smoothed $(\dot{\theta}/M)$ response of Fig. 9, it is immediately apparent that the accuracy at low frequencies below the first resonance at 86 Hz, where the Fig. 9 response is very poor, is now greatly improved and at higher frequencies up to 800 Hz, where Fig. 9 was quite good, it is a little further improved.

Similar observations apply to the comparison of $(\dot{\theta}/M)$ responses of Figs. 10 and 13 for the short beam. The accuracy of the Fig. 13 curve is less than that of Fig. 12 because fewer modes are included, but most significantly the $(\dot{\theta}/M)$ response is accurate around 30 Hz.

The conclusion of this section is that better $(\dot{\theta}/M)$ results may be obtained by identifying the A_r and C_r modal constants from $(\dot{X}/F)$ and $(\dot{X}/M)$ measurements and then calculating B_r and D_r than by trying to identify B_r and D_r directly from the inevitably less reliable $(\dot{\theta}/F)$ and $(\dot{\theta}/M)$ raw data.

7. COUPLED-BEAM ANALYSIS USING DERIVED DATA

The four mobility responses for the combined beam were again computed, this time using the derived B_r and D_r constants together with the identified A_r and C_r constants. Again these are only three distinct responses presented in Fig. 14 because $(\dot{\theta}/F)$ and $(\dot{X}/M)$ are taken as identical.

This coupled data is inaccurate above 800 Hz, the highest frequency for which the data for the long beam is reliable. Below 800 Hz the fit of the smoothed and derived data to the curve calculated from closed-form receptance

FIG. 11 MOBILITY PROPERTIES OF THE COUPLED BEAM: III

——— Theoretical ... Predicted from smoothed measurements on component beams.

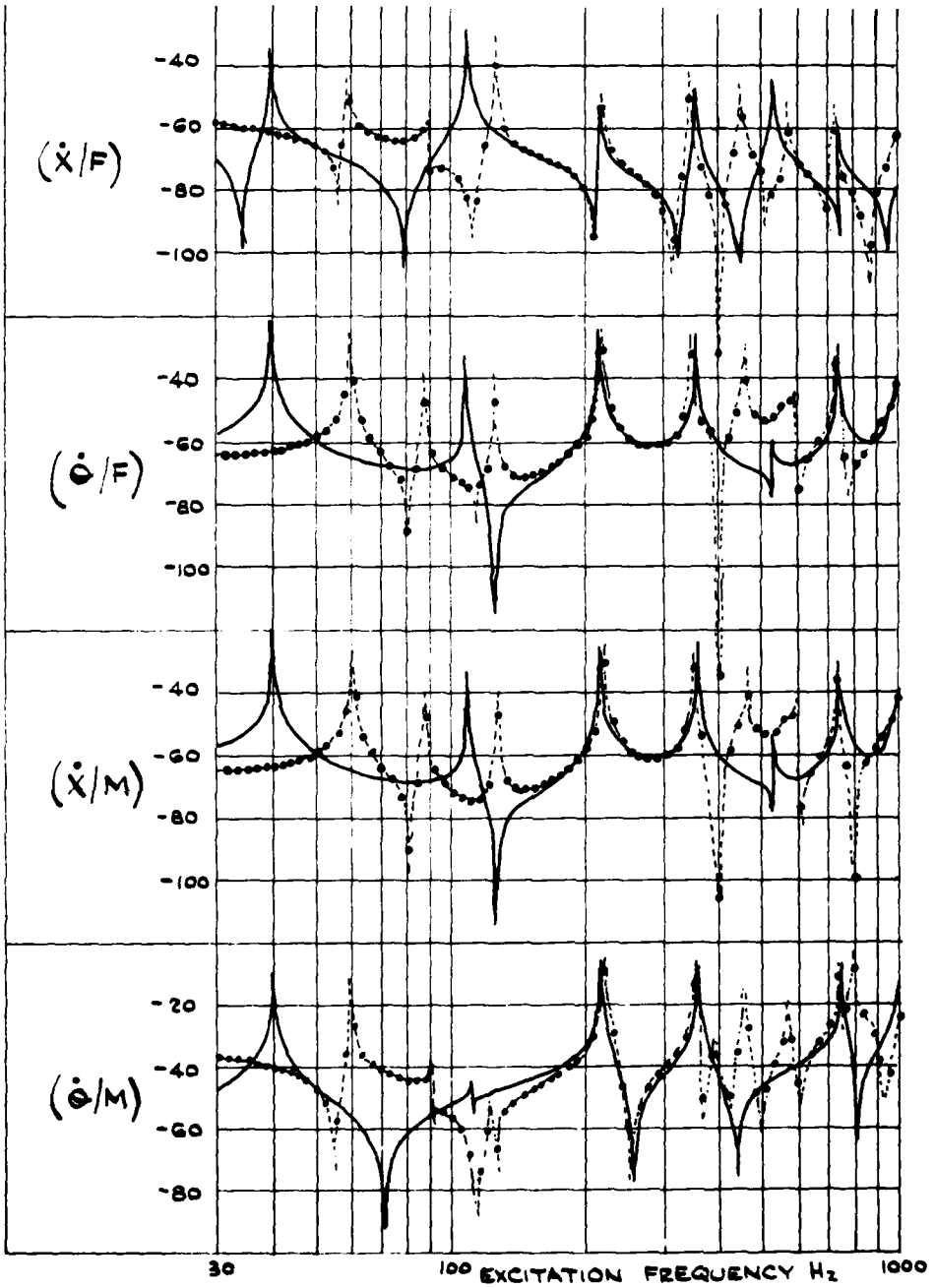

FIG. 12 MOBILITY PROPERTIES OF THE LONG BEAM: III

Tneoretical ...Smoothed measurements for $(\dot{X}/F)(\dot{X}/M)$

Derived measurements for $(\dot{\theta}/F)(\dot{\theta}/M)$

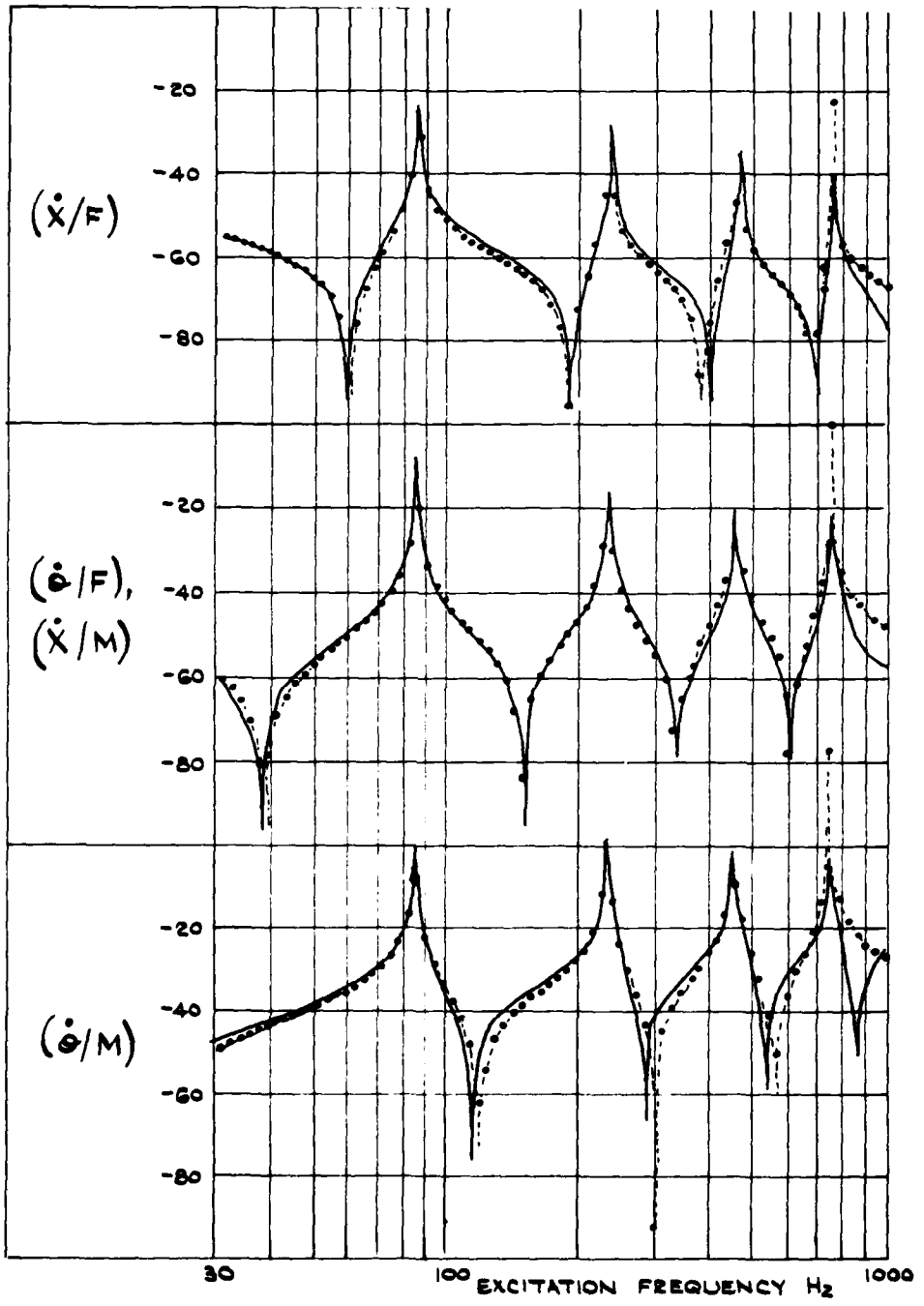

FIG. 13 MOBILITY PROPERTIES OF THE SHORT BEAM: III

Theoretical ... Smoothed Measurements for $(\dot{X}/F)(\dot{X}/M)$

Derived measurements for $(\dot{\theta}/F)(\dot{\theta}/M)$

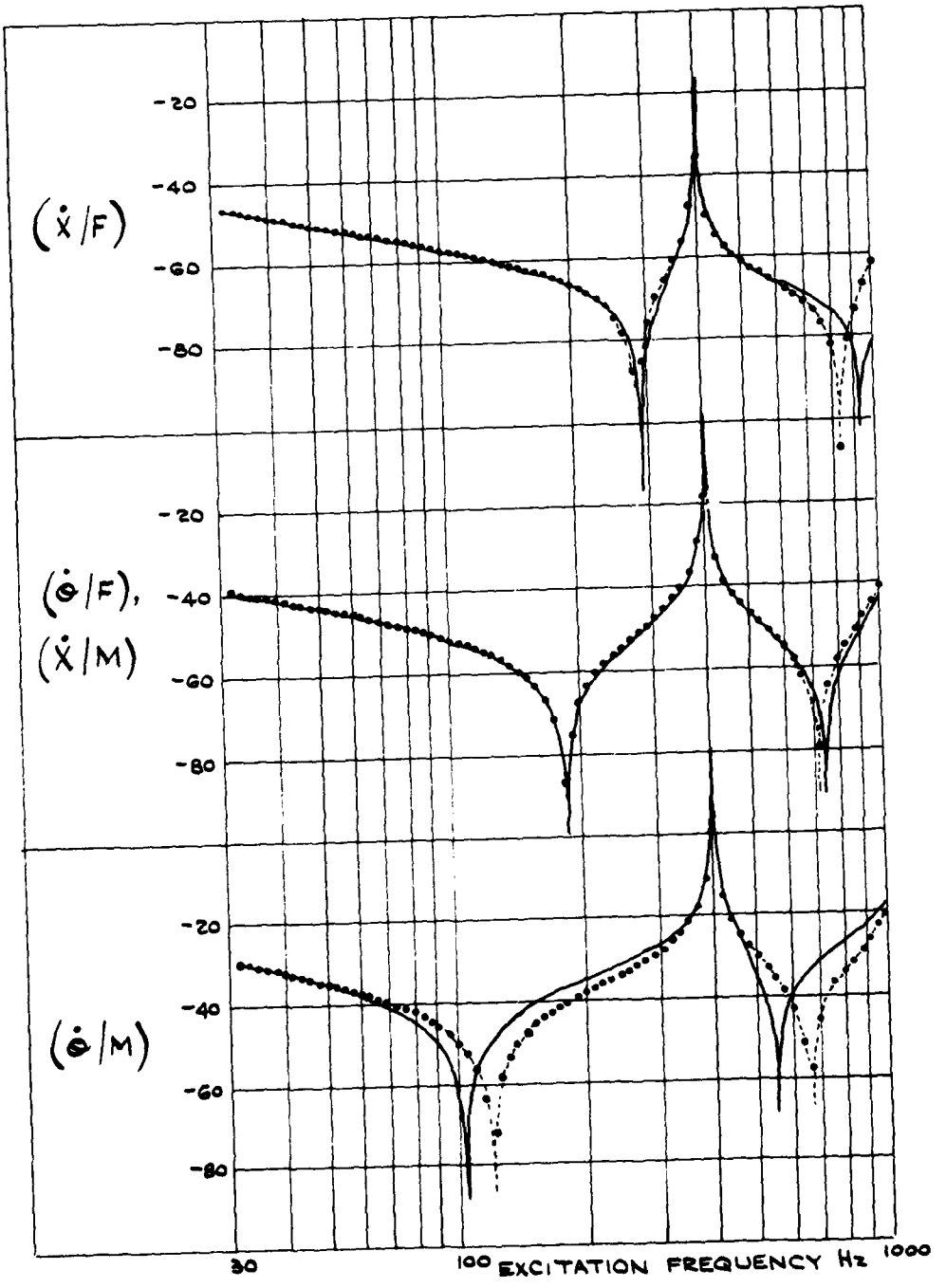

FIG. 14 MOBILITY PROPERTIES OF THE COUPLED BEAM: IV

——— Theoretical ... Predicted from Smoothed/derived measurements on component beams.

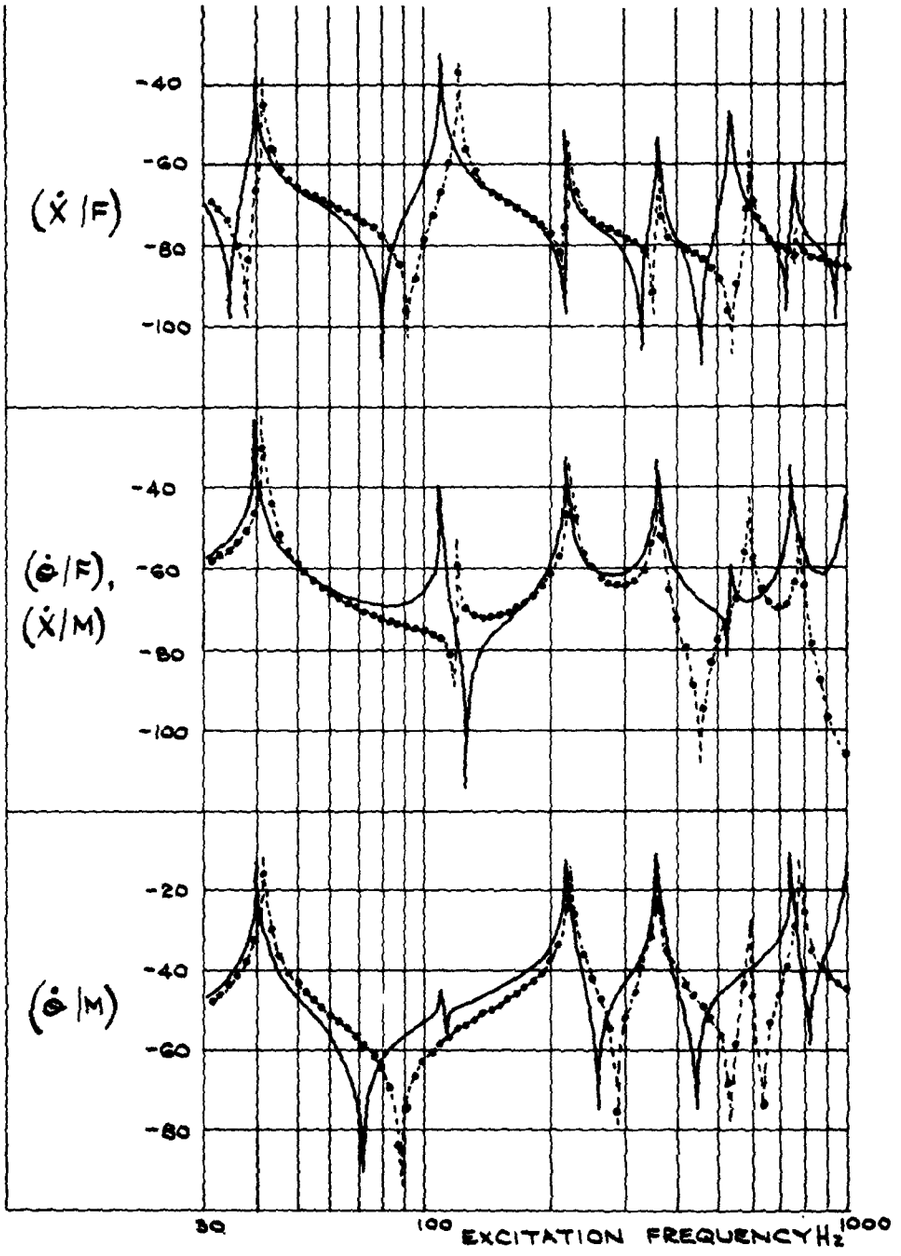

formulae is much better than either of the previous examples shown in Figs. 7 and 11. In particular, these results accurately predict the low frequency resonance at 42 Hz (close to the theoretical value of 40 Hz) which is absent from the earlier coupled-beam results. The other 5 resonances are also indicated with reasonable accuracy for the mobility ($\dot{X}/F$), and this response has the right general shape and level up to 800 Hz. The ($\dot{\theta}/F$), ($\dot{X}/M$) responses maintain good shape up to 400 Hz, although the resonance at 120 Hz is only just noticeable. The 120 Hz resonance is missed altogether from the ($\dot{\theta}/M$) response but it should be noted that the corresponding theoretical resonance is very small.

The identification and derivation process is thus more accurate for low frequencies than for high which may be explained by the inherently greater accuracy of low frequency modal constants. The results are felt to be significant mainly because it has not been possible to measure ($\dot{\theta}/M$) at all accurately at frequencies below the first resonance by any other method.

8. CONCLUSIONS

It has been demonstrated again that when experimentally determined mobility (or impedance) data are required for further analysis, due consideration must be given to all the directions in which the test structure vibrates. In particular, for beams it is necessary to include the rotational motion as well as the translational.

Measurement of rotational mobility data is hindered by the difficulty of measuring rotational response. However, a method has been presented which enables the determination of such rotational mobility data from measurements of translational responses only, thereby obviating the need to measure angular motion. The technique involves simply making two otherwise conventional mobility measurements, plus some analysis.

REFERENCES

1. D. J. Ewins and M. G. Sainsbury, "Mobility Measurement for the Vibration Analysis of Connected Structures", Shock and Vibration Bulletin, 42, Pt 1, 1972.

2. J. E. Smith, "Measurement of the Total Structural Mobility Matrix", Shock and Vibration Bulletin, 40, 1970.

3. A. L. Klosterman, "On the Experimental Determination and Use of Modal Representations of Dynamic Characteristics", University of Cincinatti, Ph.D. Thesis, 1971.

APPENDIX I. The Response of a Multi-Degree of Freedom System to Sinusoidal Excitation

The response of a n-degree of freedom system to steady-state sinusoidal excitation at an angular frequency ω, can be written in generalized coordinates q_1, q_2 etc., see ref. (3):

$$\{Q\} = \sum_{r=1}^{n} \frac{\{\psi_r\}^T \{F\} \{\psi_r\}}{m_r (\Omega_r^2 - \omega^2)} = \sum_{r=1}^{n} \gamma_r \{\psi_r\} \qquad (i)$$

where $\{Q\}$ is a column vector of response amplitudes
$\{F\}$ is a column vector of input force amplitudes
and Ω_r is the r th eigenvalue
$\{\psi_r\}$ is the eigenvector of the rth mode
m_r is the mass of the r th mode

We are particularly interested in the response Q_i caused by the single excitation F_j:-

$$Q_i = \sum_{r=1}^{n} \frac{(\psi_{rj} F_j)(\psi_{ri})}{m_r (\Omega_r^2 - \omega^2)} \qquad (ii)$$

giving

$$(Q_i/F_j) = \sum_{r=1}^{n} \frac{\psi_{rj} \psi_{ri}}{m_r (\Omega_r^2 - \omega^2)} \qquad (iii)$$

We wish to consider two responses, X ($=Q_1$) and θ ($=Q_2$), and two forces, F ($=F_1$) and M ($=F_2$)

The system being considered is continuous but we may assume that at low frequencies only a finite number of modes need be included.

Thus we can write:-

$$(X/F) = \sum_{r=1}^{n} \frac{A_r}{(\Omega_r^2 - \omega^2)} \qquad (iv)$$

$$(\theta/F) = \sum_{r=1}^{n} \frac{B_r}{(\Omega_r^2 - \omega^2)} \qquad (v)$$

$$(X/M) = \sum_{r=1}^{n} \frac{C_r}{(\Omega_r^2 - \omega^2)} \qquad (vi)$$

$$(\theta/M) = \sum_{r=1}^{n} \frac{D_r}{(\Omega_r^2 - \omega^2)} \qquad \text{(vii)}$$

Where $A_r = \phi_{r1}^2/m_r$; $B_r = \phi_{r2}\,\phi_{r1}/m_r$;

$$C_r = \phi_{r1}\,\phi_{r2}/m_r;\ D_r = \phi_{r2}^2/m_r \qquad \text{(viii)}$$

It follows that $B_r = C_r$ and $D_r = C_r^2/A_r$ (ix)

Thus all four modal constants may be deduced from A_r and C_r.

MODAL IDENTIFICATION

This is the process of determining the modal constants from measured impedance data.

Equation (iv) may be rewritten by substituting $-\omega^2 X = \ddot{X}$ to give

$$(\ddot{X}/F) = \sum_{r=1}^{n} \frac{-\omega^2 A_r}{(\Omega_r^2 - \omega^2)}$$

$$= \sum_{r=1}^{n} \frac{A_r}{(1 - \Omega_r^2/\omega^2)}$$

This quantity is the Inertance, the ratio of acceleration to force, the two quantities measured in 'impedance' tests.

There are n modes being considered, and thus there are n resonant frequencies which must be known. Inertance data must be obtained at n non-resonant angular frequencies, $\omega_1, \omega_2, \omega_3 \ldots\ldots \omega_n$.

The matrix equation relating these quantities is

$$\begin{Bmatrix} (\ddot{X}/F)_1 \\ (\ddot{X}/F)_2 \\ (\ddot{X}/F)_3 \\ \cdot \\ \cdot \\ \cdot \\ (\ddot{X}/F)_n \end{Bmatrix} = \begin{bmatrix} \frac{1}{(1 - \Omega_1^2/\omega_1^2)} & \frac{1}{(1 - \Omega_2^2/\omega_1^2)} & \cdots\cdots & \frac{1}{(1 - \Omega_n^2/\omega_1^2)} \\ \frac{1}{(1 - \Omega_1^2/\omega_2^2)} & \cdots\cdots\cdots\cdots & & \frac{1}{(1 - \Omega_n^2/\omega_2^2)} \\ \frac{1}{(1 - \Omega_1^2/\omega_3^2)} & \cdots\cdots\cdots\cdots & & \cdots\cdots\cdots\cdots \\ \cdot & \cdot & & \cdot \\ \cdot & \cdot & & \cdot \\ \cdot & \cdot & & \cdot \\ \frac{1}{(1 - \Omega_1^2/\omega_n^2)} & \cdots\cdots\cdots\cdots & & \frac{1}{(1 - \Omega_n^2/\omega_n^2)} \end{bmatrix} \begin{Bmatrix} A_1 \\ A_2 \\ A_3 \\ \cdot \\ \cdot \\ \cdot \\ A_n \end{Bmatrix}$$

or

$$\{I_A\} = [R]\,\{A\}$$

Similarly there are equations for the other modal constants:-

$$\{I_B\} = [R]\,\{B\};\ \{I_C\} = [R]\,\{C\} \text{ and } \{I_D\} = [R]\,\{D\}$$

The modal constants can thus be determined by inverting the R matrix and then pre-multiplying the appropriate response matrix

$$\{A\} = [R]^{-1}\,\{I_A\} \quad \text{and so on.}$$

APPENDIX II. Solid Body Response

If the system is free-free it has a resonance at zero frequency ($\Omega_1 = 0$). The motion is, of course, that of a solid body. The relationsnips expressed in equation (ix) do not nold for this case and it is necessary to study the geometry of the motion to discover the corrections needed.

The body has mass m and moment of inertia I_G about its centroid G.

In the first instance the effect of pure input couple M on the angular response θ and the translational response X_p of point P are required. (Fig. 15)

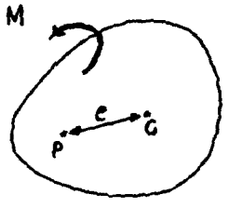

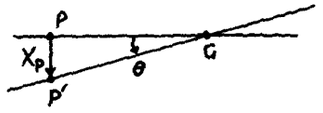

Fig. 15. Effect of Couple Input on Solid Body

Pure couple M produces rotation but no translation of G.

$M = I_G \ddot{\theta}$ $\quad \therefore (\ddot{\theta}/M) = 1/I_G$

$M = I_G(\ddot{X}_p/e)$ $\quad \therefore (\ddot{X}_p/M) = e/I_G$

Secondly, the effect of the input force F acting at P is required. (Fig. 16)

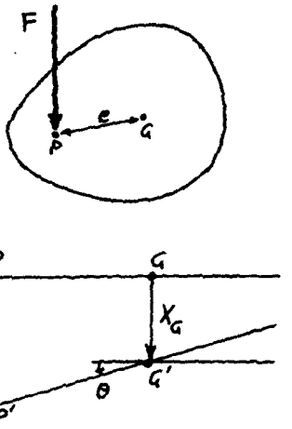

Fig. 16. Effect of Force Input on Solid Body

Force input at P produces both rotation and translation of G.

$X_p = e\,\theta + X_G$

$X_G = X_p - e\,\theta$

$F\,e = I_G\,\ddot{\theta}$ $\quad \therefore (\ddot{\theta}/F) = e/I_G$

$F = m\,\ddot{X}_G = m\,(\ddot{X}_p - e\,\ddot{\theta})$

$= m\,(\ddot{X}_p - e\,(e\,F/I_G))$

$\therefore F(1 + m\,e^2/I_G) = m\,\ddot{X}_p$

$\therefore (\ddot{X}_p/F) = 1/m + e^2/I_G$

It follows that $A_1 = 1/m + e^2/I_G$

$B_1 = e/I_G$

$C_1 = e/I_G$

$D_1 = 1/I_G$

Thus $B_1 = C_1$ and $D_1 = C_1^2/(A_1 - 1/m)$

A NEW STUDY OF THE HARMONIC OSCILLATOR

WITH NON-LINEAR FLUID DAMPING

Ralph A. Eyman
Martin Marietta Aerospace
Orlando, Florida

The frequency of all oscillating spring mass systems which rely on fluid damping will approach the natural frequency of the system as time becomes large. The dependence of resistance on velocity may be limited by the value of v^{ε} where $1<\varepsilon<2.586$.

The damped harmonic oscillator represented by a mass, spring, dashpot system is treated extensively in most applied mathematics and mechanics texts. The retarding force is known as viscous friction and is proportional to the velocity of the mass. This relation, when expressed by an equation of motion, results in a second-order linear differential equation which may be solved in closed form.

Comprehensive studies of the solutions result in such familiar terms as viscous damping, under damping, over damping, critical damping, and damped frequency. However, no dashpot behaves precisely like linear resistance and, with the exception of electrical analogues, these terms, as defined, exist only in the mathematics. Theoretically, when three-dimensional flow is considered, resistance provided by the dashpot is proportional to the fluid density and the square of the piston velocity and, at large velocities, has been considered to be proportional to nearly the cube of the velocity. Non-linear damping is elegantly treated by various mathematical techniques in many advanced mechanics and control theory texts. The author presents the results of a new study done with the aid of computer techniques.

We consider the equation,

$$m\ddot{x} + b\, f(\dot{x}) + kx = 0$$

and set

$$f(\dot{x}) = \frac{\dot{x}}{|\dot{x}|}|\dot{x}|^{\varepsilon}.$$

The equation may be rewritten as

$$\ddot{x} + 2\gamma \frac{\dot{x}}{|\dot{x}|}|\dot{x}|^{\varepsilon} + \omega_o^2 x = 0$$

where the damping coefficient and natural frequency are respectively,

$$\gamma = \frac{b}{2m}, \qquad \omega_o = \sqrt{k/m}.$$

No closed form solutions have been found for this equation except for $\varepsilon = 1$ where it takes the classical form

$$\ddot{x} + 2\gamma\dot{x} + \omega_o^2 x = 0$$

whose solutions are

$$x = \ell^{-\gamma t}(A \cos \omega_1 t + B \sin \omega_1 t), \quad \omega_o > \gamma$$

where

$$\omega_1 = \sqrt{\omega_o^2 - \gamma^2}$$

is the damped frequency and,

$$x = \ell^{-\gamma t}(C + Dt), \quad \omega_o = \gamma$$

and,

$$x = \ell^{-\gamma t}(E\ell^{\mu t} + F\ell^{-\mu t}), \quad \omega_o < \gamma$$

where,

$$\mu = \sqrt{\gamma^2 - \omega_o^2}.$$

When $\omega_o > \gamma$ the system is under-damped. For values of $\omega_o < \gamma$ it is over-damped and for the value $\omega_o = \gamma$ the system is critically damped. The value γ/ω_o is called the damping ratio.

For the purpose of this study a mass-spring system with a natural frequency of one radian per second is released from rest at a displacement of one unit. The coefficients A, B, C, D, E, and F are established and the solutions are rewritten as

$$x = \ell^{-\gamma t}(\cos \omega_1 t + \gamma \sin \omega_1 t), \qquad \gamma < 1$$

$$x = \ell^{-\gamma t}(1 + \gamma t), \qquad \gamma = 1$$

$$x = \ell^{-\gamma t}\left(\frac{\gamma + \mu}{2\mu}\ell^{\mu t} - \frac{\gamma - \mu}{2\mu}\ell^{-\mu t}\right), \quad \gamma > 1$$

where the damping ratio is γ.

The particular form of the equation is rewritten as

$$\ddot{x} + \frac{\dot{x}}{|\dot{x}|}2\gamma|\dot{x}|^{\varepsilon} + x = 0.$$

The equation was solved by numerical integration for various values of γ and ε. For the particular value of $\gamma = 1$, (which is the critical damped case in the viscous or linear damped equation) the values of $x = f(t)$ are plotted on Figure 1 for values of $\varepsilon = 1$, 1.2, 2, and 3.

For the value $\varepsilon = 1$ the curve follows the solution,

$$x = \ell^{-t}(1 + t).$$

For the value of $\varepsilon = 1.2$ the system oscillates with an initial period slightly larger than the period of the natural frequency and is observed to approach the natural frequency as time becomes larger. For the value of $\varepsilon = 2$ the initial period after the first overshoot is very near to, but still larger than 2π, and for the value of $\varepsilon = 3$, it is very near to, but smaller than 2π. In each case it approaches 2π quite rapidly. The periods for the three cases, although discrete values, are plotted as continuous functions of the number of overshoots on Figure 2. Other values of γ produce similar results (see Figure 3). The system always oscillates except where $\gamma = 1$ and $\varepsilon = 1$, the linear critical damped condition. The system even oscillates for some values of $\gamma > 1$ provided $\varepsilon > 1$ and in those cases the frequency also converges on w_o as time becomes large.

By trail and error a constant $\varepsilon = \varepsilon_n$ was found such that after the first overshoot the system always oscillates at precisely its natural frequency for <u>all</u> values of γ. Its value, to four significant figures is

$$\varepsilon_n = 2.586.$$

For values of $\varepsilon < 2.586$ the initial period is always greater than 2π and for values of $\varepsilon > 2.586$ it is always less than 2π.

The plot of the solutions of the equation,

$$\ddot{x} + \frac{\dot{x}}{|\dot{x}|}2\gamma|\dot{x}|^{2.586} + x = 0$$

is shown on Figure 4 for four values of γ which range over 4 orders of magnitude. The value $\gamma = 100$ was also tested with similar results.

Since it seems reasonable that no damped oscillator would oscillate at a frequency greater than its natural frequency the results of this study strongly suggest that ε_n is a natural constant limiting the proportionality of the dependence of resistance on velocity, v, to the value,

$$v^{2.586}.$$

It may even suggest that the dependence of all fluid friction on velocity is limited to this value.

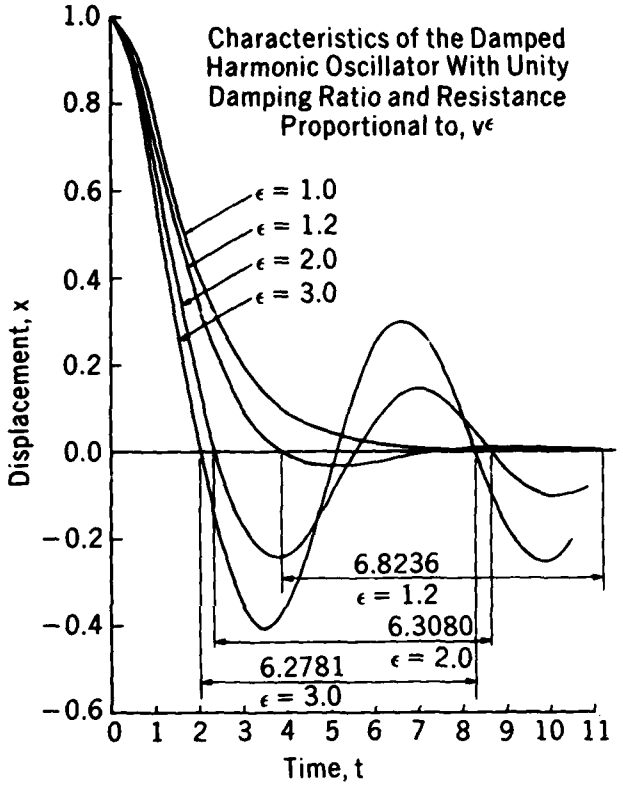

Figure 1. Harmonic Oscillator – Unity Damping

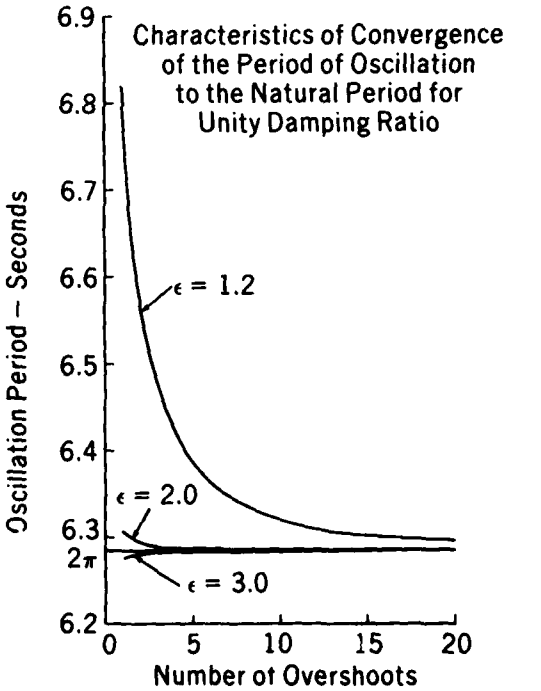

Figure 2. Convergence of Period – Unity Damping

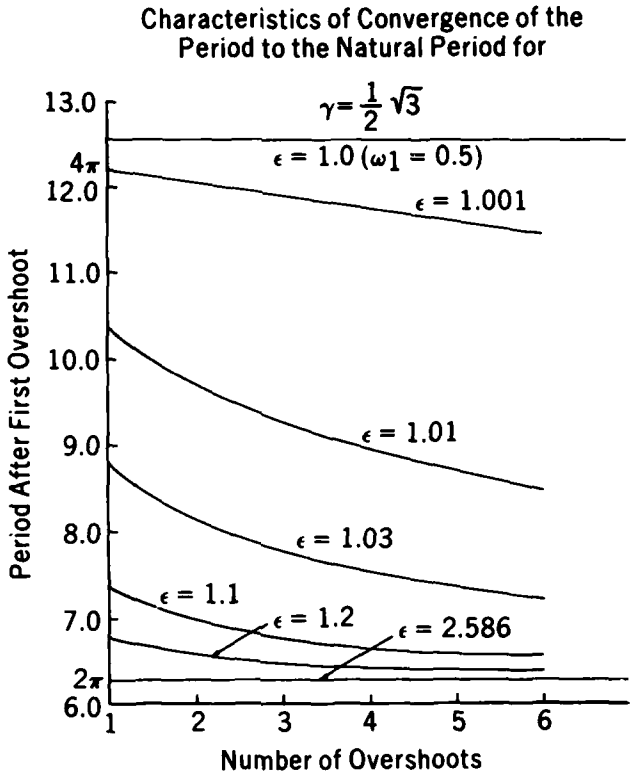

Figure 3. Convergence of Period, 0.866 Damping

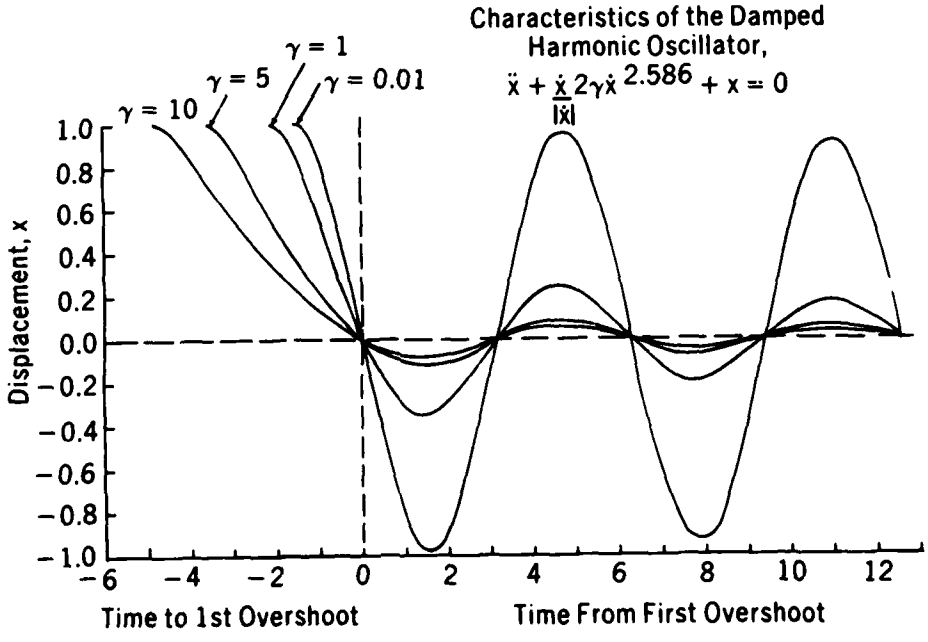

Figure 4. Damped Harmonic Oscillator, $\epsilon = 2.586$

MECHANICAL DESIGN, ANALYSIS, AND TEST OF THE STANDARD ELECTRONICS CABINET AND CONTROL DISPLAY CONSOLE FOR THE AN/BQQ-5 SONAR SET*

Richard E. Denver and Joseph M. Menichello
IBM Corporation
Federal Systems Division
Owego, New York 13827

The AN/BQQ-5 shipboard system is a sonar signal processor comprised of electronics cabinets whose function is to detect, track, and classify targets in the ocean. IBM, Federal Systems Division, has been involved in designing, building, and testing various AN/BQQ-5 equipment since 1971. This paper deals with the analysis and development shock and vibration testing leading to the mechanical design of two types of electronics units, namely, the standard electronics cabinet and the Control Display Console. As a result of the extensive structural analysis and engineering evaluation testing program performed during development, these two complex unit structures passed the formal shock and vibration qualification tests without a reportable failure.

INTRODUCTION

The AN/BQQ-5 units were designed to meet the requirements of MIL-E-16400, which requires qualification to MIL-STD-167 and MIL-S-901C for vibration and shock environments, respectively. To ensure compliance with these requirements, a basic philosophy was established early in the development stage of design. This governing philosophy for shipboard equipment within IBM is twofold:

1) Design sufficient structural rigidity, or stiffness, to ensure that fundamental equipment resonances are substantially greater than the maximum forcing frequency specified in MIL-STD-167. In this manner, amplification at resonance is avoided and the corresponding potential fatigue damage is precluded.

2) Design sufficient strength in the structural elements to keep stresses resulting from the Navy Hi-Impact shock testing of MIL-S-901C within allowable material limits.

DESIGN

Within the AN/BQQ-5 shipboard system are several basic electronic units, two of which are discussed in this paper. The standard electronics cabinet design is utilized as the basis for a large percentage of the total system while the Control Display Console is the most unique and complex.

STANDARD ELECTRONICS CABINET

Three variations of the standard electronic cabinet exist, each designed with two vertical slide-out chassis which carry most of the electronics. When in the closed position, each slide-out chassis of the largest cabinet height (65 inches) mates with the housing by means of five 12-inch diameter bullpins in the rear and 9-5/16 inch diameter bullpins around the front latch. In addition, each front latch contains 16 bolts and strikers to positively attach the chassis to the cabinet housing.

The primary load-carrying structure in the cabinet housing is shown in Figure 1. The structure consists of an A357 aluminum alloy casting both top and bottom. The sides are a one-piece extruded 6061-T6 aluminum alloy, which forms an integral wall incorporating corner posts, inner and outer skins, and longitudinal flutes for cooling air. The extrusions are welded to the top and bottom castings. The cabinet is divided into two sections by a vertical partition which is designed to form fluted ducts for cooling air. The rear of the cabinet is a removable 1/8-inch thick panel attached by flathead screws.

* This work was performed under Contract N00024-70-C-1300 with NAVSEA Systems Command, Code 660F1.

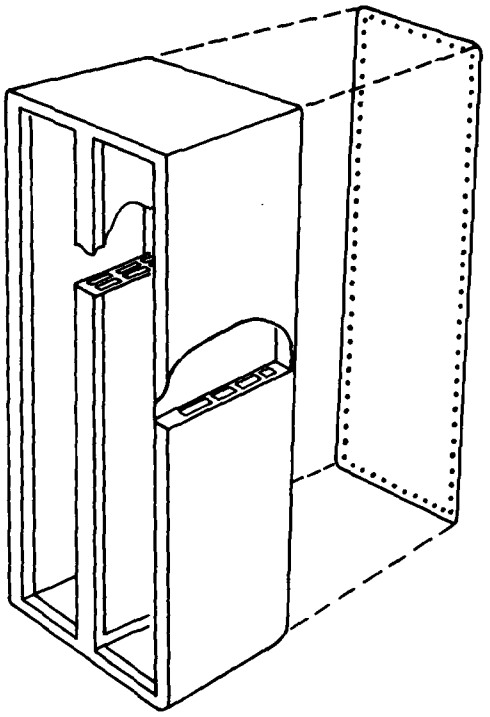

Figure 1. Primary Structure for Standard Cabinet

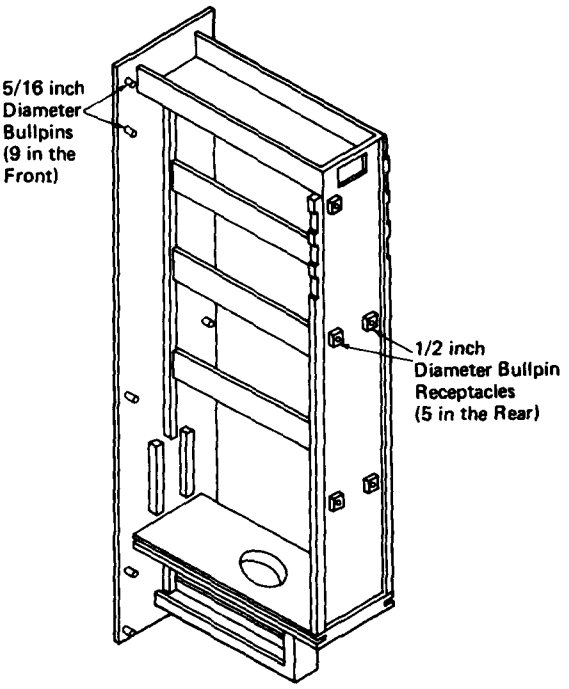

Figure 2. SHF Module Gate Frame

The cabinet houses two slide-out chassis constructed of a one-piece, high strength aluminum alloy casting. For the ease of manufacturing, the alloy options are K01, A357, or A356. The casting is machined to accept the full length latch on front, slides on top and bottom, and electronic subassemblies attached to each side. A sketch of the slide-out chassis gate is shown in Figure 2 (also Figures 3 and 4).

CONTROL DISPLAY CONSOLE

The Control Display Console is designed with five slide-out chassis - two separate CRT chassis, one combined memory drum unit and drum power supply chassis, and two Standard Hardware Program (SHP) (Naval Air Facility, Indianappolis) chassis. The structure is designed in two halves to comply with submarine installation size restrictions. Each half is constructed in a similar fashion and they are bolted together to form one integral unit (Figure 5).

The base of each half is an A357 aluminum alloy casting. The top is a solid plate of 6061-T6 aluminum. The main frame members are generally

Figure 3. Standard Cabinet with Gate A Open

Figure 4. Standard Cabinet with Gates A & B Closed

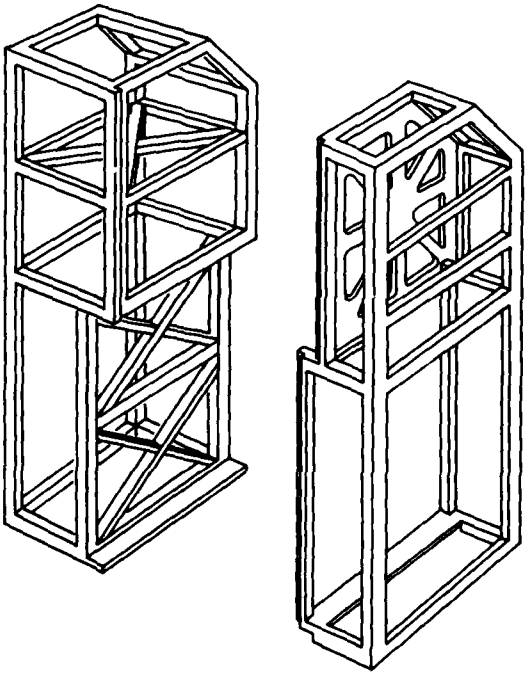

Figure 5. Primary Frame Structure for the Control Display Console

6061-T6 aluminum extrusions. The top plate, bottom casting, and extrusions are welded together to form the basic frame. The sides and rear are 1/8-inch thick aluminum panels of 6061-T6 alloy, which are attached by flathead screws. An additional doghouse extends the full height on the rear to form a return air duct for cooling the electronics.

The lower half of the Control Display Console contains two similar SHP slide-out chassis. A picture of the left-side chassis, when in the extended position, is shown in Figure 6. This figure shows the hinged double SHP gate opened in the maintenance position. Figure 7 shows the primary structure for both gates. As indicated in the sketch, the entire chassis slides out on two slides located one above the other. The slides are attached to the K01 T43 aluminum "L" shaped single SHP gate casting. The double SHP gate is attached by a hinge to the single SHP frame.

Figure 6. Control Display Console Lower SHP Left-side Chassis in the Extended Position

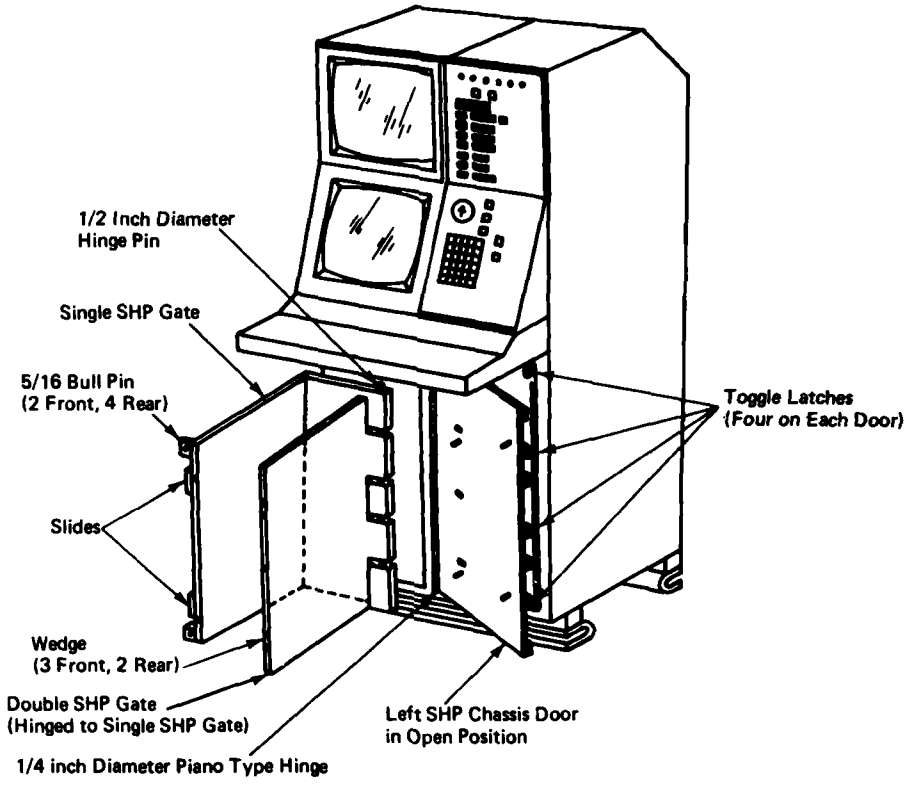

Figure 7. Control Display Console Primary Structure for Lower *Left SHP Chassis*

The single SHP gate, double SHP gate, hinged door, and Control Display Console frame are integrally locked together, when in the closed position, by bullpins and specifically designed wedges and toggle latches. Some of these devices and their locations are shown in Figures 7 and 8. The rear of the double SHP gate attaches to the single SHP gate through two 17-4 PH (H900) steel wedges in addition to the hinge, which is 1/2 inch diameter 17-4 PH (H900) steel. The wedges are designed to act similar to bullpins; however, they are wedge shaped to provide engagement as the double SHP gate swings in an arc to mate to the single SHP gate. The hinge and wedge provide positive attachment between the two gates at the rear. The SHP gates then mate to the Control Display Console frame in the rear with six 5/16 inch diameter 17-4 PH (H900) bullpins - four on the single and two on the double SHP chassis.

The front of the single SHP gate attaches to the Control Display Console structure through 2-5/16 inch diameter bullpins. The SHP front door is 3/8 inch thick 6061-T6 aluminum and is designed to provide additional support to the front of the SHP gates. The door is attached to the center front member of the Control Display Console by a 1/4 inch diameter 17-4 PH (Condition A) continuous hinge. As the door is pivoted to the closed position, three wedges engage with the front edge of the double SHP gate. The door then attaches to the Control Display Console structure along the side with four specially designed toggle latches. These four toggle latches serve two purposes: (1) they act as the wedges to resist shock forces in shear, and (2) they also act as thumbscrews to engage the wedges and bullpins and hold the chassis in the closed position. In addition, the front SHP door also has two 303 stainless steel 1/4 inch diameter thumbscrews - they attach to the front edge of double SHP gate to pull the gates tight to the door to ensure full engagement of the wedges, and to prevent motion of the chassis from front to rear.

The upper and lower CRT chassis, shown in Figures 9 and 10, are constructed of a one piece A356-T6 aluminum casting supported on each side with a slide. When in the closed position, the casting mates with the frame by means of 2-5/16 inch bullpins front and rear. The bullpins are made

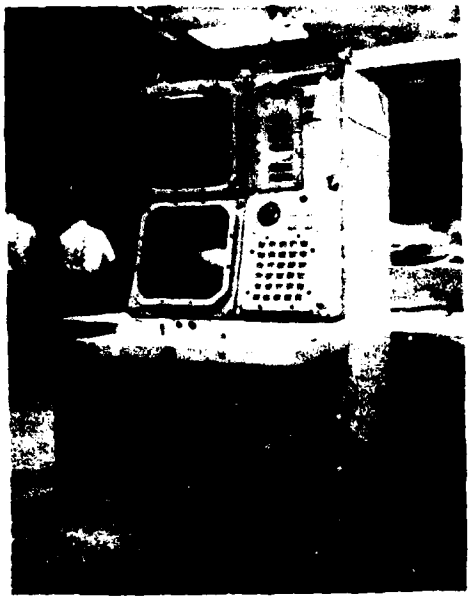

Figure 8. Control Display Console

Figure 9. Control Display Console Upper CRT in the Extended Position

from 17-4 PH (H900) steel. The chassis is held in the closed position by four 1/4 inch diameter thumbscrews made of 303 stainless steel. Power supplies, transformers, and other electronics attach directly to the casting or to brackets. The CRT itself is potted with foam within a continuous metal shield. The shield attaches to the casting through stainless steel tabs, which are spot welded to the CRT shield.

The drum chassis extends on two slides located one above the other along the right side of the Control Display Console. In the closed position, the chassis is supported by four 5/16 inch bullpins, both front and rear. These eight bullpins are made from 17-4 (H900) steel. The chassis is held in the closed position by six 1/4 inch diameter thumbscrews made of 303 stainless steel. The chassis is a cast A356-T6 aluminum frame, and the front panel is a separate casting of the same material. The drum itself is mounted in the lower section of the drawer. The upper half contains the drum power supply and the static inverter (Figure 11).

Figure 10. Control Display Console Lower CRT in the Extended Position

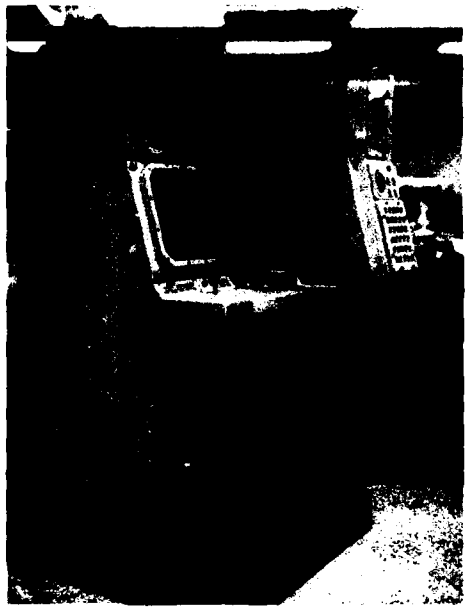

Figure 11. Control Display Console Drum Chassis in the Extended Position

STRUCTURE ANALYSIS

The design of each structure was aided by computerized structural analysis from the inception of the design through the initial structural drawing release. In the early phases, the analysis was confined to determining a lower bound for the natural frequency of each structure (using the Mechanical Analysis (MECHA) computer program) to ensure that the resonances were above the maximum forcing frequency of 33 Hz. To prevent amplification, a minimum resonance of 45 Hz was established as a goal.

Preliminary math models were made to represent the major structural members of both units. Due to limited number of degrees of freedom allowed in the MECHA program, and also due to lack of detailed layout information in the early stages of design when the primary member sizes were being established, not all the stiffnesses were represented in the math model. These initial analytical vibration results indicated that the primary structural resonances for both units were above the minimum established goal of 45 Hz and attention was then given to a more detailed static analysis to ensure every structural elements would survive the high impact hammer drop test.

To ensure that both units meet the shock requirements, much more detailed structural analyses were performed using the Structural Design Language (STRUDL) program. The standard cabinet was divided into two parts for analysis. A model was developed for one of the slide-out gates. For this model, the support points were taken as the bullpins and latch strikers that attach between the gates and the frame. The reaction forces at the support points were then applied as loads to the detailed cabinet model. The slide-out gate model was composed of 88 joints and 113 members with 497^{o} of freedom. The math model for the cabinet frame was comprised of 121 nodes with 6^{o} of freedom permitted at each node except at the eight support points.

The Control Display Console math model was also divided into several parts. A model was developed for each type of the slide-out chassis, namely, the upper CRT chassis, drum chassis, and lower SHP chassis. For the models, the support points were taken as the bullpins, thumbscrews, or toggle latches that attach between chassis and frame. The reaction forces at the support points were then applied as loads to the detailed Control Display Console model. In total, approximately 450 joints, or 2700^{o} of freedom, were used to represent the Control Display Console Frame and contained subassemblies. It should be noted that as the design progressed, this model was continually updated to reflect the latest design changes. Extensive interfacing between the design and analysis groups eliminated any overstressed conditions.

From test data obtained from the Navy, a 70g load factor was applied to the weight of each unit in the vertical direction to simulate maximum loading during the medium weight hammer drop test.

To simulate loading during the inclined medium weight hammer drop test, load factors are applied as follows: 61g vertically and 25g along two horizontal axes. These factors are simultaneously applied to simulate shock loading when the unit is rotated 45^{o} and then inclined 30^{o} around one corner and shocked from below as required by MIL-S-901C.

VIBRATION AND SHOCK TESTING

Development vibration and shock testing were performed on both standard cabinet and Control Display Console structures early in the design stage to confirm the integrity of the mechanical design.

STANDARD ELECTRONICS CABINET

The vibration testing consisted of approximately 4.6 hours of testing per plane to include the following:

1) Exploratory Vibration Test:

   4 to 33 Hz at 0.02/inch DA
   15 seconds/discrete frequency

2) Variable Frequency Test:

   4 to 15 Hz at 0.06 inch DA
   16 to 25 Hz at 0.04 inch DA
   26 to 33 Hz at 0.02 inch DA
   5 minutes/discrete frequency

3) Endurance Test:

   2 hour dwell at 33 Hz with a 0.020 inch DA.

A resonance search was performed prior to the start and at the completion of each of the three planes of vibration. This was performed in addition to the requirements of MIL-STD-167B to determine the resonant frequency of the system, and to verify that there was no structural weakening during the approximately 4-1/2 hours of vibration per plane.

The results of vibration testing confirmed the analytical predictions. The natural frequencies found are listed below as a function of direction.

Direction	Frequency (Hz)
Vertical	66
Side to Side	75
Front to Rear	80

Since the maximum forcing frequency was 33 Hz, the maximum transmissibility measured during testing was 1.2. No degradation was observed during the vibration testing.

The shock testing was performed in accordance with the requirements of MIL-S-901C. As required by the performance specification, a soft deck simulator was inserted between the cabinet and anvil during the shock testing. Twelve blows were delivered to the test specimen, six of which were to determine the spring bed natural frequency. The following chart is a chronological summary of the shock testing.

Orientation	Hammer Height (ft)	Table Travel (in)	Number of Blows
Vertical	0.75	3	2
	3.25	3	1
	5.50	3	1
	5.50	1.5	1
Inclined	0.75	3	4
	3.25	3	1
	5.50	3	1
	5.50	1.5	1

The standard cabinet was loaded with simulated weights to achieve a total unit weight of 900 pounds. The vertical and 30^{o} incline vibration and shock test setups are shown in Figures 12 through 15. Table 1 is a summary of the results determined from the testing.

There was approximately 15% attenuation across the supporting C feet during the six shock blows. The 0.25 inch thick L stabilizing brackets at the top showed permanent yielding at the corner radii. This does not cause concern since the cantilevered brackets are designed to yield. There was no observable fracturing or yielding within the cabinet itself. The gates were opened after each of the six blows without difficulty or binding. All rear bull pins and lock nuts remained in their preset positions.

After reviewing the reduced acceleration data, the following conclusions can be drawn:

1) With the deck simulator, the medium weight hammer imposes acceleration magnitudes of between 50g and 90g into and within the cabinet, along the hammer blow axis. The half-sine time durations are approximately 12 ms.

2) Inclining the unit 30^{o} generally had little effect on the acceleration levels as recorded in the vertical plane. Accelerations of approximately 50g were experienced in the major and minor planes during this inclined position.

3) The gates remained essentially rigid within the structure. That is, there was no noticeable shifting between the two. Also, the same acceleration levels were experienced on the SHP card as on the supporting chassis.

4) The cabinet acceleration from the 3-foot hammer drop and 3-inch anvil travel is approximately 30% less than that experienced from the 5.5-foot hammer drop and 1.5-inch anvil travel.

5) An attenuation factor of approximately 6 was experienced across the Navy deck simulator for the three shock blows in the vertical plane. The acceleration level on the anvil was 550g.

Figure 12. Vertical Axis Test Setup

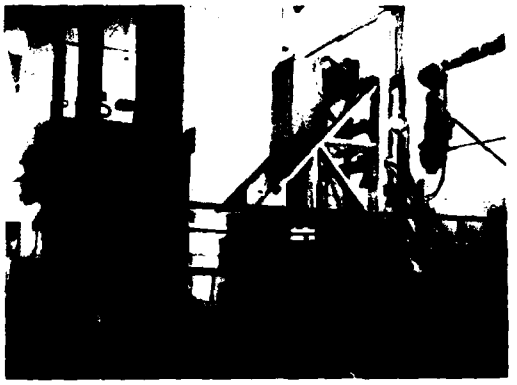

Figure 14. Vertical Fixture Test Setup

Figure 13. Vertical Axis Test Setup - Left Side

Figure 15. 30° Incline Test Setup

Table 1

SUMMARY OF SHOCK TEST RESULTS FOR THE STANDARD ELECTRONICS CABINET

No.	Accelerometer Location	Response Acceleration, g*					
		Vertical			30^{o} Inclination		
1	Bedspring, top	55	90	90	70	90	85
2	SHP Fin	85	80	100	45	55	60
3	Gate, Left latch	70	90	90	55	75	75
4	Cabinet, top	15	60	nil	50	85	30
5	Gate, left rear	65	85	100	50	65	70
6	Cabinet, base, front	50	70	65	50	60	70
7	Gate, right latch	60	80	80	-	-	-
	Fixture support	-	-	-	60	90	90
8	Gate, right rear	60	60	70	40	50	50
9	Cabinet, top	nil	nil	nil	50	50	60
10	Cabinet, cross member, rear	50	60	70	40	50	50
Test Conditions							
	Hammer height (ft)	3	5.5	5.5	3	5.5	5.5
	Anvil Travel (in)	3	3	1.5	3	3	1.5

*All the responses are in the vertical axis with the exception of two. Accelerometer number 4 is oriented in the major or side-to-side axis and number 9 is in the minor or front-to-back axis.

CONTROL DISPLAY CONSOLE

The Control Display Console was loaded with simulated weights with the exception of a live CRT, drum memory, and Parameter Select Matrix (PRASMA) assemblies. The total unit weight was 1100 pounds. The following relates a summary of the testing performed.

Sinusoidal sweeps were performed along the three principal unit axes preceding and following vibration in that axis. In addition to identifying structural resonances, these tests also served as an indicator of structural integrity as testing proceeded.

The vibration testing consisted of approximately 4.6 hours of testing per plane to include the following:

1) Exploratory Vibration Test:

   4 to 33 Hz at 0.02/inch DA
   15 seconds/discrete frequency

2) Variable Frequency Test:

   4 to 15 Hz at 0.06 inch DA
   16 to 25 Hz at 0.04 inch DA
   26 to 33 Hz at 0.02 inch DA
   5 minutes/discrete frequency

3) Endurance Test:

   2 Hour Dwell at 33 Hz with a 0.020 inch DA.

Through a low level exploratory vibration test, it was determined that unit resonance in all three planes was above 55 Hz, well above the maximum frequency of the test specification. The fundamental natural frequencies determined from the resonance search data were found to be:

Direction	Frequency (Hz)
Vertical	57
Side to Side	(Fixture resonance at 55 to 60 Hz. Did not detect any resonance below 55 Hz)
Front to Rear	59

In our test range, a transmissibility of one (1) was seen. No mechanical degradation was experienced during or as a result of the vibration testing. (See Figures 16, 17 and 18.)

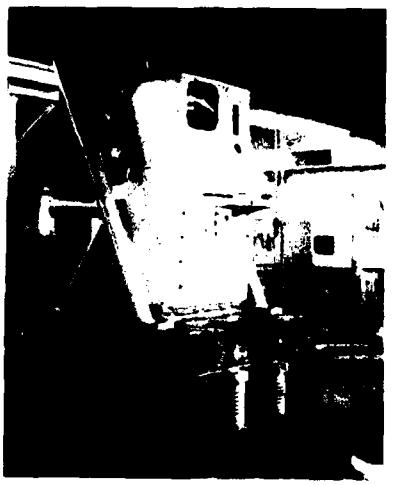

Figure 16. Control Display Console Vertical Shock Test Configuration

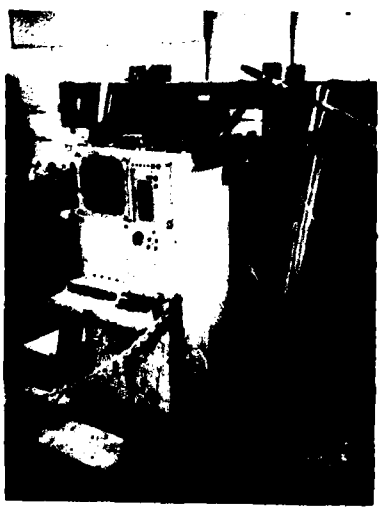

Figure 17. Control Display Console Vertical Shock Test Configuration

Figure 18. Control Display Console 30° Incline Shock Test Configuration

The Control Display Console shock testing was conducted similarly to the standard cabinet testing. Once again, the soft deck simulator was used an 12 blows were delivered to the test item. Table 2 summarizes the shock testing showing response acceleration to the medium weight hammer drop as a function of location within the console.

The reduced acceleration data reveals, in general, the same conclusions that apply to the standard cabinet. However, due to the more complex construction of the console, the frequency content of the shock responses at the various locations monitored within the console varies considerably in contrast to the predominance of a single frequency throughout the cabinet.

Table 2

SUMMARY OF SHOCK TEST RESULTS FOR THE CONTROL DISPLAY CONSOLE

No.	Accelerometer Location	Orientation	Response Acceleration, g*					
			Vertical			30^{o} Inclination		
1	Fixture	Vertical	70	80	90	100	100	100+
3		Vertical	60	65	75	70	70	65
4	Top of "C" Foot	Front-to-Rear	40	45	50	70	70	60
5		Side-to-Side	25	25	30	50	70	60
6		Vertical	85	90	100	90	90	100
7	Top of Console	Front-to-Rear	45	45	45	85	80	70
8		Side-to-Side	-	35	65	85	70	70
9	Sidewall,	Vertical	70	75	75	80	80	90
10	Center	Front-to-Rear	20	25	60	60	70	60
Test Conditions								
Hammer height (ft)			3.25	5.5	5.5	3.25	5.5	5.5
Table Travel (in)			3	3	1.5	3	3	1.5

*Peak Magnitude

CONCLUSION

As a result of the extensive structural analysis and development testing performed during design of these units, as well as several other unique designs which are not discussed in this paper, there were no structural failures or indications of impending failures throughout the entire shock and vibration test program. In addition, the unit structures were effective in controlling the acceleration inputs to the electronics to a tolerable level during shock and vibration testing. The success of the system can be attributed largely to the high natural frequency design set as a fundamental design goal. This goal was accomplished in two primary steps:

1) Design, by analysis, of the primary structures and subassembly structures with a high stiffness to weight ratio

2) Interconnection of the primary structures and subassembly structures by means of rigid interconnection hardware, such as the bullpins and cabinet gate latch which were developed at the Naval Electronics Laboratory Center, San Diego.

The analysis and testing led to mechanical packaging concepts that resulted in low centers of gravity and favorable packaging density.

The Control Display Console has the unique distinction of being the first console to withstand the Navy medium weight hammer drop without a single problem.

ACKNOWLEDGEMENT

The authors wish to express their gratitude to the Design department of the Navy Underwater Sound Laboratory, Code EA151, for the technical assistance and guidance offered in support of the AN/BQQ-5 mechanical design.

DISCUSSION

Mr. Austin (Supervisor of Shipbuilding): I noticed that one of your slides showed cooling ducts. I am not clear whether it was air or water cooling. Did you check to see whether you had any air borne noise problems when it is running?

Mr. Panaro: It is a liquid to air cooled system. It has a liquid supply where the liquid supplies the cooling and the air circulates.

Mr. Austin: Did you make any airborne noise measurements in the air circulation system?

Mr. Panaro: Yes.

Mr. Austin: To what standard was that?

Mr. Denver: We ran both a structureborne noise test and an airborne noise test to satisfy MIL-STD-740B.

SHOCK SPECTRA, RESIDUAL, INITIAL AND MAXIMAX AS CRITERIA OF SHOCK SEVERITY

Charles T. Morrow
Advanced Technology Center, Inc.
Dallas, Texas

For estimating the severity of a mechanical shock, one would like to know the response time histories at the failure points of the structure or equipment to which the shock is applied. In practice, before shock testing, one can not count on advance knowledge of either the time histories or the identity of the failure points. A typical test item, though not completely linear, is, however, above all a mechanical filter. Consequently, for shock data reduction and for specification of test severities, there has been a trend away from input time histories (e.g. pulse shapes) toward spectral descriptions such as the shock spectrum. The validity of the latter is usually based on an assumption of failure by brittle fracture or other mechanism such that knowledge of peak response should be sufficient. Energy considerations in addition would provide a more general foundation.

However, even on the assumption of brittle fracture, specification of a simple shock spectrum without further qualification does not necessarily control the severity of a shock if the resonators of the test item are not necessarily simple. When the shock to be simulated occurs in the absence of sustained acceleration, a lower limit on residual and an upper limit on initial or maximax are appropriate. When the shock to be simulated occurs in the presence of sustained acceleration, lower limits on pulse height and initial oscillatory spectrum and an upper limit on residual may be adequate.

For shock testing by means of an electronic shaker system, there has been a recent tendency to synthesize the input time history not as a pulse shape or filtered pulse, but as a sum of a series of transients. It is shown that if these are to be applied simultaneously, their effect does not necessarily differ from that of a simple pulse.

INTRODUCTION

A shock is defined to be an excitation of duration comparable to or shorter than the response times of the resonances of hardware responding to it, and which results in transient responses of the resonators.

Since the first time the shock spectrum was used as a means for specifying the severity of a shock test, there has been a simmering controversy over the validity of such application. Debate never reached the intensity of that over random vibration, but it is still with us. Recently, the controversy has taken on new dimensions through a growing interest in synthesis of shock test input time histories by means of superposed electrical transients. An attempt will be made here at a partial resolution of the matter or at least an identification of some of the issues.

However, differences of opinion about shock spectra can start at a very elementary level. For example, it has been stated that the applicability of such spectra is dependent on an assumption that all resonators in an item to be tested are simple mechanical resonators. But the shock spectrum originated as M. A. Biot's earthquake spectrum[1]. In one classic paper, Biot defined his concept in terms of simple resonators and then related it to the response of a building with distributed parameters, the response of a building with two degrees of freedom, and the effect of the building foundation. At another extreme, papers have been prepared on the use of the shock spectrum or the optimization of its use, on the assumption that the test engineer knows in advance the failure modes and associated transfer functions for the item to be tested. But all environmental tests for qualification of hardware are intended to have validity in the absence of such knowledge. In prac-

tice, failure modes and transfer functions are seldom known in any detail in advance.

Recently, there has been an interest in synthesizing shocks for a shaker table by summing electrical transients. For many test programs, it is more economical to proceed from vibration to shock without transferring the test item to a drop tower. The superposed transients are attractive in part because many shocks to be simulated, especially pyrotechnic shocks transmitted through structure, have similar constituents. They appear to offer an opportunity, compared, say, to a terminal peak sawtooth signal subject to the same filters and potentiometers used in vibration equalization, to achieve an adequate shock spectrum with less shaker excursion and with less peak acceleration applied to the mounting points of the test item.

Since transients applied singly put energy into a system gradually, the proposed techniques have raised some questions about when the peak response actually occurs after initiation of the shock, and what measures should be undertaken to control this. But the decay rates of the transients in the synthesized shock input are not necessarily simply related to the timing of peak responses.

To see the principle, let us cast aside practical considerations, such as permissible shaker excursion and allowable complexity of test apparatus, and conduct a mental experiment. Let us pass a terminal peak sawtooth signal through a set of contiguous third octave filters, and associated attenuators, and recombine the outputs. We are in effect using filters with Q's of approximately three to produce some highly damped transients, and then combining these. Let us also use a much larger number of contiguous filters with Q's of ten or a hundred, and a correspondingly larger number of attenuators. The transients decay much more slowly, and we might expect peak responses to occur later. But, as a special case, let us set the attenuators in each setup for equal gains through the contiguous filters. If the filter sets have suitable phase characteristics and sufficient total bandwidth, the final result of recombinations in either setup is the original sawtooth. Consequently, when the applied shock time history has a relatively smooth residual spectrum, as in the case of the terminal peak sawtooth, the decay times of any transients used for its synthesis may have very little correlation with the time required to build up peak responses.

What is a "suitable" phase characteristic for reproduction of the original sawtooth pulse and how can it be obtained? A constant frequency bandwidth filter set inherently tends to have such a characteristic. A constant fractional octave bandwidth filter set may not unless a phase compensator is added. The filters nearer the low end of the spectrum individually take longer to respond and to recover. The responses of the test item in this frequency range may occur later. A more fundamental way of looking at this, however, with fewer pitfalls, is to observe that this filter set, as opposed to the constant bandwidth set, may have a frequency-dependent phase rate. A phase compensating network for this is quite feasible. It can be inactive, with primarily inductive and capacitative elements, or active, with resistors, capacitors and semiconductor devices. Whatever can be done by analog circuitry can also be accomplished in a different way by digital circuitry. Except for the concept of phase compensation, which is not treated, Broch[2] gives an excellent brief discussion of spectrum shaping by contiguous filters.

In connection with shock synthesis by transients, perhaps the most quoted paper is by Favour, LeBrun and Young[3]. These authors devised an ingenious application of the Fast Fourier Transform algorithm to synthesize an input "transient" for a random vibration test system such that the corresponding excitation to the test item will have a prescribed time history. But the excitation at the output of the system is not referred to as a transient. It could equally well in principle be a standard pulse. The input to their system is less important, and not necessarily distinctly transient in character. If the random test system were suitably equalized in amplitude and phase versus frequency, the input could be either a standard pulse or identical to whatever final time history is desired.

In the present paper, there is no intent to deny that the fractional octave filter set without phase compensation may have virtues, or that synthesis by Fourier transform methods may have merit. However, the effect of a shock will be analyzed in terms of shock spectra without reference to whatever means may have been used for synthesis. Further, for simplest interpretation of analysis results, it will be assumed that the excitation time history is such that transient responses of the test item are all initiated at essentially the same time.

The primary concern will be what kind of shock spectral lower limit will ensure that a test shock is an adequate simulation of another shock in the sense that responses, particularly of coupled resonators in the test item will be at least as severe. An adequate test in this sense is the basic responsibility of the specification writer. As a matter of convenience he may be the person to determine upper limits as well or in other words to apply upper and lower limits to a nominal spectrum. He may have good reason in a particular situation to prescribe a lower spectral requirement than would follow directly from this paper, and take his risks.

In the discussion that follows, we will make use of excerpts from an environmental specification the author took part in preparing some years ago and a paper[4] prepared at about the same time that served as a partial founda-

tion for the approach taken. The specification was adequate for its time, but the language was not sufficiently precise for some trends that have taken place since. The paper contained some gaps in logic and was not carried through to some conclusions that are more evident in retrospect. The analysis, with suitable modifications, will be reproduced in an appendix, partly to provide in the record a more satisfactory account to support further investigation the author has in mind.

The basic approach is an Idealized Model Analysis - the analysis of something simpler and more understandable than an actual or typical test item, but which will support conclusions that have high probability of being sufficiently valid for the engineering task. Spectral analysis in terms of the responses of possible simple resonators[5] is taken as partial evidence of equivalence of two shocks, or alternately that one is at least as severe as the other. Investigation of higher order responses[4] corresponding to multiple degree of freedom systems is taken as additional evidence. But if the higher order responses have suitable simple relationships to responses of simple resonators, only the latter need be known.

In brief, the purpose of this paper from here on is to clarify some fragments of past history and update and extend an earlier paper that supported some early engineering decisions.

Some Shock Specification History

The shock spectrum originated in a paper by M. A. Biot and was used in an exploratory way by I. Vigness and his associates at the Naval Research Laboratory to compare test shocks with shipboard shocks they were intended to simulate. The author learned about it during a session of the shock and vibration symposium and especially a question period in which Vigness participated. The first use of the spectrum to specify a test shock, to the author's knowledge, was in an environmental specification the author took part in preparing in 1955. Excerpts given in Appendix I include a suggestion that the test requirement be met by means of a terminal peak sawtooth pulse of acceleration. This had already been proved feasible[6]. This sawtooth, in contrast to the half sine wave and square wave, had no nulls in its residual spectrum. As no one yet had a better idea, the pulse shape for practical purposes became an auxiliary mandatory requirement.

Since then, there has been a trend toward specifying this pulse without reference to a spectrum (with some simplification of wording) without reference to a pulse shape. The former approach at least puts a superior pulse shape to use, although, if one considers response time history to be more important than excitation time history, dealing with tolerances without reference to spectra is clumsy. For example, Figure 1 shows some variations within typical time domain tolerances that can have drastic effect on response. Because of this consideration, the spectral approach is preferable in principle, but it has its own pitfalls.

The dual approach with the spectrum more basic was utilized in anticipation of possible pyrotechnic shock, and in part to try to put an end to a practice of simulating shocks by pulses of comparable peak acceleration and effective duration regardless of radically different wave shapes. This practice, widely accepted at the time by shock and vibration engineers and aerospace engineers in general for lack of a better idea, has evidently disappeared. It tended to yield deficient energy at some frequencies and excessive energy at others, especially low frequencies.

But note that except for the subtle words "in both plus and minus directions", the first excerpt would imply a maximax spectrum. It could be satisfied by either the initial (primary) or residual. The latter is $2\pi f$ times the magnitude of the Fourier transform and related to the spectral energy of the pulse. The former has no definite relation of spectral energy and at sufficiently high frequencies reduces to the peak acceleration of the excitation time history. Its use could have amounted to merely a sophisticated way of prescribing a minimum peak acceleration for an applied pulse. Except for the quoted subtle words, the "spectral" requirement by itself could be met by a centrifuge, which undoubtedly would have undertested some coupled resonators, and possibly overtested some low and high frequency resonators.

The pressures of initial planning of a large program do not provide the best atmosphere for generating or even preserving subtle wordings in an environmental specification. In the long run it would have been better to have prescribed a minimum residual spectrum explicitly. For the most part, this should be encouraged today. A minimum Fourier transform or spectrum could have been prescribed, but its relationship to the residual spectrum had not yet been discovered, and it was too abstract an idea for that time.

Care in wording of a spectral shock requirement would be of minor importance except for the fact that simple resonators are probably the exception rather than the norm in equipment to be shock tested.

Summary of the Analysis

The exploratory analysis of some fifteen years ago has been extended to close some gaps of logic, express the final formulas in more meaningful form, and reveal some new fundamental relationships. For conformity with present shock and vibration usage, it has been found desirable to start from a different definition fro the Laplace transform. This definition and the relationship between the Fourier

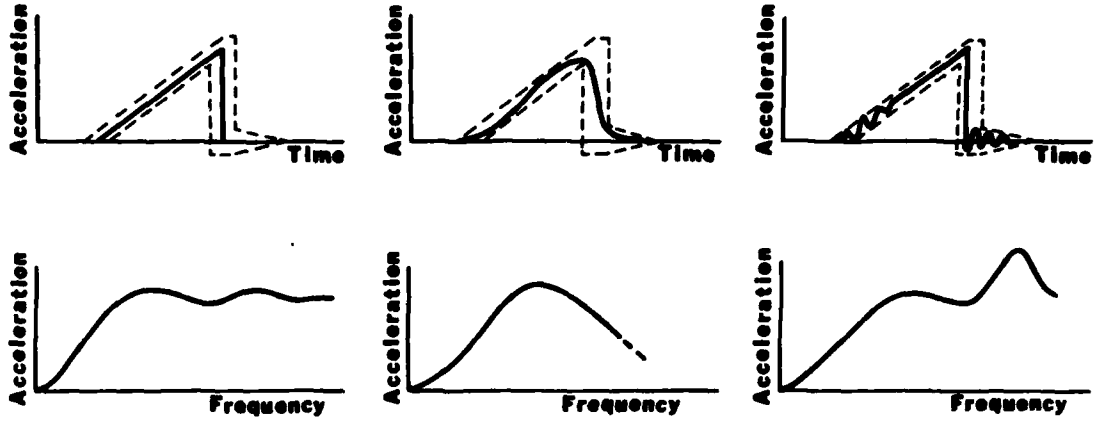

(a) TOLERANCES AND NOMINAL PULSE (b) ROUNDED CORNERS (c) RINGING

FIGURE 1. Effect of Variations in Pulse Shape, within Tolerances, on Undamped Residual Shock Spectrum.

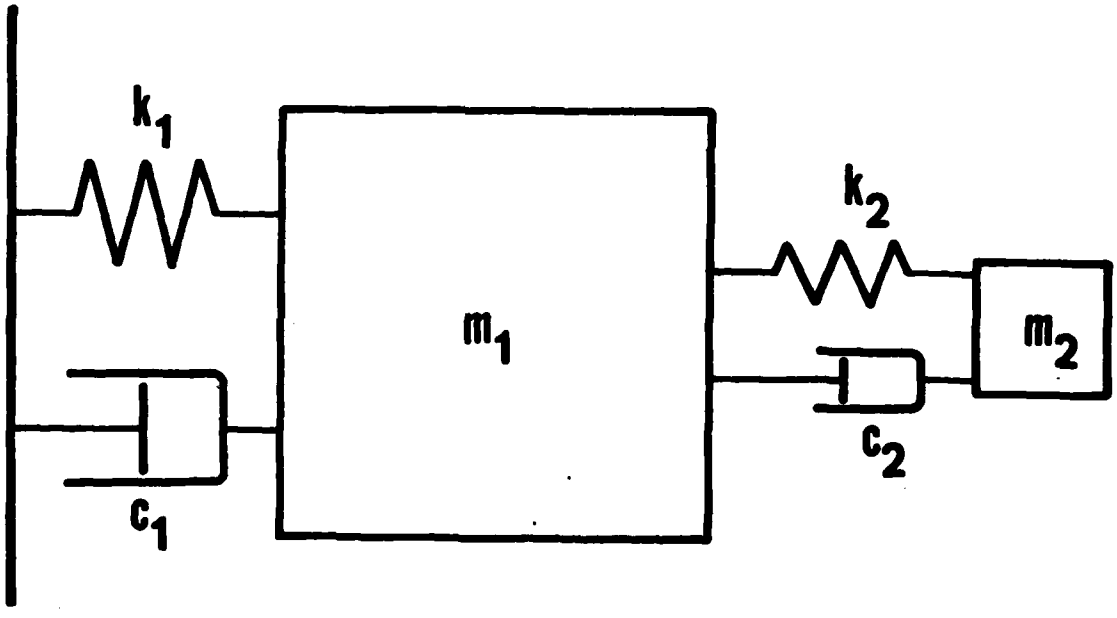

FIGURE 2. Two Coupled Resonators

and Laplace transforms are discussed in Appendix 2. Several forms of the Heaviside expansion theorem are given in Appendix 3. The analysis is given in Appendices 4 and 5.

The idealized model for the analysis consists of two (or more) simple resonators mounted sequentially as in Figure 2. Motion of the mass of the final resonator, corresponding to the whipping of a potentiometer wiper or other light appendage, could be related to frequent causes of damage or malfunction. The model is made to represent more of a worst case, and the mathematics is simplfied, by assuming no dynamical loading of one resonator by another. If one shock is more severe than another, not only for a simple resonator, but for this compound idealized model as well, we can have more confidence that this comparison holds true generally, regardless of the particular dynamics of the test item.

The peak acceleration of the second mass as a function of the two resonance frequencies, for any particular shock excitation, is defined to be the second order shock spectrum for that excitation. (Three coupled resonators would lead to a third order shock spectrum). In Appendix 4, responses of the second mass, or second order responses, are calculated for several elementary excitations, some of which (e.g. ramp and step functions) could be combined sequentially in time to form standard acceleration pulses such as sawtooth and square wave. Excitation and corresponding responses are expressed in terms of the Laplace transform and Heaviside expansion theorem. Each response is shown to be a sum of transmitted excitation, possibly modified by a factor involving the complex frequencies characterizing the two resonators, plus a pair of transients, called initial oscillatory responses, at the frequencies of the resonators. The peak of the sum of the two transients as a function of the two resonance frequencies is defined to be a second order initial oscillatory shock spectrum. In Appendix 5, it is shown that second order residual responses and spectra are of the same form as the initial oscillatory and have the same relation to Laplace and Fourier transform of the entire pulse as the latter have to transforms of the initial elementary excitation. If the frequency of the first resonator of Figure 1 were allowed to increase beyond limit, the analysis would reduce to an analysis of first order or ordinary responses and shock spectra.

We are now in a position to make a number of observations that will become apparent to the reader who has time and patience to read the analysis with sufficient care.

Significant Observations From The Analysis

1. From Equation (47) we conclude that the second order undamped residual spectrum, obtained by summing the peak accelerations of the net residual transients for each pair of resonator frequencies, is simply related to the first order undamped residual spectrum in such a way that only the latter need be known to provide reasonable evidence of an adequate test. Suppose that the test item contains two coupled resonators with resonance frequencies f_1 and f_2 arbitrarily chosen. If at f_1 and f_2, shock A has higher undamped residual shock spectrum values than shock B, the corresponding second order undamped residual shock spectrum values will also be higher for shock A. More generally, if of two shocks one has a higher first order undamped residual shock spectrum for every frequency in the region of interest, that shock also has a higher second order undamped residual shock spectrum for every pair of frequencies in the region of interest.

2. Equation (47) was derived from Equation (46), which involved the Fourier transform. Likewise, Equation (39) involved the Fourier transform. If the exponentials are combined to yield trigonometric functions of time, it becomes evident that the first order undamped residual spectrum is $2\pi f$ times the magnitude of the Fourier transform - a fact already well known. Consequently, Observation 1 can be reinterpreted to say that one shock will have a higher second order undamped residual shock spectrum than another if for every frequency the magnitude of its Fourier transform is greater.

3. We can define a second order damped residual shock spectrum as the peak acceleration of the two residual decaying transients of two coupled damped resonators, subject to the no-loading condition, as a function of the complex frequencies of the resonators. With no damping, the peak values of the two transients would eventually sum arithmetically unless the frequencies were in a harmonic relationship, in which case the peak value for the combined transients would be determined in part by relative phase regardless of frequency relationship.

4. The first order damped residual response is proportional to the Laplace transform of the shock excitation, evaluated for the complex frequency of the simple resonator, and of course, decays exponentially with time. Accordingly, the magnitude of the Laplace transform, multiplied by the magnitude of the complex frequency, yields an upper limit for the damped residual spectrum. A conservative lower limit may be obtained by diminishing the magnitude of the transform by the decay occurring during one complete period. A less conservative lower limit can be computed for each specific complex frequency. If the phase of the transform is also known, the residual spectrum can be computed exactly and will be found to be, unlike the undamped residual spectrum, not completely symmetrical for the positive and negative directions of acceleration, but the assymmetry will be small except for high damping.

5. The second order damped residual response consists of two damped sinusoids differing at least in frequency (not necessarily in exponent-

ial decay rate). Each term is given by the corresponding first order residual response (involving the Laplace transform) multiplied by a factor reflecting the relationship between the two complex frequencies. The sum of the magnitudes of the two terms is an upper limit to the second order damped residual shock spectrum, whose actual value will be somewhat dependent on the relative timing and phasing of the response transients. But the transients are larger for the test shock whose Laplace transform is greater than that of the shock to be simulated, for every complex frequency of interested. For any complex frequency, the Laplace transform has a magnitude proportional to the corresponding Fourier transform obtained by setting the decay constant equal to zero. Consequently, except for effects of timing and phasing, it is sufficient that the Fourier transform or first order undamped residual spectrum be greater for every frequency for the test shock than the shock to be simulated.

6. The statements concerning residual response and residual spectra apply also to initial oscillatory response and initial oscillatory spectra, discussed in the Summary of the Analysis, and actually treated more directly than residual response and spectra in Appendix 4. Consequently, the initial oscillatory spectrum may have application when it is desired to simulate shock in the presence of sustained acceleration. This will be explained more fully in a later section.

7. The step function, as in the example of Equation (43) appears unchanged in the response of any order, damped or undamped, except for superposed transients. So therefore, does a square wave. A ramp function appears unchanged if there is no damping. As a practical matter, a pulse made up of a finite number of steps and ramps appears essentially unchanged if damping is low. The superposed transients are, however, altered at each successive application of an elementary excitation.

Application To Shock Test Requirements

Unless it is specifically stated otherwise, we assume low damping in the test item, and an absence of isolators. Initially, we assume that the shock to be simulated occurs when there is negligible vibration or steady acceleration. Some aspects of the simultaneous vibration problem have been treated in a previous paper[7]. We do not at any time restrict the actual test item to simple internal resonators. The observations listed above lead directly to some conclusions about shock testing policy.

If shock testing, for simplicity, is to focus on any one spectral description, that should be the Fourier spectrum or undamped residual shock spectrum, certainly not initial or maximax[8]. However, consideration of additional spectra can provide the specification writer with greater assurance of adequacy and the test and design engineers with more protection against overtest.

The specification writer can feel confident a test is adequate if he prescribes a minimum residual undamped shock spectrum that is an envelope of the maximum composite spectrum of the shock to be simulated. As a practical compromise, the lowest damping available on commercial shock spectrum computers may be acceptable in place of zero damping. Then if the designer is to be protected against a requirement to overdesign, the test procedure should state a maximum initial or maximax spectrum or refer to a pulse shape (e.g. a terminal peak sawtooth) such that the initial spectrum is unlikely to be excessive.

If high damping is anticipated in the test item, the specification writer may feel more confident the test is adequate if he also places lower limits on damped residual spectra. However, a more detailed study of possible responses to contemplated excitations would be desirable to ensure this is worth the effort and complication or determine how far it should be carried.

The possibility of gaining further confidence in the adequacy of a shock test condition, by placing an upper limit on the length of time before peak response occurs, is not excluded. Its value may be dependent on what approaches to shock synthesis become popular in the future, or what other restrictions on such approaches may be included in future specifications.

The terminal peak sawtooth has one feature that has not received much previous attention - it initiates all transient responses at essentially the same time. With practical mechanical implementation or with gradual spectral shaping by equalizing filters and attenuators, there can be some small phase shifts as a function of response frequency, but a generally simple effect is preserved. For simulation of cryogenic shock, long duration in the sawtooth and large associated low-frequency spectral content are not often necessary. When these can be reduced sufficiently, the excursion becomes small enough for available shakers. If the low-frequency content is reduced by an equalizer, the primary effect is to reduce the effective duration without altering the sharpness of the final dropoff or the corresponding high-frequency effect.

The terminal peak sawtooth and simple variants derived by equalization tend to be conservative, or more severe than the collections of transients they are most often used to simulate. If the associated spectrum is an envelope of field conditions, their valleys, of course, tend to be filled in. The responses start more or less simultaneously and generally earlier than for the shock to be simulated, so that less energy is lost before peak response occurs.

Shock in the Present of Steady Acceleration

Now let us suppose that the shock to be simulated occurs when steady acceleration is not negligible. It is not economical or usually even feasible to operate a shock tester in a centrifuge. As points of departure, the specification writer may consider two other options. He can increase the residual shock spectrum by the amount of the steady acceleration. This is likely to overtest some parts while undertesting others. Alternately, if the spectral level and steady acceleration are not too different he can prescribe a square wave acceleration pulse, which appears unaltered in the first and higher order responses, but taper off the end more gradually to deemphasize residual response. He can require that the level of the initial step function be at least equal to the steady acceleration to be simulated, for some minimum length of time, and specify a lower limit on the initial oscillatory spectrum. To protect the designer against a requirement to overtest, the test procedure should now place an upper limit on the residual spectrum. The consequent test would be more suited to a drop tower than a shaker.

Special Considerations Related to Isolators

Isolators behave at low frequencies like simple resonators. Sway or rattle space must be planned for them in the design, whereas this is seldom allowed to any extent for any other parts. Their resonance frequencies, unlike those of other parts, cannot arbitrarily be pushed high in frequency. Consequently, the low-frequency character of vibration and shock tests becomes more critical when isolators are contemplated. Once a resonance frequency has been established for an isolator, the corresponding sway space required for shock is related to the maximax spectrum rather than the residual. There is some virtue, therefore, for adequacy of test, in placing a lower limit on the maximax test spectrum, at low frequencies, to be ignored if isolators are not used. There is also merit in reexamining some standard shock specifications, whose origins date back many years, for possible excessive or inadequate demands on sway space.

Conclusion

Our primary conclusion is that the maximax and initial shock spectra should be given less importance, and the residual spectrum, or alternately Fourier spectrum, should be given more[8]. However, a judicious use of several shock spectrum concepts, according to the application, with more careful wording of specifications, will be beneficial.

The Idealized Model Analysis used here can and probably will be extended. It is hoped that the interpretations given here will help to bring about more agreement on the role of shock spectra, or at least refocus some of the differences of opinion.

APPENDIX 1

Excerpts From Airborne Electronic Equipment WS-107A Environmental Test Requirements, 3 January 1956

Shock Test Requirements:

3.2.2.9 Shock - A shock whose shock spectrum in both plus and minus directions is at least 100 g from 100 cps to 700 cps. The shock is to be applied at least once along each of three orthogonal axes through the mounting points that are used to connect to the missile unless the component is vibration mounted in the missile; in this case, the shock shall be applied at the points where the vibration mounts connect to the equipment component.

From Section 6.1.3, Supporting Information:

A preferred pulse shape is a terminal peak sawtooth which rises to 100 g in approximately 6 milliseconds with as sharp a peak as possible and a minimum of superposed oscillation and drops abruptly to zero, as may be obtained by fastening the component to a rigid carriage and dropping it onto a properly shaped lead pellet. The drop carriage for this type of pulse and any other supporting structure that is not nominally part of the component as mounted in the missile should be free of resonances in the range up to 1500 cps so as to apply the standard specified condition to the mounting points; this supporting structure should not be designed to simulate part of the airframe. The carriage should also be heavier than the component so as to make the deceleration independent of internal resonances of the component. The sawtooth pulse shape is recommended because its theoretical shock spectrum is smooth and free of nulls, and because it is relatively easy to obtain.

APPENDIX 2

Transforms

There are several ways of defining the Fourier and Laplace transforms, depending on whether one prefers to think in terms of frequency f in Hz or of angular frequency $\omega = 2\pi f$, and any importance one places on consistency with the Heaviside operational calculus. Any choices

will yield essentially the same results. For simplicity, except for a slight complication in the forms of the Heaviside expansion theorem, we will define the Fourier transform of a time function a(t) to be

$$F(f) = \int_{-\infty}^{\infty} a(t)e^{-j2\pi ft}\,dt \qquad (1)$$

and the Laplace transform to be

$$L(s) = \int_{0}^{\infty} a(t)e^{-st}\,dt \qquad (2)$$

where $s = \sigma + j\omega$ is called the complex frequency.

In respect to the role of frequency, the Laplace transform is a generalization of the Fourier transform, whereas integration only from t = 0 turns out to be a useful restriction, convenient for transient phenomena. The Fourier transform interprets a(t) in terms of a summation of steady-state sinusoids. The Laplace transform interprets a(t) more in terms of exponentially decaying transients.

If a(t) is zero at least for negative t and has a Fourier transform, this may be obtained from the Laplace transform by setting $s = j2\pi f$. All practical shock time functions of interest have a Fourier transform.

The Laplace transforms of many functions may be found directly from the definition of Equation (2). For example, consider the unit step function, given, for positive t by

$$a(t) = 1 . \qquad (3)$$

It follows that

$$L(s) = 1/s \qquad (4)$$

Furthermore, if

$$a(t) = e^{-\alpha t} , \qquad (5)$$

the Laplace transform is

$$L(s) = 1/(s + \alpha) \qquad (6)$$

From Equations (5) and (6) we can obtain the transform of the unit impulse

$$a(t) = \delta(t) , \qquad (7)$$

which is zero except at t = 0 but has an integral equal to unity.

Note that for

$$a(t) = \alpha e^{-\alpha t} , \qquad (8)$$

whose transform is

$$L(s) = \alpha/(s + \alpha) , \qquad (9)$$

$$\int_{0}^{\infty} a(t) = 1$$

regardless of the value of α. If we let α increase beyond limit, Equation (10) approaches a unit impulse and Equation (9) yields its transfrom as

$$L(s) = 1 . \qquad (10)$$

It can be shown that

$$a_0(t) = \frac{d}{dt} a(t) , \qquad (11)$$

has a transform

$$L_0(s) = s\,L(s) - \lim_{t_{pos} \to 0} a(t) , \qquad (12)$$

with the last term equal to zero for most functions that interest us.

Conversely, if

$$a_0(t) = \int_{0}^{t} a(t)\,dt , \qquad (13)$$

the corresponding transform is

$$L_0(s) = \frac{1}{s} L(s) . \qquad (14)$$

Finally, if

$$a_0(t) = a(t-\tau) , \qquad (15)$$

for $t \geq \tau$, the transform is

$$L_0(s) = e^{-\tau s} L(s) . \qquad (16)$$

It can also readily be shown from Equation (2) that the transform of the sum of terms is the sum of the transforms of the individual terms.

APPENDIX 3

The Heaviside Expansion Theorem

Our immediate task is to establish statements of the Heaviside expansion theorem that, taken together, are sufficiently general for our purposes. First, we assume a time function, such as an exponentially decaying sinusoid, whose Laplace transform is given by the ratio of two real polynomials of order m in the complex frequency s, neither containing multiple roots nor s = 0 as a root:

$$L_0(s) = \frac{N_0(s)}{D_0(s)} \tag{17}$$

The denominator can be written as a product

$$D_0(s) = (s-s_1) \cdots (s-s_n) , \tag{18}$$

with any complex or imaginary roots occuring in pairs as conjugates, since $D_0(s)$ is real.

To obtain an elementary version of the expansion theorem, Equation (17) is expanded in partial fractions:

$$\begin{aligned} L_0(s) &= \sum_{k=1}^{m} \frac{N_0(s_k)}{(s-s_k)D_0'(s_k)} \\ &= \sum_{k=1}^{m} \frac{N_0(s)}{\frac{d}{ds}D_0(s)}\Big|_{s=s_k} \cdot \frac{1}{s-s_k} \\ &= \sum_{k=1}^{m} \frac{(s-s_k)N_0(s)}{D_0(s)}\Big|_{s=s_k} \cdot \frac{1}{s-s_k} \\ &= \sum_{k=1}^{m} (s-s_k)L_0(s)\Big|_{s=s_k} \cdot \frac{1}{s-s_k} . \end{aligned} \tag{19}$$

But, from Equations (5) and (6), the Laplace transform of $e^{s_k t}$ is $1/(s-s_k)$. Accordingly, we take inverse transforms term by term to obtain the time function.

$$a_0(t) = \sum_{k=1}^{m} (s-s_k)L_0(s)\Big|_{s=s_k} e^{s_k t} , \tag{20}$$

which is one form of the Heaviside expansion theorem in the notation most convenient for our use.

We are interested next in what happens if s is a factor in the numerator. If the transform of a(t) is

$$L(s) = N(s)/D(s) \tag{21}$$

and

$$L_0(s) = sL(s) = sN(s)/D(s) , \tag{22}$$

we can apply Equation (14) term by term to the Heaviside expansion of Equation (23) to obtain

$$\begin{aligned} a_0(t) &= \sum_{k=1}^{m} s_k(s-s_k)L(s)\Big|_{s=s_k} e^{s_k t} - \lim_{t_{pos}\to 0} a(t) \\ &= \sum_{k=1}^{m} (s-s_k)L_0(s)\Big|_{s=s_k} e^{s_k t} - \lim_{t_{pos}\to 0} a(t) , \end{aligned} \tag{23}$$

which is the same as Equation (20) except for the final term, which will be zero later when responses are considered, for the response of a resonator must be a continuous function that starts from zero.

Next, we are interested in the form Equation (20) takes for a Laplace transform with s a factor, possibly multiple, in the denominator. Let

$$L_0(s) = \frac{N(s)}{sD(s)} = \frac{1}{s} L(s) \tag{24}$$

The Heaviside expansion now contains a term for s = 0.

$$a_0(t) = L(0) + \sum_{k=0}^{m} (s-s_k)L_0(s)\Big|_{s=0} e^{s_k t} \tag{25}$$

Now Let

$$a_0(t) = \frac{N(s)}{s^2 D(s)} = \frac{1}{s^2} L(s) = \frac{1}{s} \cdot \frac{1}{s} L(s) . \tag{26}$$

The principle of Equations (13) and (14) can be applied term by term to the expansion in Equation (25), to obtain the new

$$a_0(t) = tL(0) + \sum_{k=0}^{m} (s-s_k)L_0(s)\Big|_{s=s_k} (e^{s_k t}-1) \tag{27}$$

Similarly, for

$$L_0(s) = \frac{N(s)}{s^3 D(s)} = \frac{1}{s^3} L(s) = \frac{1}{s} \cdot \frac{1}{s^2} L(s) , \tag{28}$$

$$a_0(t) = \frac{t^2}{2} L(0) + \sum_{k=0}^{m} (s-s_k)L_0(s)\Big|_{s=s_k} (e^{s_k t}-1-s_k t) . \tag{29}$$

More generally, for

$$L_0(s) = \frac{N(s)}{s^n D(s)} = \frac{1}{s^n} L(s) , \tag{30}$$

with n a positive integer,

$$a_0(t) = \frac{t^{n-1}}{(n-1)!} L(0)$$

$$+ \sum_{k=0}^{m} (s-s_k)L_0(s)|_{s=s_k} \left[e^{s_k t} - 1 - s_k t - \cdots - \frac{(s_k t)^{n-2}}{(\alpha-2)!}\right] \quad (31)$$

In Equations (27), (29) and (31), we see the s_k summation, if it is non-zero, developing a polynomial in $s_k t$ more allied to the first term and more appropriately lumped together with it.

If, as a special case of Equation (30),

$$L_0(s) = \frac{1}{s^n} , \quad (32)$$

the time function of Equation (33) becomes

$$a_0(t) = \frac{t^{n-1}}{(n-1)!} \quad (33)$$

Finally, if any time function $a_0(t)$ is delayed by a time τ before initiation, application of Equation (15) and (17), term by term, to any of the previous expansions alters the $e^{sk t}$ terms in the s_k summation to

$$\sum_{k=0}^{m} (s-s_k)L_0(s)|_{s=s_k} e^{-\tau s_k} e^{s_k t}$$

$$= \sum_{k=0}^{m} (s-s_k)L_0(s) e^{s_k(t-\tau)} , \quad (34)$$

and converts any polynomial in $s_k t$ from this source to a polynomial in $s_k(t-\tau)$ for $t \geq \tau$, all of which amounts simply to a delay by the time τ.

Accordingly, we can build up a pulse by a succession of ramp or step functions, or other fundamental excitations, initiated at successive instants. The time functions that are nonzero in any chosen time interval are additive, as are their Laplace transforms, or their Heaviside expansions, term by term. Consequently, versions of the expansion theorem apply also to such synthesized pulses.

APPENDIX 4

Responses and Response Spectra

The transfer function of an undamped simple mechanical resonator of angular resonance frequency $\omega_1 = 2\pi f_1$, excited at the base, either without loading of the source, or measured with the loading present, is given by

$$\frac{\omega_1^2}{s^2 + \omega_1^2} = \frac{\omega_1^2}{(s-j\omega_1)(s+j\omega_1)} . \quad (35)$$

This is obtained by taking the Laplace transform of the terms of the differential equation and dividing the transform of the response by the transform of the excitation.

The Laplace transform of the response of the resonator,

$$L_1(s) = \frac{\omega_1^2}{s^2+\omega_1^2} L_0(s) , \quad (36)$$

still fulfills the requirements for application of the expansion theorem. Accordingly, the first order undamped response for positive time, corresponding to Equations (17) and (19), is

$$a_1(t) = \sum_{k=1}^{m} \frac{\omega_1^2(s-s_k)L_0(s)}{(s_k-j\omega_1)(s_k+j\omega_1)} |_{s=s_k} e^{s_k t}$$

$$- \frac{j\omega_1}{2} L_0(j\omega_1) e^{j\omega_1 t} + \frac{j\omega_1}{2} L_0(-j\omega_1) e^{-j\omega_1 t}$$

$$= \sum_{k=1}^{m} \frac{\omega_1^2(s-s_k)L_0(s)}{(s_k^2+\omega_1^2)} |_{s=s_k} e^{s_k t} \quad (37)$$

$$- j\frac{2\pi f_1}{2} F_0(f_1) e^{j\omega_1 t} + j\frac{2\pi f_1}{2} F_0(-f_1) e^{-j\omega_1 t}$$

where $F_0(f_1)$ and $F_0(-f_1)$ represent the Fourier transform of the excitation, evaluated for $f = \pm f_1$.

The last two terms of Equations (37) represent a sinusoidal initial oscillatory response of peak value equal to the magnitude of the Fourier transform, so that the initial oscillatory shock spectrum is given by

$$a_{1p}(f_1) = 2\pi f_1 |F_0(f_1)| , \quad (38)$$

an important relationship, which has been proved independently for the residual spectrum, and holds generally for any function whose Fourier transform exists. If $a_0(t)$ decreases rapidly to a negligible value, as in the case of

$$a_0 = e^{-\alpha t} \sin \omega t$$

or

$$a_0 = e^{-\alpha t} ,$$

the initial oscillatory spectrum becomes also the residual spectrum. Similarly, if a pulse such as a square wave is synthesized by successive application of two or more elementary excitations, the residual response consists of

a sum of terms at the frequency f_1, yielding a residual spectrum conforming to Equation (40), with $F_0(f_1)$ interpreted as the Fourier transform of the entire pulse.

As an example of application of Equation (37), consider the unit impulse excitation given by Equation (7), with its Laplace transform given by Equation (10). The first order undamped response is

$$a_1(t) = -j\omega_1 e^{j\omega_1 t} + j\omega_1 e^{-j\omega_1 t} = \omega_1 \sin \omega_1 t \ , \tag{39}$$

which is simply the initial oscillatory (or residual) response with no trace of the excitation.

The response corresponding to Equations (21), (22) and (23), in consideration of Equations (11) and (12) is also given by Equation (37), since the response of a resonator mass to any shock must be continuous and start from zero.

The response corresponding to Equations (24) and (25) is

$$a_1(t) = L(0) + \sum_{k=1}^{m} \frac{\omega_1^2(s-s_k)L_0(s)}{(s^2+\omega_1^2)}\Big|_{s=s_k} e^{s_k t} - j\frac{2\pi f_1}{2} F_0(f_1)e^{j\omega_1 t} + j\frac{2\pi f_1}{2} F_0(-f_1)e^{-j\omega_1 t} \ . \tag{40}$$

As a special case, consider the step function represented by Equation (3) for positive t, and whose transform is given by Equation (4). The response is

$$a_1(t) = 1 - \frac{1}{2} e^{j\omega_1 t} - \frac{1}{2} e^{-j\omega_1 t} = 1 - \cos \omega_1 t \ . \tag{41}$$

The step function is the only elementary excitation that appears unchanged in the first order undamped or damped response. In fact, it appears unchanged in the response, undamped or damped, of any order. Consequently the only pulses that appear unchanged in the undamped or damped response of any order are made of successive step functions, as, for example, a square wave. The ramp function and excitations proportional to an odd power of time appear unchanged in undamped responses of any order, as the time polynomials, which occur twice, cancel to zero. For other elementary excitations, the s_k summation does not disappear, or the terms that yield an oscillatory or residual response at resonator frequency also give a modification of the original pulse. "Hash" produced on a basic square wave by a resonant fixture does not appear unchanged in the response.

First order undamped responses are given in Table 4-1 for several elementary excitations. Initial oscillatory (or residual) spectra are given in the right hand column. Responses and spectra for complete pulses are well covered in the literature[3,4] and are not given here, but many can be readily constructed from the table (by addition of delayed responses, not spectra) or from the previous analyses.

Ot obtain the second order undamped response, we replace the transfer function of Equation (35) by[6]

$$\frac{\omega_1^2\omega_2^2}{(s^2+\omega_1^2)(s^2+\omega_2^2)} = \frac{\omega_1^2\omega_2^2}{(s-j\omega_1)(s+j\omega_1)(s-j\omega_2)(s+j\omega_2)} \tag{42}$$

The second order response corresponding to Equations (26), (27) and (42), as a typical example, becomes

$$\begin{aligned} a_2(t) = L(0) + \sum_{k=1}^{m} \frac{\omega_1^2\omega_2^2(s-s_k)L_0(s)}{(s_k^2+\omega_1^2)(s_k^2+\omega_2^2)}\Big|_{s=s_k} e^{s_k t} \\ - \frac{f_2^2}{f_1^2-f_2^2}\frac{j2\pi f_1}{2} F_0(f_1)e^{j\omega_1 t} \\ + \frac{f_2^2}{f_1^2-f_2^2}\frac{j2\pi f_1}{2} F_0(-f_1)e^{-j\omega_1 t} \\ - \frac{f_1^2}{f_2^2-f_1^2}\frac{j2\pi f_2}{2} F_0(f_2)e^{j\omega_2 t} \\ + \frac{f_1^2}{f_2^2-f_1^2}\frac{j2\pi f_2}{2} F_0(f_2)e^{-j\omega_2 t} \ . \end{aligned} \tag{43}$$

TABLE 4-1

First Order Undamped Responses and Spectra for Fundamental Excitations

	$a_0(t)$	$L_0(s)$	First Term	$a_1(t)$ for Positive t: s_k Summation	$a_1(t)$ for Positive t: Initial Oscillatory (or Residual)	Initial Oscillatory (or Residual) Spectrum
1	$\delta(t)$	1	0	0	$-j\omega_1 e^{j\omega_1 t} + j\omega_1 e^{-j\omega_1 t} = \omega_1 \sin\omega_1 t$	ω_1
2	1	$\frac{1}{s}$	1	0	$-\cos\omega_1 t$	1
3	t	$\frac{1}{s^2}$	t	0	$-\frac{1}{\omega_1}\sin\omega_1 t$	$\frac{1}{\omega_1}$
4	$\sin\omega t$	$\frac{\omega}{s^2+\omega^2}$	0	$\frac{\omega_1^2 \sin\omega t}{\omega_1^2-\omega^2}$	$-\frac{\omega\omega_1 \sin\omega_1 t}{\omega_1^2-\omega^2}$	$\frac{\omega\omega_1}{\lvert\omega_1^2-\omega^2\rvert}$
5	$\cos\omega t$	$\frac{s}{s^2+\omega^2}$	0	$\frac{\omega_1^2 \cos\omega t}{\omega_1^2-\omega^2}$	$-\frac{\omega_1^2 \cos\omega_1 t}{\omega_1^2-\omega^2}$	$\frac{\omega_1^2}{\lvert\omega_1^2-\omega^2\rvert}$
6	e^{-at}	$\frac{1}{s+a}$	0	$\frac{\omega_1^2}{a^2+\omega_1^2}e^{-at}$	$\frac{-\omega_1^2\cos\omega_1 t + a\omega_1\sin\omega_1 t}{a^2+\omega_1^2}$	$\frac{\omega_1}{\sqrt{a^2+\omega_1^2}}$
7	$e^{-at}\sin\omega t$	$\frac{\omega}{(s+a)^2+\omega^2}$	0	$\frac{\omega_1^2[a^2-\omega^2+\omega_1^2]\sin\omega t+2a\omega\omega_1^2\cos\omega t}{[a^2+(\omega-\omega_1)^2][a^2+(\omega+\omega_1)^2]}e^{-at}$	$\frac{a\omega_1[a^2+\omega^2-\omega_1^2]\sin\omega_1 t-2a\omega\omega_1^2\cos\omega_1 t}{[a^2+(\omega-\omega_1)^2][a^2+(\omega+\omega_1)^2]}$	$\frac{a\omega_1}{\sqrt{[a^2+(\omega-\omega_1)^2][a^2+(\omega+\omega_1)^2]}}$
8	$e^{-at}\cos\omega t$	$\frac{s}{(s+a)^2+\omega^2}$	0	$\frac{-\omega_1^2[a^2+\omega^2-\omega_1^2]\cos\omega t+\frac{a\omega_1^2}{\omega}[a^2+\omega^2+\omega_1^2]}{[a^2+(\omega-\omega_1)^2][a^2+(\omega+\omega_1)^2]}e^{-at}$	$\frac{\omega_1^2[a^2+\omega^2-\omega_1^2]\cos\omega_1 t+2a\omega_1^3\sin\omega_1 t}{[a^2+(\omega-\omega_1)^2][a^2+(\omega+\omega_1)^2]}$	$\frac{\omega_1^2}{\sqrt{[a^2+(\omega-\omega_1)^2][a^2+(\omega+\omega_1)^2]}}$

Unless the two initial oscillatory response sinusoids are in a harmonic relationship, their peaks in the positive or negative direction will soon occur at the same time. Therefore the second order undamped initial oscillatory shock spectrum becomes

$$a_{2p}(f_1,f_2) = \left|\frac{f_2^2}{f_1^2-f_2^2}\right| a_{1p}(f_1) + \left|\frac{f_1^2}{f_2^2-f_1^2}\right| a_{1p}(f_2) , \quad (44)$$

and is completely determined by the first order initial oscillatory shock spectrum. If a pulse is synthesized by successive application of time functions, or if the initial excitation dies away rapidly, these remarks apply to residual response and residual spectra, as will be evident from Appendix 5.

Starting from Equations (3) and (6) would remove the first term of Equation (43).

To obtain the response of a damped resonator, we replace the transfer function of Equation (35) by

$$\frac{\alpha_1^2+\omega_1^2}{(s+\alpha_1)^2+\omega_1^2} = \frac{\alpha_1^2+\omega_1^2}{(s+\alpha_1-j\omega_1)(s+\alpha_1+j\omega_1)} \quad (45)$$

where

$$\alpha_1 = \omega_1/2Q_1 . \quad (46)$$

and

$$\omega_1 = \sqrt{k/m-c^2/4m^2} , \quad (47)$$

with standard notation for mass, damping and stiffness.

The response, formerly given by Equation (37), becomes

$$a_1(t) = L(0) + \sum_{k=1}^{m} \frac{(\alpha_1^2+\omega_1^2)(s-s_k)L_0(s)}{(s_k+\alpha_1)^2+\omega_1^2}\Big|_{s=s_k} e^{s_k t} + \frac{(\alpha_1^2+\omega_1^2)L_0(s)}{(s+\alpha_1+j\omega_1)}\Big|_{s=-\alpha_1+j\omega_1} e^{(-\alpha_1+j\omega_1)t} + \frac{(\alpha_1^2+\omega_1^2)L_0(s)}{(s+\alpha_1-j\omega_1)}\Big|_{s=-\alpha_1-j\omega_1} e^{(-\alpha_1-j\omega_1)t} \quad (48)$$

For the special case of the unit function represented by Equation (3) and whose transform is given by Equation (4), this reduces to

$$a_1 = 1 - e^{-\alpha_1 t}\cos\omega_1 t - (\alpha_1/\omega_1) e^{-\alpha_1 t}\sin\omega_1 t = 1 - e^{-\alpha_1 t}\cos\omega_1 t - (1/2Q_1) e^{-\alpha_1 t}\sin\omega_1 t . \quad (49)$$

To obtain the second order damped response, corresponding to the model of Figure 2, we replace the transfer function of Equation (42 by

$$\frac{(\alpha_1^2+\omega_1^2)(\alpha_2^2+\omega_2^2)}{[(s+\alpha_1)^2+\omega_1^2][(s+\alpha_2)^2+\omega_2^2]} = \frac{(\alpha_1^2+\omega_1^2)(\alpha_2^2+\omega_2^2)}{(s+\alpha_1-j\omega_1)(s+\alpha_1+j\omega_1)(s+\alpha_2-j\omega_2)(s+\alpha_2+j\omega_2)} \quad (50)$$

The response, formerly given by Equation (43) becomes

$$a_2(t) = L_0(0) + \sum_{k=1}^{m} \frac{(\alpha_1^2+\omega_1^2)(\alpha_2^2+\omega_2^2)(s-s_k)L_0(s)}{[(s+\alpha_1)^2+\omega_1^2][(s+\alpha_2)^2+\omega_2^2]}\Big|_{s=s_k} e^{s_k t} + \frac{(\alpha_1^2+\omega_1^2)(\alpha_2^2+\omega_2^2)L_0(s)}{(s+\alpha_1+j\omega_1)[(s+\alpha_2)^2+\omega_2^2]}\Big|_{s=-\alpha_1+j\omega_1} e^{(-\alpha_1+j\omega_1)t} + \frac{(\alpha_1^2+\omega_1^2)(\alpha_2^2+\omega_2^2)L_0(s)}{(s+\alpha_1-j\omega_1)[(s+\alpha_2)^2+\omega_2^2]}\Big|_{s=-\alpha_1-j\omega_1} e^{(-\alpha_1-j\omega_1)t} + \frac{(\alpha_1^2+\omega_1^2)(\alpha_2^2+\omega_2^2)L_0(s)}{[(s+\alpha_1)^2+\omega_1^2](s+\alpha_2+j\omega_2)}\Big|_{s=-\alpha_2+j\omega_2} e^{(-\alpha_2+j\omega_2)t} + \frac{(\alpha_1^2+\omega_1^2)(\alpha_2^2+\omega_2^2)L_0(s)}{[(s+\alpha_1)^2+\omega_1^2](s+\alpha_2-j\omega_2)}\Big|_{s=-\alpha_2-j\omega_2} e^{(-\alpha_2-j\omega_2)t} \quad (51)$$

For the step function, this reduces to

$$a_2(t) = 1 - \frac{(\alpha_2^2+\omega_2^2)[\alpha_1(\omega_2/\omega_1)(\alpha_1-\alpha_2) + (\alpha_1-\alpha_2)^2+\omega_1^2-\omega_2^2]e^{-\alpha_1 t}\cos\omega_1 t}{[(\alpha_1-\alpha_2)^2+(\omega_1-\omega_2)^2][\alpha_1-\alpha_2)^2+(\omega_1+\omega_2)^2]}$$

$$- \frac{(\alpha_2^2+\omega_2^2)[\alpha_1(\alpha_1-\alpha_2)^2-\alpha_1(\omega_1^2-\omega_2^2)-\omega_1\omega_2(\alpha_1-\alpha_2)]e^{-\alpha_1 t}\sin\omega_1 t}{[(\alpha_1-\alpha_2)^2+(\omega_1-\omega_2)^2][\alpha_1-\alpha_2)^2+(\omega_1+\omega_2)^2]}$$

$$- \frac{(\alpha_1^2+\omega_1^2)[\alpha_2(\omega_1/\omega_2)(\alpha_2-\alpha_1)+(\alpha_2-\alpha_1)^2+\omega_2^2-\omega_1^2]e^{-\alpha_2 t}\cos\omega_2 t}{[(\alpha_1-\alpha_2)^2+(\omega_1-\omega_2)^2][(\alpha_1-\alpha_2)^2+(\omega_1+\omega_2)^2]}$$

$$- \frac{(\alpha_1^2+\omega_1^2)[\alpha_2(\alpha_2-\alpha_1)^2-\alpha_2(\omega_2^2-\omega_1^2)-\omega_1\omega_2(\alpha_2-\alpha_1)]e^{-\alpha_2 t}\sin\omega_2 t}{[(\alpha_1-\alpha_2)^2+(\omega_1-\omega_2)^2][(\alpha_1-\alpha_2)^2+(\omega_1+\omega_2)^2]} . \qquad (52)$$

APPENDIX 5

Residual Response

We now wish to show that relationship of the initial oscillatory responses to transforms hold also for the more familiar residual responses, taking the first order response as an example.

It can readily be shown from the rules of complex algebra that the last two terms of Equation (47), representing the first order residual response, combine into a decaying sinusoid whose magnitude is $(\alpha_1^2+\omega_1^2)/\omega_1$ times the magnitude of $L_0(-\alpha_1+j\omega_1)$.

Now, if two or more elementary excitations are used successively to produce a pulse of finite duration, the residual response will consist of the sum of transients, like the last two terms, successively excited. Let us consider as an example two successive excitations as in the square wave, the first initiated at $t = 0$, and the second initiated at $t = \tau$. Let their transforms as functions of time after starting time $L_{01}(s)$ and $L'_{02}(s)$. Let the transform of the second excitation as a function t be $l_{02}(s)$. We wish to show specifically that the residual response has a magnitude $(\alpha_1^2+\omega_1^2)/\omega_1$ times the magnitude of the Laplace transform of the entire pulse.

$$L_0(s) = L_{01}(s) + L_{02}(s). \qquad (53)$$

But, from Equation (15)

$$L_{02}(s) = e^{-\tau s} L'_{02}(s) . \qquad (54)$$

The residual response is given by the sum of transients

$$\frac{\alpha_1^2+\omega_1^2}{2j\omega_1} L_{01}(-\alpha_1+j\omega_1)e^{(-\alpha_1+j\omega_1)t}$$

$$+ \frac{\alpha_1^2+\omega_1^2}{-2j\omega_1} L_{01}(-\alpha_1-j\omega_1)e^{(-\alpha_1-j\omega_1)t}$$

$$+ \frac{\alpha_1^2+\omega_1^2}{2j\omega_1} L'_{02}(-\alpha_1+j\omega_1)e^{(-\alpha_1+j\omega_1)(t-\tau)}$$

$$+ \frac{\alpha_1^2+\omega_1^2}{-2j\omega_1} L'_{02}(-\alpha_1-j\omega_1)e^{(-\alpha_1-j\omega_1)(t-\tau)}$$

$$= \frac{\alpha_1^2+\omega_1^2}{2j\omega_1} L_{01}(-\alpha_1+j\omega_1)e^{(-\alpha_1+j\omega_1)t}$$

$$+ \frac{\alpha_1^2+\omega_1^2}{-2j\omega_1} L_{01}(-\alpha_1-j\omega_1)e^{(-\alpha_1-j\omega_1)t}$$

$$+ \frac{\alpha_1^2+\omega_1^2}{2j\omega_1} L_{02}(-\alpha_1+j\omega_1)e^{(-\alpha_1+j\omega_1)t}$$

$$+ \frac{\alpha_1^2+\omega_1^2}{-2j\omega_1} L_{02}(-\alpha_1-j\omega_1)e^{(-\alpha_1-j\omega_1)t}$$

$$= \frac{\alpha_1^2+\omega_1^2}{2j\omega_1} L_0(-\alpha_1+j\omega_1)e^{(-\alpha_1+j\omega_1)t}$$

$$+ \frac{\alpha_1^2+\omega_1^2}{-2j\omega_1} L_0(-\alpha-j\omega_1)e^{(-\alpha_1-j\omega_1)t} , \qquad (55)$$

which proves the point for the Laplace transform. If, now, the damping approaches zero, this expression becomes

$$-j\frac{2\pi f_1}{2} F_0(f_1)\, e^{j\omega_1 t} + j\frac{2\pi f_1}{2} F_0(-f_1)\, e^{-j\omega t} \quad (56)$$

where here $F_0(f_1)$ is used to represent the Fourier transform of the entire pulse. The relation of the undamped residual spectrum to the Fourier transform has been proved more simply by means of a Duhamel integral.[9]

REFERENCES

1. M. A. Biot, "Analytical and Experimental Methods in Engineering Seismology", Transactions of the American Society of Civil Engineers, No. 108, pp. 365-385, 1943.

2. J. T. Broch, Application of B&K Equipment to Mechanical Vibration and Shock Measurements, 1972 edition.

3. J. D. Favour, J. M. LeBrun and J. P. Young, "Transient Waveform Control of Electromagnetic Vibration Test Equipment", Shock and Vibration Bulletin 40, Part 2, pp. 157-171, December 1969.

4. C. T. Morrow, "The Shock Spectrum as a Criterion of Severity of Shock Impulses", Journal of the Acoustical Society of America, Vol. 29, No. 5, pp. 596-602, May 1957.

5. L. S. Jacobsen and R. S. Ayre, "A Comparative Study of Pulse and Step-Type Loads on a Simple Vibratory System", Technical Report 16, Structures and Dynamics, Contract N6-ORI 154 Task 1, Stanford University, 1952.

6. C. T. Morrow and H. I. Sargeant, "Sawtooth Shock as a Component Test", Journal of the Acoustical Society of America, Vol. 28, No. 5, pp. 959-965, Sept. 1956.

7. C. T. Morrow, "Shock Analysis Errors in the Presence of Vibration", Shock and Vibration Bulletin 43, Part 1, pp. 55-59, June 1973.

8. C. T. Morrow, "Residual versus Initial (Primary) Shock Spectra", The Shock and Vibration Digest, Vol. 3, No. 4, pp. 5-6, April 1971.

9. S. Rubin, "Concepts in Shock Data Analysis", Chapter 23 of SHOCK AND VIBRATION HANDBOOK, Volume 2, edited by C. M. Harris and C. E. Crede, McGraw-Hill, 1961.